

Copyright © 2005

by the Board of Trustees of the Leland Stanford Junior University

Stanford, California 94305

*Copying permitted for all internal purposes of the Sponsors of
Stanford Exploration Project*

Preface

The electronic version of this report¹ makes the included programs and applications available to the reader. The markings [ER], [CR], and [NR] are promises by the author about the reproducibility of each figure result. Reproducibility is a way of organizing computational research that allows both the author and the reader of a publication to verify the reported results. Reproducibility facilitates the transfer of knowledge within SEP and between SEP and its sponsors.

ER denotes Easily Reproducible and are the results of processing described in the paper. The author claims that you can reproduce such a figure from the programs, parameters, and makefiles included in the electronic document. The data must either be included in the electronic distribution, be easily available to all researchers (e.g., SEG-EAGE data sets), or be available in the SEP data library². We assume you have a UNIX workstation with Fortran, Fortran90, C, X-Windows system and the software downloadable from our website (SEP makerules, SEPlib, and the SEP latex package), or other free software such as SU. Before the publication of the electronic document, someone other than the author tests the author's claim by destroying and rebuilding all ER figures. Some ER figures may not be reproducible by outsiders because they depend on data sets that are too large to distribute, or data that we do not have permission to redistribute but are in the SEP data library.

CR denotes Conditional Reproducibility. The author certifies that the commands are in place to reproduce the figure if certain resources are available. SEP staff have only attempted to make sure that the makefile rules exist and the source codes referenced are provided. The primary reasons for the CR designation is that the processing requires 20 minutes or more, or commercial packages such as Matlab or Mathematica.

M denotes a figure that may be viewed as a movie in the web version of the report. A movie may be either ER or CR.

NR denotes Non-Reproducible figures. SEP discourages authors from flagging their figures as NR except for figures that are used solely for motivation, comparison, or illustration of the theory, such as: artist drawings, scannings, or figures taken from SEP reports not by the authors or from non-SEP publications.

Our testing is currently limited to LINUX 2.4 (using the Portland Group Fortran90 compiler), but the code should be portable to other architectures. Reader's suggestions are welcome. For more information on reproducing SEP's electronic documents, please visit

<<http://sepwww.stanford.edu/r> `esear ch/r edoc />`.

¹<http://sepwww.stanford.edu/private/docs/sep123>

²http://sepwww.stanford.edu/public/docs/sepdata/lib/toc_html/

SEP-123 — TABLE OF CONTENTS

Imaging

<i>Biondi B.</i> , Angle-domain common image gathers for anisotropic migration	1
<i>Biondi B.</i> , Residual moveout in anisotropic angle-domain common image gathers	25
<i>Shragge J.</i> , Wave-equation migration from topography: Imaging Husky	49
<i>Artman B.</i> , Direct migration: The only way	57
<i>Artman B. and Clapp R. G.</i> , Nondestructive testing by migration	69

Inversion

<i>Valenciano A. A. and Biondi B.</i> , Wave-equation angle-domain Hessian	75
<i>Valenciano A. A., Biondi B., and Guitton A.</i> , Target-oriented wave-equation inversion: Sigbee model	83
<i>Clapp R. G.</i> , AMO inversion to a common azimuth dataset	91
<i>Wang H.</i> , Iterative linearized migration and inversion	101

Multiples

<i>Alvarez G.</i> , Mapping of water-bottom and diffracted	129
<i>Wang H.</i> , Imaging primaries and multiples simultaneously with depth-focusing	155

Rock Physics

<i>Berryman J. G.</i> , Geomechanical analysis with rigorous error estimates for a double-porosity reservoir model	161
------------------------------------------------------------------------------------------------------------------------------	-----

SEP article published or in press, 2004-05	173
SEP phone directory	177

Research personnel	179
SEP sponsors for 2004-05	183

Angle-domain common image gathers for anisotropic migration

*Biondo Biondi*¹

ABSTRACT

I present a general methodology for computing Angle-Domain Common Image Gathers (ADCIGs) in conjunction with anisotropic wavefield-continuation migration. The method is based on the transformation of the prestack image from the subsurface-offset domain to the angle domain by use of slant stacks. The processing sequence is the same as for the computation of ADCIGs for the isotropic case, though the interpretation of the relationship between the slopes measured in the prestack image and the aperture angles are more complex. I demonstrate that the slopes measured by performing slant stack along the subsurface-offset axis of the prestack image are a good approximation of the phase aperture angles, and that they are exactly equal to the phase aperture angles for flat reflectors in Vertical Transverse Isotropic (VTI) media. In the general case of dipping reflectors, the true aperture angles can be easily computed as a function of the reflector dip and anisotropic slowness at the reflector.

I derive the relationships between phase angles and slopes measured in the prestack image from both a “plane-wave” viewpoint and a “ray” viewpoint. The two derivations are consistent with each other, as demonstrated by the fact that in the special case of flat reflectors they lead to exactly the same expression. The ray-theoretical derivation is based on a novel generalization of kinematic migration to the computation of prestack images as a function of the subsurface offset. This theoretical development leads to the linking of the kinematics in ADCIGs with migration-velocity errors, and thus it enables the use of ADCIGs for velocity estimation.

I apply the proposed method to the computation of ADCIGs from the prestack image obtained by anisotropic migration of a 2-D line extracted from a Gulf of Mexico 3-D data set. The analysis of the error introduced by neglecting the difference between the true phase aperture angle and the angles computed through slant stack shows that these errors are negligible and can be safely ignored in realistic situations. On the contrary, group aperture angles can be quite different from phase aperture angles and thus ignoring the distinction between these two angles can be detrimental to practical applications of ADCIGs.

¹email: biondo@sep.stanford.edu

INTRODUCTION

Angle-Domain Common Image Gathers (ADCIGs) have become a common tool for analyzing prestack images obtained by wavefield-continuation migration. They can be used for both updating migration velocity after wavefield-continuation migration (Biondi and Sava, 1999; Clapp and Biondi, 2000), as well as the analysis of amplitudes as a function of aperture angle (Wang et al., 2005).

All the present methods for computing ADCIGs in conjunction with wavefield migration are limited to isotropic migration; this is true for both the methods applied during downward continuation before imaging (Prucha et al., 1999), and the methods applied on the prestack migrated image as a post-processing operator (Sava and Fomel, 2003; Rickett and Sava, 2002; Biondi and Tisserant, 2004). Similarly, the quantitative analysis of the residual moveout measured in ADCIGs caused by migration-velocity errors is also limited to the isotropic case (Biondi and Symes, 2003; Biondi and Tisserant, 2004).

In this paper I generalize the methodologies for computing and analyzing ADCIGs to prestack images obtained by wavefield-continuation anisotropic migration. In a companion paper (Biondi, 2005) I derive the expressions for computing residual moveout in ADCIGs as a function of errors in the anisotropic parameters used for migration. This work is practically motivated by two current trends in the seismic exploration industry: 1) data are recorded with increasingly longer offsets, widening the range of propagation angles and thus making the inclusion of anisotropic effects crucial to the complete focusing of reflections, 2) anisotropic prestack depth migration is increasingly being used in areas, like near or under salt bodies, where the image quality, and consequently the velocity estimation process, could benefit from the use of wavefield-continuation migration (Bear et al., 2003; Sarkar and Tsvankin, 2004).

The main conceptual differences between isotropic ADCIGs and anisotropic ADCIGs are related to the fact that in anisotropic wave propagation the phase angles and velocities are different from the group angles and velocities (Tsvankin, 2001). Therefore, I will first address the question of which aperture angles we are measuring in the ADCIGs. I demonstrate that the transformation to angle domain maps the reflection into the phase-angle domain. Strictly speaking, this mapping is exact only for events normal to the isotropic axis of symmetry (e.g. flat events for Vertical Transverse Isotropic (VTI) media), because the presence of dips biases the estimates. This bias is caused by the difference in propagation velocity between the incident and the reflected waves, and thus for VTI media it is small unless the anisotropy is strong and the dips steep. The real-data example shown in this paper indicates that, for realistic values of anisotropy, the errors caused by the geological dips are small and can be neglected. This approximation greatly simplifies the computation of ADCIGs and thus makes their application more attractive. When the accuracy of this approximation is not sufficient, the true aperture angles can be easily computed from the measured slopes in the prestack image by iteratively solving a system of two non-linear equations, which usually converge to the solution in only few iterations.

The methodology developed in this paper is limited to the the imaging of acoustic data and thus is limited to the acoustic approximation of elastic anisotropic wave propagation. Further-

more, the numerical examples are limited to VTI media defined by their vertical velocity and two of the three Thomsen parameters: ϵ , δ , and η . However, the basic concepts have a general validity and the generalization to more general anisotropic media, such as Tilted Transverse Isotropic (TTI) media should be fairly straightforward, though outside the scope of this paper.

PHASE AND GROUP ANGLES AND VELOCITIES

In anisotropic wave propagation the phase angles and velocities are different from the group angles and velocities. In this section I briefly review the concepts of phase and group angles and velocities and the relationships between these physical quantities. I also define the particular approximation to a VTI medium that I use in the numerical examples.

The transformation from phase velocity \tilde{V} to group velocity V is conventionally defined as the following (Tsvankin, 2001):

$$V = \sqrt{\tilde{V}^2 + \left(\frac{d\tilde{V}}{d\tilde{\theta}}\right)^2}, \quad (1)$$

where $\tilde{\theta}$ is the phase propagation angle. The associated transformation from phase angles to group angles θ is defined as:

$$\tan\theta = \frac{\tan\tilde{\theta} + \frac{1}{V} \frac{d\tilde{V}}{d\tilde{\theta}}}{1 - \frac{1}{V} \frac{d\tilde{V}}{d\tilde{\theta}} \tan\tilde{\theta}}. \quad (2)$$

Notice that throughout this paper I use the tilde symbol to distinguish between phase quantities (with a tilde) and group quantities (without a tilde).

Dellinger and Muir (1985) propose, and heuristically motivate, the following symmetric relations for the inverse transforms:

$$\tilde{S} = \sqrt{S^2 + \left(\frac{dS}{d\theta}\right)^2}, \quad (3)$$

where \tilde{S} and S are respectively the phase slowness and the group slowness, and

$$\tan\tilde{\theta} = \frac{\tan\theta + \frac{1}{\tilde{S}} \frac{dS}{d\theta}}{1 - \frac{1}{\tilde{S}} \frac{dS}{d\theta} \tan\theta}. \quad (4)$$

I use the heuristic relation in equation 4 to derive some of the analytical results presented in this paper. Furthermore, I use all the above relationships to compute the kinematic numerical results presented in this paper.

The numerical results, though not the analytical results, are also dependent on the choice of a specific approximation of the anisotropic phase-velocity function. I used the following

VTI approximation for the phase velocity:

$$\tilde{V}_{\text{VTI}}^2(\theta) = \frac{V_V^2 \cos^2 \theta + V_H^2 \sin^2 \theta + \sqrt{(V_V^2 \cos^2 \theta + V_H^2 \sin^2 \theta)^2 + V_V^2 (V_N^2 - V_H^2) \sin^2 2\theta}}{2}, \quad (5)$$

where V_V , V_H , V_N , are respectively the vertical velocity, the horizontal velocity and the NMO velocity. Following Fowler (2003), the corresponding approximation for the group velocity is the following:

$$S_{\text{VTI}}^2(\theta) = \frac{S_V^2 \cos^2 \theta + S_H^2 \sin^2 \theta + \sqrt{(S_V^2 \cos^2 \theta + S_H^2 \sin^2 \theta)^2 + S_V^2 (S_N^2 - S_H^2) \sin^2 2\theta}}{2}, \quad (6)$$

where S_V , S_H , S_N , are respectively the vertical slowness, the horizontal slowness and the NMO slowness.

The numerical results obtained by modeling and migrating synthetic seismic data and by migrating the real data were obtained by source-receiver depth continuation (upward for modeling and downward for migration) using the following dispersion relation:

$$k_z = \frac{\omega}{V_V} \sqrt{\frac{\omega^2 - V_H^2 k_x^2}{\omega^2 + (V_N^2 - V_H^2) k_x^2}}, \quad (7)$$

where ω is the temporal frequency, and k_x and k_z are respectively the horizontal and vertical wavenumbers. The dispersion relation shown in equation 7 corresponds to the velocity and slowness functions in equations 5 and 6 (Fowler, 2003).

ANGLE GATHERS BY ANISOTROPIC DOWNWARD-CONTINUATION MIGRATION

In this section I develop the theory for anisotropic ADCIGs from the “plane-wave” viewpoint. I assume that in the proximity of the reflection point the source wavefield and the receiver wavefield are plane waves and I derive the relationships between the propagation angles of these plane waves and the slopes computed in the prestack image. This assumption is not restrictive because the source and receiver wavefields can always be considered as the superposition of plane waves.

In anisotropic media, when the reflector is dipping with respect to the normal to the isotropic axis of symmetry (horizontal direction for VTI) the incident and reflected aperture angles differ. This difference is caused by the fact that, although the phase slowness is function of the propagation angle, Snell law requires that the components parallel to the reflector of the incident and reflected slowness vectors must match at the interface. However, we can still define an “average” aperture angle $\tilde{\gamma}$ and “average” dip angle $\tilde{\alpha}_x$ using the following relationships:

$$\tilde{\gamma} = \frac{\tilde{\beta}_r - \tilde{\beta}_s}{2}, \quad \text{and} \quad \tilde{\alpha}_x = \frac{\tilde{\beta}_s + \tilde{\beta}_r}{2}, \quad (8)$$

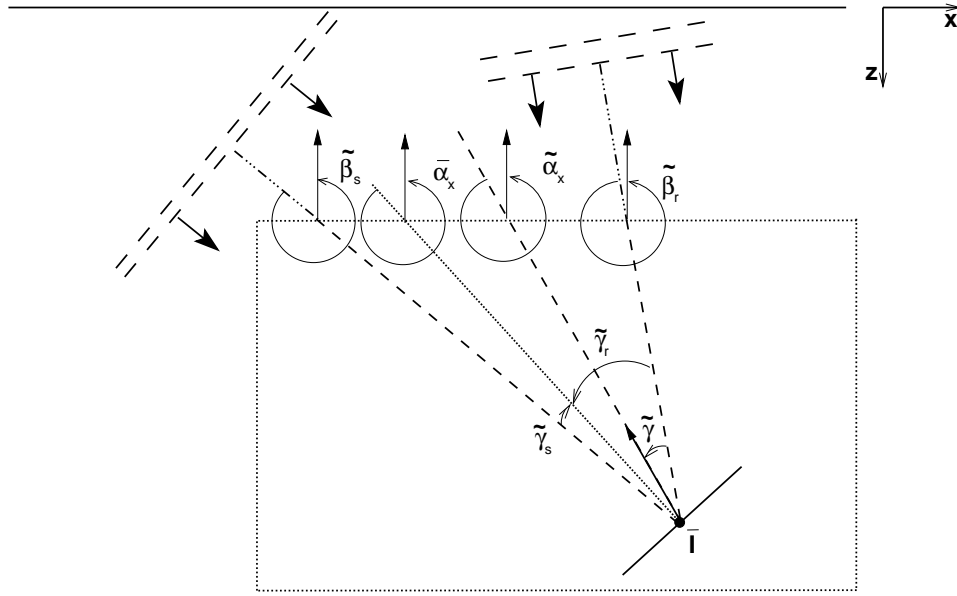


Figure 1: Sketch representing the reflection of a plane wave from a planar reflector in an anisotropic medium. The angles marked in the figure are all phase angles. They are defined as follows: $\tilde{\beta}_s$ and $\tilde{\beta}_r$ are the propagation angles of the incident and reflected plane waves, $\tilde{\gamma}_s$ and $\tilde{\gamma}_r$ are the true aperture angles for the the incident and reflected plane waves, $\bar{\alpha}_x$ is the true geological dip angle, $\tilde{\gamma}$ are $\tilde{\alpha}_x$ the average aperture angle and the average dip angle.

biondo1-cig-aniso-v3 [NR]

where the $\tilde{\beta}_s$ and $\tilde{\beta}_r$ are the phase angles of the incident and reflected plane waves, respectively.

Figure 1 shows the geometric interpretation of these angles. Notice that the average dip angle $\tilde{\alpha}_x$ is different from the true geological dip angle $\bar{\alpha}_x$, and that the average aperture angle $\tilde{\gamma}$ is obviously different from the true aperture angles $\tilde{\gamma}_s$ and $\tilde{\gamma}_r$. However, these five angles are related and, if needed, the true angles can be derived from the average angles, as shown in Appendix A.

Prestack images defined in the subsurface-offset (h_ξ) domain are transformed into the angle domain by applying slant stacks. The transformation axis is thus the physical dip of the image along the subsurface offset; that is, $\partial z_\xi / \partial h_\xi$. The dip angles can be similarly related to the midpoint dips in the image; that is, $\partial z_\xi / \partial m_\xi$. Following the derivation of acoustic isotropic ADCIGs by Sava and Fomel (2003) and of converted-waves ADCIGs by Rosales and Rickett (2001), we can write the following relationships between the propagation angles

and the derivative measured from the wavefield:

$$\left. \frac{\partial t}{\partial z_\xi} \right|_{(m_\xi = \bar{m}_\xi, h_\xi = \bar{h}_\xi)} = \tilde{S}_s \cos(\tilde{\alpha}_x - \tilde{\gamma}) - \tilde{S}_r \cos(\tilde{\alpha}_x + \tilde{\gamma}), \quad (9)$$

$$\left. \frac{\partial t}{\partial m_\xi} \right|_{(z_\xi = \bar{z}_\xi, h_\xi = \bar{h}_\xi)} = \tilde{S}_s \sin(\tilde{\alpha}_x - \tilde{\gamma}) + \tilde{S}_r \sin(\tilde{\alpha}_x + \tilde{\gamma}), \quad (10)$$

$$\left. \frac{\partial t}{\partial h_\xi} \right|_{(z_\xi = \bar{z}_\xi, m_\xi = \bar{m}_\xi)} = \tilde{S}_s \sin(\tilde{\alpha}_x - \tilde{\gamma}) - \tilde{S}_r \sin(\tilde{\alpha}_x + \tilde{\gamma}), \quad (11)$$

where \tilde{S}_s and \tilde{S}_r are the phase slownesses for the source and receiver wavefields, respectively. We obtain the expression for the offset dip by taking the ratio of equation 11 with equation 9, and similarly for the midpoint dips by taking the ratio of equation 10 with equation 9, and after some algebraic manipulations, we obtain the following expressions:

$$\left. \frac{\partial z_\xi}{\partial h_\xi} \right|_{(m_\xi = \bar{m}_\xi)} = \frac{\tan \tilde{\gamma} + \frac{\tilde{S}_r - \tilde{S}_s}{\tilde{S}_r + \tilde{S}_s} \tan \tilde{\alpha}_x}{1 - \frac{\tilde{S}_r - \tilde{S}_s}{\tilde{S}_r + \tilde{S}_s} \tan \tilde{\alpha}_x \tan \tilde{\gamma}}, \quad (12)$$

$$\left. \frac{\partial z_\xi}{\partial m_\xi} \right|_{(h_\xi = \bar{h}_\xi)} = \frac{\tan \tilde{\alpha}_x + \frac{\tilde{S}_r - \tilde{S}_s}{\tilde{S}_r + \tilde{S}_s} \tan \tilde{\gamma}}{1 - \frac{\tilde{S}_r - \tilde{S}_s}{\tilde{S}_r + \tilde{S}_s} \tan \tilde{\gamma} \tan \tilde{\alpha}_x}. \quad (13)$$

In contrast with the equivalent relationships valid for isotropic media, these relationships depend on both the aperture angle $\tilde{\gamma}$ and the dip angle $\tilde{\alpha}_x$. The expression for the offset dip (equation 9) simplifies into the known relationship valid in isotropic media when either the difference between the phase slownesses is zero, or the dip angle $\tilde{\alpha}_x$ is zero. In VTI media this happens for flat geological dips. In a general TTI medium this condition is fulfilled when the geological dip is normal to the axis of symmetry.

Solving for $\tan \tilde{\gamma}$ and $\tan \tilde{\alpha}_x$ we obtain the following:

$$\tan \tilde{\gamma} = \frac{\frac{\partial z_\xi}{\partial h_\xi} - \Delta_{\tilde{\gamma}} \tan \tilde{\alpha}_x}{1 + \frac{\partial z_\xi}{\partial h_\xi} \Delta_{\tilde{\gamma}} \tan \tilde{\alpha}_x}, \quad (14)$$

$$\tan \tilde{\alpha}_x = \frac{\frac{\partial z_\xi}{\partial m_\xi} - \Delta_{\tilde{\gamma}} \tan \tilde{\gamma}}{1 + \frac{\partial z_\xi}{\partial m_\xi} \Delta_{\tilde{\gamma}} \tan \tilde{\gamma}}, \quad (15)$$

where for convenience I substituted the symbol $\Delta_{\tilde{\gamma}}$ for the “normalized slowness difference” $(\tilde{S}_r - \tilde{S}_s)/(\tilde{S}_r + \tilde{S}_s)$.

Substituting equation 15 in equation 14, and equation 14 into equation 15, we get the following two quadratic expressions that can be solved to estimate the angles as a function of the dips measured from the image:

$$\left[\frac{\partial z_\xi}{\partial m_\xi} \Delta_{\tilde{\gamma}} - \frac{\partial z_\xi}{\partial h_\xi} \Delta_{\tilde{\gamma}}^2 \right] \tan^2 \tilde{\gamma} + [1 - \Delta_{\tilde{\gamma}}^2] \tan \tilde{\gamma} + \frac{\partial z_\xi}{\partial m_\xi} \Delta_{\tilde{\gamma}} - \frac{\partial z_\xi}{\partial h_\xi} = 0, \quad (16)$$

$$\left[\frac{\partial z_\xi}{\partial h_\xi} \Delta_{\tilde{\gamma}} - \frac{\partial z_\xi}{\partial m_\xi} \Delta_{\tilde{\gamma}}^2 \right] \tan^2 \tilde{\alpha}_x + [1 - \Delta_{\tilde{\gamma}}^2] \tan \tilde{\alpha}_x + \frac{\partial z_\xi}{\partial h_\xi} \Delta_{\tilde{\gamma}} - \frac{\partial z_\xi}{\partial m_\xi} = 0. \quad (17)$$

These are two independent quadratic equations in $\tan \tilde{\gamma}$ and $\tan \tilde{\alpha}_x$ that can be solved independently. If the “normalized slowness difference” $\Delta_{\tilde{\gamma}}$ between the slowness along the propagation directions of the source and receiver wavefields are known, we can directly compute $\tilde{\gamma}$ and $\tilde{\alpha}_x$, and then the true $\tilde{\beta}_s$ and $\tilde{\beta}_r$. One important case in this category is when we image converted waves.

For anisotropic velocities, the slownesses depend on the propagation angles, and thus the normalized difference depends on the unknown $\tilde{\gamma}$ and $\tilde{\alpha}_x$. In practice, these equations can be solved by a simple iterative process that starts by assuming the “normalized difference” to be equal to zero. In all numerical test I conducted this iterative process converges to the correct solution in only a few iterations, and thus is not computationally demanding.

If the anisotropic slowness function were spatially homogeneous, equations 16 and 17 could be solved iteratively in the Fourier domain, and the transformation to the average angles $\tilde{\gamma}$ and $\tilde{\alpha}_x$ could be computed exactly without the need of estimating the apparent reflector dip in the space domain. When the anisotropic parameters are a function of the spatial variables; that is, in the majority of the real situations, the solution of equations 16 and 17 requires the estimation of the local reflector dip in the space domain. If necessary, the reflectors’ dip can be either extracted from the interpretation of the horizons of interest, or can be automatically estimated from the image by applying one of the several methods that have been presented in the literature (see for example Fomel (2002)). In practice, the estimation of the reflector dip is seldom necessary. The numerical and real-data examples shown below indicate that for practical values of the anisotropy parameters the dependency of the estimate from the dip angles can be safely ignored for small dips, and it is unlikely to constitute a problem for steep dips.

KINEMATIC ANALYSIS OF ADCIGS BY INTEGRAL MIGRATION

The analysis shown in the previous section provides the fundamental equations to relate the offset and midpoint dips measured from prestack images to the phase angles at the reflection point. However, the previous analysis is not directly applicable to the analysis of the kinematic properties of events in the ADCIGs because it is based on plane waves. An important application of ADCIGs is the measurements of residual moveout along the aperture angle (i.e. departure from flatness) caused by velocity errors. To achieve this goal we must relate traveltimes errors accumulated during the propagation in the overburden to movements of the migrated events in the ADCIG. This task is easier in the ray domain than in the plane-wave domain because traveltimes errors are naturally evaluated along rays, which are related to group velocity and angles. To overcome this obstacle toward the use of ADCIGs for velocity estimation, in this section I introduce an integral formulation of the methodology to compute angle gathers that enables a simple link between ADCIGs and kinematics. The following analysis has also the theoretical value of being independent from the migration method applied to compute the prestack images (integral method or wavefield-continuation method) and thus of providing a conceptual link between the angle gathers obtained using different migration methods.

My analysis is based on the conceptual generalization of integral (Kirchhoff) migration to

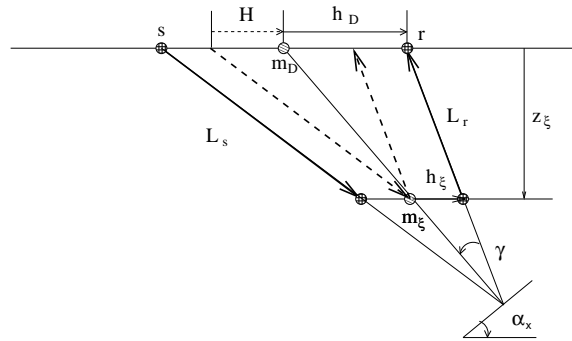


Figure 2: Geometry used for evaluating the impulse response of the generalized integral migration.

`biondo1-imp-resp` [NR]

the computation of sub-surface offset gathers. Integral migration is defined by the summation surfaces over which the data are integrated to compute the image at every point in the image space. The shapes of these summation surfaces are usually computed as the sum of the time delays from the image point (z_ξ, m_ξ) in the subsurface to the source and receiver locations at the surface. The basic idea underlying the generalization I introduce in this paper, is that we can compute the summation surfaces by evaluating the time delays starting not from the same point in the subsurface for both the source and receiver rays, but starting from two points horizontally shifted by $\pm h_\xi$ with respect to the image point. The summation of data along these surfaces produces a prestack image as a function of the subsurface offset that is kinematically equivalent to the image created by wavefield-continuation migrations such as source-receiver downward continuation, or shot-profile migration in conjunction to the generalized imaging condition discussed by Rickett and Sava (2002). Therefore, the kinematic analysis that follows, and its conclusions, are independent from the migration method applied to compute the prestack images. An interesting observation is that the ADCIGs computed using this generalization of integral migration should be immune from the artifacts that affect angle gathers computed by conventional integral migration and discussed by Stolk and Symes (2003).

Generalized migration impulse response in parametric form

Integral migration can be conceptually performed by spreading the data along spreading surfaces as well as by summing data along the summation surfaces discussed above. The spreading surfaces are duals of the summation surfaces and represent the impulse response of the migration operator. In homogeneous anisotropic medium the shape of the impulse responses of the generalized integral migration can be easily evaluated analytically as a function of the subsurface offset h_ξ , in addition to the usual image depth z_ξ and midpoint m_ξ . Figure 2 illustrates the geometry used to evaluate this impulse response. Notice that the angles in this figure (α_x and γ) are missing a tilde because they are group angles, and not phase angles as in the previous section. In an isotropic medium these angles are the dip and aperture angles, but in an anisotropic medium these angles are not easily related to the geological dip and the reflection aperture angles. They can be thought of as convenient parameters to evaluate the impulse response.

Simple trigonometry applied to Figure 2 allows us to express the impulse response in parametric form, as a function of α_x and γ . If we migrate an impulse recorded at time t_D , midpoint

m_D and surface offset h_D , the migration impulse response can be expressed as follows:

$$z_\xi = L(\alpha_x, \gamma) \frac{\cos^2 \alpha_x - \sin^2 \gamma}{\cos \alpha_x \cos \gamma}, \quad (18)$$

$$m_\xi = m_D - L(\alpha_x, \gamma) \frac{\sin \alpha_x}{\cos \gamma}, \quad (19)$$

$$h_\xi = h_D - H = h_D - L(\alpha_x, \gamma) \frac{\sin \gamma}{\cos \alpha_x}, \quad (20)$$

with

$$L(\alpha_x, \gamma) = \frac{L_s + L_r}{2}. \quad (21)$$

In a isotropic medium the half path-length L would be simply given by $t_D/2S$, but in an anisotropic medium it is function of the angles. Its two components L_s and L_r can be calculated by solving the following system of linear equations:

$$t_D = S_s L_s + S_r L_r, \quad (22)$$

$$z_s - z_r = L_s \cos(\alpha_x - \gamma) - L_r \cos(\alpha_x + \gamma) = 0. \quad (23)$$

Equation 22 constraints the total travelttime to be equal to the impulse time, and equations 23 constraints the depth of the end point of the two rays (z_s and z_r) to be equal, since the subsurface offset is assumed to be horizontal. The solution of this system of equation yields the following for the half path-length:

$$L(\alpha_x, \gamma) = \frac{L_s + L_r}{2} = \frac{t_D}{(S_r + S_s) + (S_r - S_s) \tan \alpha_x \tan \gamma}. \quad (24)$$

The combination of equation 24 and equations 18–20 enables the evaluation of the generalized migration impulse response in a arbitrary homogeneous anisotropic medium.

Figure 3 shows a 3-D rendering of the impulse response computed using the previous equations for an impulse with $t_D = .9$ seconds, $m_D = 0$ kilometers, and $h_D = .4$ kilometers, and vertical slowness $S_V = 1$ s/km. The anisotropic parameters correspond to the Taylor Sand as described by Tsvankin (2001) using the three Thomsen parameters: $\epsilon = 0.110$, $\delta = -0.035$, and $\eta = .155$. The gray line (green in color) superimposed onto the impulse response is the result of cutting the surface at zero subsurface offset, and thus corresponds to the conventional impulse response of prestack migration. The black line superimposed onto the impulse response is the result of cutting the surface at zero midpoint. In Figure 4 these two lines are superimposed onto the corresponding vertical sections cut from the images computed by an anisotropic wavefield source-receiver migration applied with the same parameters described above. Figure 4b shows the conventional migration impulse response, whereas Figure 4a shows the zero-midpoint section. The lines computed by applying the kinematic equations perfectly match the impulse responses computed using wavefield migration, confirming the accuracy of the kinematic equations.

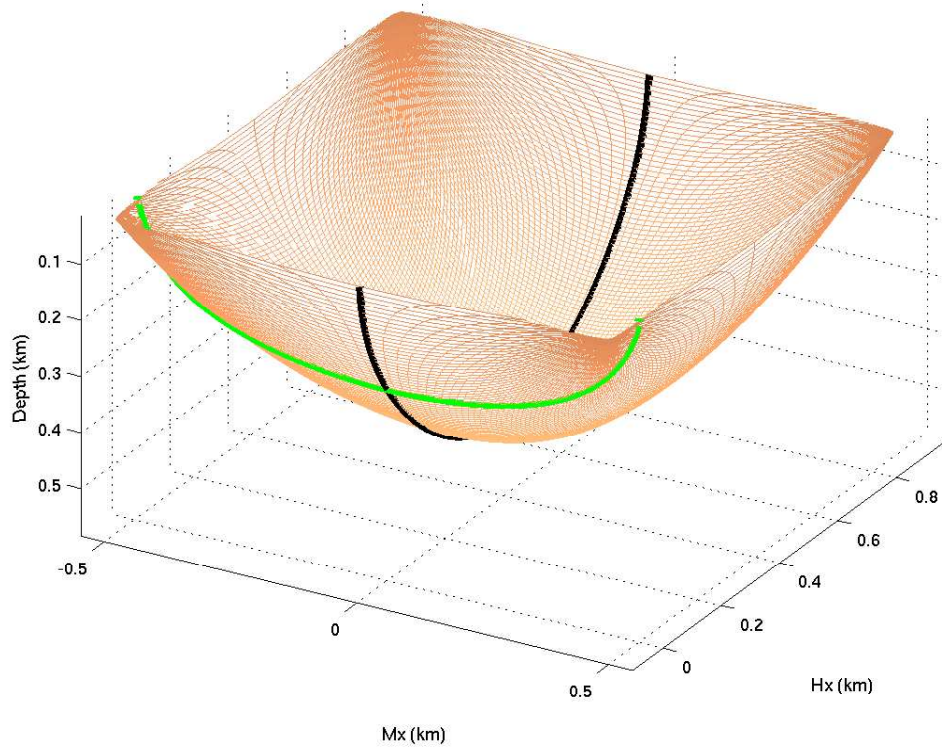
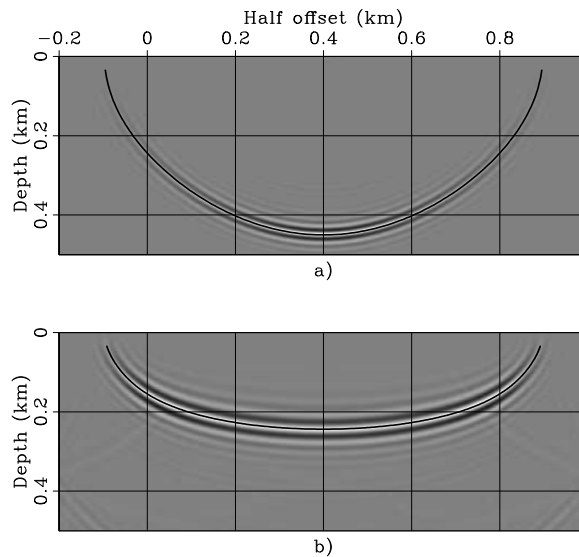


Figure 3: Impulse response of generalized anisotropic prestack migration. The gray line (green in color) superimposed onto the impulse response corresponds to the conventional impulse response of prestack migration. `biondo1-surf_taylor_hxd_dot_4` [CR]

Figure 4: Vertical sections cut from the impulse response computed by an anisotropic wavefield source-receiver migration. The lines superimposed onto the images correspond to the lines superimposed onto the surface shown in Figure 3 and are computed by applying the kinematic expressions presented in equations 18–24. `biondo1-Surf-taylor_hxd_4-overn` [CR]



Analytical evaluation of the tangent plane to the impulse response

The expression for the generalized impulse response of prestack anisotropic migration leads to the analytical evaluation of the offset dip and midpoint dip along the planes tangent to the impulse response, as a function of the group angles and velocity. In this section I demonstrate that in the simple case of flat reflectors this analysis leads to exactly the same results as the phase-space analysis presented in the previous section. The derivation of the general relationships expressed in equations 13 and 12, which are valid for an arbitrary reflector's dip, is left to the reader.

By applying elementary analytical geometry, I demonstrate in Appendix B that the derivative of the depth with respect to the subsurface offset, at constant midpoint, is given by:

$$\left. \frac{\partial z_\xi}{\partial h_\xi} \right|_{m_\xi = \bar{m}_\xi} = - \frac{\frac{\partial z_\xi}{\partial \alpha_x} \frac{\partial m_\xi}{\partial \gamma} - \frac{\partial z_\xi}{\partial \gamma} \frac{\partial m_\xi}{\partial \alpha_x}}{\frac{\partial m_\xi}{\partial \alpha_x} \frac{\partial h_\xi}{\partial \gamma} - \frac{\partial m_\xi}{\partial \gamma} \frac{\partial h_\xi}{\partial \alpha_x}}, \quad (25)$$

and the derivative of the depth with respect to the midpoint, at constant subsurface offset, is given by:

$$\left. \frac{\partial z_\xi}{\partial m_\xi} \right|_{h_\xi = \bar{h}_\xi} = - \frac{\frac{\partial z_\xi}{\partial \alpha_x} \frac{\partial h_\xi}{\partial \gamma} - \frac{\partial z_\xi}{\partial \gamma} \frac{\partial h_\xi}{\partial \alpha_x}}{\frac{\partial m_\xi}{\partial \alpha_x} \frac{\partial h_\xi}{\partial \gamma} - \frac{\partial m_\xi}{\partial \gamma} \frac{\partial h_\xi}{\partial \alpha_x}}. \quad (26)$$

In the special case of flat reflectors the $\partial z_\xi / \partial \alpha_x$ and $\partial h_\xi / \partial \gamma$ vanish, and thus equation 25 simplifies into the following expression:

$$\begin{aligned} \left. \frac{\partial z_\xi}{\partial h_\xi} \right|_{(m_\xi = \bar{m}_\xi, \alpha_x = 0)} &= \frac{\left(\frac{\partial z_\xi}{\partial \gamma} \Big|_{L=\bar{L}} + \frac{\partial L}{\partial \gamma} \cos \gamma \right) \frac{\partial m_\xi}{\partial \alpha_x}}{\left(\frac{\partial h_\xi}{\partial \gamma} \Big|_{L=\bar{L}} - \frac{\partial L}{\partial \gamma} \sin \gamma \right) \frac{\partial m_\xi}{\partial \alpha_x}} \\ &= \frac{\frac{\partial z_\xi}{\partial \gamma} \Big|_{L=\bar{L}} + \frac{\partial L}{\partial \gamma} \cos \gamma}{\frac{\partial h_\xi}{\partial \gamma} \Big|_{L=\bar{L}} - \frac{\partial L}{\partial \gamma} \sin \gamma}. \end{aligned} \quad (27)$$

By substituting into equation 27 the appropriate derivative of the image coordinates and of the half path-length with respect to the angles, all provided in Appendix A, I further simplify the expression into the following:

$$\left. \frac{\partial z_\xi}{\partial h_\xi} \right|_{(m_\xi = \bar{m}_\xi, \alpha_x = 0)} = \frac{\tan \gamma + \frac{1}{S} \frac{\partial S}{\partial \gamma}}{1 - \frac{1}{S} \frac{\partial S}{\partial \gamma} \tan \gamma}. \quad (28)$$

Finally, by applying the transformation from group angles into phase angles expressed in equation 4, I obtain the final result that for flat reflectors the subsurface-offset dip is exactly equal to the tangent of the phase aperture angle $\tilde{\gamma}$; that is:

$$\left. \frac{\partial z_\xi}{\partial h_\xi} \right|_{(m_\xi = \bar{m}_\xi, \alpha_x = 0)} = \tan \tilde{\gamma}. \quad (29)$$

Numerical examples of aperture angle along impulse responses

The analytical kinematic results can be verified by numerical computations of impulse responses by wavefield migration and transformation of the resulting prestack image cubes into the angle domain. Figure 5 shows four zero subsurface-offset sections cut through the impulse responses computed by wavefield-continuation anisotropic migration for three anisotropic rocks and for an isotropic rock. The first anisotropic rock is the Taylor Sand defined above. The second is the Mesa Clay Shale as defined by Tsvankin (2001) using the three Thomsen parameters: $\epsilon = 0.189$, $\delta = 0.204$, and $\eta = -.01$. The third is derived from the Green River Shale as described by Tsvankin (2001) by halving the anisotropic parameters (ϵ and δ); that is, it is defined by the three Thomsen parameters: $\epsilon = 0.0975$, $\delta = -0.11$, and $\eta = .266$. The strong anelliptic nature of the original Green River Shale ($\eta = .74$) causes the group-slowness approximation in equation 6 to break down, and makes the kinematic computations based on ray tracing, and thus on group velocity and angles, inconsistent with wavefield migrations based on the dispersion relation in equation 7. Hereupon I will refer to this rock, for obvious reasons, as the GreenLight River Shale. Notice that the GreenLight River Shale is still strongly elliptical.

The other parameters defining the impulse responses are the same as for Figure 3; that is, $t_D = .9$ seconds, $m_D = 0$ kilometers, and $h_D = .4$ kilometers, and vertical slowness $S_V = 1$ s/km. Figure 5a shows the isotropic case, Figure 5b shows the Taylor Sand case, Figure 5c shows the Mesa Clay Shale case, and Figure 5d shows the GreenLight River Shale case. As in Figure 4, the line superimposed onto the images represent the impulse response computed using the kinematic expressions in equations 18–24. The kinematic curves perfectly predict the shape of the images even for very steep dips.

Figure 6 shows two-dimensional slices cut through the cube obtained by the transformation to the angle domain of the impulse responses shown in Figure 5. The slices are cut at the midpoint and depth corresponding to the expected location of the impulse responses; that is, at the location tracked by the lines shown in Figure 5. There are three lines superimposed onto the angle-domain images. The solid lines display the numerical computation of $\arctan(\partial z_\xi / \partial h_\xi)$ by applying equation 25. They perfectly track, as expected, the results of the transformation of the prestack images to angle domain. The dotted lines display the phase aperture angle $\tilde{\gamma}$. As expected, they overlap with the solid line around the zero midpoint (i.e. flat reflector), and depart from them at larger midpoints, which correspond to steeper reflections. However, the error introduced by ignoring the difference between $\arctan(\partial z_\xi / \partial h_\xi)$ and $\tilde{\gamma}$ is small, and likely to be negligible in most practical situations. Finally, the dashed lines display the group aperture angle γ . The differences between γ and $\tilde{\gamma}$ are substantial, up to 20% in some cases. Ignoring them might be detrimental to the application of ADCIGs. Notice that in the isotropic case the three lines perfectly overlap and all of them match the image.

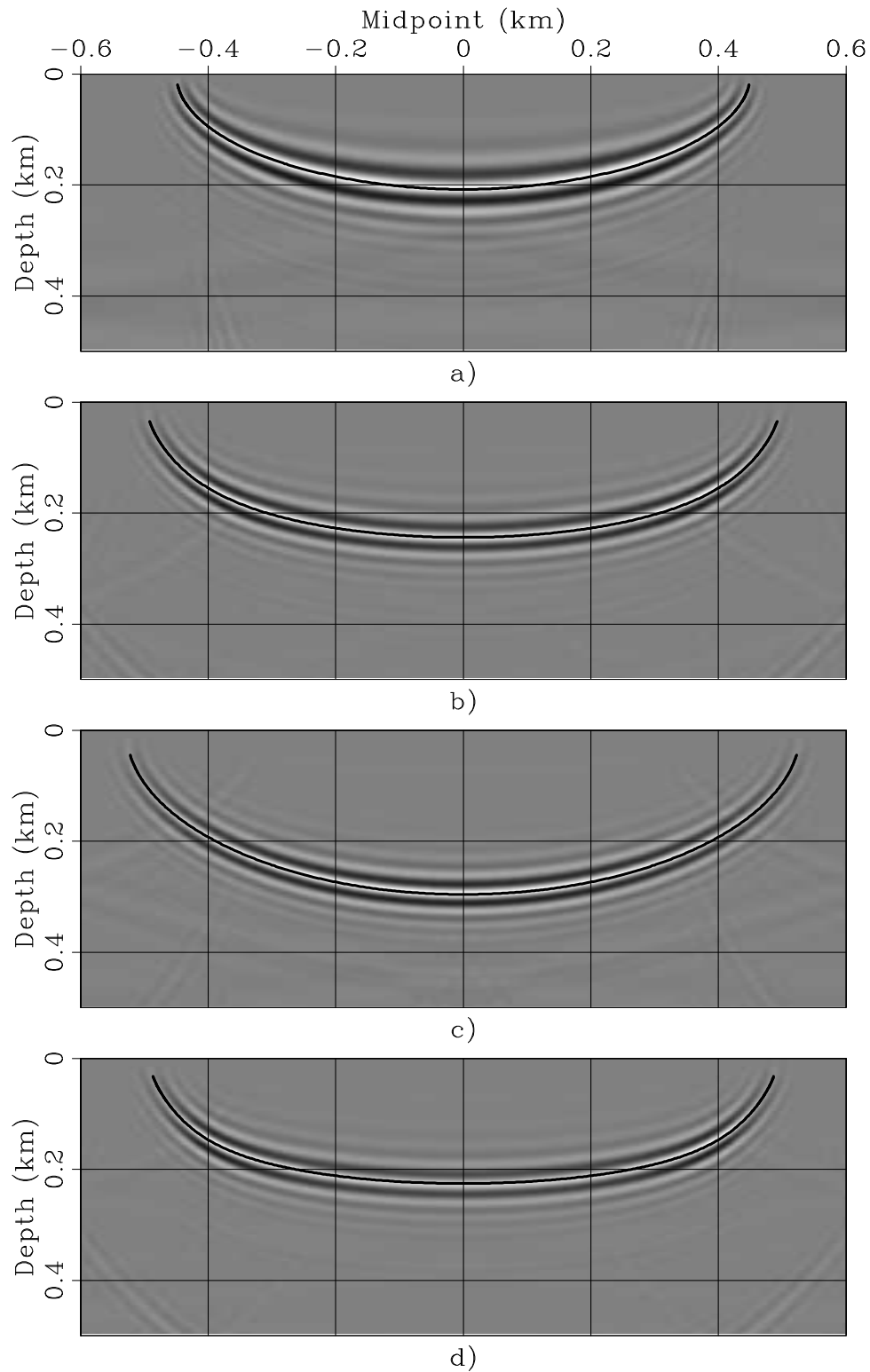


Figure 5: Impulse responses evaluated at zero subsurface offset for four rock types: a) Isotropic, b) Taylor Sand, c) Mesa Clay Shale, and d) GreenLight River Shale. Superimposed onto the images are the impulse responses computed by the kinematic expressions presented in equations 18–24. `biondo1-Quad_hxd_4-overn` [CR]

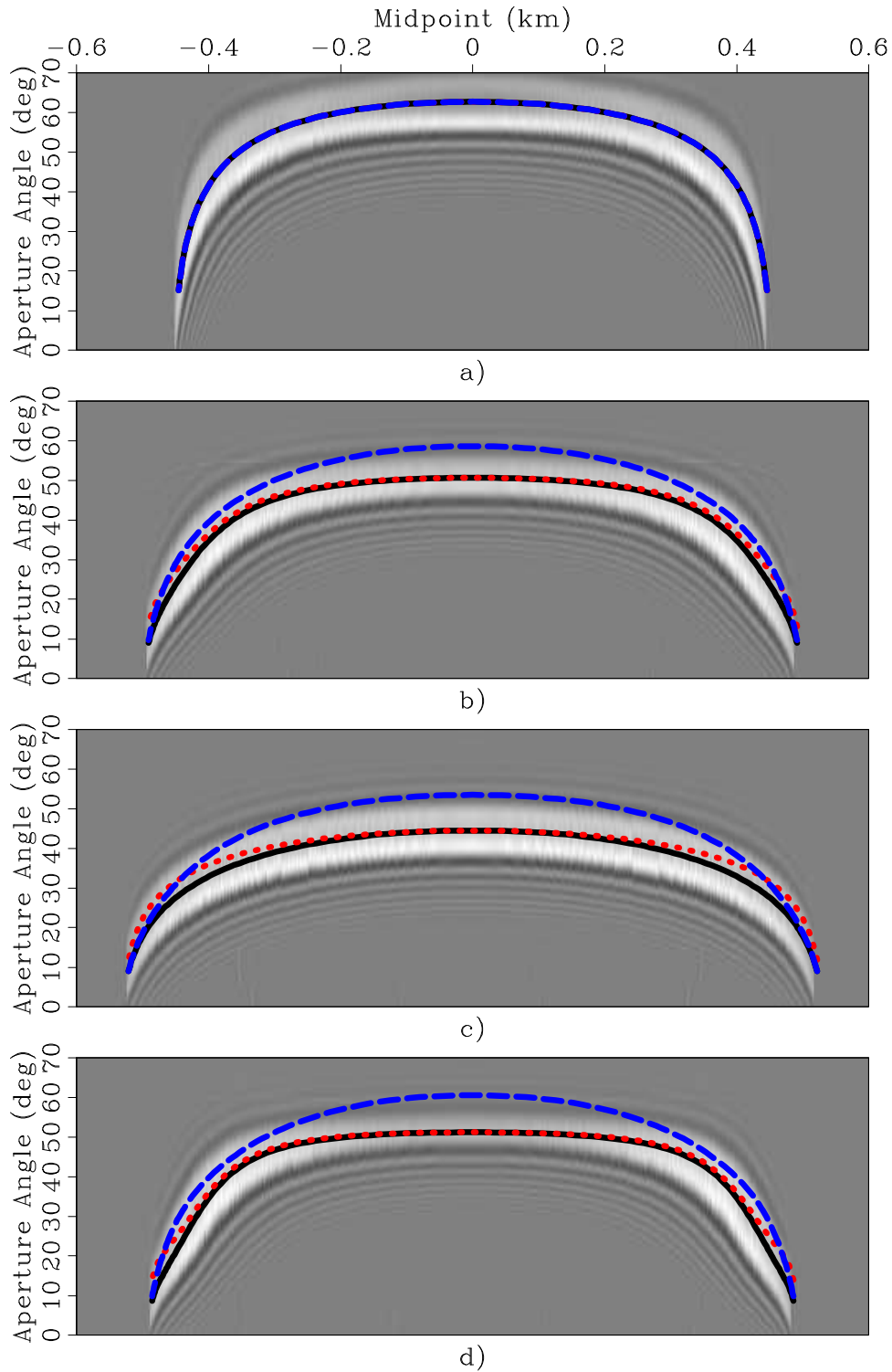


Figure 6: Slices of the impulse responses transformed into the angle-domain for four rock types: a) Isotropic, b) Taylor Sand, c) Mesa Clay Shale, and d) GreenLight River Shale. Superimposed onto the images there are the curves computed by applying the kinematic analysis: γ (dashed line), $\tilde{\gamma}$ (dotted line), and $\arctan(\partial z_{\xi}/\partial h_{\xi})$ (solid line).

`biondo1-Quad_Mx-Ang_hxd_4-overn` [CR]

GULF OF MEXICO DATA EXAMPLE

To illustrate the proposed methodology for computing ADCIGs from prestack images obtained by anisotropic migration, I migrated a 2-D line extracted from a 3-D data set that was kindly provided to SEP by ExxonMobil. I chose the location of the 2-D line in an area where the sediments are mostly flat in the cross-line direction and where the salt flanks are mostly perpendicular to the in-line direction.

The data set was acquired in the Gulf of Mexico over an existing reservoir. Therefore several borehole seismic data sets were available in addition to the surface data to constraint the estimation of the anisotropic parameters. ExxonMobil provided SEP with three anisotropic-parameter cubes resulting from a joint inversion of the surface data and the borehole data (Krebs et al., 2003). Figure 7 shows the vertical slices cut through these cubes at the cross-line location corresponding to the 2-D line that I migrated. Panel a) displays the vertical velocity, panel b) displays the values of δ , and panel c) displays the values of η . To avoid artifacts caused by sharp parameter contrasts, for migration I removed the salt body from the functions displayed in Figure 7. I “infilled” the salt body with sediment-like values by interpolating the functions inward starting from the sediment values at the salt-sediment interface.

Figure 8 shows the result of anisotropic prestack depth migration. All the reflectors are nicely imaged, including the steep salt flank on the right-hand side of the salt body. The shallow tract of the salt flank on the left-hand side of the body is poorly imaged because it has large cross-line dip components. The two vertical lines superimposed onto the image identify the surface location of the ADCIGs displayed in Figure 9. The two black bars superimposed onto the image identify the reflections for which I analyzed the ADCIG in details. Figure 9 shows two ADCIGs computed by slant stacking the prestack image along the subsurface axis. Both CIGs show fairly flat moveout, indicating that the anisotropic velocity model used for migration is accurate, though not perfect. The shallow reflections show the most noticeable departure from flatness (they frown downward) because these reflectors were not the focus of the velocity model-building efforts. The CIGs are taken at the location indicated by the vertical black lines in Figure 8; the CIG shown in panel a) is taken at the surface location of 3,725 meters and the CIG shown in panel b) is taken at the surface location of 11,625 meters. Within these two CIGs, I selected for detailed analysis the reflections corresponding to the black bars superimposed onto the image because they represent two ‘typical’ cases where the accuracy of the estimation of the reflection-aperture angle might be important. The shallow black bar on the left identifies a flat reflector illuminated with a wide range of aperture angles, up to 60 degrees. The wide angular range is potentially useful for constraining the value of the anisotropic parameters in the sediments. The deep black bar on the right identifies one of the potential reservoir sands, and thus it is a potential target for Amplitude Versus Angle (AVA) analysis using ADCIGs.

The plots in Figure 10 show the differences between the true phase aperture angle computed by iteratively solving the system of equations 16 and 17 and the aperture angle estimated by slant stacks (solid line) and the group aperture angle (dashed line). The group angles are computed by applying equation 2. The plot in panel a) corresponds to the shallow black bar on the left. The reflector is flat and the velocity parameters at the reflector are:

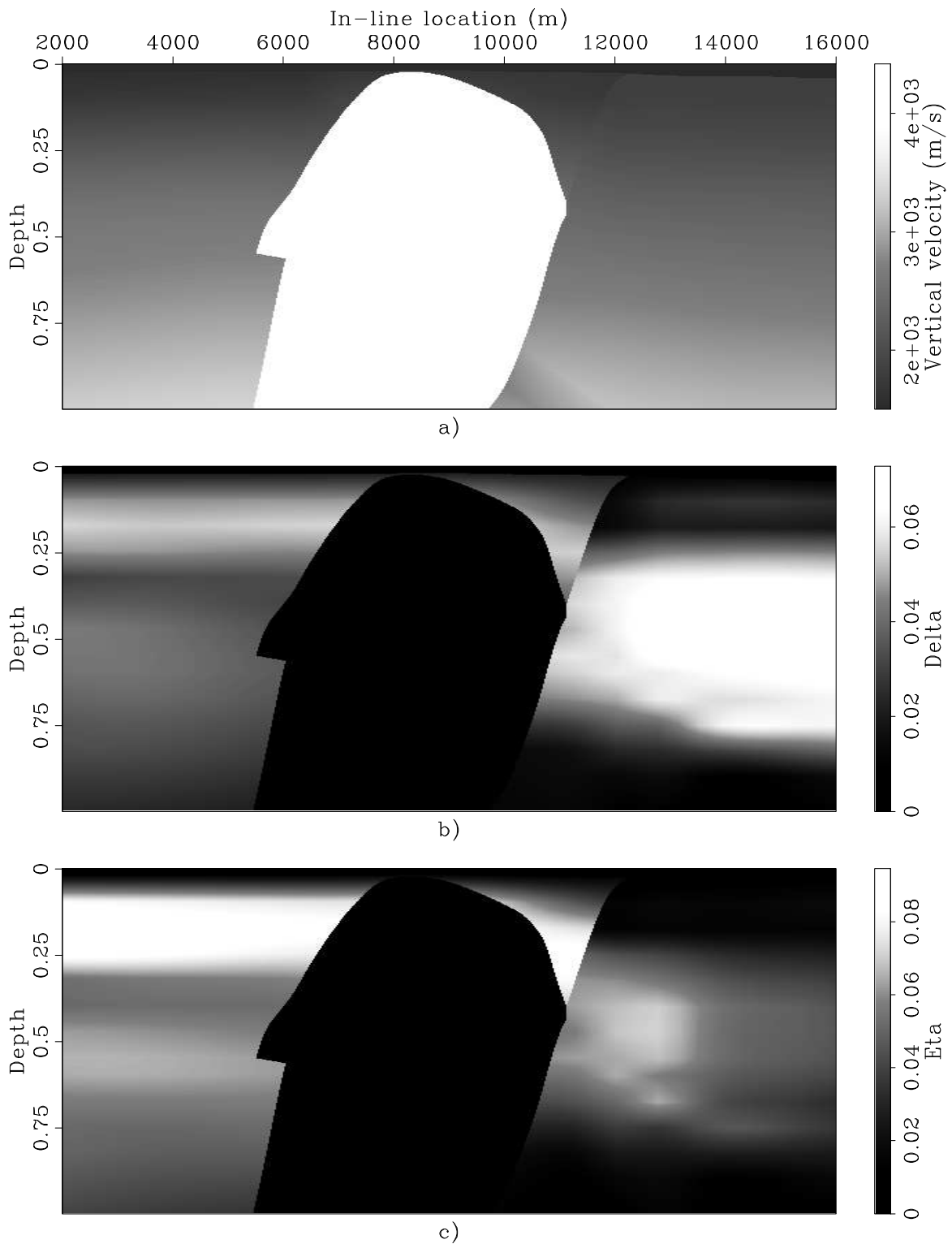


Figure 7: Vertical slices cut through the anisotropic velocity parameters cubes. Panel a) shows the vertical velocity field, panel b) shows the δ field, and panel c) shows the η field. I removed the salt body from the parameters functions used for migration, to avoid artifacts caused by sharp parameter discontinuities. [biondo1-Par-Sections-overn](#) [CR]

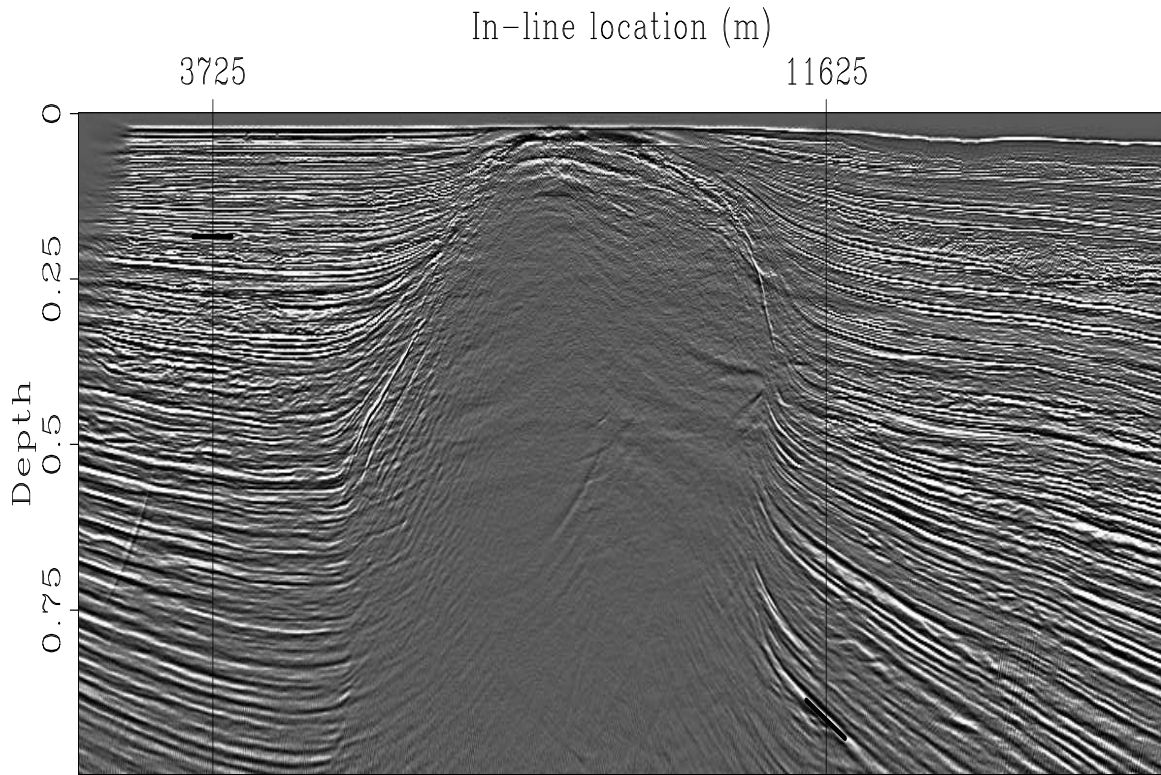


Figure 8: Image obtained by anisotropic prestack migration. The two vertical lines superimposed onto the image identify the surface location of the ADCIGs displayed in Figure 9. The two black bars superimposed onto the image identify the reflections analyzed in Figure 10. biondo1-Bar-Section-overn [CR]

$V_V = 1,995$ m/s, $\epsilon = 0.058$, $\delta = 0.0524$, and $\eta = .0905$. As expected, the aperture angles estimated by slant stack are exactly the same as the true ones because the reflector is flat. The maximum difference between the group aperture angle and the phase aperture angle is at 60 degrees, where the group angle is smaller by about 9 degrees than the phase angle; that is, about an error of about 15%.

The plot in panel b) corresponds the reservoir reflector (the deep black bar on the right). The dip of the reflector is about 25 degrees and the velocity parameters at the reflector are: $V_V = 3,060$ m/s, $\epsilon = 0.028$, $\delta = 0.0133$, and $\eta = .0144$. This area is weakly anisotropic (black in Figure 7b in Figure 7c) and thus the angular errors are small (≤ 1 degree) even if the reflector is dipping. Finally, the plot in panel c) corresponds to the hypothetical situation in which the reservoir was located in a more strongly anisotropic area than it actually is. To test the accuracy limits of approximating the phase aperture angles with the subsurface-offset slopes in the prestack image, I set the anisotropic parameters to be the highest value in the section; that is: $\epsilon = 0.172$, $\delta = 0.07$, and $\eta = .09$, and kept the vertical velocity and reflector's dip the same as in the previous case. The reflector is dipping and consequently the aperture angle estimated by slant stacks is lower than the true aperture angle. However, the error is small (≤ 2 degree) even at large aperture angle, and even smaller (≤ 1 degree) within

the angular range actually illuminated by the data ($0 \leq \tilde{\gamma} \leq 30^\circ$). Even in this “extreme” case the angular error is unlikely to have any significant negative effect on the accuracy of the AVA analysis of the reservoir reflection.

CONCLUSIONS

The methodology for computing and analyzing ADCIGs that has been recently developed for isotropic media can be generalized to prestack images computed using anisotropic prestack migration. This generalization opens the possibility of performing residual moveout velocity analysis and AVA analysis after anisotropic wavefield-continuation migration.

The transformation to angle domain performed by slant-stacking the prestack image along the subsurface-offset axis generates angle gathers that are approximately function of the phase aperture angle. When the accuracy of this approximation is not sufficient, the computation of the true aperture angles requires the measurement from the image of the geological dips of the reflections.

The differences between the true phase angle and the subsurface-offset slopes measured by slant stacks are caused by the difference in propagation velocity between the incident and the reflected waves. In a general TTI medium, the differences vanish for events normal to the isotropic axis of symmetry. In a VTI medium the differences vanish for flat reflectors and they are small unless the anisotropy is strong, the dips steep, and the aperture angle wide. This conclusion is supported by the detailed analysis of the ADCIGs generated by migrating a real data set in the presence of fairly strong anisotropy and steep salt flanks.

ACKNOWLEDGMENTS

I would like to thank the ExxonMobil Exploration Company for making the Gulf of Mexico data set used in this paper data available to SEP through the generous efforts of Ruth Gonzalez and Joe Reilly. The anisotropic parameters cube were kindly shared with us by Laura Bear and Jerry Krebs, also at ExxonMobil.

REFERENCES

- Bear, L., Dickens, T., and Traynin, P., 2003, Incorporating nonseismic information for improved imaging with anisotropic PSDM: 73rd Ann. Internat. Meeting, Soc. of Expl. Geophys., Expanded Abstracts, 949–952.
- Biondi, B., and Sava, P., 1999, Wave-equation migration velocity analysis: 69th Ann. Internat. Meeting, Soc. of Expl. Geophys., Expanded Abstracts, 1723–1726.
- Biondi, B., and Symes, W. W., 2003, Angle-domain common-image gathers for migration velocity analysis by wavefield-continuation imaging: *Geophysics*, **69**, 1283–1298.

- Biondi, B., and Tisserant, T., 2004, 3-D angle-domain common-image gathers for migration velocity analysis: *Geophysical Prospecting*, **52**, 575–591.
- Biondi, B., 2005, Residual moveout in anisotropic angle-domain common image gathers: **SEP-123**.
- Clapp, R., and Biondi, B., 2000, Tau domain migration velocity analysis using angle CRP gathers and geologic constrains: 70th Ann. Internat. Meeting, Soc. of Expl. Geophys., Expanded Abstracts, 926–929.
- Dellinger, J., and Muir, F., 1985, Two domains of anisotropy: **SEP-44**, 59–62.
- Fomel, S., 2002, Applications of plane-wave destruction filters: *Geophysics*, **67**, 1946–1960.
- Fowler, P., 2003, Practical VTI approximations: a systematic anatomy: *Journal of Applied Geophysics*, **69**, 347–367.
- Krebs, J., Bear, L., and Liu, J., 2003, Integrated velocity model estimation for accurate imaging: 73rd Ann. Internat. Meeting, Soc. of Expl. Geophys., Expanded Abstracts, 2084–2087.
- Prucha, M., Biondi, B., and Symes, W. W., 1999, Angle-domain common-image gathers by wave-equation migration: 69th Ann. Internat. Meeting, Soc. Expl. Geophys., Expanded Abstracts, 824–827.
- Rickett, J., and Sava, P., 2002, Offset and angle-domain common image-point gathers for shot-profile migration: *Geophysics*, **67**, 883–889.
- Rosales, D. A., and Biondi, B., 2005, Converted-mode angle-domain common-image gathers for migration velocity analysis: **SEP-120**, 283–296.
- Rosales, D. A., and Rickett, J., 2001, PS-wave polarity reversal in angle domain common-image gathers: 71th Ann. Internat. Meeting, Soc. Expl. Geophys., Expanded Abstracts, 1843–1846.
- Sarkar, D., and Tsvankin, I., 2004, Anisotropic migration velocity analysis: Application to a data set from West Africa: 74th Ann. Internat. Meeting, Soc. of Expl. Geophys., Expanded Abstracts, 2399–2402.
- Sava, P., and Fomel, S., 2003, Angle-domain common-image gathers by wavefield continuation methods: *Geophysics*, **68**, 1065–1074.
- Stolk, C. C., and Symes, W. W., 2003, Kinematic artifacts in prestack depth migration: *Geophysics*, **69**, 562–575.
- Tsvankin, I., 2001, *Seismic signatures and analysis of reflection data in anisotropic media*: Elsevier Science.
- Wang, J., Khuel, H., and Sacchi, M., 2005, High-resolution wave-equation avo imaging: Algorithm and tests with a data set from the western canadian sedimentary basin: *Geophysics*, **70**, S91–S99.

APPENDIX A

CONVERSION FROM AVERAGE ANGLES TO TRUE APERTURE ANGLES

In this appendix I present the expressions for evaluating the true reflection angles $\tilde{\gamma}_s$ and $\tilde{\gamma}_r$ for the incident and reflected plane waves, from the ‘normalized slowness difference’ $\Delta_{\tilde{S}} = (\tilde{S}_r - \tilde{S}_s)/(\tilde{S}_r + \tilde{S}_s)$ and from the average aperture angles $\tilde{\gamma}$ computed by solving equations 16 and 17.

Rosales and Biondi (2005) derived these relationships as follows:

$$\tan \tilde{\gamma}_s = \frac{\frac{1+\Delta_{\tilde{S}}}{1-\Delta_{\tilde{S}}} \sin 2\tilde{\gamma}}{1 + \frac{1+\Delta_{\tilde{S}}}{1-\Delta_{\tilde{S}}} \cos 2\tilde{\gamma}} \quad (\text{A-1})$$

$$\tan \tilde{\gamma}_r = \frac{\sin 2\tilde{\gamma}}{\frac{1+\Delta_{\tilde{S}}}{1-\Delta_{\tilde{S}}} + \cos 2\tilde{\gamma}}. \quad (\text{A-2})$$

It is easy to verify that when $\Delta_{\tilde{S}} = 0$ (isotropic case) we get, as expected, $\tilde{\gamma}_s = \tilde{\gamma}_r = \tilde{\gamma}$.

APPENDIX B

ANALYTICAL EVALUATION OF THE TANGENT PLANE TO THE IMPULSE RESPONSE

In this appendix I derive the expressions for evaluating the derivatives of image depth z_ξ with respect to the subsurface offset h_ξ and the midpoint m_ξ ; these derivatives are computed along the tangent plane to the impulse response of the generalized migration operator, which is defined in equations 18–24.

I start by deriving the equation for the vector normal to the impulse-response surface, \vec{n} :

$$\begin{aligned} \vec{n} &= \begin{vmatrix} \vec{z}_\xi & \vec{m}_\xi & \vec{h}_\xi \\ \frac{\partial z_\xi}{\partial \alpha_x} & \frac{\partial m_\xi}{\partial \alpha_x} & \frac{\partial h_\xi}{\partial \alpha_x} \\ \frac{\partial z_\xi}{\partial \gamma} & \frac{\partial m_\xi}{\partial \gamma} & \frac{\partial h_\xi}{\partial \gamma} \end{vmatrix} \\ &= \left(\frac{\partial m_\xi}{\partial \alpha_x} \frac{\partial h_\xi}{\partial \gamma} - \frac{\partial m_\xi}{\partial \gamma} \frac{\partial h_\xi}{\partial \alpha_x} \right) \vec{z}_\xi + \left(-\frac{\partial z_\xi}{\partial \alpha_x} \frac{\partial h_\xi}{\partial \gamma} + \frac{\partial z_\xi}{\partial \gamma} \frac{\partial h_\xi}{\partial \alpha_x} \right) \vec{m}_\xi + \left(\frac{\partial z_\xi}{\partial \alpha_x} \frac{\partial m_\xi}{\partial \gamma} - \frac{\partial z_\xi}{\partial \gamma} \frac{\partial m_\xi}{\partial \alpha_x} \right) \vec{h}_\xi, \end{aligned} \quad (\text{B-1})$$

where \vec{z}_ξ , \vec{m}_ξ , and \vec{h}_ξ are respectively the unit vectors along the three dimensions z_ξ , m_ξ , and h_ξ .

The equation of the tangent plane at the image point with coordinates $(\bar{z}_\xi, \bar{m}_\xi, \bar{h}_\xi)$ is given

by:

$$\begin{aligned}
T(z_\xi, m_\xi, h_\xi) &= \left(\frac{\partial m_\xi}{\partial \alpha_x} \frac{\partial h_\xi}{\partial \gamma} - \frac{\partial m_\xi}{\partial \gamma} \frac{\partial h_\xi}{\partial \alpha_x} \right) (z_\xi - \bar{z}_\xi) \\
&+ \left(-\frac{\partial z_\xi}{\partial \alpha_x} \frac{\partial h_\xi}{\partial \gamma} + \frac{\partial z_\xi}{\partial \gamma} \frac{\partial h_\xi}{\partial \alpha_x} \right) (m_\xi - \bar{m}_\xi) \\
&+ \left(\frac{\partial z_\xi}{\partial \alpha_x} \frac{\partial m_\xi}{\partial \gamma} - \frac{\partial z_\xi}{\partial \gamma} \frac{\partial m_\xi}{\partial \alpha_x} \right) (h_\xi - \bar{h}_\xi) = 0. \tag{B-2}
\end{aligned}$$

The derivative of the depth with respect to the subsurface offset, at constant midpoint, is given by:

$$\left. \frac{\partial z_\xi}{\partial h_\xi} \right|_{m_\xi = \bar{m}_\xi} = - \frac{\left. \frac{\partial T}{\partial h_\xi} \right|_{m_\xi = \bar{m}_\xi}}{\left. \frac{\partial T}{\partial z_\xi} \right|_{m_\xi = \bar{m}_\xi}} = - \frac{\frac{\partial z_\xi}{\partial \alpha_x} \frac{\partial m_\xi}{\partial \gamma} - \frac{\partial z_\xi}{\partial \gamma} \frac{\partial m_\xi}{\partial \alpha_x}}{\frac{\partial m_\xi}{\partial \alpha_x} \frac{\partial h_\xi}{\partial \gamma} - \frac{\partial m_\xi}{\partial \gamma} \frac{\partial h_\xi}{\partial \alpha_x}}. \tag{B-3}$$

and similarly the derivative of the depth with respect to the midpoint, at constant subsurface offset, is given by:

$$\left. \frac{\partial z_\xi}{\partial m_\xi} \right|_{h_\xi = \bar{h}_\xi} = - \frac{\left. \frac{\partial T}{\partial m_\xi} \right|_{h_\xi = \bar{h}_\xi}}{\left. \frac{\partial T}{\partial z_\xi} \right|_{h_\xi = \bar{h}_\xi}} = - \frac{\frac{\partial z_\xi}{\partial \alpha_x} \frac{\partial h_\xi}{\partial \gamma} - \frac{\partial z_\xi}{\partial \gamma} \frac{\partial h_\xi}{\partial \alpha_x}}{\frac{\partial m_\xi}{\partial \alpha_x} \frac{\partial h_\xi}{\partial \gamma} - \frac{\partial m_\xi}{\partial \gamma} \frac{\partial h_\xi}{\partial \alpha_x}}. \tag{B-4}$$

To evaluate equations B-3–B-4, we need to evaluate the following partial derivatives, obtained by differentiating the expressions in equations 18–20:

$$\begin{aligned}
\frac{\partial z_\xi}{\partial \alpha_x} &= -L(\alpha_x, \gamma) \frac{\tan \alpha_x}{\cos \alpha_x \cos \gamma} (\cos^2 \alpha_x + \sin^2 \gamma) + \frac{\partial L(\alpha_x, \gamma)}{\partial \alpha_x} \frac{\cos^2 \alpha_x - \sin^2 \gamma}{\cos \alpha_x \cos \gamma}, \\
\frac{\partial z_\xi}{\partial \gamma} &= -L(\alpha_x, \gamma) \frac{\tan \gamma}{\cos \alpha_x \cos \gamma} (\cos^2 \gamma + \sin^2 \alpha_x) + \frac{\partial L(\alpha_x, \gamma)}{\partial \gamma} \frac{\cos^2 \alpha_x - \sin^2 \gamma}{\cos \alpha_x \cos \gamma}, \\
\frac{\partial m_\xi}{\partial \alpha_x} &= -L(\alpha_x, \gamma) \frac{\cos \alpha_x}{\cos \gamma} - \frac{\partial L(\alpha_x, \gamma)}{\partial \alpha_x} \frac{\sin \alpha_x}{\cos \gamma}, \\
\frac{\partial m_\xi}{\partial \gamma} &= -L(\alpha_x, \gamma) \frac{\sin \gamma \sin \alpha_x}{\cos^2 \gamma} - \frac{\partial L(\alpha_x, \gamma)}{\partial \gamma} \frac{\sin \alpha_x}{\cos \gamma}, \\
\frac{\partial h_\xi}{\partial \alpha_x} &= -L(\alpha_x, \gamma) \frac{\sin \gamma \sin \alpha_x}{\cos^2 \alpha_x} - \frac{\partial L(\alpha_x, \gamma)}{\partial \alpha_x} \frac{\sin \gamma}{\cos \alpha_x}, \\
\frac{\partial h_\xi}{\partial \gamma} &= -L(\alpha_x, \gamma) \frac{\cos \gamma}{\cos \alpha_x} - \frac{\partial L(\alpha_x, \gamma)}{\partial \gamma} \frac{\sin \gamma}{\cos \alpha_x}. \tag{B-5}
\end{aligned}$$

The derivative of path length are evaluated as follows:

$$\begin{aligned}
\frac{\partial L}{\partial \alpha_x} &= \frac{-t_D}{[(S_r + S_s) + (S_r - S_s) \tan \alpha_x \tan \gamma]^2} \\
&\left[\left(\frac{\partial S_r}{\partial \alpha_x} + \frac{\partial S_s}{\partial \alpha_x} \right) + \left(\frac{\partial S_r}{\partial \alpha_x} - \frac{\partial S_s}{\partial \alpha_x} \right) \tan \alpha_x \tan \gamma + \frac{(S_r - S_s) \tan \gamma}{\cos^2 \alpha_x} \right], \tag{B-6}
\end{aligned}$$

and

$$\frac{\partial L}{\partial \gamma} = \frac{-t_D}{[(S_r + S_s) + (S_r - S_s) \tan \alpha_x \tan \gamma]^2} \left[\left(\frac{\partial S_r}{\partial \gamma} + \frac{\partial S_s}{\partial \gamma} \right) + \left(\frac{\partial S_r}{\partial \gamma} - \frac{\partial S_s}{\partial \gamma} \right) \tan \alpha_x \tan \gamma + \frac{(S_r - S_s) \tan \alpha_x}{\cos^2 \gamma} \right]. \quad (\text{B-7})$$

Application to the isotropic case

The application to the isotropic case is simpler than the anisotropic case because the derivative of the path length is zero, but it is instructive since it verifies known results through a completely different derivation. Substituting equations B-5 into equation B-3, I obtain:

$$\begin{aligned} \left. \frac{\partial z_\xi}{\partial h_\xi} \right|_{m_\xi = \bar{m}_\xi} &= - \frac{L^2 \tan \gamma \left[\frac{\tan^2 \alpha_x}{\cos^2 \gamma} (\cos^2 \alpha_x + \sin^2 \gamma) - \frac{1}{\cos^2 \gamma} (\cos^2 \gamma + \sin^2 \alpha_x) \right]}{L^2 [1 - \tan^2 \alpha_x \tan^2 \gamma]} \\ &= - \frac{L^2 \tan \gamma \left[-1 + \sin^2 \alpha_x \left(\frac{1}{\cos^2 \gamma} - \frac{1}{\cos^2 \gamma} \right) + \tan^2 \alpha_x \tan^2 \gamma \right]}{L^2 [1 - \tan^2 \alpha_x \tan^2 \gamma]} \\ &= \tan \gamma, \end{aligned} \quad (\text{B-8})$$

which shows that $\partial z_\xi / \partial h_\xi$ is independent from the dip angle α_x . This expression is consistent with the 2-D analysis by Sava and Fomel (2003) and the 3-D analysis by Biondi and Tisserant (2004).

Figure 9: ADCIGs computed from the prestack image by slant stacking along the subsurface offset axis. The CIG shown in panel a) is taken at the surface location of 3,725 meters, and the CIG shown in panel b) is taken at the surface location of 11,625 meters.

biondo1-Duo-aniso-overn [CR]

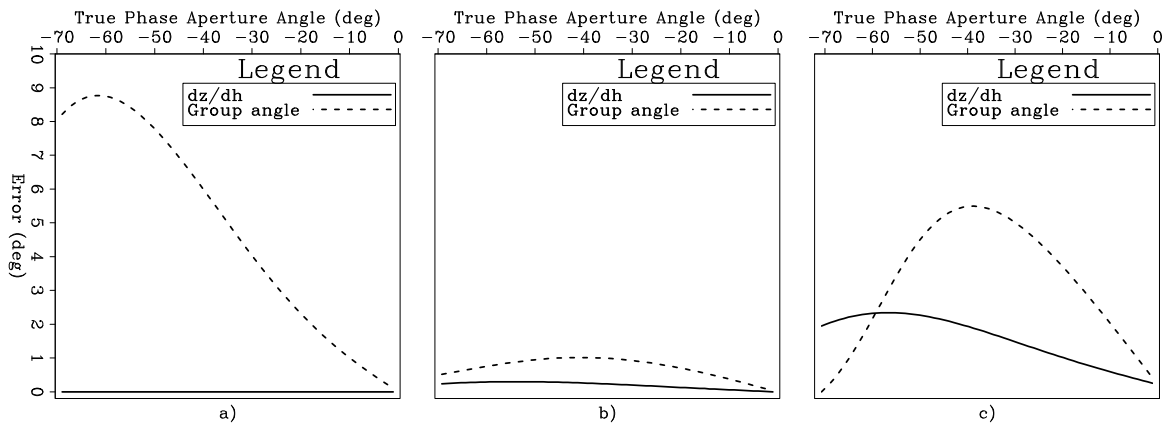
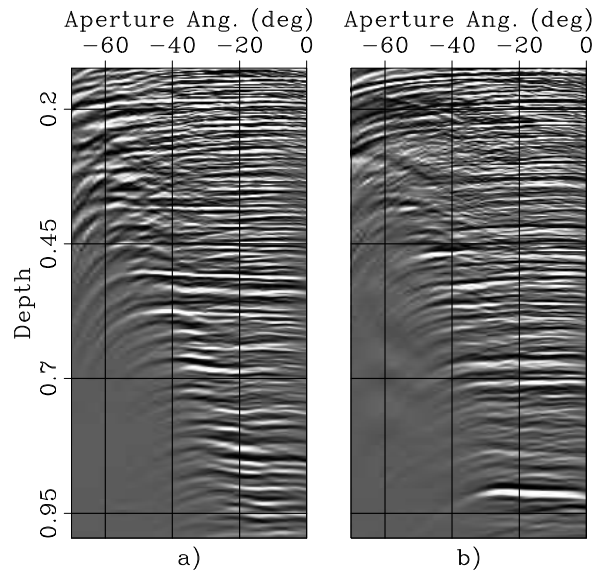


Figure 10: Differences between the true phase aperture angle and the aperture angle estimated by slant stacks (solid line) and the group aperture angle (dashed line). The plot in panel a) corresponds to the reflection identified with the shallow black bar on the left in Figure 8. The plot in panel b) corresponds the reservoir reflector (the deep black bar on the right). The plot in panel c) corresponds to the hypothetical situation in which the reservoir reflector was located in a more strongly anisotropic area than it actually is.

biondo1-Trio-Ang-overn [CR]

Residual moveout in anisotropic angle-domain common image gathers

*Biondo Biondi*¹

ABSTRACT

To enable the analysis of the Residual Moveout (RMO) in Angle-Domain Common Image Gathers (ADCIGs) after anisotropic wavefield-continuation migration, I develop the fundamental concepts for quantitatively relating perturbations in anisotropic parameters to the corresponding reflector movements in ADCIGs. I then apply the general methodology to the particular case of RMO analysis of reflections from flat reflectors in a Vertical Transverse Isotropic (VTI) medium. This analysis shows that the RMO in migrated ADCIGs is a function of both the phase aperture angle and the group aperture angle.

Several numerical examples demonstrate the accuracy of the RMO curves predicted by my kinematic analysis. The synthetic examples also show that the approximation of the group angles by the phase angles may lead to substantial errors for events reflected at wide aperture angles.

The results obtained by migrating a 2-D line extracted from a Gulf of Mexico 3-D data set confirm the accuracy of the proposed method. The RMO curves predicted by the theory exactly match the RMO function observed in the ADCIGs computed from the real data.

INTRODUCTION

The analysis of Residual Moveout (RMO) in Common Image Gathers (CIGs) after prestack migration is an essential step for updating migration velocity. When the migration velocity is inaccurate, the inconsistency of the migrated events along either the offset axis or the aperture-angle axis is proportional to the migration velocity errors. Measuring the RMO in ADCIGs provides the quantitative information necessary to update the velocity function in a Migration Velocity Analysis (MVA) procedure.

Today, MVA is the procedure most commonly employed to estimate isotropic migration velocity in complex media. The technology for anisotropic MVA is much less mature than for isotropic MVA. Recently, important progress has been made toward the development of anisotropic MVA in conjunction with Kirchhoff migration. Sarkar and Tsvankin (2003, 2004b) analyze the effect of velocity errors on offset-domain CIGs produced by Kirchhoff migration. They demonstrate the effectiveness of their method by successfully applying it to a West Africa data set (Sarkar and Tsvankin, 2004a). Krebs et al. (2003) and Bear et al. (2003) integrate

¹email: biondo@sep.stanford.edu

borehole-seismic data and nonseismic information in an MVA process based on Kirchhoff migration.

Wavefield-continuation is capable of producing better images than Kirchhoff migration does in the presence of complex overburden that causes multipathing of the propagating wavefield, as often it occurs when imaging below or in proximity of salt bodies. To perform MVA after wavefield-continuation the RMO function is measured from Angle Domain Common Image Gathers (ADCIGs) (Biondi and Sava, 1999; Clapp and Biondi, 2000). Since all the present methods for computing ADCIGs in conjunction with wavefield migration are limited to isotropic migration, the quantitative analysis of RMO in ADCIGs is also limited to the isotropic case (Biondi and Symes, 2003; Biondi and Tisserant, 2004). In this paper, I provide the basic analytical tools necessary to perform anisotropic migration velocity analysis by analyzing the RMO function in ADCIGs. This paper builds on the results presented in a companion paper (Biondi, 2005) that develops a method for computing ADCIGs after anisotropic migration and lays the foundations for the kinematic analysis of anisotropic ADCIGs. I apply the general theory to the specific case of defining the RMO function measured from flat reflectors in VTI media, because in this case the methodology is simple both to derive and to apply. However, the same concepts could be applied to more general situations, though at the expense of additional complexities that could obfuscate the fundamental concepts.

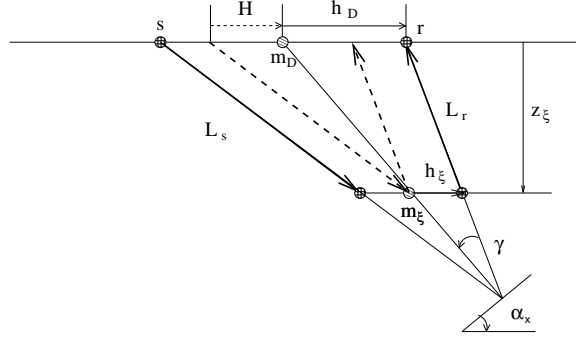
In (Biondi, 2005) I show that in anisotropic media the ADCIGs are approximately functions of the phase aperture angle, and exactly so for flat reflectors in VTI media. In this paper I demonstrate that the RMO function depends on both the phase and the group aperture angles. This dependency of the RMO function on the group angles adds some complexity to the RMO analysis because the computation of group angles from phase angles, which are measured from the ADCIGs, depends on the background anisotropic velocity evaluated at the reflector point. The synthetic-data examples show that neglecting the dependency on the group angles, and assuming that group angles are equal to phase angles, leads to substantial inaccuracy in the predicted RMO function. Fortunately, the additional computational cost of computing group angles is negligible, and thus it should not be an obstacle to the application of the proposed methodology.

ANGLE-DOMAIN COMMON IMAGE GATHERS AND KINEMATIC ANISOTROPIC MIGRATION

In (Biondi, 2005) I develop the theory of ADCIGs in anisotropic media from both a “plane-wave” viewpoint and a “ray” viewpoint. The two methods are equivalent and yield the same results, but the ray-theoretical approach is the natural starting point for analyzing RMO functions in ADCIGs. The kinematic approach is based on the conceptual generalization of integral (Kirchhoff) migration to the computation of a prestack image that include the sub-surface offset dimension. The image-space of integral migration are usually restricted to the zero subsurface-offset section; that is, with the integral operators (either summation surfaces or spreading surfaces) evaluated when source and receiver rays meet at the reflection point. The image space can be expanded to include non-zero subsurface offsets by integrating the data

Figure 1: Geometry used for evaluating the impulse response of integral migration generalized to produce a prestack image function of the subsurface offset h_ξ .

`biondo2-imp-resp` [NR]



over surfaces evaluated with the end points of the source and receiver rays horizontally shifted with respect to each other, instead of being coincidental at the image point. Figure 1 illustrates this concept and provide the basis for computing the kinematics of the generalized migration operator.

Since the transformation to ADCIGs operates in the image space, I analyze the spreading surfaces (impulse responses) of the generalized prestack migration operator, which are defined in the image space. In homogeneous anisotropic medium the shape of the impulse responses of the generalized integral migration can be easily evaluated analytically as a function of the subsurface offset h_ξ , in addition to the usual image depth z_ξ and midpoint m_ξ . Figure 1 illustrates the geometry used to evaluate this impulse response.

Assuming an arbitrary homogeneous anisotropic medium, simple trigonometry applied to Figure 1 allows us to express the impulse response in parametric form, as a function of the group dip angle α_x and the group aperture angle γ . If we migrate an impulse recorded at time t_D , midpoint m_D and surface offset h_D , the migration impulse response can be expressed as follows:

$$z_\xi = L(\alpha_x, \gamma) \frac{\cos^2 \alpha_x - \sin^2 \gamma}{\cos \alpha_x \cos \gamma}, \quad (1)$$

$$m_\xi = m_D - L(\alpha_x, \gamma) \frac{\sin \alpha_x}{\cos \gamma}, \quad (2)$$

$$h_\xi = h_D - H = h_D - L(\alpha_x, \gamma) \frac{\sin \gamma}{\cos \alpha_x}, \quad (3)$$

with the average half-path length $L(\alpha_x, \gamma)$ given by:

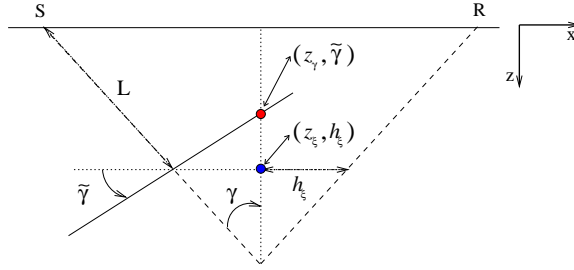
$$L(\alpha_x, \gamma) = \frac{L_s + L_r}{2} = \frac{t_D}{(S_r + S_s) + (S_r - S_s) \tan \alpha_x \tan \gamma}, \quad (4)$$

where S_s and S_r are the group slowness along the source and receiver rays, respectively.

In 2-D, The ADCIGs are computed by applying a slant-stack decomposition on the prestack image along the subsurface offset axis, at constant midpoint. The kinematics of the transfor-

Figure 2: Geometry of the transformation to the angle domain. The image point in the subsurface-offset domain (z_ξ, h_ξ) moves to the image point in angle domain $(z_\gamma, \tilde{\gamma})$.

biondo2-cig-2d-aniso-mva-flat-v1
[NR]



mation are defined by the following change of variables:

$$\hat{\gamma} = \arctan \left. \frac{\partial z_\xi}{\partial h_\xi} \right|_{m_\xi = \bar{m}_\xi}, \quad (5)$$

$$z_\gamma = z_\xi - h_\xi \left. \frac{\partial z_\xi}{\partial h_\xi} \right|_{m_\xi = \bar{m}_\xi}, \quad (6)$$

where z_γ is the depth of the image point after the transformation. In the general case, the angle $\hat{\gamma}$ is related to the reflection aperture angle in a non-trivial way. However, in (Biondi, 2005) I demonstrate that for flat reflectors the slope of the impulse response along the subsurface offset axis, is equal to the tangent of the phase aperture angle $\tilde{\gamma}$; that is,

$$\left. \frac{\partial z_\xi}{\partial h_\xi} \right|_{(m_\xi = \bar{m}_\xi, \alpha_x = 0)} = \frac{\tan \gamma + \frac{1}{S} \frac{\partial S}{\partial \gamma}}{1 - \frac{1}{S} \frac{\partial S}{\partial \gamma} \tan \gamma} = \tan \tilde{\gamma}. \quad (7)$$

Notice that throughout this paper I use the tilde symbol to distinguish between phase quantities (with a tilde) and group quantities (without a tilde). Appendix A summarizes the relationships between group angles and velocities and phase angles and velocities. Equation A-4 is directly used to derive the result in equation 7.

Substituting equation 7 in equations 5 and 6 we obtain

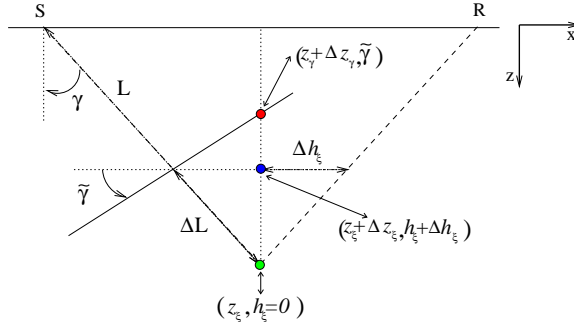
$$\tilde{\gamma} = \arctan \left. \frac{\partial z_\xi}{\partial h_\xi} \right|_{m_\xi = \bar{m}_\xi}, \quad (8)$$

$$z_\gamma = z_\xi - h_\xi \tan \tilde{\gamma}. \quad (9)$$

Figure 2 provides a geometrical interpretation of the transformation to angle domain of an image point with non-zero subsurface offset. The transformation to angle domain moves the image point in the subsurface-offset domain (z_ξ, h_ξ) to the image point in angle domain $(z_\gamma, \tilde{\gamma})$. The depth of the image point in angle domain is determined by the intersection of the lines passing through the points $(z_\xi, m_\xi \pm h_\xi)$ and tilted by $\mp \tilde{\gamma}$ with respect to the horizontal. When the migration velocity is correct, and the image is fully focused at zero subsurface offset, the transformation to angle domain does not change the depth of the image point and the reflections are imaged at the same depth for all aperture angles. On the contrary, when the reflections are not focused at zero offset, the transformation to angle domain maps the events at different depths for each different angle. The variability of the depth z_γ with the aperture angle is described by the RMO function that we want to measure and quantify as a function of the perturbations in anisotropic parameters encountered along the propagation paths.

Figure 3: Linearized perturbations of the image-point locations (both in the subsurface-offset domain and the angle domain) caused by changes in the ray length L , as evaluated using the first term in equation 11.

biondo2-cig-2d-aniso-delta1-flat-v1
[NR]



ANISOTROPIC RESIDUAL MOVEOUT FOR FLAT REFLECTORS

The generalization of kinematic anisotropic migration and the analysis of the kinematics of the offset-to-angle transformation presented in the previous section enables a simple analysis of the residual moveout (RMO) in ADCIGs caused by errors in anisotropic velocity parameters. In this section I derive the RMO function by linearizing the relationship of the imaging depth in the angle domain with respect to perturbations in the anisotropic parameters. The linearization is evaluated around the correct migration velocity function; that is, when the image in the subsurface-offset domain is well focused at zero offset.

As in the previous section, I limit my analysis to reflections from flat interfaces. However, a generalization of the flat-events analysis to dipping events should be conceptually straightforward, though not necessarily simple from the analytical point of view. Furthermore, I derive relationships assuming that the velocity perturbations are limited to a homogeneous half-space above the reflector. The same relationships can be easily adapted to the case of a homogeneous layer above the reflector by transforming the depth variable into a relative depth with respect to the top of the layer under consideration. At the end of this section I present the fundamental relationship for broadening the application of the theory to heterogeneous media. This relationship links the traveltime perturbations to the reflector movements and it can be used in a ray-based tomographic velocity-update procedure.

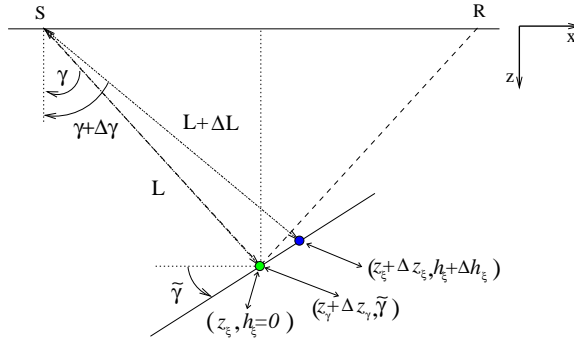
A VTI velocity function, either group or phase, is described by the following vector of three velocities $\mathbf{V} = (V_V, V_H, V_N)$, or by the corresponding vector of three slownesses $\mathbf{S} = (S_V, S_H, S_N)$ used in equation C-1. I define the perturbations as the combination of one multiplicative factor for each of the velocities and one multiplicative factor for all velocities; that is, the perturbed velocity ${}_{\rho}\mathbf{V}$ is defined as:

$${}_{\rho}\mathbf{V} = ({}_{\rho}V_V, {}_{\rho}V_H, {}_{\rho}V_N) = \rho_V (\rho_{V_V} V_V, \rho_{V_H} V_H, \rho_{V_N} V_N). \quad (10)$$

The velocity-parameter perturbations is thus defined by the following four-components vector $\rho = (\rho_V, \rho_{V_V}, \rho_{V_H}, \rho_{V_N})$.

Differentiating, the expression for the depth of the image point in the angle domain z_{γ} (equation 9) with respect to the i -th component in the perturbation vector, we obtain the fol-

Figure 4: Linearized perturbations of the image-point locations (both in the subsurface-offset domain and the angle domain) caused by changes in the aperture angle γ , as evaluated using the second term in equation 11. Notice that the image point in the angle domain does not move, no matter how large the corresponding movement in the subsurface-offset domain is.



biondo2-cig-2d-aniso-delta2-flat-v1
[NR]

lowing:

$$\frac{\partial z_\gamma}{\partial \rho_i} = \frac{\partial z_\gamma}{\partial L} \frac{\partial L}{\partial \rho_i} + \frac{\partial z_\gamma}{\partial \gamma} \frac{\partial \gamma}{\partial \rho_i} + \frac{\partial z_\gamma}{\partial \tilde{\gamma}} \frac{\partial \tilde{\gamma}}{\partial \rho_i} \quad (11)$$

$$= \frac{\partial z_\gamma}{\partial L} \frac{\partial L}{\partial S} \left(\frac{\partial S}{\partial \rho_i} + \frac{\partial S}{\partial \gamma} \frac{\partial \gamma}{\partial \rho_i} \right) + \frac{\partial z_\gamma}{\partial \gamma} \frac{\partial \gamma}{\partial \rho_i} + \frac{\partial z_\gamma}{\partial \tilde{\gamma}} \frac{\partial \tilde{\gamma}}{\partial \rho_i} \quad (12)$$

$$= \frac{\partial z_\gamma}{\partial L} \frac{\partial L}{\partial S} \frac{\partial S}{\partial \rho_i} + \left(\frac{\partial z_\gamma}{\partial L} \frac{\partial L}{\partial S} \frac{\partial S}{\partial \gamma} + \frac{\partial z_\gamma}{\partial \gamma} \right) \frac{\partial \gamma}{\partial \rho_i} + \frac{\partial z_\gamma}{\partial \tilde{\gamma}} \frac{\partial \tilde{\gamma}}{\partial \rho_i}. \quad (13)$$

In Appendix B I demonstrate that the terms multiplying the partial derivatives with respect to the angles are zero, and equation 13 simplifies into:

$$\frac{\partial z_\gamma}{\partial \rho_i} = \frac{\partial z_\gamma}{\partial L} \frac{\partial L}{\partial S} \frac{\partial S}{\partial \rho_i}, \quad (14)$$

where

$$\frac{\partial z_\gamma}{\partial L} = \frac{\partial z_\xi}{\partial L} - \frac{\partial h_\xi}{\partial L} \tan \tilde{\gamma} = \cos \gamma + \sin \gamma \tan \tilde{\gamma}, \quad (15)$$

and

$$\frac{\partial L}{\partial S(\gamma)} = -\frac{z_\xi}{S(\gamma) \cos \gamma}, \quad (16)$$

and consequently

$$\frac{\partial z_\xi}{\partial \rho_i} = -\frac{z_\gamma (1 + \tan \gamma \tan \tilde{\gamma})}{S(\gamma)} \frac{\partial S}{\partial \rho_i}. \quad (17)$$

Figures 3 and 4 graphically illustrate the image perturbations related to the first two terms in equation 11. Figure 3 shows the movement of the image points (both in the subsurface-offset domain and the angle domain) caused by changes in the ray length L . Figure 4 provides

a geometrical explanation of why the second term in equation 11 vanishes. It shows that perturbations in the aperture angle γ cause the subsurface-offset domain image point to move along the tangent to the wavefront (tilted with the phase angle $\tilde{\gamma}$). Since this movement is constrained along the tangent, the image point in the angle domain does not move, no matter how large the movement in the subsurface-offset domain is.

RMO function with uniform scaling of velocity

In case of uniform scaling of velocity, the derivative of the imaging depth z_γ with respect to the perturbation component ρ_V has the following simple form:

$$\frac{\partial z_\gamma}{\partial \rho_V} = z_\xi (1 + \tan \gamma \tan \tilde{\gamma}), \quad (18)$$

because the derivative of the slowness with respect to a uniform scaling of the velocity has the following simple form:

$$\frac{\partial S(\gamma)}{\partial \rho_V} = -S(\gamma), \quad (19)$$

that causes the derivative $\partial L/\partial \rho_V = -z_\xi/\cos \gamma$ to be independent from the “local” shape of the anisotropic slowness function. Intuitively, this simplification is related to the fact that the “shape” of the wavefronts is not affected by a uniform scaling of the velocity.

The residual moveout Δz_{RMO} is defined as the difference between the reflector movement at finite aperture angle $\tilde{\gamma}$ and the reflector movement at normal incidence. From equation 18 the partial derivative of Δz_{RMO} with respect to ρ_V is equal to the following expression:

$$\frac{\partial \Delta z_{\text{RMO}}}{\partial \rho_V} = z_\xi \tan \gamma \tan \tilde{\gamma}. \quad (20)$$

When the medium is isotropic, and the phase angles are equal to the group angles, the RMO expression in equation 20 becomes the RMO expression introduced by Biondi and Symes (2003).

The dependency of equation 20 from the group angles increases the complexity of its use because it requires the transformation of phase angles (measured directly from the ADCIGs) into group angles by applying equation A-2. The computational cost of evaluating equation A-2 is negligible, but its use makes the computations dependent on the local values of the background anisotropic velocity function. On the other hand, the following numerical examples show that substantial errors are introduced when the distinction between the group and phase angles is neglected, and the phase angle is used instead of the group angle in equation 20.

RMO function with arbitrary scaling of velocity

The expressions of the derivative of z_γ with respect to arbitrary perturbations of individual velocity components (i.e. V_V , V_H , and V_N) are slightly more complex than with respect to ρ_V

because the wavefronts are deformed when the velocity components are unevenly perturbed. These derivatives can be expressed as:

$$\frac{\partial z_\gamma}{\partial \rho_{V_V}} = -\frac{z_\xi}{S(\gamma)} \frac{\partial S(\gamma)}{\partial \rho_{V_V}} (1 + \tan \gamma \tan \tilde{\gamma}), \quad (21)$$

$$\frac{\partial z_\gamma}{\partial \rho_{V_H}} = -\frac{z_\xi}{S(\gamma)} \frac{\partial S(\gamma)}{\partial \rho_{V_H}} (1 + \tan \gamma \tan \tilde{\gamma}), \quad (22)$$

$$\frac{\partial z_\gamma}{\partial \rho_{V_N}}, = -\frac{z_\xi}{S(\gamma)} \frac{\partial S(\gamma)}{\partial \rho_{V_N}} (1 + \tan \gamma \tan \tilde{\gamma}). \quad (23)$$

The partial derivatives of the RMO function Δz_{RMO} are directly derived from the partial derivatives of z_γ , taking into account that for flat reflectors only the vertical velocity component V_V influences the image depth of normal incidence. The derivatives of Δz_{RMO} can thus be written as follows:

$$\frac{\partial \Delta z_{\text{RMO}}}{\partial \rho_{V_V}} = -\frac{z_\xi}{S(\gamma)} \frac{\partial S(\gamma)}{\partial \rho_{V_V}} (1 + \tan \gamma \tan \tilde{\gamma}) - z_\xi, \quad (24)$$

$$\frac{\partial \Delta z_{\text{RMO}}}{\partial \rho_{V_H}} = -\frac{z_\xi}{S(\gamma)} \frac{\partial S(\gamma)}{\partial \rho_{V_H}} (1 + \tan \gamma \tan \tilde{\gamma}), \quad (25)$$

$$\frac{\partial \Delta z_{\text{RMO}}}{\partial \rho_{V_N}} = -\frac{z_\xi}{S(\gamma)} \frac{\partial S(\gamma)}{\partial \rho_{V_N}} (1 + \tan \gamma \tan \tilde{\gamma}). \quad (26)$$

The expressions for the derivatives of the slowness function with respect to the perturbation parameters depend on the particular form chosen to approximate the slowness function. Appendix C presents a particular approximation to the VTI group slowness function and derives the corresponding partial derivatives to be substituted in equations 21–23 and in equations 24–26. I used the same approximation to the VTI group slowness for the numerical experiments shown in this paper.

Conversion of depth errors into traveltimes errors in heterogeneous media

The RMO functions derived above can be directly used in a layered-based vertical updating of the velocity function after migration. However, in complex media it is often desirable to invert the depth errors measured from ADCIGs into velocity-parameter perturbations through a tomographic procedure. To be able to apply a tomographic method, we must perform an additional step to convert the depth errors measured from ADCIGs into traveltimes errors. This depth-to-time conversion can be easily accomplished by slightly rewriting the chain of partial derivatives in equation 14, and obtain the following relationship:

$$\frac{\partial z_\gamma}{\partial t} = \frac{\partial z_\gamma}{\partial L} \frac{\partial L}{\partial t} = \frac{\cos \gamma + \sin \gamma \tan \tilde{\gamma}}{S(\gamma)}, \quad (27)$$

which can be directly applied to convert depth errors into traveltimes perturbations to be used in tomography.

It is immediate to verify that in the isotropic case, in which $\tilde{\gamma} = \gamma$, equation 27 simplifies into the following relationship:

$$\frac{\partial z_\gamma}{\partial t} = \frac{1}{\cos \gamma S(\gamma)}, \quad (28)$$

which is equivalent to the relationship derived for isotropic MVA by Biondi and Symes (2003).

Synthetic-data examples of RMO function in ADCIGs

To verify the accuracy of the RMO functions derived in this section I performed several numerical tests using synthetic data modeled and migrated using an anisotropic source-receiver migration and modeling program. This program performed depth extrapolation by numerically solving the following dispersion relation:

$$k_z = \frac{\omega}{V_V} \sqrt{\frac{\omega^2 - V_H^2 k_x^2}{\omega^2 + (V_N^2 - V_H^2) k_x^2}}, \quad (29)$$

where ω is the temporal frequency, and k_x and k_z are respectively the horizontal and vertical wavenumbers. This dispersion relation corresponds to the slowness functions in equation C-1 (Fowler, 2003), which was used to compute the RMO functions according to the theory developed above.

To test the theory under realistic and diverse anisotropic conditions, in the numerical examples I used three sets of anisotropic Thomsen parameters representing three different rocks described by Tsvankin (2001):

- Taylor Sand : $\epsilon = 0.110$ $\delta = -0.035$, $\rightarrow \eta = .155$,
- Mesa Clay Shale : $\epsilon = 0.189$, $\delta = 0.204 \rightarrow \eta = -.010$,
- GreenLight River Shale : $\epsilon = 0.0975$, $\delta = -0.11$, $\rightarrow \eta = .266$.

The GreenLight River Shale is derived from the Green River Shale described by Tsvankin (2001) by halving the anisotropic parameters (ϵ and δ), because the strong anelliptic nature of the original one ($\eta = .74$) causes the group-slowness approximation in equation C-1 to break down. Consequently, the kinematic computations based on ray tracing, and thus on group velocity and angles, become inconsistent with wavefield migration based on the dispersion relation in equation 29. Notice that the GreenLight River Shale is still the most anelliptic among the set of rocks I am using.

The first set of numerical experiments tests the RMO equation with uniform scaling of velocity expressed in equation 20. In addition to the three anisotropic cases described above, this RMO function is tested also for the special case of isotropic velocity. The second set tests the generalized RMO functions expressed in equations 24–26. Only the three anisotropic cases are tested because there is no meaningful isotropic case to test the generalized RMO function. In all the synthetic-data examples I plot the correct RMO curve computed by applying either equation 18 or equations 24–26, and the approximate RMO curve computed using

an “isotropic” approximation and ignoring the distinction between the group aperture angle γ and the phase aperture angle $\tilde{\gamma}$.

Figure 5 shows ADCIGs when an anisotropic velocity was perturbed by $\rho_V = .99$. The four panels correspond to four rock types: a) Isotropic, b) Taylor Sand, c) Mesa Clay Shale, and d) GreenLight River Shale. Superimposed onto the images are the RMO functions computed using equation 20. The solid line was computed by computing $\tan \gamma$ from $\tan \tilde{\gamma}$ by applying equation A-2, whereas the dashed line was computed by approximating $\tan \gamma$ as equal to $\tan \tilde{\gamma}$. The RMO curves computed using the correct group angle perfectly match the residual moveout of the images. On the contrary, when the phase angles are used instead of the group angles, significant errors are introduced even for such a small perturbation in the parameters ($\rho_V = .99$). It is interesting to notice that the errors are larger for the rock types exhibiting strong anelliptic anisotropy (Taylors Sand and GreenLight River Shale) than for the strongly anisotropic but quasi-elliptical rock (Mesa Clay Shale).

The expression for the RMO function derived in equation 20 is based on a linearization, and thus when the perturbations in velocity parameters are large it is not as accurate as it is when the perturbations are small (e.g. $\rho_V = .99$). Figure 6 illustrates this fact by showing a similar experiment as the one shown in Figure 5, but with a perturbation 10 times larger; that is, with $\rho_V = .9$. As in Figure 5, the four panels correspond to four rock types: a) Isotropic, b) Taylor Sand, c) Mesa Clay Shale, and d) GreenLight River Shale, and the lines superimposed onto the images are the RMO functions computed by using the correct values for $\tan \gamma$ (solid lines), and by using $\tan \tilde{\gamma}$ in place of $\tan \gamma$ (dashed lines). With large perturbations, the predicted RMO functions differ from the actual RMO functions at wide aperture angles even when the correct values of the group angles are used in equation 20. However, even with such large perturbations the predicted RMO functions are still useful approximations of the actual RMO functions. In particular, it can be observed that the predicted RMO function correctly approximates the differences in shape of the actual RMO function among the rock types. These shape variations are related to the variations in shape of the wavefronts, which are reflected in the predicted RMO function through the variations in the mapping from phase angles to group angles. Figures 7 and 8 show examples of the application of the generalized RMO functions expressed in equations 24–26. As in Figures 5–6, I show the ADCIGs for three different anisotropic rock types, but, differently from the previous figures, not for the isotropic case. The order of the rock types is the same as in Figures 5–6; that is: panels a) correspond to Taylor Sand, panels b) to Mesa Clay Shale, and panels c) to GreenLight River Shale. Furthermore, as in Figures 5–6, one figure (Figure 8) shows the ADCIG obtained with a smaller perturbation than the ADCIGs shown in the other figure (Figure 7). The ADCIGs shown in Figure 7 were obtained by performing *isotropic* migration on the synthetic data modeled assuming *anisotropic* velocity. The ADCIGs shown in Figure 8 were computed by scaling by .25 the parameter perturbations used to compute Figure 7. The lines superimposed onto the images are the RMO functions computed by using the correct values for $\tan \gamma$ (solid lines), and by using $\tan \tilde{\gamma}$ in place of $\tan \gamma$ (dashed lines).

The predicted RMO functions accurately track the actual RMO functions when the parameter perturbations are sufficiently small to be within the range of accuracy of the linearization at the basis of the derivation of equation 20 (Figure 8). But even when the perturbations are

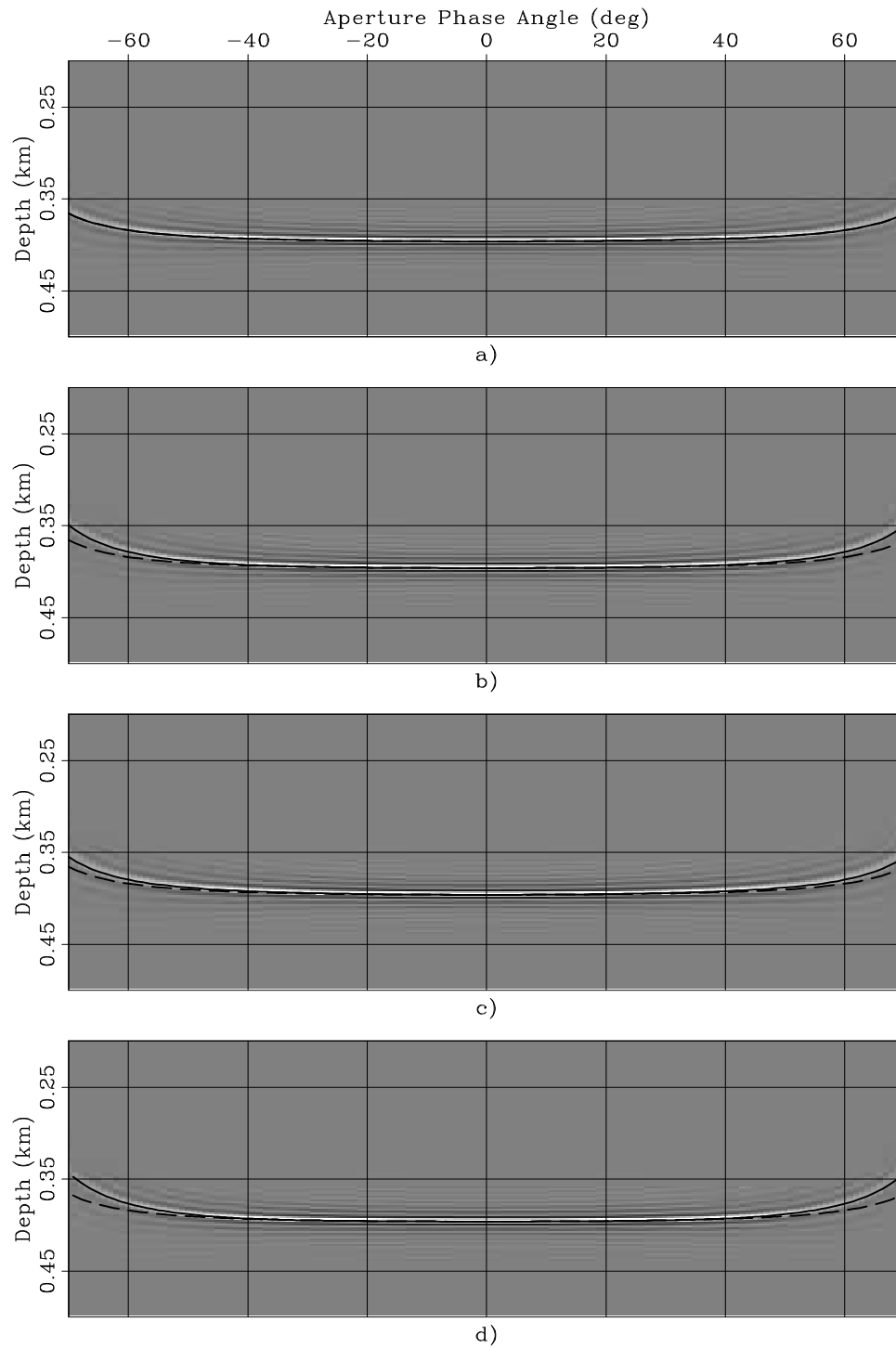


Figure 5: ADCIGs obtained when a constant anisotropic velocity was perturbed by $\rho_V = .99$ for four rock types: a) Isotropic, b) Taylor Sand, c) Mesa Clay Shale, and d) GreenLight River Shale. Superimposed onto the images are the RMO functions computed using equation 20. The solid line was computed when $\tan \gamma$ was derived from $\tan \tilde{\gamma}$ by applying equation A-2, whereas the dashed line was computed by approximating $\tan \gamma$ as equal to $\tan \tilde{\gamma}$.

biondo2-Quad_Aniso-rho.99_overn [CR]

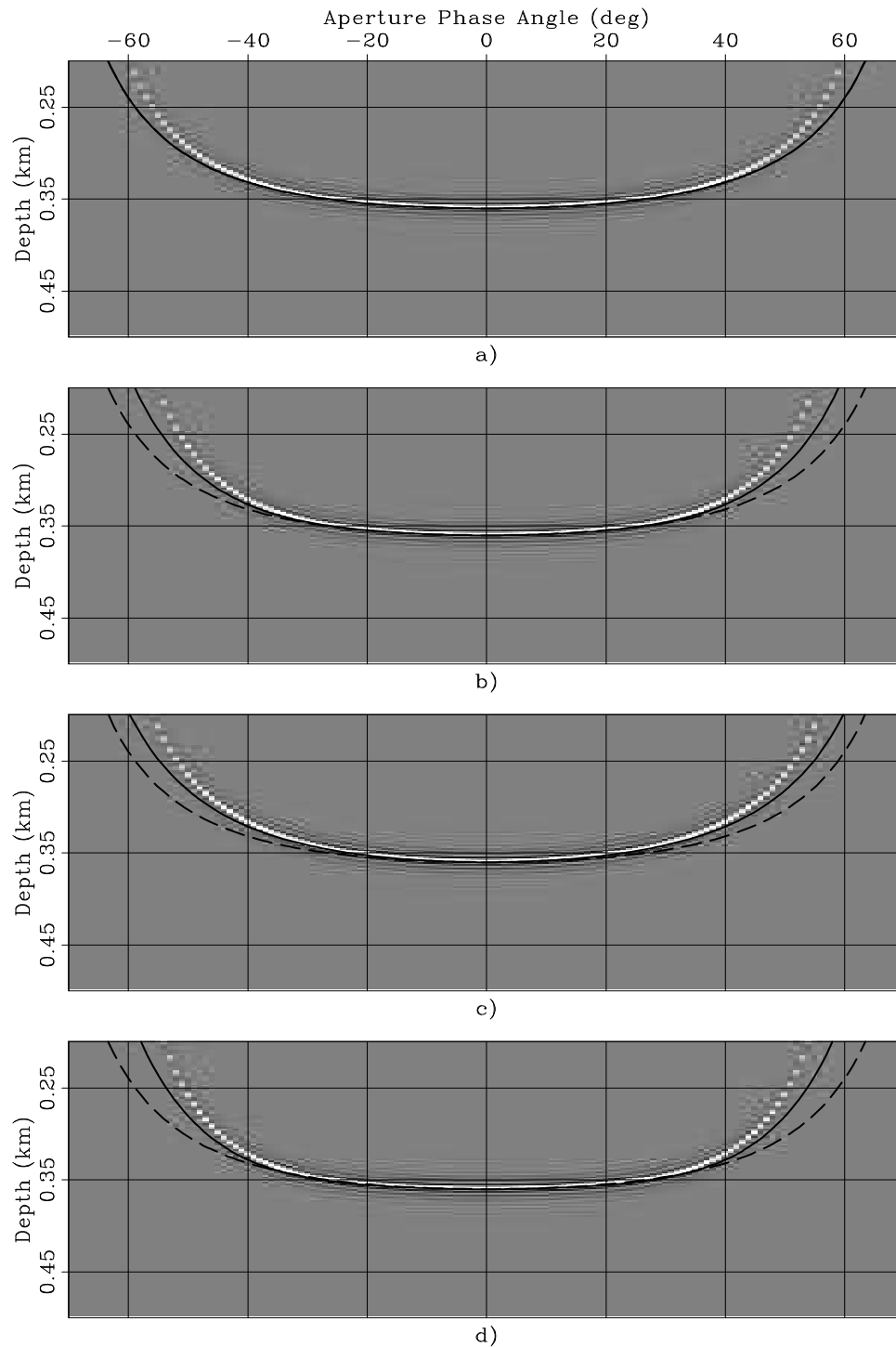


Figure 6: ADCIGs obtained when a constant anisotropic velocity was perturbed by $\rho_V = .9$ for four rock types: a) Isotropic, b) Taylor Sand, c) Mesa Clay Shale, and d) GreenLight River Shale. Superimposed onto the images are the RMO functions computed using equation 20. The solid line was computed when $\tan \gamma$ was derived from $\tan \tilde{\gamma}$ by applying equation A-2, whereas the dashed line was computed by approximating $\tan \gamma$ as equal to $\tan \tilde{\gamma}$.

`biondo2-Quad_Aniso-rho.9_overn` [CR]

large (Figure 7) and cause a substantial RMO (up to 30% of the reflector depth) the predicted RMO functions are excellent approximations of the actual RMO functions.

The RMO functions associated with the two strongly anelliptic rocks (Taylor Sand and GreenLight River Shale) exhibit a characteristic oscillatory behavior; the events at narrow-aperture angles are imaged deeper than the normal incidence event, whereas the events at wide-aperture angles are imaged shallower. This oscillatory behavior is well predicted by the analytical RMO function introduced in equations 24–26.

In contrast, the approximation of the group angles with the phase angles (dashed lines in the figures) seriously deteriorates the accuracy of the predicted RMO functions. Notice that, in contrast with the uniform-perturbation case illustrated in Figures 5– 6, the dashed lines are different among the panels, because the derivatives of the slowness function with respect to the perturbation parameters depend on the anisotropic parameters of the background medium.

GULF OF MEXICO DATA EXAMPLE

To test the accuracy of the RMO functions derived in this paper, I migrated a 2-D line extracted from a 3-D data set that was kindly provided to SEP by ExxonMobil. To minimize 3-D effects, the location of the 2-D line was chosen in an area where the sediments are mostly flat in the cross-line direction and where the salt flanks are mostly perpendicular to the in-line direction.

The data set was acquired in the Gulf of Mexico over an existing reservoir. Therefore several borehole seismic data sets were available in addition to the surface data to constraint the estimation of the anisotropic parameters. ExxonMobil provided SEP with three anisotropic-parameter cubes resulting from a joint inversion of the surface data and the borehole data (Krebs et al., 2003). Figure 9 shows the vertical slices cut through these cubes at the cross-line location corresponding to the 2-D line that I migrated. Panel a) displays the vertical velocity, panel b) displays the values of δ , and panel c) displays the values of η . To avoid artifacts caused by sharp parameter contrasts, for migration I removed the salt body from the functions displayed in Figure 9. I “infilled” the salt body with sediment-like values by interpolating the functions inward starting from the sediment values at the salt-sediment interface.

Figure 10 compares the result of anisotropic prestack depth migration (panel a) with the results of isotropic depth migration obtained using as migration velocity the vertical velocity function (panel b). The anisotropic-migration image is clearly superior to the isotropic-migration image that shows clear sign of undermigration of the salt-flanks reflections as well of the sediments terminating against the salt body. All the reflectors are nicely imaged by the anisotropic migration, except for the shallow tract of the salt flank on the left-hand side of the body because it has large cross-line dip components.

Figure 11 shows two examples of ADCIGs computed from both the anisotropic and the isotropic migration results. The CIGs shown in panel a) and b) are taken at surface location of 3,725 meters (left vertical black line in Figure 10) and the CIGs shown in panel c) and d) are taken at surface location of 11,625 meters (right vertical black line in Figure 10). The

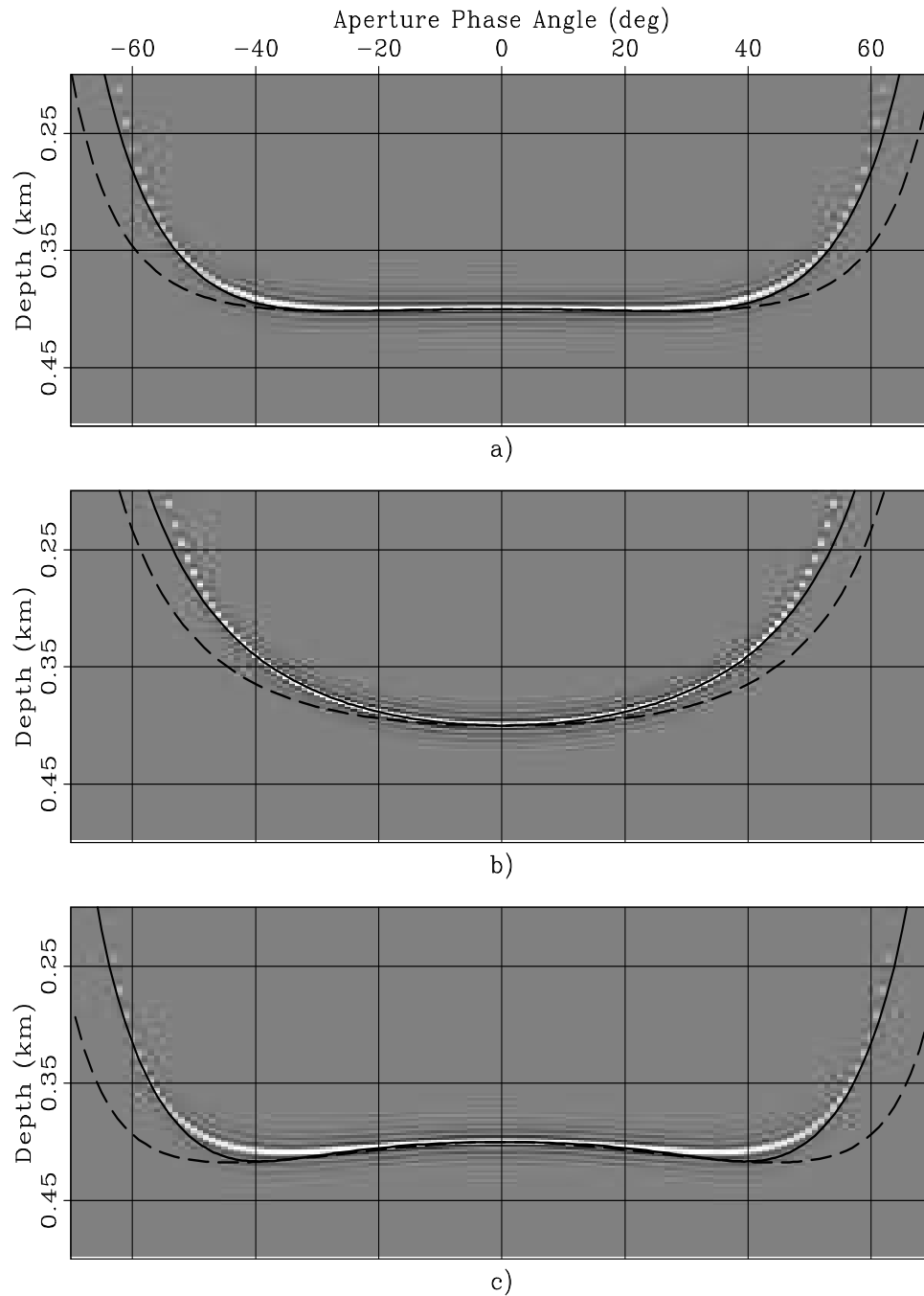


Figure 7: ADCIGs obtained when data modeled with an *anisotropic* velocity have been migrated using an *isotropic* velocity. The anisotropic data were modeled assuming three rock types: a) Taylor Sand, b) Mesa Clay Shale, and c) GreenLight River Shale. Superimposed onto the images are the RMO functions computed using equation 20. The solid line was computed when $\tan \gamma$ was derived from $\tan \tilde{\gamma}$ by applying equation A-2, whereas the dashed line was computed by approximating $\tan \gamma$ as equal to $\tan \tilde{\gamma}$. biondo2-Trio_Aniso-iso_overn
[CR]

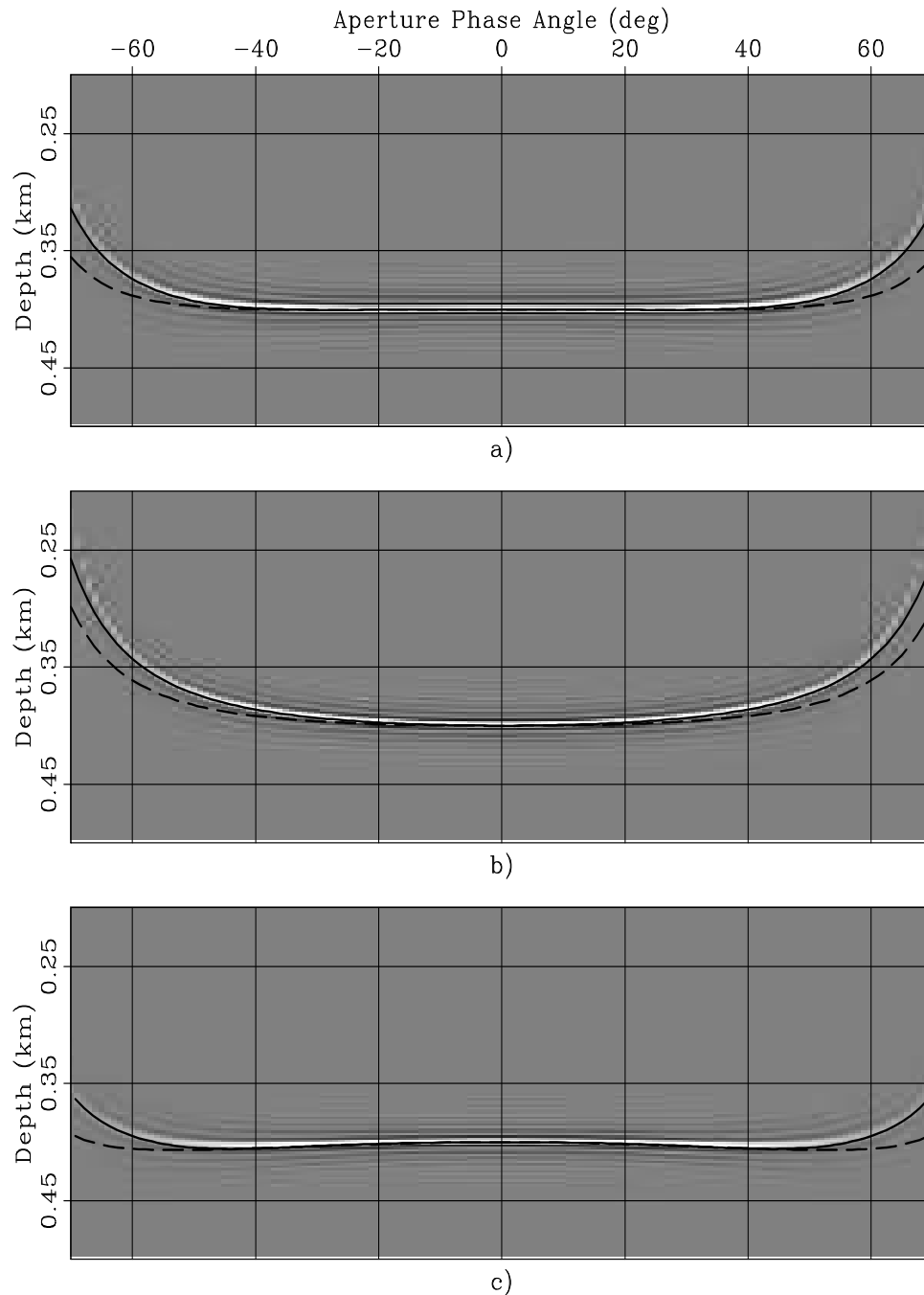


Figure 8: ADCIGs obtained when data modeled with an *anisotropic* velocity have been migrated using a *less anisotropic* velocity; that is, with anisotropic parameters obtained by scaling by .25 the parameter perturbations used to compute Figure 7. The anisotropic data were modeled assuming three rock types: a) Taylor Sand, b) Mesa Clay Shale, and c) GreenLight River Shale. Superimposed onto the images are the RMO functions computed using equation 20. The solid line was computed when $\tan \gamma$ was derived from $\tan \tilde{\gamma}$ by applying equation A-2, whereas the dashed line was computed by approximating $\tan \gamma$ as equal to $\tan \tilde{\gamma}$.

biondo2-Trio_Aniso-scaled_overn [CR]

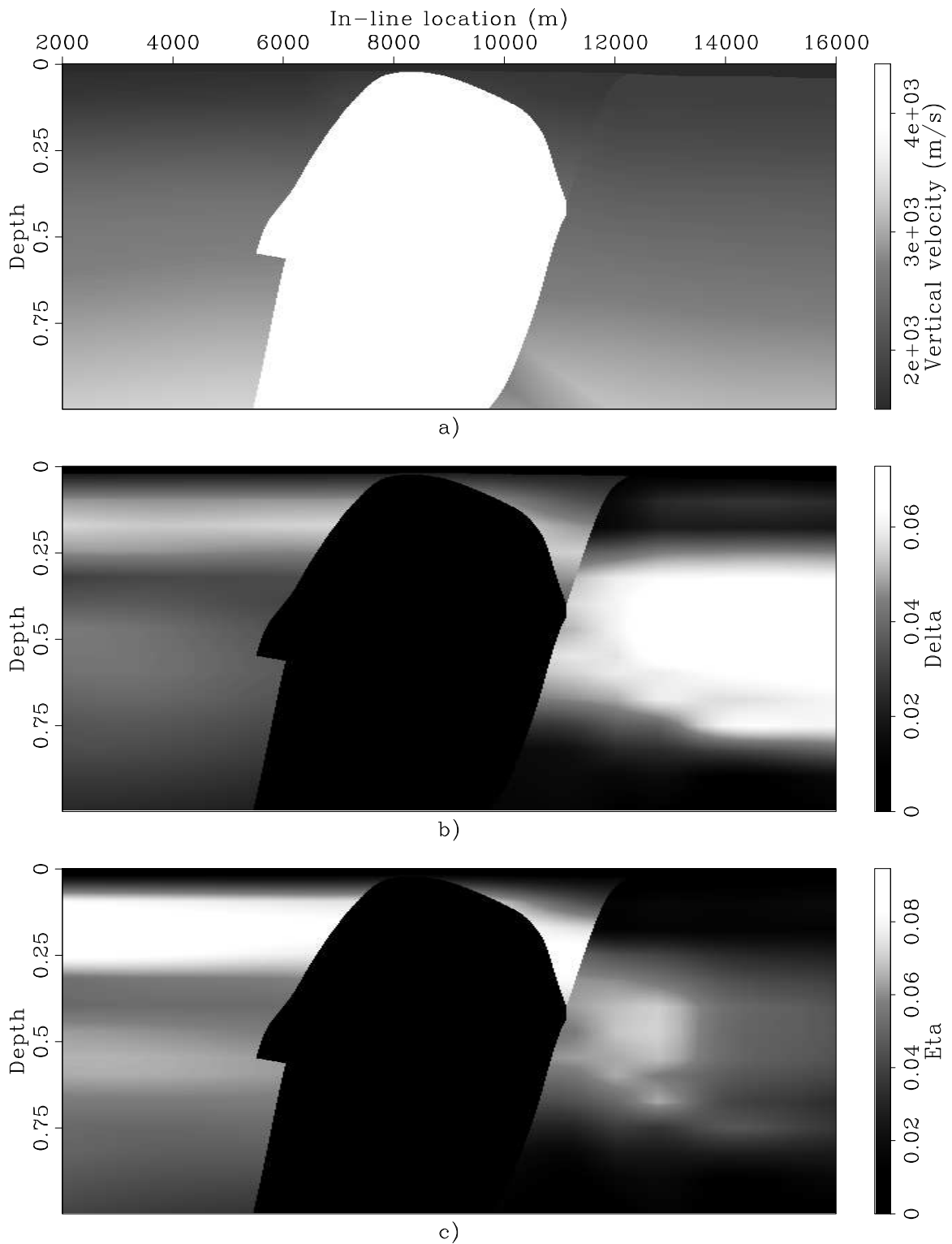


Figure 9: Vertical slices cut through the anisotropic velocity parameters cubes. Panel a) shows the vertical velocity field, panel b) shows the δ field, and panel c) shows the η field. I removed the salt body from the parameters functions used for migration, to avoid artifacts caused by sharp parameter discontinuities. [biondo2-Par-Sections-overn](#) [CR]

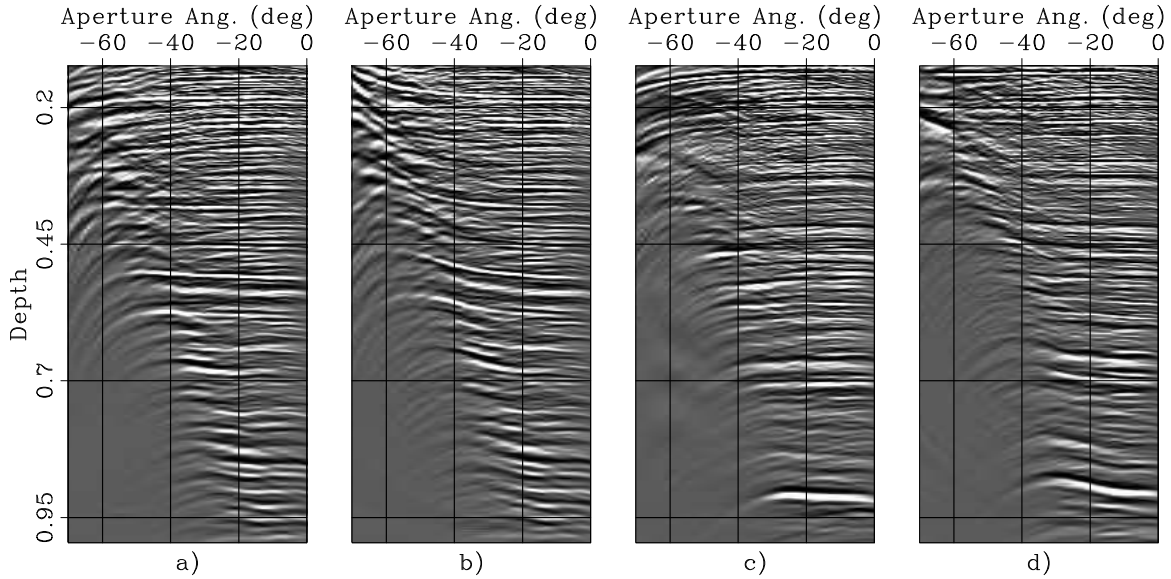


Figure 11: ADCIGs computed by anisotropic migration (panels a) and c)) and isotropic migration (panels b) and d)). The ADCIG shown in panels a) and b) are taken at the surface location of 3,725 meters. The ADCIG shown in panel c) and d) are taken at the surface location of 11,625 meters. `biondo2-Quad-aniso-iso-overn` [CR]

ADCIGs obtained by anisotropic migration (panels a and c) are uniformly flatter than the ADCIGs obtained by isotropic migration (panels b and d). The ADCIGs obtained by isotropic migration display the typical hockey-stick behavior commonly seen in CIGs computed by isotropic Kirchhoff migration in anisotropic media. Although the isotropic migration image is evidently not well focused, this result does not preclude the possibility that an isotropic migration velocity could be defined to focus the data satisfactorily. However, an isotropic migration with a different velocity model would also position the reflectors at substantially different locations. These location would not equally match the depth measured from the wells (Bear et al., 2003).

The RMO function derived in this paper assumes a homogeneous layer above the reflector to be analyzed. To test the accuracy of the expressions for the RMO function I therefore estimated the average anisotropic parameters between the sea floor and two reflectors, one shallow and the other deep, easily identifiable in the ADCIG located at 3,725 meters (Figure 11a). Figures 12 and 13 show the result of my analysis.

Figure 12c shows the ADCIG obtained after anisotropic migration using the following average parameters below the sea floor: $V_V = 1,750$ m/s, $\epsilon = 0.11$, $\delta = 0.04$, and $\eta = .065$. Figure 12d shows the ADCIG obtained after isotropic migration using $V_V = 1,750$ m/s. The shallow reflection of interest is flat in Figure 12c, whereas it is smiling upward in Figure 12d. For comparison, Figures 12a and 12b show a zoom of Figures 11a and 11b into the same window of the ADCIGs as the one displayed in Figures 12c and 12d. The curve superimposed onto both Figures 12b and 12d was computed using the generalized RMO functions expressed in equations 24–26. The computed RMO function perfectly overlaps the event in the ADCIG

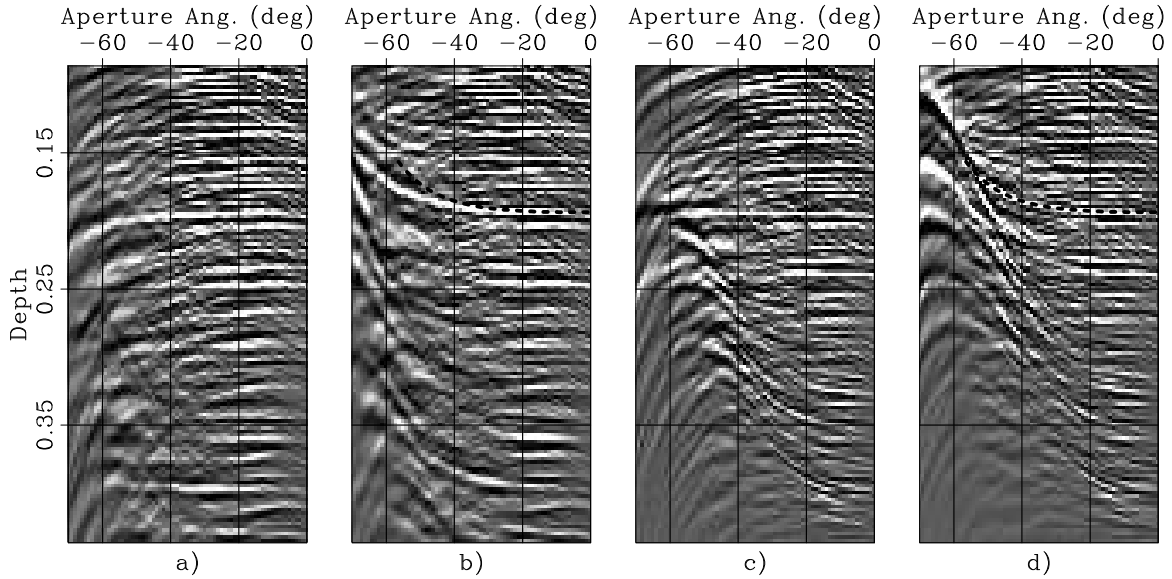


Figure 12: ADCIGs taken at the surface location of 3,725 meters and with the layer below the sea floor being: a) anisotropic and heterogeneous, b) isotropic and heterogeneous, c) anisotropic and homogeneous ($V_V = 1,750$ m/s, $\epsilon = 0.11$, $\delta = 0.04$, and $\eta = .065$), d) isotropic and homogeneous ($V_V = 1,750$ m/s). The RMO curve that is superimposed onto panels b) and d) is computed using equations 24–26. biondo2-Quad-Aniso-shallow-overn [CR]

in Figure 12d. In contrast, the computed RMO function overestimates the moveout in the ADCIG obtained by migrating the data using the original isotropic model (Figure 12b). The cause of this discrepancy is the ray bending induced by the vertical gradient in the original heterogeneous model. Because of ray bending the events propagate more vertically, and thus more slowly, in the heterogeneous medium than in the homogeneous one. In cases when explicit raytracing though the background velocity is necessary to compute the RMO function, equation 27 provides the necessary link between the traveltim perturbations accumulated along the rays and the depth perturbations measured in the ADCIGs.

The ADCIGs shown in Figure 13 display a behavior similar to the ones shown in Figure 12. Since the reflection of interest is now deep, the half-space below the sea floor is characterized by higher average parameters than for the shallow reflection; that is: $V_V = 2,000$ m/s, $\epsilon = 0.143$, $\delta = 0.045$, and $\eta = .09$. As before, the reflection of interest in ADCIG migrated using these parameters (Figure 13c) is flat, whereas the same reflection in the ADCIG migrated with isotropic migration with the same vertical velocity ($V_V = 2,000$ m/s) is smiling upward (Figure 13d). As before, the RMO curve computed using equations 24–26 perfectly overlaps the event in the ADCIG shown in Figure 13d, whereas it overestimates the moveout in the ADCIG obtained by migrating the data using the original isotropic model (Figure 13b).

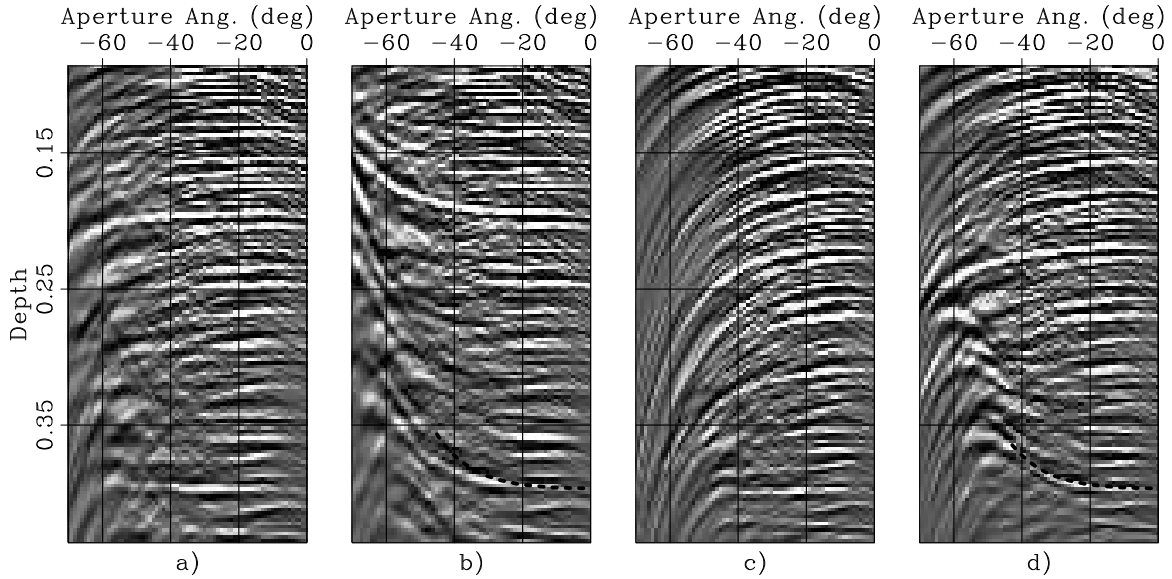


Figure 13: ADCIGs taken at the surface location of 3,725 meters and with the layer below the sea floor being: a) anisotropic and heterogeneous, b) isotropic and heterogeneous, c) anisotropic and homogeneous ($V_V = 2,000$ m/s, $\epsilon = 0.143$, $\delta = 0.045$, and $\eta = .09$), d) isotropic and homogeneous ($V_V = 2,000$ m/s). The RMO curve that is superimposed onto panels b) and d) is computed using equations 24–26. biondo2-Quad-Aniso-deep-overn [CR]

CONCLUSIONS

The methodology presented in this paper enables the use of ADCIGs to iteratively estimate anisotropic velocity parameters in conjunction with anisotropic wavefield-continuation migration. This advancement should enable the performance of MVA in areas where the overburden is both anisotropic and complex to require anisotropic wavefield-continuation migration.

The linearized analysis of depth perturbations in ADCIGs obtained by anisotropic migration shows that the RMO function observed when the migration velocity is inaccurate is a function of both the phase aperture angle and the group aperture angle. The synthetic-data examples show that the linearized expression of the RMO function accurately predicts the actual RMO function measured after wavefield migration.

The real data results confirm the accuracy of the theory developed in this paper. The RMO curves predicted by the theory match extremely well the RMO functions observed in the ADCIG migrated according to the assumptions underlying the theory. We observe fairly large differences in RMO functions observed between the ADCIGs computed assuming an isotropic homogeneous half-space hanging from the sea floor and the ADCIGs computed assuming an isotropic heterogeneous model. These discrepancies demonstrate the sensitivity of the RMO analysis to the accuracy with which the background velocity predicts the actual ray bending. This sensitivity is higher for anisotropic media because of the velocity dependence on the

propagation angle, suggesting that a tomographic MVA might be even more necessary for anisotropic media than for isotropic ones.

Tomographic updating of the anisotropic parameters from ADCIGs can be based on the same fundamental concepts used to derive the RMO functions presented and tested in this paper. I therefore derive the linearized relationship between depth errors measured in ADCIGs and travelttime errors accumulated along the wavepaths. This relationship should lead to the development of anisotropic MVA methods based on tomographic velocity-updating procedures.

ACKNOWLEDGMENTS

I would like to thank the ExxonMobil Exploration Company for making the Gulf of Mexico data set used in this paper data available to SEP through the generous efforts of Ruth Gonzalez and Joe Reilly. The anisotropic parameters cube were kindly shared with us by Laura Bear and Jerry Krebs, also at ExxonMobil.

REFERENCES

- Bear, L., Dickens, T., and Traynin, P., 2003, Incorporating nonseismic information for improved positioning with anisotropic PSDM: 73rd Ann. Internat. Meeting, Soc. of Expl. Geophys., Expanded Abstracts, 949–952.
- Biondi, B., and Sava, P., 1999, Wave-equation migration velocity analysis: 69th Ann. Internat. Meeting, Soc. of Expl. Geophys., Expanded Abstracts, 1723–1726.
- Biondi, B., and Symes, W. W., 2003, Angle-domain common-image gathers for migration velocity analysis by wavefield-continuation imaging: *Geophysics*, **69**, 1283–1298.
- Biondi, B., and Tisserant, T., 2004, 3-D angle-domain common-image gathers for migration velocity analysis: *Geophysical Prospecting*, **52**, 575–591.
- Biondi, B., 2005, Angle-domain common image gathers for anisotropic migration: SEP-123.
- Clapp, R., and Biondi, B., 2000, Tau domain migration velocity analysis using angle CRP gathers and geologic constrains: 70th Ann. Internat. Meeting, Soc. of Expl. Geophys., Expanded Abstracts, 926–929.
- Dellinger, J., and Muir, F., 1985, Two domains of anisotropy: SEP-44, 59–62.
- Fowler, P., 2003, Practical VTI approximations: a systematic anatomy: *Journal of Applied Geophysics*, **69**, 347–367.
- Krebs, J., Bear, L., and Liu, J., 2003, Integrated velocity model estimation for accurate imaging: 73rd Ann. Internat. Meeting, Soc. of Expl. Geophys., Expanded Abstracts, 2084–2087.

Sarkar, D., and Tsvankin, I., 2003, Analysis of image gathers in factorized vti media: *Geophysics*, **68**, 2016–2025.

Sarkar, D., and Tsvankin, I., 2004a, Anisotropic migration velocity analysis: Application to a data set from West Africa: 74th Ann. Internat. Meeting, Soc. of Expl. Geophys., Expanded Abstracts, 2399–2402.

Sarkar, D., and Tsvankin, I., 2004b, Migration velocity analysis in factorized vti media: *Geophysics*, **69**, 708–718.

Tsvankin, I., 2001, *Seismic signatures and analysis of reflection data in anisotropic media*: Elsevier Science.

APPENDIX A

PHASE AND GROUP ANGLES AND VELOCITIES

In anisotropic wave propagation the phase angles and velocities are different from the group angles and velocities. In this appendix I briefly review the concepts of phase and group angles and velocities and the relationships between these physical quantities.

The transformation from phase velocity \tilde{V} to group velocity V is conventionally defined as the following (Tsvankin, 2001):

$$V = \sqrt{\tilde{V}^2 + \left(\frac{d\tilde{V}}{d\tilde{\theta}}\right)^2}, \quad (\text{A-1})$$

where $\tilde{\theta}$ is the phase propagation angle. The associated transformation from phase angles to group angles θ is defined as:

$$\tan \theta = \frac{\tan \tilde{\theta} + \frac{1}{V} \frac{d\tilde{V}}{d\tilde{\theta}}}{1 - \frac{1}{V} \frac{d\tilde{V}}{d\tilde{\theta}} \tan \tilde{\theta}}. \quad (\text{A-2})$$

Dellinger and Muir (1985) propose, and heuristically motivate, the following symmetric relations for the inverse transforms:

$$\tilde{S} = \sqrt{S^2 + \left(\frac{dS}{d\theta}\right)^2}, \quad (\text{A-3})$$

where \tilde{S} and S are respectively the phase slowness and the group slowness, and

$$\tan \tilde{\theta} = \frac{\tan \theta + \frac{1}{\tilde{S}} \frac{dS}{d\theta}}{1 - \frac{1}{\tilde{S}} \frac{dS}{d\theta} \tan \theta}. \quad (\text{A-4})$$

I use the heuristic relation in equation A-4 to derive some of the analytical results presented in this paper. Furthermore, I use all the above relationships to compute the kinematic numerical results presented in this paper.

APPENDIX B

INDEPENDENCE OF DEPTH PERTURBATIONS FROM ANGLE PERTURBATIONS

In this appendix I demonstrate that the terms in equation 13 multiplying the partial derivatives with respect to the angles; that is, $\partial\gamma/\partial\rho_i$ and $\partial\tilde{\gamma}/\partial\rho_i$, are zero when evaluated at the point when the events are correctly migrated at zero subsurface offset. We are interested in estimating the RMO function measured for an incorrect velocity. That RMO function can be seen as a perturbation around the image obtained with the correct velocity.

After simple evaluation of partial derivatives the term multiplying $\partial\gamma/\partial\rho_i$ in equation 13 can be written as the following:

$$\begin{aligned} \left(\frac{\partial z_\gamma}{\partial L} \frac{\partial L}{\partial S(\gamma)} \frac{\partial S(\gamma)}{\partial \gamma} + \frac{\partial z_\gamma}{\partial \gamma} \right) &= -\frac{z_\xi (\cos \gamma + \sin \gamma \tan \tilde{\gamma})}{S(\gamma) \cos \gamma} \frac{\partial S(\gamma)}{\partial \gamma} - L (\sin \gamma - \cos \gamma \tan \tilde{\gamma}) \\ &= -z_\xi \left[(1 + \tan \gamma \tan \tilde{\gamma}) \frac{\partial S(\gamma)}{\partial \gamma} + \tan \gamma - \tan \tilde{\gamma} \right], \end{aligned} \quad (\text{B-1})$$

that can be easily demonstrated to be equal to zero after substitution of the relationship between phase angles and group angles presented in equation A-4.

The term multiplying $\partial\tilde{\gamma}/\partial\rho_i$ is equal to

$$\frac{\partial z}{\partial \tilde{\gamma}} = -h_\xi \frac{1}{\cos^2 \tilde{\gamma}}, \quad (\text{B-2})$$

which is obviously equal to zero when the subsurface offset is zero, the point around which we are interested in expanding the RMO function.

APPENDIX C

DERIVATIVES OF VTI SLOWNESS FUNCTION WITH RESPECT TO THE PERTURBATION PARAMETERS

In this Appendix I present the analytical expressions for the derivatives of the group slowness function with respect to the velocity-perturbation parameters ($\rho_{V_V}, \rho_{V_H}, \rho_{V_N}$). These derivatives depend on the particular form chosen to approximate the slowness function. In this paper I use following approximation of the VTI slowness function (Fowler, 2003):

$$\begin{aligned} S_{\text{VTI}}^2(\theta) &= \frac{S_V^2 \cos^2 \theta + S_H^2 \sin^2 \theta + \sqrt{(S_V^2 \cos^2 \theta + S_H^2 \sin^2 \theta)^2 + S_V^2 (S_N^2 - S_H^2) \sin^2 2\theta}}{2} \\ &= \frac{S_{\text{EII}}^2(\theta) + \sqrt{S_{\text{EII}}^4(\theta) + S_V^2 (S_N^2 - S_H^2) \sin^2 2\theta}}{2}, \end{aligned} \quad (\text{C-1})$$

where

$$S_{\text{Ell}}^2(\theta) = S_V^2 \cos^2 \theta + S_H^2 \sin^2 \theta \quad (\text{C-2})$$

is the elliptical component.

The derivatives are then written as:

$$\left. \frac{\partial S_{\text{VTI}}(\theta)}{\partial \rho_{V_V}} \right|_{\rho=1} = \frac{S_{\text{Ell}}(\theta)}{2S_{\text{VTI}}(\theta)} \frac{\partial S_{\text{Ell}}(\theta)}{\partial \rho_{V_V}} + \frac{2 \frac{\partial S_{\text{Ell}}(\theta)}{\partial \rho_{V_V}} S_{\text{Ell}}^3(\theta) - S_V^2 (S_N^2 - S_H^2) \sin^2 2\theta}{4S_{\text{VTI}}(\theta) \sqrt{S_{\text{Ell}}^4(\theta) + S_V^2 (S_N^2 - S_H^2) \sin^2 2\theta}} \quad (\text{C-3})$$

$$\left. \frac{\partial S_{\text{VTI}}(\theta)}{\partial \rho_{V_H}} \right|_{\rho=1} = \frac{S_{\text{Ell}}(\theta)}{2S_{\text{VTI}}(\theta)} \frac{\partial S_{\text{Ell}}(\theta)}{\partial \rho_{V_H}} + \frac{2 \frac{\partial S_{\text{Ell}}(\theta)}{\partial \rho_{V_H}} S_{\text{Ell}}^3(\theta) + S_V^2 S_H^2 \sin^2 2\theta}{4S_{\text{VTI}}(\theta) \sqrt{S_{\text{Ell}}^4(\theta) + S_V^2 (S_N^2 - S_H^2) \sin^2 2\theta}} \quad (\text{C-4})$$

$$\left. \frac{\partial S_{\text{VTI}}(\theta)}{\partial \rho_{V_N}} \right|_{\rho=1} = \frac{-S_V^2 S_N^2 \sin^2 2\theta}{4S_{\text{VTI}}(\theta) \sqrt{S_{\text{Ell}}^4(\theta) + S_V^2 (S_N^2 - S_H^2) \sin^2 2\theta}}, \quad (\text{C-5})$$

where the derivatives of the elliptical component with respect to ρ_{V_V} and ρ_{V_H} are:

$$\left. \frac{\partial S_{\text{Ell}}(\theta)}{\partial \rho_{V_V}} \right|_{\rho=1} = \frac{-S_V^2 \cos^2 \theta}{S_{\text{Ell}}(\theta)} \quad (\text{C-6})$$

$$\left. \frac{\partial S_{\text{Ell}}(\theta)}{\partial \rho_{V_H}} \right|_{\rho=1} = \frac{-S_H^2 \sin^2 \theta}{S_{\text{Ell}}(\theta)}. \quad (\text{C-7})$$

Short Note

Wave-equation migration from topography: Imaging Husky

Jeff Shragge¹

INTRODUCTION

Imaging land seismic data is wrought with many technical challenges that arise during different stages of seismic investigation: acquisition (e.g. irregular geometry), preprocessing (e.g. ground-roll suppression, statics), velocity estimation (e.g. near-surface complexity) and migration (e.g. rugged topography, uncertain velocities). Each of these complicating factors needs addressing before satisfactory final images are generated. Given the completion of each pre-migration processing step, one may choose from a variety of migration techniques; however, velocity profiles and geologic structures often are sufficiently complex to warrant wave-equation imaging. A caveat, though, is that wave-equation migration (WEM) is usually implemented with regularly sampled data on Cartesian meshes. Hence, conventional WEM from topography usually requires data regularization prior to migration.

Topographic data regularization approaches often include pre-migration datuming using statics corrections. These basic processes use vertical time-shifting of the wavefield to estimate the data recorded on a flat datum above or below the true acquisition surface. Standard migration techniques (e.g. wave-equation or Kirchhoff) may then be applied directly to the regularized dataset. However, the vertical wavefield propagation assumption usually is not satisfied in areas characterized by fast near-surface velocities and strong velocity gradients (e.g. in the Canadian Rocky Mountain Foothills) due to limited accuracy at propagation angles that deviate significantly from vertical. Hence, more advanced techniques able to incorporate topography are needed. A short and not exhaustive list of such methods (e.g. using more kinematically correct Kirchhoff operators (Bevc, 1997)) is presented in Shragge and Sava (2004).

In general, most wave-equation processing solutions to topographic data irregularity use a strategy of forcing data to conform to Cartesian geometry. The converse of this situation is to tailor wave-equation migration implementation to coordinate system meshes defined by the acquisition geometry. Shragge and Sava (2004), following the latter strategy, extend wave-equation migration to “topographic coordinate systems” conformal to acquisition topography. Although Shragge and Sava (2004) applied this approach to synthetic 2D data, they neither tested the algorithm on field data nor compared it to more conventional imaging from standard topography approaches (e.g. Kirchhoff migration). This paper addresses these issues

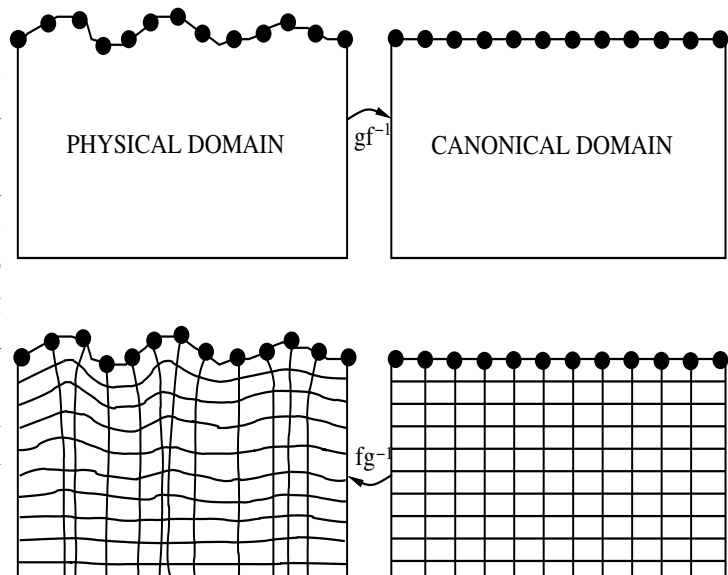
¹email: jeff@sep.stanford.edu

with imaging experiments using the Husky 2D land dataset acquired in the Canadian Rocky Mountain Foothills.

NON-TECHNICAL TECHNIQUE OVERVIEW

This section briefly describes the wave-equation migration from topography (TopoWEM) approach presented in Shragge and Sava (2004). Two theoretical developments are central to the technique: i) generating an orthogonal grid conformal with the acquisition surface using a conformal mapping approach; and ii) adapting wave-propagation physics to be consistent with the geometry of the computational mesh using Riemannian wavefield extrapolation (RWE) (Sava and Fomel, 2005). Conformal mapping transforms can be manipulated to generate an orthogonal coordinate system by computing a mapping from a topographically influenced domain to a rectangular mesh (c.f. Figure 1). First, the image of the boundary points in the physical domain (upper left) is found in the canonical domain (upper right) through composite mapping $g \cdot f^{-1}$ (where g and f^{-1} represent mappings from the physical domain to the unit circle and from the unit circle to a rectangle, respectively). A uniform mesh, specified in the canonical domain (lower right), is then mapped to the physical domain (bottom left) using the inverse relation $g^{-1} \cdot f$, creating an orthogonal mesh conformal to the topographic surface.

Figure 1: Cartoon showing the conformal mapping transform between topographic and rectangular domains. Top left: topographic domain with data acquisition points; Top right: domain boundary in top left mapped to a rectangular domain under mapping $g \cdot f^{-1}$; Bottom right: uniform grid in canonical domain; and bottom left: (locally) orthogonal grid in physical domain generated by mapping grid in bottom right under relation $g^{-1} \cdot f$. [jeff1-map1] [NR]



The second step is to specify the RWE extrapolation equations appropriate for the generated topographic coordinate system. This approach specifies a wave-equation dispersion appropriate for one-way wavefield extrapolation in generalized coordinate systems. Shragge and Sava (2004) discusses how to perform wave-equation migration directly from topographic coordinate systems, and illustrates this approach with a synthetic 2D data example.

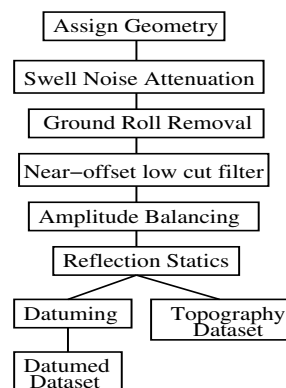
HUSKY 2D LAND DATASET

The Husky 2D land spec dataset was acquired by Husky Oil and Talisman Energy in a complex fold and thrust belt of the Canadian Rocky Mountain Foothills. This dataset, released by Husky Oil to aid industry technological development, was the focus of a processing workshop at the SEG's 1995 Annual General Meeting. The dataset consists of 143 shot-records, with a nominal source and receiver spacing of 100 m and 20 m, respectively. Shot-records contain approximately 300 channels per shot in a split-spread geometry with a maximum offset of ± 4000 m. Overall, this high-quality field dataset exhibits many typical data attributes: realistic near-surface effects, elevation changes, and associated geologic information and ambiguity. In addition, the dataset is in a location of minimal 3D structure, which provides a good test for 2D imaging algorithms.

Preprocessing

Although the Husky dataset is of high quality, significant preprocessing is required to enhance signal quality. Data processing steps, applied using the proprietary OMEGA processing package, are listed in Figure 2. After geometry assignment, a swell-noise debursting algorithm was applied in the shot- and receiver-record and CMP domains to reduce anomalous low-frequency noise. Ground roll suppression and near-offset bandpass filtering subsequently reduced ground roll and airwave noise. Application of de-spiking and surface-consistent amplitude modules improved the relative amplitude balance across the shot-record and offset panels.

Figure 2: Husky data processing flow chart. jeff1-flow [NR]



Static time shifts were then compiled to generate a second datumed dataset. This dataset was generated by applying two static time shifts - one from the source/receiver location to an intermediate CMP datum, and a second to a constant elevation of -1800 m (assuming a 3200 m/s replacement velocity layer). Reflection statics (that optimized the power of the constant velocity scan stack) also were applied to both datasets. Figure 3 presents a comparison of a shot-record before and after data processing.

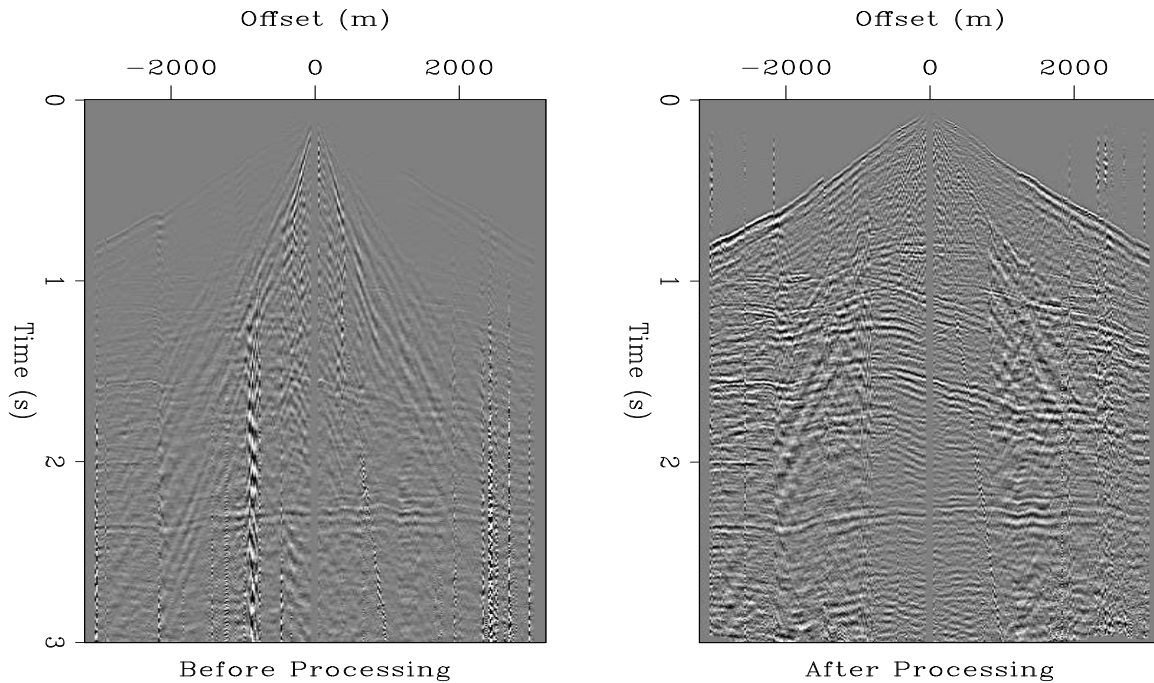


Figure 3: Sample Husky dataset shot-record before (left) and after (right) preprocessing. `jeff1-data_examp` [CR]

Migration Velocity Profile

Husky Oil also included a geologically derived velocity model in their deliverables. The near-surface component of this model is shown in top panel of figure 4. The model was developed from the combination of surface geologic observations, well-ties from 8-10 nearby wells and walk-away VSPs. Refraction tomography inversion of first-break arrival times (c.f. figure 3) provided a better estimate of the near-surface velocity profile (middle panel). The top 200 m of the refraction tomography model were grafted onto the geologic model, which was subsequently smoothed to create the migration velocity profile (bottom panel). The full migration velocity profile (figure 5) shows an intricate near-surface geologic environment characterized by complex faulting and folding and strong velocity contrast. Near-surface velocities are seismically fast with values ranging between 3600 m/s and 4800 m/s.

Imaging Results

Imaging tests were conducted on the topographic (WEM) and datumed (Kirchhoff migration) datasets. Figure 6 presents the results of imaging with the TopoWEM approach. Near-surface dipping reflectors are well-imaged, as are those above and at the basement. Note, though, that reflectors are somewhat broken up in some locations, especially in the basement. Angle gathers (not shown here) are generally flat; however, the presence of residual curvature indicates velocity model inaccuracy, and suggests that additional work to improve the currently

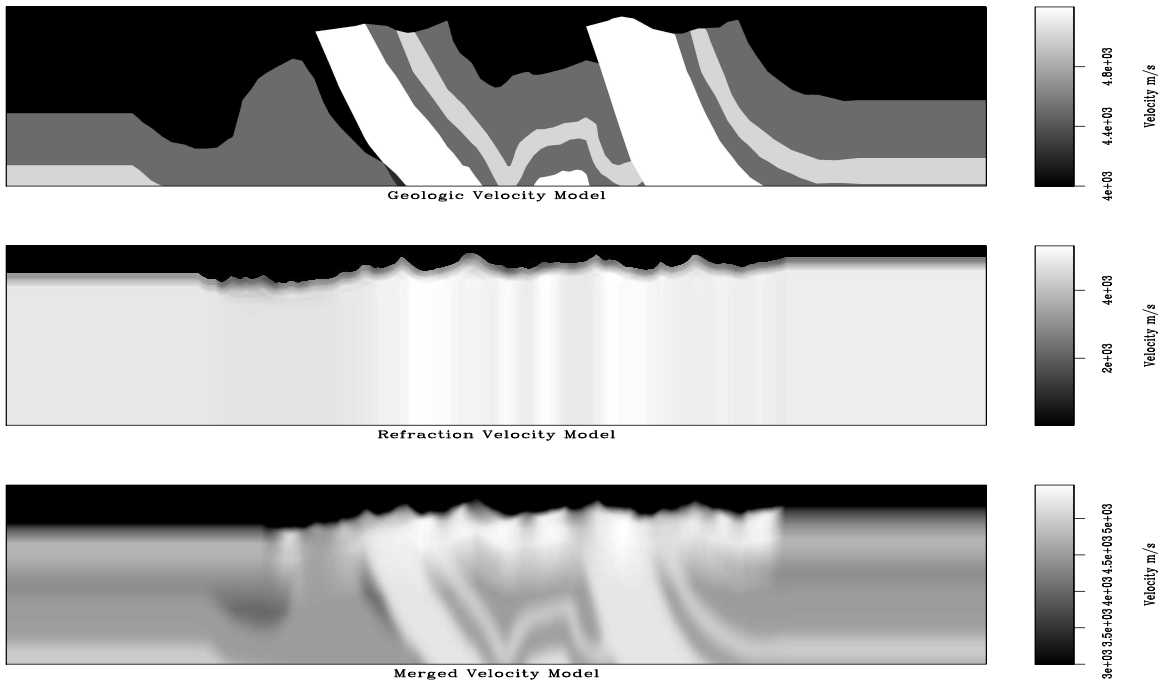


Figure 4: Initial velocity profile. Top: geologic velocity model; Middle: refraction tomography velocity profile; and Bottom: merged geologic and refraction velocity profiles. `jeff1-vel_init` [CR]

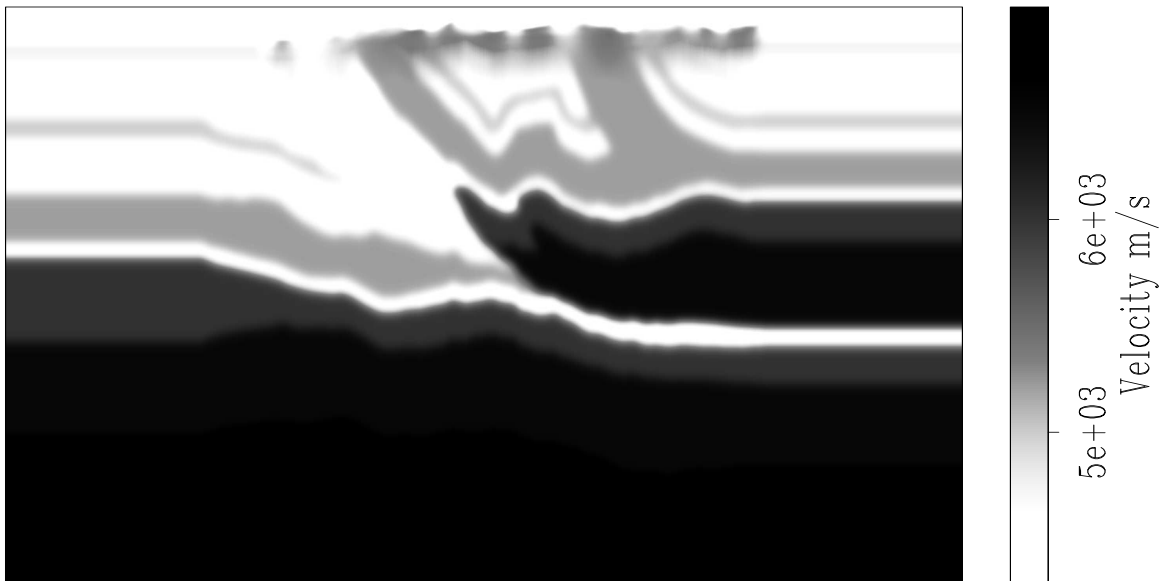
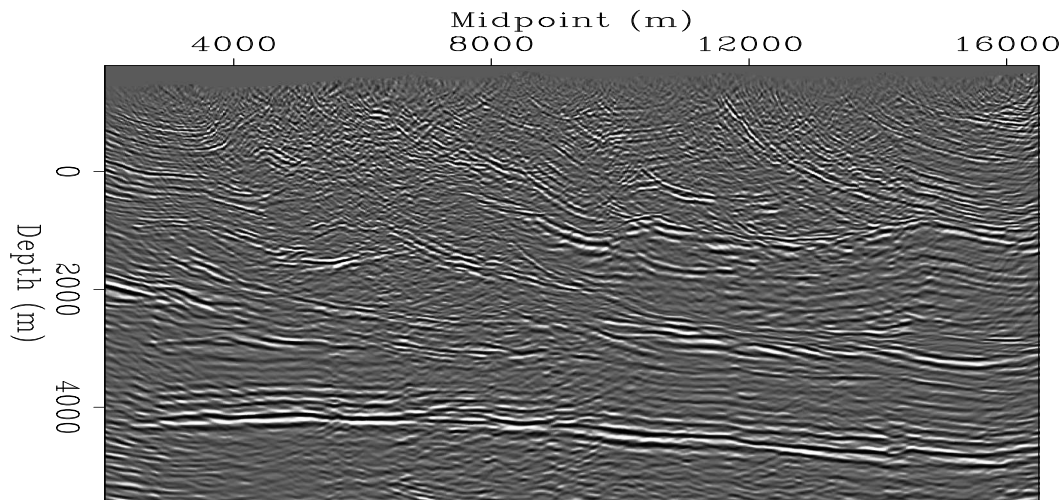


Figure 5: Migration velocity profile. `jeff1-vel_final` [CR]

geologically derived velocity model is warranted.



WEM from Topography – 3 Slow and 7 Geom. refs

Figure 6: Imaging results for wave-equation migration from topography. jeff1-TopoWEM1
[CR]

Figure 7 presents the results of migrating the datumed dataset using a Kirchhoff algorithm. Image quality is good at mid-to-basement depths; however, near-surface reflectors observed in the TopoWEM image are not visible. This could be due to additional internal velocity model smoothing in the proprietary Kirchhoff migration code, or to the failure of the vertical datuming approximation, which distorts wave-propagation paths and defocuses the near-surface image. (A Kirchhoff migration test from topography has not yet been conducted.)

CONCLUDING REMARKS

The Husky data migration test results indicate that the TopoWEM approach is a viable migration from topography technique. This approach produced images of near-surface structure superior to Kirchhoff migration from a flat datum. However, future tests will create a better benchmark by comparing these results to Kirchhoff migration from topography. Kirchhoff migration from a flat datum results were similar at mid-to-basement depths indicating that the major imaging advantage probably is localized to the near-surface. Subsurface gathers for images indicate, however, that further work is needed to improve the velocity model, which may lead to a more definitive statement about the relative merits of the TopoWEM approach.

ACKNOWLEDGMENTS

I would like to thank the Seismic Imaging team at ExxonMobil Upstream Research for providing a good environment that allowed me to conduct the work reported in this paper. A big

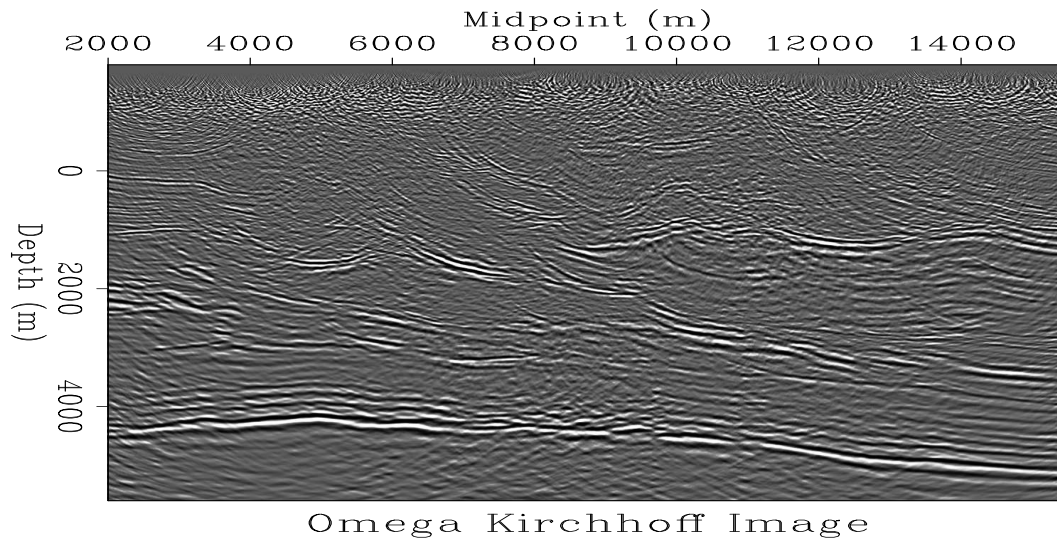


Figure 7: Imaging results for Kirchhoff migration of dataset from a flat datum. jeff1-Kirch
[CR]

thank-you to Tom Dickens for both excellent mentorship and his assistance with the data pre-processing. Husky Oil and Talisman Energy are acknowledged for releasing the Husky dataset used in these field test results.

REFERENCES

- Bevc, D., 1997, Flooding the topography: Wave-equation datuming of land data with rugged acquisition topography: *Geophysics*, **62**, 1558–1569.
- Sava, P., and Fomel, S., 2005, Riemannian wavefield extrapolation: *Geophysics*, pages T45–T56.
- Shragge, J., and Sava, P., 2004, Incorporating topography into wave-equation imaging through conformal mapping: *SEP-117*, 27–42.

Direct migration: The only way

Brad Artman¹

ABSTRACT

Correlating transmission wavefields to produce reflection wavefields contains in its rigorous definition the mandate of processing data due to only a single source. If more than one source is contained in the wavefield, crosstalk between the sources will produce a data volume that is not the same as shot gathers with impulsive sources at each receiver location. When attempting to image the subsurface with the truly unknown ambient noise field, parameterizing the field data by individual sources is impossible.

For truly passive data, the source and time axis are inextricably combined, naturally and by processing. This changes direct migration to something more akin to planewave migration. Since the direct arrival from each source can not be expected to sum together with a common time-delay, the summation manufactures a source wavefront with temporal topography rather than a planewave.

The Fourier transform of field data as a single wavefield provides insight into how sources are summed during correlation. Also, the transform simultaneously stacks away useless waiting periods between useful energy bursts and reduces the data volume. Previously, white, zero-phase source functions were invoked to avoid the summation problem. However, neither assumption is likely in the real environment of a long term experiment.

INTRODUCTION

Through one-way reciprocity, Wapenaar et al. (2004) shows how to synthesize reflection data from passively collected seismic data for 3D inhomogeneous media. Key in the proof is the distinction that correlations from only single sources may be calculated and then summed over many sources to produce the correct result. This is simple when utilizing earthquake codas (Nowack et al., 2003) or using novel experimental geometries for active surveys (Yu and Schuster, 2004). This is impossible when imaging with truly passive data where the source is the unknown ambient noise field.

I assume that field data from a passive recording campaign can neither be parameterized by nor separated into wavefields from individual sources. In this case, correlation of the entire long data volume leads to an unavoidable summation of the wavefields from all the subsurface sources. Through Fourier analysis of correlation, I will show this inherent summation due to processing all sources as one large wavefield.

¹email: brad@sep.stanford.edu

Summing the wavefields from all sources violates the rigorous definition of the result of correlating traces from a passive data collection. The output volume is not identical to the conventional reflection experiment. This report assumes the utility (Artman and Shragge, 2003) and mathematic justification (Artman et al., 2004) for direct migration of passive data as a starting point. Several synthetic models are presented to highlight the complexity introduced by not separating individual wavefields for processing as well as successful imaging with the direct migration technique. Finally, images from the passive array installed at the Valhall oil prospect in the North sea will be introduced.

WAVEFIELD SUMMATION

To calculate the Fourier transform of the reflection response of the subsurface, $R(\mathbf{x}_r, \mathbf{x}_s, \omega)$, Wapenaar et al. (2004), proves

$$2\Re[R(\mathbf{x}_r, \mathbf{x}_s, \omega)] = \delta(\mathbf{x}_s - \mathbf{x}_r) - \int_{\partial D_m} T(\mathbf{x}_r, \xi, \omega) T^*(\mathbf{x}_s, \xi, \omega) d^2\xi . \quad (1)$$

The vector \mathbf{x} will correspond herein to horizontal coordinates, where subscripts r and s indicate different station locations from a transmission wavefield. After correlation they acquire the meaning of receiver and source locations, respectively, associated with an active survey. The RHS represents summing correlations of windows of passive data around the occurrence of individual sources, at locations ξ , on the domain boundary ∂D_m that surrounds the subsurface region of interest. The transmission wavefields $T(\xi)$ contain only one subsurface source.

Equation 1 dictates that the correlations of transmission wavefields must only be from individual transmission wavefields recorded over an interval, t , during which a single source is actively probing the subsurface. In this case, the zero-time of the correlations are correctly shared by the output of each correlation operation since each result is zero-phase. If more than one source function is active during a time window, or it is impractical to window the raw data around individual sources, the result of correlating the raw data will not yield the reflection wavefield R .

In practice, raw data are collected over a long time and sources are weak and/or overlapping. For transmission wavefields, the time axis and the shot axis are naturally combined. If we assume that n_s individual sources, and the reflections that occur t seconds afterward, are distributed at intervals within the total recording time τ , field data can only be parameterized $T_f(\mathbf{x}_r, \tau)$. Both t and τ represent the real time axis, though I will parameterize different wavefields with them with the understanding that $\max(t)$ is the two-way time to the deepest reflector of interest and τ is the real time axis from the beginning to the end of the total recording time such that

$$\max(\tau) = \max(t)n_s + \sum_j^{n_s} \text{wait-time}_j . \quad (2)$$

I will further adopt the conventions ω for the frequency domain dual variable of t , and ϖ for the frequency domain dual variable of τ .

Without knowing when sources happen, and acknowledging that the wait-time between shots can also be negative, it is impossible to separate field data into individual wavefields when attempting to image with the ambient noise field. In this case, equation 1 can only be implemented with a single time function of length τ

$$\tilde{R}(\mathbf{x}_r, \mathbf{x}_s, \varpi) = T_f(\mathbf{x}_r, \varpi) T_f^*(\mathbf{x}_s, \varpi). \quad (3)$$

The immediate ramification of this formulation can be considered by Fourier analysis. Correlation of more than a few hundred samples is more efficiently performed in the Fourier domain, $C(\omega) = B(\omega)A^*(\omega)$, so I will first consider the general definition of the discrete Fourier transform (DFT). The DFT of a signal $f(\tau)$ can be evaluated for a particular frequency ϖ ,

$$F|_{\varpi} = \text{DFT}[f(\tau)]|_{\varpi} = \frac{1}{\sqrt{n_{\tau}}} \sum_{\tau} f(\tau) e^{-i\varpi\tau}. \quad (4)$$

If the long function $f(\tau)$ is broken into N short sections, $g_n(t)$, of the same length, the amplitude of a particular frequency ϖ can also be calculated

$$\text{DFT}[f(\tau)]|_{\varpi} = N^{-3/2} \sum_{n=1}^N \text{DFT}[g_n(t)]|_{\varpi} = N^{-3/2} \text{DFT}\left[\sum_{n=1}^J g_n(t)\right]|_{\varpi} \quad (5)$$

by simply changing the order of summation for convenience. The only requirement for the equation above is for both of the two different length transforms to contain the particular frequency being calculated (ie. a particular frequency where $\varpi = \omega$ is possible as dictated by the Fourier sampling theorem). The longer transform has many more frequencies at a smaller sampling interval between the shared values calculated by the short transform of the stacked data.

For passive field data, $f(\tau)$ is $T_f(\tau)$, and the $g_n(t)$ are $T(\mathbf{x}_r, \xi, t)|_{\xi=n}$ as well as background noise between sources. Thus, correlating a single long recording from many sources implicitly stacks the wavefields from individual sources at each frequency. For passive data, the time axis and the shot axis are combined in nature (by sources refusing to wait in turn) and in processing (by seismologists incapable of or refusing to process individual time windows). However, this transform only supports a time signal of length t and is aliasing the long field record.

What of the intermediate frequencies ϖ that would be lost by stacking the time windows? It is necessary to remove these. Fine sampling in frequency carries information about the late time samples of the signal's dual representation. After correlation, shot records in the time domain must be windowed to remove late lag correlations which are superpositions of correlations of the different sources convolved with the earth model. These are completely uninterpretable in terms of the desired product $R(\mathbf{x}_r, \mathbf{x}_s, t)$ and will be noise in further processing. If the result needs truncation after inverse transform, it is more efficient to only transform the part of the result desired.

Time windowing has a Fourier dual operation. The Fourier sampling theorem, solved for Δt is

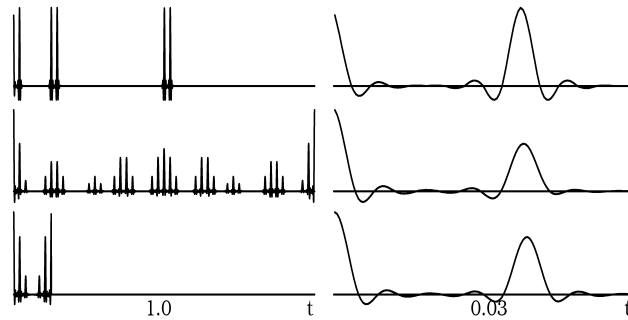
$$\Delta t = 1/(N\Delta f).$$

Subsampling the frequency axis increases Δf by a , and reduces the number of samples to N/a . The new time domain trace length is $\Delta t N/a$. Removing every other frequency, $a = 2$, halves the length of the trace in the time domain. This process is the Fourier dual of reducing the Nyquist frequency by subsampling the time axis. Importantly, the ability to rearrange the order of summation in equation 5 or subsample the Fourier domain representation of signal to alias it means that the spectra of the two different length transforms are not related by smoothing. Instead, the short one is a subsampled version of the long one where all frequency samples shared by the two are identical.

The left column of Figure 1 shows a processing flow of a simple time domain signal with a zoomed in view of each trace (the first 32^{nd} of the axis) on the right. The top trace is the input signal. The middle trace is its autocorrelation. The bottom trace maintains a part of the autocorrelation result deemed important. To compute the bottom trace, the input was subsampled by 8 in the Fourier domain, multiplied by its conjugate, and inverse transformed. To facilitate plotting, the trace was padded with zeros. Identical results are obtained by time-domain stacking and Fourier domain subsampling as long as the level of decimation does not alias the acausal lags of the correlation into the positive lags.

Figure 1: Right column is 32x zoom of left beginning at $t = 0$. (top) Idealized signal of three identical subsurface sources. (middle) Auto-correlation. (bottom) Autocorrelation performed with every 8^{th} frequency. Zero values are padded on the bottom trace to facilitate plotting.

brad1-freq [ER]



Subsampling in one domain is not an identical operation to windowing in the dual domain. The periodicity of the Fourier transform dictates that subsampling leads to aliasing rather than true truncation. Aliasing the time domain is more efficiently performed by summing short time windows before making the correlations and thereby greatly reducing the amount of computation required. Knowing that the late time lags of correlation are aphysical for passive imaging, the above analysis shows that only the frequency samples at intervals ω , associated with records of length t , need to be inverse transformed after correlation. Since correlation is linear, we only need to calculate the frequency domain representation of the field data at this reduced sampling interval. The definition of the DFT shows that this is equivalent to first stacking the long time axis of the data. The random background and instrument noise between sources is diminished by the stacking of the time axis which also decimates a potentially enormous data volume.

Under the assumption that all the source functions recorded in the data are white and uncorrelated, the summation of the source wavefields may not be to harmful and $\tilde{R} \approx R$. Further, if the sources are all continuously ringing, and thus zero-phase over the recording, the correlations will not have residual phase. In my previous reports, both of these assumptions

were made (sometimes not intentionally), which I now believe highly improbably for a real earth experiment. To utilize bursts of local seismicity for imaging, cross-correlating traces to make shot gathers makes $\tilde{R} \neq R$. The situation is directly analogous to summing two or more shot-records. While it may be useful for some applications, this sum can not be treated as a single record with an impulsive source. Cross-talk is introduced due to the inability to separate energy from the distinct experiments.

Stacking wavefields

The time domain stacking shown in equation 5 that is implied by correlating field data with equation 3 can be explored by considering two transmission wavefields, $a(\mathbf{x}_r, t)$ and $b(\mathbf{x}_r, t)$, from individual sources. When placed randomly on the field record with wait-time s τ_a and τ_b

$$T_f(\tau) = a * \delta(t - \tau_a) + b * \delta(t - \tau_b). \quad (6)$$

Correlation in the Fourier domain by equation 3 yields

$$T_f T_f^* = AA^* + BB^* + AB^* e^{-i\varpi(\tau_a - \tau_b)} + BA^* e^{-i\varpi(\tau_b - \tau_a)}. \quad (7)$$

The sum of the first two terms is the result dictated by equation 1. The second two are extra. If $|\tau_b - \tau_a| > \max(t)$, one term will be purely acausal, and the other at very late lags that can be windowed away in the time domain. However, if the operation is performed in the Fourier domain, circular correlation is actually implemented and energy from the cross-terms may not so easily be avoided. If $|\tau_b - \tau_a| < \max(t)$, the cross-terms are included in the correlated gathers.

Redefine A and B as the impulse response of the earth, I_e , convolved with source functions, F which now contain their phase delays. As such, the cross-terms of equation 7 are

$$AB^* = (F_a I_e)(F_b I_e)^* = F_a F_b^* I_e^2 = F_c I_e^2. \quad (8)$$

Like the first two terms in equation 7, the cross-terms have the desired information about the earth. However, the source function f_c included is not zero phase. These terms are the *other-terms* or virtual multiples in Schuster et al. (2004). If the source functions are random series, terms with residual phase (such as $F_c I_e^2$ above) within the gathers will decorrelate and diminish in strength as the length of f and the number of cross-terms increases. While we may hope to collect a large number of sources, it is probably unreasonable to expect many of them to be random series of great length.

The inclusion of these cross-terms in the correlation output produces a data volume

$$\tilde{R}(\mathbf{x}_r, \mathbf{x}_s, \varpi) \neq R(\mathbf{x}_r, \mathbf{x}_s, \omega).$$

The ratio of desirable zero-phase terms to cross-terms containing residual phase decreases as $1/(n_s - 1)$. \tilde{R} is not especially useful however. The inclusion of the cross-terms between the experiments returns a data volume that may not be more interpretable than the raw data. This

will be the case if the individual source functions are correlable or not conveniently located along the τ -axis such that all of their correlated phase terms, F_c in equation 8, are zero. These virtual multiple events will likely be more problematic than conventional multiples as every reflector can be repeated $n_s!/(n_s - 2)!$ times.

Figure 2 shows the effect of the cross terms expanded in equation 8. The figure is directly analogous to Figure 1, though with two important differences. First, there are overlapping source function-reflection pairs. Second, the direct arrivals are spaced randomly along the time axis rather than engineering them to lie at the first sample of one of the short subsections. The second source arrives at the receiver before the reflection from the first source. The third source is randomly placed at the far end of the trace. The traces on the right are zoomed versions of their counterparts to the left. The result desired by a passive seismologist trying to produce a zero-offset trace from R , bottom trace Figure 1, can not be produced. The middle trace was correlated in the Fourier domain and transformed back to time. The bottom trace was computed by stacking eight windows from the input before correlation. The difference between the two output traces is not from reordering the summation for the Fourier transform in equation 5. Actually, this is the aliasing of the autocorrelation result itself. Both methods produce the wrong result at almost all times. They are however correct and identical at one location: zero-lag.

Figure 2: Right panel is 32x zoom of left. (top) Idealized signal of three identical subsurface sources. First two direct-reflection pairs overlap. (middle) Autocorrelation. (bottom) Autocorrelation performed after stacking 8 constituent windows. Zero values are padded on the bottom trace to facilitate plotting. brad1-freq2
[ER]

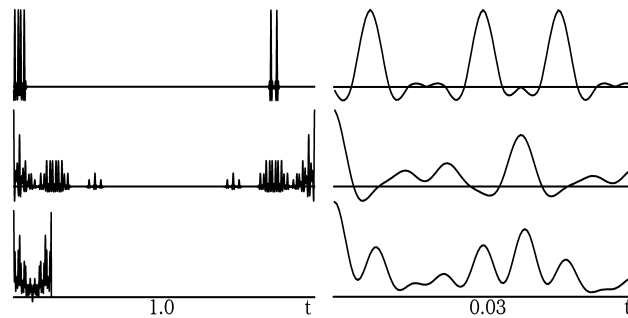


Figure 3 shows a more complicated example of the effective summation of source terms during the Fourier transform. The first two panels are individual transmission wavefields from sources at the left side of the model and just to the right of the center of the model. Notice that the wavefields have been carefully windowed to assure that the minimum traveltime for the two wavefields is the same. The model is a constant velocity medium with two diffractors in the center. The right panel is the sum of 225 similar sources covering the bottom of the velocity model. Summing the many shots has created a zero-offset data volume that could be migrated with a planewave migration algorithm. Cross-correlating this data to produce shot-gathers produces several dozen flat plane-waves and only the faintest hint of a ringing train of diffraction hyperbolas. $\hat{R} \neq R$ due to processing T_f rather than the individual $T(\xi)$ records. Figure 4 mimics Figure 3 directly without having taken care to align the direct arrivals to the same time sample. The summation of all 225 wavefields gives the result on the right. Cross-correlating this data to produce shot-gathers makes a very messy plot.

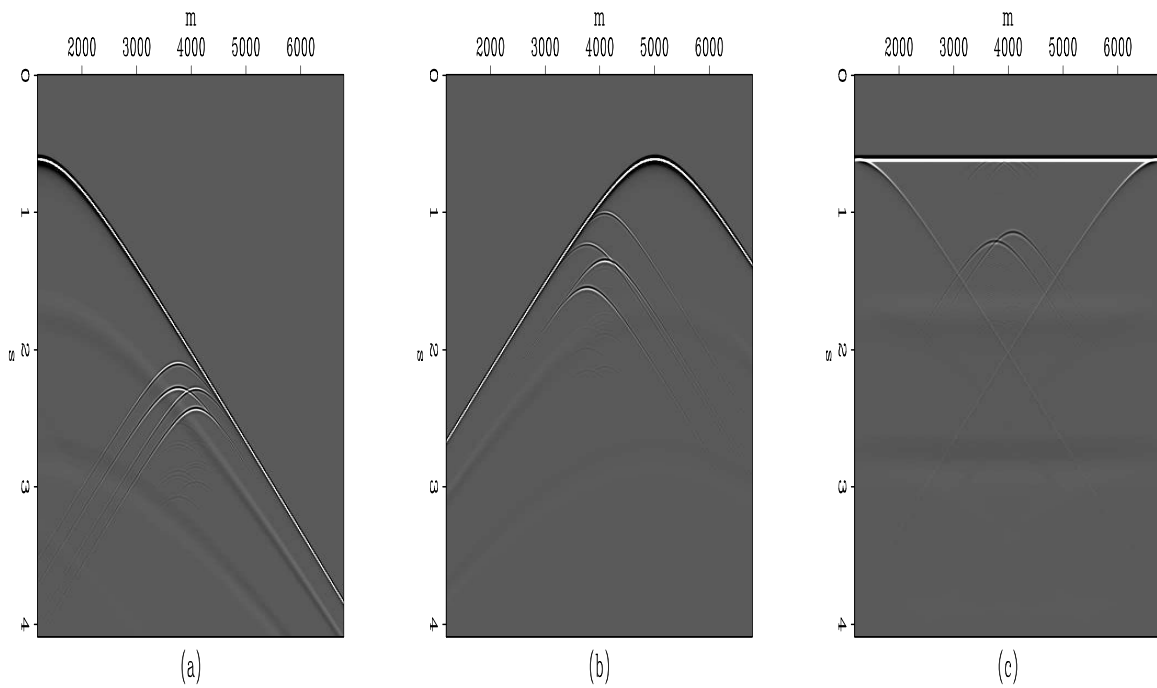


Figure 3: (a) Transmission wavefield from a subsurface source below $x = 1200m$ in a model containing two diffractors. (b) Transmission wavefield from source below $x = 5000m$. (c) Sum of 225 modeled wavefields. `brad1-diff.noshift` [CR]

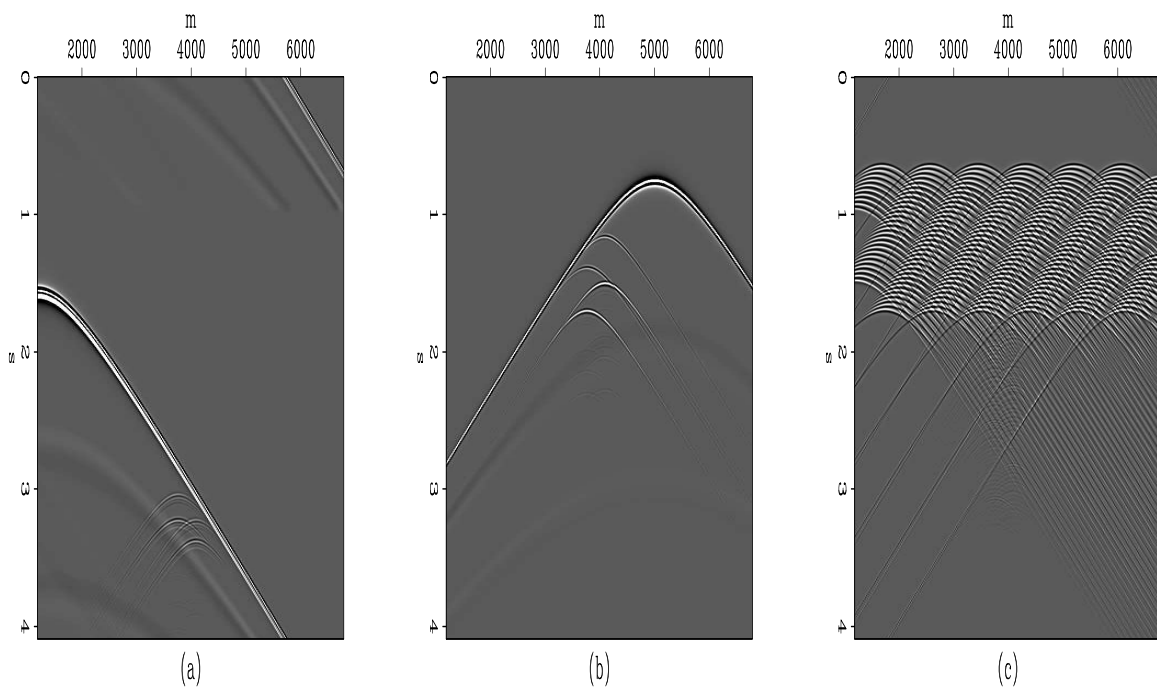


Figure 4: (a) Transmission wavefield from a source below $x = 1200m$ in a model containing two diffractors. (b) Transmission wavefield from source below $x = 5000m$. (c) Sum of all wavefields. `brad1-diff.shift` [CR]

$$\begin{array}{ccc}
\text{shot-profile migration} & & \text{passive imaging} \\
\hline
U_{z=0}(\mathbf{x}_r + \mathbf{h}; \mathbf{x}_s, t) \otimes D_{z=0}(\mathbf{x}_r - \mathbf{h}; \mathbf{x}_s, t) & = & T_{z=0}(\mathbf{x}_r + \mathbf{h}; \xi, t) \otimes T_{z=0}(\mathbf{x}_r - \mathbf{h}; \xi, t) \\
\downarrow \text{SSR}^{-1} \quad \quad \quad \downarrow \text{SSR}^{+1} & & \downarrow \text{SSR}^{-1} \quad \quad \quad \downarrow \text{SSR}^{+1} \\
U_{z=1}(\mathbf{x}_r + \mathbf{h}; \mathbf{x}_s, t) \otimes D_{z=1}(\mathbf{x}_r - \mathbf{h}; \mathbf{x}_s, t) & = & T_{z=1}^{-}(\mathbf{x}_r + \mathbf{h}; \xi, t) \otimes T_{z=1}^{+}(\mathbf{x}_r - \mathbf{h}; \xi, t)
\end{array}$$

Figure 5: Equivalence of shot-profile migration of reflection data and direct migration of passive wavefields. $T(\xi, t)$ are the wavefields of equation 1. \mathbf{x}_s has a similar meaning to ξ . Only first and second levels of the iterative process are depicted. $\sum_{\mathbf{x}_s}$ and \sum_{ω} produces the image $i_z(\mathbf{x}_r, \mathbf{h})$ for both methods.

DIRECT MIGRATION

The correlated wavefield \tilde{R} is not usable by the majority of available reflection migration data tools. The source axis summation explained above does not remove all of the potential time delays. However, field data can still be migrated with a scheme that includes separate extrapolation and correlation (for imaging) steps. Artman and Shragge (2003) shows the applicability of direct migration for transmission wavefields with a shot-profile algorithm. Artman et al. (2004) provides the mathematical justification (for zero phase source functions). Simply stated, both Fourier domain extrapolation across a depth interval and correlation are diagonal square matrices, and thus commutable. This means that the correlation required to calculate the earth's reflection response from transmission wavefields can be performed after extrapolation with the shot-profile imaging condition (Rickett and Sava, 2002)

$$i_z(\mathbf{x}, \mathbf{h}) = \delta_{\mathbf{x}, \mathbf{x}_r} \sum_{\mathbf{x}_{s_k}} \sum_{\omega} U_z(\mathbf{x}_r + \mathbf{h}; \mathbf{x}_{s_k}, \omega) D_z^*(\mathbf{x}_r - \mathbf{h}; \mathbf{x}_{s_k}, \omega), \quad (9)$$

where T is used for both upcoming, U , and downgoing, D , wavefields.

Figure pictorially demonstrates how direct migration of field passive seismic data fits into the framework of shot-profile migration to produce the 0^{th} and 1^{st} depth levels of the zero offset image. The sum over frequency has been omitted to reduce complexity in the figure. Also, after the first extrapolation step, with the two different phase-shift operators, the two transmission wavefields are no longer identical, and can be redefined U and D . This is noted with superscripts on the T wavefields at depth.

Shot-profile migration becomes planewave migration if conventional shot-gathers are summed for wavefield U , and a horizontal plane source is modeled for wavefield D . Partial summation of conventional shot-records will introduce cross-talk into the image. Only by summing enough shots so that their destructive interference cancels out their cross-talk can one produce a high quality image. For raw passive data, the sum over sources leads to an areal wave with complicated temporal topography. Moving the sum over shots in the imaging condition of equation 9 to operate on the wavefields rather than their correlation, changes shot-profile

$$\begin{array}{c}
\text{planewave migration} \\
\hline
(\sum_{\mathbf{x}_s} U_{z=0}(\mathbf{x}_r + \mathbf{h}; \mathbf{x}_s, t)) \otimes (\sum_{\mathbf{x}_s} D_{z=0}(\mathbf{x}_r - \mathbf{h}; \mathbf{x}_s, t)) \\
\begin{array}{ccc}
\downarrow & & \downarrow \\
\text{SSR}^{-1} & & \text{SSR}^{+1} \\
\downarrow & & \downarrow \\
U_{z=1}(\mathbf{x}_r + \mathbf{h}, t) & \otimes & D_{z=1}(\mathbf{x}_r - \mathbf{h}, t)
\end{array} \\
\end{array}
=
\begin{array}{c}
\text{passive wavefront imaging} \\
\hline
T_{z=0}(\mathbf{x}_r + \mathbf{h}, \tau) \otimes T_{z=0}(\mathbf{x}_r - \mathbf{h}, \tau) \\
\begin{array}{ccc}
\downarrow & & \downarrow \\
\text{SSR}^{-1} & & \text{SSR}^{+1} \\
\downarrow & & \downarrow \\
T_{z=1}^{-}(\mathbf{x}_r + \mathbf{h}, \tau) & \otimes & T_{z=1}^{+}(\mathbf{x}_r - \mathbf{h}, \tau)
\end{array}
\end{array}$$

Figure 6: Equivalence of direct migration with simultaneous migration all shots in a reflection survey. $T(\tau)$ is the field data wavefield of equation 3. Only first and second levels of the iterative process are depicted. \sum_{ω} produces the image $i_z(\mathbf{x}_r, \mathbf{h})$ for both methods.

migration to something akin to planewave migration which I will call wavefront migration.² Like planewave migration, after even a few wavefields have been combined, the best course of action is to sum all the sources to attain good areal coverage of the source wavefront to minimize cross-talk. Figure shows the change source summation has on both conventional shot migration and direct passive migration. Notice the parameterization of $T(\tau)$ meaning field data (where the depth subscript displaces the use of T_f). Importantly, the data input into the migration needs to have the late lags windowed before input into the migration as they have no correspondence to the subsurface structure. This can be accomplished by any of the three options discussed above: correlation followed by windowing, DFT followed by subsampling, or stack followed by DFT and correlation.

SYNTHETIC EXAMPLES

Data was also synthesized through a model containing two synclines. Figure 7a shows summed wavefields with the same direct arrival time. Panel (b) is the sum of the same wavefields after applying random phase delays to each. Panel (b) has all sources firing within the 4 seconds plotted, which results in some wrap-around. Bandlimited impulses were used as sources without any addition of randomness. Figure 8 shows zero offset images produced by direct migration of the data shown in Figure 7. Panel (b) is not as high quality as panel (a). A faint reflection mimicking the first event can be seen at $z = 350m$. This could be in part from events wrapping around the time axis when applying their respective phase delays. This is probably a worst-case result, that can be avoided by processing a time-window several times longer than the minimum, t . Given the dramatic departure of the data Figure 7b) from a horizontal planewave source, significant energy may also be at $\mathbf{h} \neq 0$. The most obvious difference is the diminution of the multiple from the first reflector at $z = 485$. The second reflector is much clearer in panel (b) without its interference.

²As such, the subsurface offset axis of the image will probably not be densely populated. To fill the offset axis, multiple planewave migrations can be summed after convolving the data with various ray parameters (Sun et al., 2001; Liu et al., 2002).

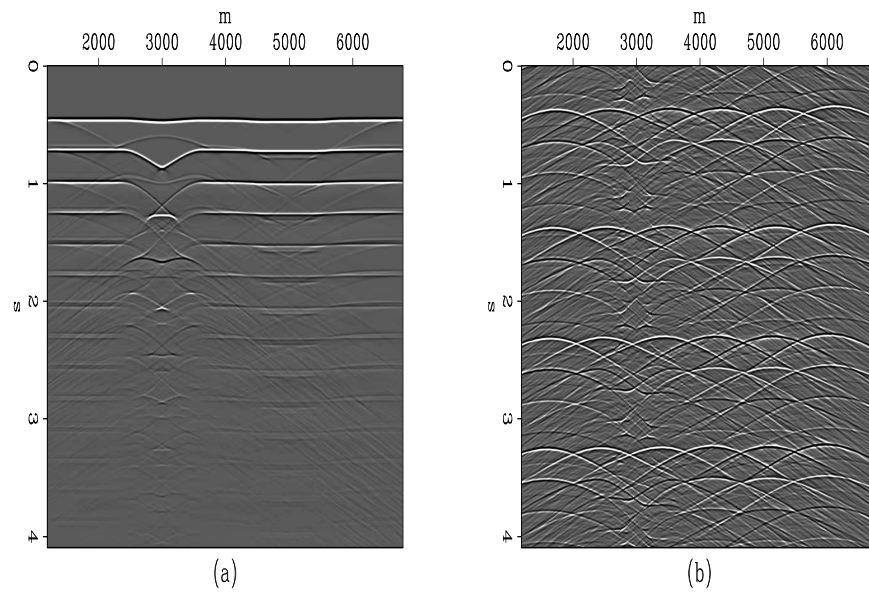


Figure 7: (a) Perfectly stacked shots from a double syncline model. (b) Stack of wavefields after applying a random time delay in the Fourier domain. `brad1-dat.syn` [CR]

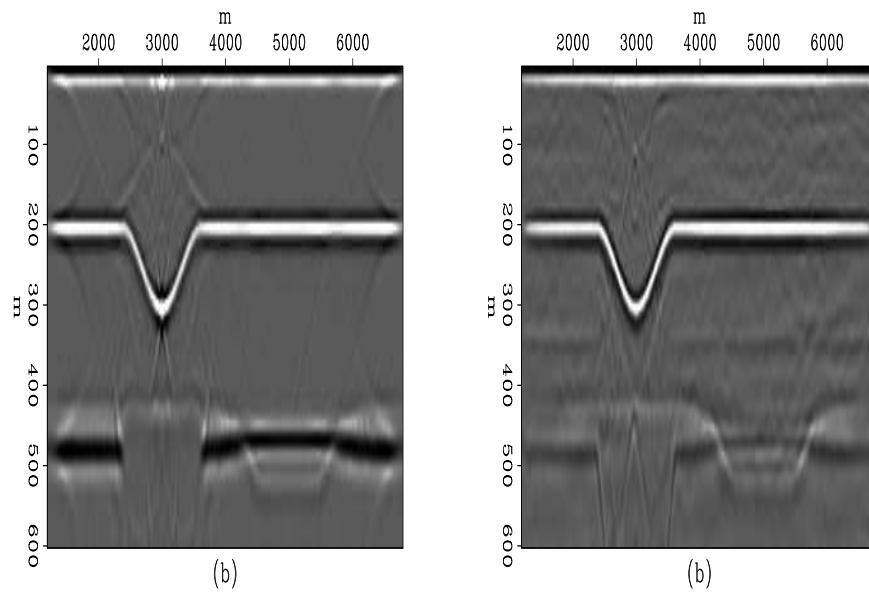


Figure 8: (a) $h = 0$ image produced by direct migration of Figure 7 panel (a). (b) $h = 0$ image produced by direct migration of Figure 7 panel (b). `brad1-mig.syn.norand` [CR]

CONCLUSION

Processing windowed subsets of a passive survey may be advantageous. If time-localized events are present, such as teleseismic arrivals, one can process smaller time windows when sure of significant contribution to the image. Without knowing of if or how many sources are active within the bulk of the data, long correlations of the raw data are an almost inevitable approximation (equation 3) to the rigorous definition for synthesizing shot-gathers from transmission wavefields (equation 1). Accepting this reality, first aliasing the time data reduces the computation cost for a DFT by $1/n_\tau$ (where n_τ is the number of samples in the long input trace)³ without any further approximation. Rather, it simply capitalizes on the original approximation without having to assume uncorrelable white source functions.

The inherent aliasing within the approximation sums the source functions within the output. This superposition of sources does not produce $R(\mathbf{x}_r, \mathbf{x}_s, \omega)$ under realistic situations. Instead the result is, $\sum_{\mathbf{x}_s} R(\mathbf{x}_r, \mathbf{x}_s, \varpi)$. This data volume can only be migrated with an algorithm that can accept generalized source functions (parameterized by space and time), and uses a correlation imaging condition. Both of these conditions are enjoyed by shot-profile migration.

Migrating all sources at the same time removes the redundant information from a reflector as a function of incidence angle. This makes velocity updating after migration impossible. At this early stage, I contend that passive surveys will only be conducted in actively studied regions where very good velocity models are already available. If this becomes a severe limit, the incorporation of planewave migration strategies can fill the offset dimension of the image.

In practice, the length of the aliased windows should probably be several times longer than the minimum time to the deepest reflector. Multiple sources within this time are handled perfectly by direct migration, and the risk of adding the end of the reflection series to the beginning of the record will be minimized. The decision can be determined by whatever compute resources are available for the size of the data set collected. However, if the time support of the wavefield migrated is many times longer than appropriate for the deepest reflector of interest, aphysical correlation lags will introduce coherent noise into the image that will look exactly like reflections.

REFERENCES

- Artman, B., and Shragge, J., 2003, Passive seismic imaging: AGU Fall Meeting, Eos Transactions of the American Geophysical Union, Abstract S11E-0334.
- Artman, B., Draganov, D., Wapenaar, C., and Biondi, B., 2004, Direct migration of passive seismic data: 66th Conference and Exhibition, EAGE, Extended abstracts, P075.
- Liu, F., Stolt, R., Hanson, D., and Day, R., 2002, Plane wave source composition: An accurate phase encoding scheme for prestack migration: Soc. of Expl. Geophys., 72nd Ann. Internat. Mtg, 1156-1159.

³ n_τ will be $O(10^7)$ for just one day of data collected at 0.004s sampling rate.

- Nowack, R. L., Dasgupta, S., Schuster, G. T., and Sheng, J., 2003, Correlation migration of scattered teleseismic body waves with application to the 1993 cascadia experiment:, *in* Fall Meet. Suppl. Abstract S32A-0835.
- Rickett, J. E., and Sava, P. C., 2002, Offset and angle-domain common image-point gathers for shot-profile migration: *Geophysics*, **67**, no. 03, 883–889.
- Schuster, G., Yu, J., Sheng, J., and Rickett, J., 2004, Interferometric/daylight seismic imaging: *Geophysics Journal International*, **157**, 838–852.
- Sun, P., Zhang, S., and Zhao, J., 2001, An improved plane wave prestack depth migration method: *Soc. of Expl. Geophys.*, 71st Ann. Internat. Mtg, 1005–1008.
- Wapenaar, K., Thorbecke, J., and Draganov, D., 2004, Relations between reflection and transmission responses of three-dimensional inhomogeneous media: *Geophysical Journal International*, **156**, 179–194.
- Yu, J., and Schuster, G., 2004, Enhancing illumination coverage of vsp data by cross-correlogram migration:, *in* 74th Ann. Internat. Mtg. Soc. of Expl. Geophys., 2501–2504.

Short Note

Nondestructive testing by migration

Brad Artman & Robert G. Clapp¹

INTRODUCTION

In the spring of 2005, engineers from Lawrence Livermore National Laboratories² contacted SEP to ask about the potential to use geophysical algorithms for nondestructive investigation of manufactured/machined parts. The conversation was sparked by emphasis from the LLNL management to search for existing solutions to their suite of current problems. Dr. Lehman presented SEP with a problem of investigating the interior of a layered manufactured product with a potential delamination or rugosity of an interior layer. As opposed to standard geophysical problems, the velocity/density structure of the target is completely determined.

The velocity model of the product is three two layers submerged in water. This makes the total 1D velocity model: 11mm of 1500m/s, 3mm of 4100m/s, and 30mm of 2670m/s. Data given to SEP was modeled with the elastic ED3D finite difference code from Livermore. Center frequency 2.25 MHz. First presented to our group was a data volume consisting of a single shot and 100 receiver locations over 80mm of the surface giving a receiver spacing of 0.8081mm. The target to identify was 1mm negative step in the center of the model. The zero-offset time to the anomaly is approximately 0.04 ms. However, the only shot modeled was at the extreme left of the model space.

The most obvious problem identifiable from a geophysical perspective was a strong multiple train generated from energy ringing within the high velocity middle layer. Secondly, from the standpoints of either multiple removal or imaging, the lack of redundant information from multiple shot locations were immediately identified as problematic. In all other respects, the laboratory conditions available to collect data with no velocity uncertainty promised highly successful application of conventional geophysical processing technology.

A full fold, $n_s = n_r$, data volume was modeled and delivered to SEP during the summer. Also modeled by LLNL was a similar data volume with a up/down double spoon/scallop anomaly at the base of the third layer. With standard migration algorithms, we were able to image both targets with resolution of 0.1mm vertically and about 0.40405mm horizontally. Intrabed multiples from the second layer were not time-coincident in the middle half of the offset range, so no multiple attenuation efforts were required after the far offset traces were

¹email: brad@sep.stanford.edu, bob@sep.stanford.edu

²Dr. Sean Lehman(lehman2@llnl.gov), Dr. Karl Fisher(fisher34@llnl.gov)

removed before imaging. Source-receiver, shot-profile, and zero ray parameter planewave migrations were implemented. Given the simplicity and cleanliness of the data, zero-offset images from all approaches were practically identical.

DATA AND MIGRATION RESULTS

Figure 1 shows the data after the far offsets have been removed. A multiple train caused by the fast middle layer has died down over the inner offsets at the time of the anomaly. Therefore, removing the far offsets, we were able to create a nearly multiple free data volume for imaging purposes. The middle half of the total offset range was kept. Figure 2 is the image produced by shot-profile migration using all the available data. Figure 3 shows the image for the step anomaly and the scallop anomaly. Identical images were created by stacking all of the shots and migrating with a planar horizontal source function, and source-receiver migration (not shown).

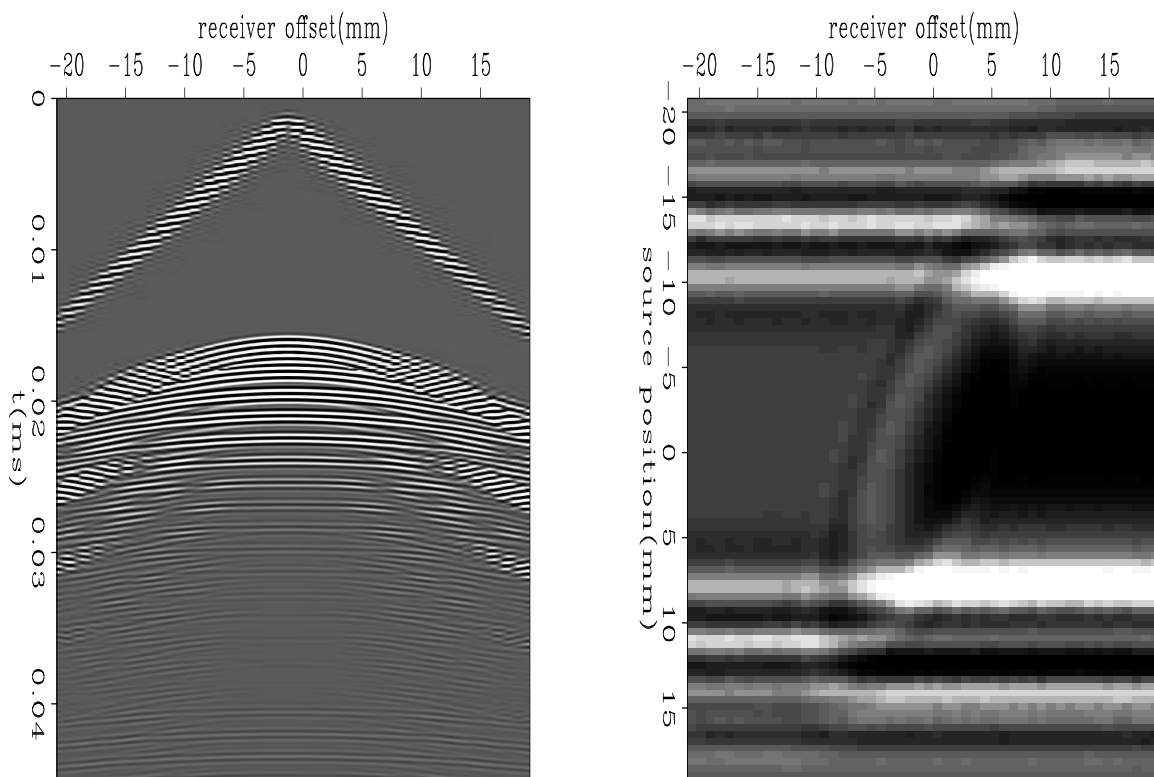


Figure 1: Shot record and time slice of the inner offsets of modeled data. The time slice shows the anomaly. `brad2-data` [CR]

To understand the importance of multiple shots, two single shot data volumes were migrated with shot-profile migration. Figure 4 is the image from a shot located at the left edge of the model space. The bottom reflector is very poorly imaged, and there is no indication of the anomaly. If the shot were located directly over the anomaly, as in Figure 5, the anomaly is noticeable though the quality of the image is poor.

Figure 2: Shot-profile migration using all available data. Interference from intrabed multiples from middle layer decreases image quality. `brad2-alloffsmig` [CR]

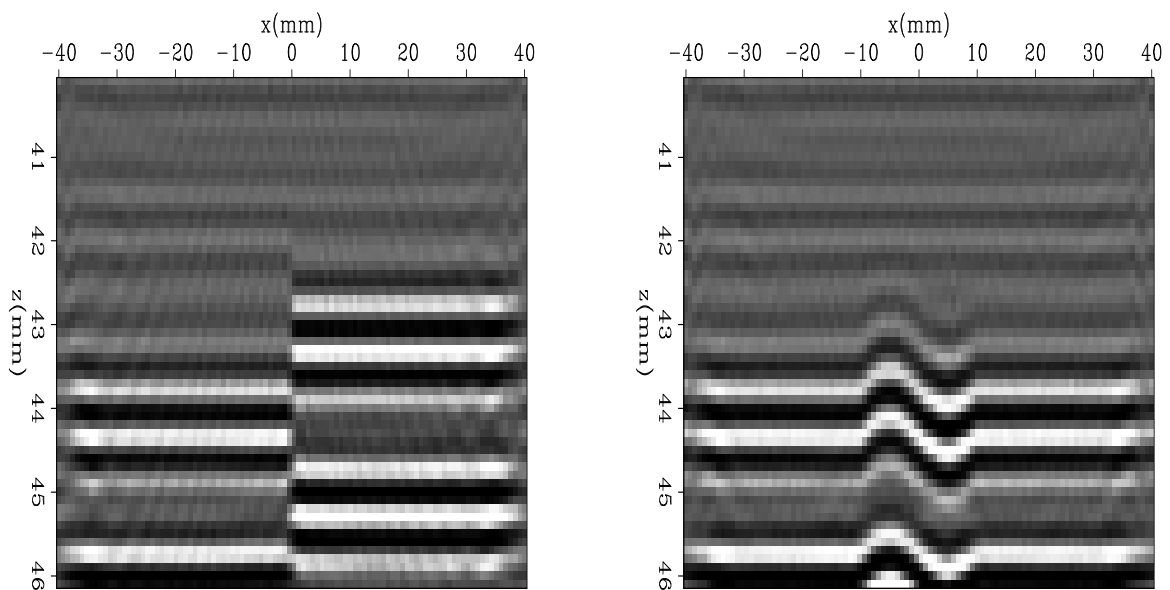
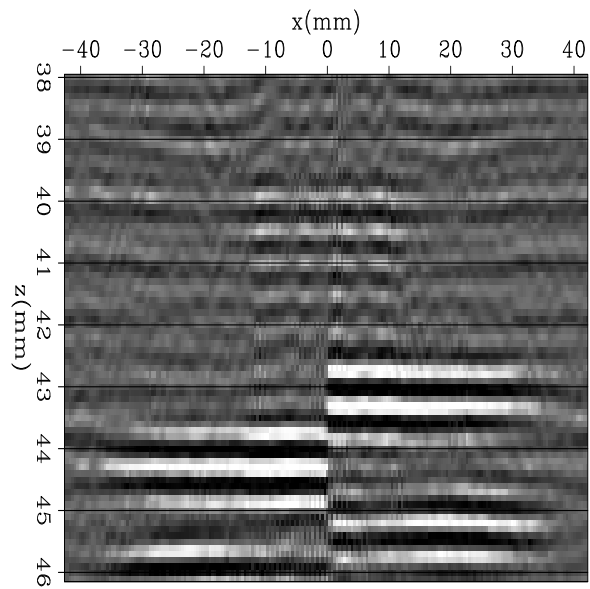


Figure 3: Both data sets produce very clean images when only near offset traces are migrated. Image produced with shot-profile migration. `brad2-shotmig` [CR]

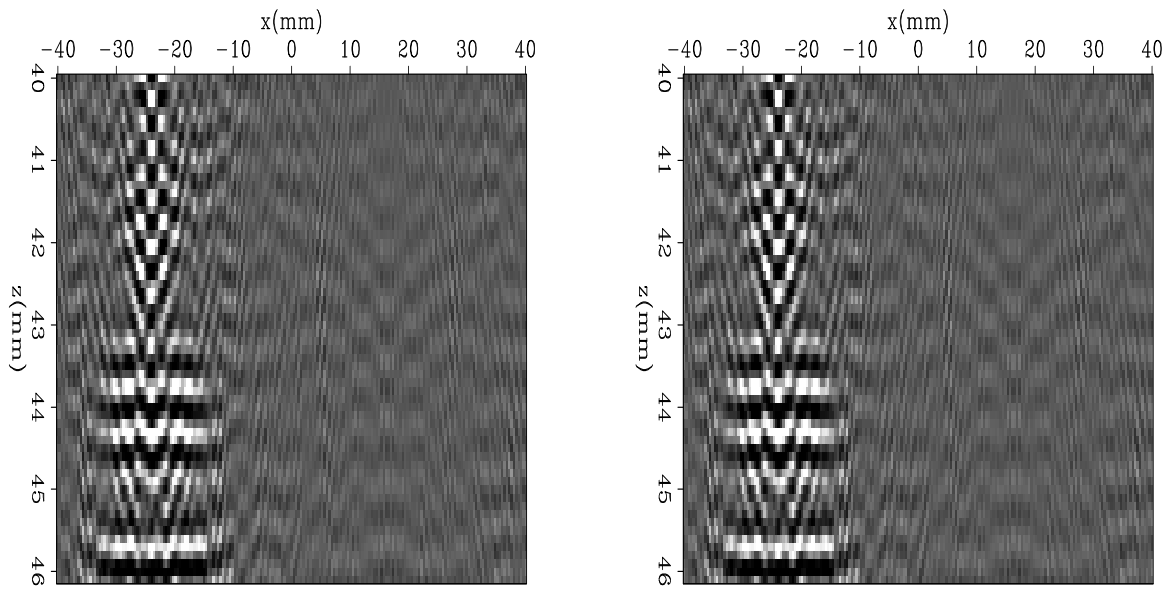


Figure 4: Image from a single shot at the far left edge of the model. `brad2-oneshot` [CR]

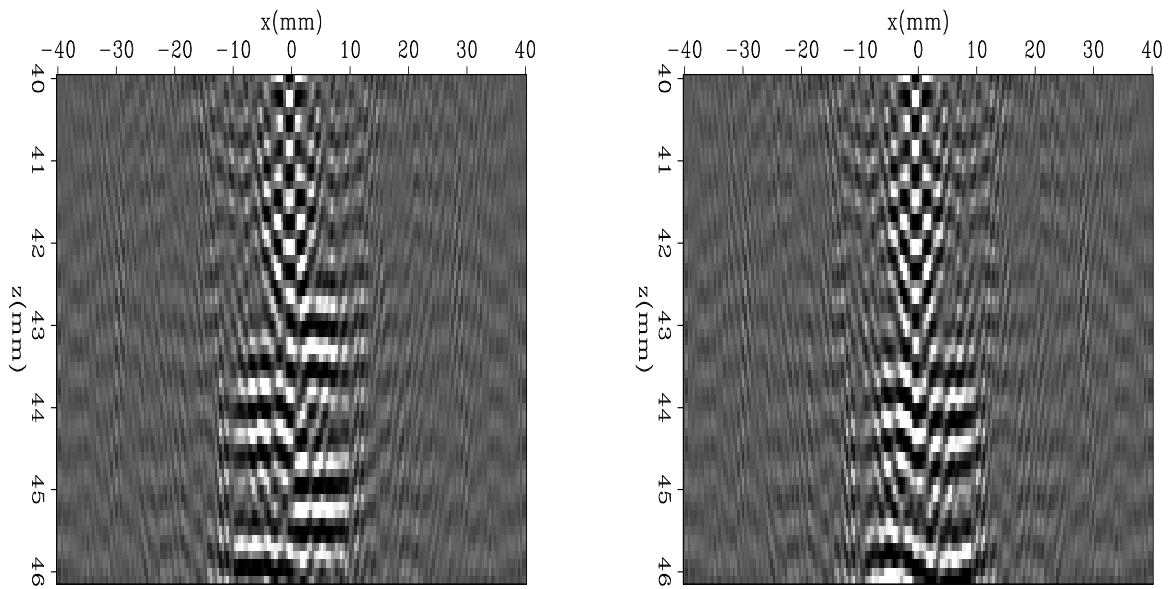


Figure 5: Image from a single shot directly over the anomaly. `brad2-censhot` [CR]

CONCLUSION

The modeled data given to SEP was produced to mimic a real manufactured product that the engineers at LLNL need to non-destructively test for potential defects. Laboratory apparatus will be used to collect data over a third dimension which also shares the same elastic properties. Simple geophysical migration techniques with acoustic depth algorithms were able to simply image both the step and scalloped anomalies in the modeled data. The various imaging algorithms tried (prestack source-receiver, prestack shot-profile, and zero ray parameter planewave) were all similarly successful.

Producing equivalent results, the least expensive solution is the best. Therefore, we can confidently advise the LLNL engineers that acquisition of a full fold multi-offset data volume is not required for this simple problem. However, many shot locations are imperative. Due to the intrabed multiple generator in the center of the product, the near offsets that are not contaminated with multiple energy are the most important. The most expedient method to collect the best and smallest data for their needs is to modify their laboratory equipment to allow the source piezoelectric element to record a zero offset trace after firing. This will allow for rapid data acquisition, over whatever third dimension may be required, and computationally inexpensive imaging.

Wave-equation angle-domain Hessian

Alejandro A. Valenciano and Biondo Biondi¹

ABSTRACT

A regularization in the reflection angle dimension (and, more generally in the reflection and azimuth angles) is necessary to stabilize the wave-equation inversion problem. The angle-domain Hessian can be computed from the subsurface-offset Hessian by an offset-to-angle transformation. This transformation can be done in the image space following the Sava and Fomel (2003) approach. To perform the inversion, the angle-domain Hessian matrix can be used explicitly, or implicitly as a chain of the offset-to-angle operator and the subsurface offset Hessian matrix.

INTRODUCTION

Seismic imaging using non-unitary migration operators (Claerbout, 1992) often produce images with reflectors correctly positioned but biased amplitudes (Nemeth et al., 1999; Duquet and Marfurt, 1999; Ronen and Liner, 2000; Chavent and Plessix, 1999). One way to solve this problem is to use the inversion formalism introduced by Tarantola (1987) to solve geophysical imaging problems, where the image can be obtained by weighting the migrated image with the inverse of the Hessian matrix. However, when the dimensions of the problem get large, the explicit calculation of the Hessian matrix and its inverse becomes unfeasible.

Valenciano and Biondi (2004) proposed computing the Hessian in a target-oriented fashion to reduce the size of the problem. The zero-offset inverse image can be estimated as the solution of a non-stationary least-squares filtering problem, by means of a conjugate gradient algorithm (Valenciano et al., 2005b,a). This approach, renders unnecessary an explicit computation of inverse of the Hessian matrix.

In this paper, we define the wave-equation angle-domain Hessian from the subsurface offset wave-equation Hessian via an angle-to-offset transformation following the Sava and Fomel (2003) approach. To perform the inversion, the angle-domain Hessian matrix can be used explicitly or, implicitly as a chain of the offset-to-angle operator and the subsurface offset Hessian matrix.

The definition of the wave-equation angle-domain Hessian allows the angle-domain regularization required to stabilize the wave equation inversion problem (Prucha et al., 2000; Kuehl and Sacchi, 2001). It also allows to obtain a prestack inverse image, adding the possibility of

¹**email:** valencia@sep.stanford.edu, biondo@sep.stanford.edu

doing amplitude vs. angle (AVA) analysis for reservoir characterization.

LINEAR LEAST-SQUARES INVERSION

Tarantola (1987) formalizes the geophysical inverse problem by giving a theoretical approach to compensate for experimental deficiency (e.g., acquisition geometry, complex overburden), while being consistent with the acquired data. His approach can be summarized as follows: given a linear modeling operator \mathbf{L} , compute synthetic data \mathbf{d} , using,

$$\mathbf{d} = \mathbf{L}\mathbf{m}, \quad (1)$$

where \mathbf{m} is a reflectivity model. Given the recorded data \mathbf{d}_{obs} , a quadratic cost function,

$$S(\mathbf{m}) = \|\mathbf{d} - \mathbf{d}_{obs}\|^2 = \|\mathbf{L}\mathbf{m} - \mathbf{d}_{obs}\|^2, \quad (2)$$

is formed. The reflectivity model $\hat{\mathbf{m}}$ that minimizes $S(\mathbf{m})$ is given by

$$\hat{\mathbf{m}} = (\mathbf{L}'\mathbf{L})^{-1}\mathbf{L}'\mathbf{d}_{obs} \quad (3)$$

$$\hat{\mathbf{m}} = \mathbf{H}^{-1}\mathbf{m}_{mig}, \quad (4)$$

where \mathbf{L}' (migration operator) is the adjoint of the linear modeling operator \mathbf{L} , \mathbf{m}_{mig} is the migration image, and $\mathbf{H} = \mathbf{L}'\mathbf{L}$ is the Hessian of $S(\mathbf{m})$.

The main difficulty with this approach is the explicit calculation of the Hessian inverse. In practice, it is more feasible to compute the least-squares inverse image as the solution of the linear system of equations,

$$\mathbf{H}\hat{\mathbf{m}} = \mathbf{m}_{mig}, \quad (5)$$

by using an iterative conjugate gradient algorithm.

The inversion inherent in equation 5 needs regularization. Prucha et al. (2000) and Kuehl and Sacchi (2001) propose smoothing the image in the offset ray parameter dimension, which is equivalent to the same procedure in the reflection angle dimension. This idea can be generalize to include the azimuth dimension.

The least squares solution of equation 5 is obtained using the fitting goals,

$$\begin{aligned} \mathbf{H}(\mathbf{x}, \Theta; \mathbf{x}', \Theta')\hat{\mathbf{m}}(\mathbf{x}, \Theta) - \mathbf{m}_{mig}(\mathbf{x}, \Theta) &\approx 0, \\ \mathbf{D}(\Theta)\hat{\mathbf{m}}(\mathbf{x}, \Theta) &\approx 0, \end{aligned} \quad (6)$$

where $\Theta = (\theta, \alpha)$ are the reflection and the azimuth angles, and $\mathbf{D}(\Theta)$ is a smoothing operator in the reflection and azimuth angle dimensions.

The next sections show how to include the subsurface offset dimension in the Hessian computation and how to go from subsurface offset to reflection and azimuth angle dimensions following the Sava and Fomel (2003) approach.

EXPANDING HESSIAN DIMENSIONALITY

Valenciano et al. (2005b) define the zero subsurface-offset Hessian by using the adjoint of the zero subsurface-offset migration as the modeling operator \mathbf{L} . Then the zero-offset inverse image can be estimated as the solution of a non-stationary least-squares filtering problem, by means of a conjugate gradient algorithm (Valenciano et al., 2005b,a). But, from the results reported by Prucha et al. (2000), Kuehl and Sacchi (2001), and Valenciano et al. (2005a), regularization in the reflection angle dimension is necessary to stabilize the wave-equation inversion problem.

Subsurface-offset Hessian

The prestack migration image (subsurface offset domain) for a group of shots positioned at $\mathbf{x}_s = (x_s, y_s, 0)$ and a group of receivers positioned at $\mathbf{x}_r = (x_r, y_r, 0)$ can be given by the adjoint of a linear operator \mathbf{L} acting on the data-space $\mathbf{d}(\mathbf{x}_s, \mathbf{x}_r; \omega)$ as

$$\begin{aligned} \mathbf{m}(\mathbf{x}, \mathbf{h}) &= \mathbf{L}' \mathbf{d}(\mathbf{x}_s, \mathbf{x}_r; \omega) \\ &= \sum_{\omega} \sum_{\mathbf{x}_s} \sum_{\mathbf{x}_r} \mathbf{G}'(\mathbf{x} + \mathbf{h}, \mathbf{x}_s; \omega) \mathbf{G}'(\mathbf{x} - \mathbf{h}, \mathbf{x}_r; \omega) \sum_{\mathbf{h}}' \sum_{\mathbf{x}}' \mathbf{d}(\mathbf{x}_s, \mathbf{x}_r; \omega), \end{aligned} \quad (7)$$

where $\mathbf{G}(\mathbf{x}, \mathbf{x}_s; \omega)$ and $\mathbf{G}(\mathbf{x}, \mathbf{x}_r; \omega)$ are the Green functions from shot position \mathbf{x}_s and receiver position \mathbf{x}_r to a model space point $\mathbf{x} = (x, y, z)$, and $\mathbf{h} = (h_x, h_y, h_z)$ is the subsurface offset. The symbols $\sum_{\mathbf{h}}'$ and $\sum_{\mathbf{x}}'$ are spray (adjoint of the sum) operators in the subsurface offset and model space dimensions, respectively.

The synthetic data can be modeled (as the adjoint of equation 7) by the linear operator \mathbf{L} acting on the model space $\mathbf{m}(\mathbf{x}, \mathbf{h})$ with $\mathbf{x} = (x, y, z)$ and $\mathbf{h} = (h_x, h_y)$

$$\begin{aligned} \mathbf{d}(\mathbf{x}_s, \mathbf{x}_r; \omega) &= \mathbf{Lm}(\mathbf{x}, \mathbf{h}) \\ &= \sum_{\mathbf{x}} \sum_{\mathbf{h}} \mathbf{G}(\mathbf{x} - \mathbf{h}, \mathbf{x}_r; \omega) \mathbf{G}(\mathbf{x} + \mathbf{h}, \mathbf{x}_s; \omega) \sum_{\mathbf{x}_r}' \sum_{\mathbf{x}_s}' \sum_{\omega}' \mathbf{m}(\mathbf{x}, \mathbf{h}), \end{aligned} \quad (8)$$

where the symbols $\sum_{\mathbf{x}_r}'$, $\sum_{\mathbf{x}_s}'$, and \sum_{ω}' are spray operators in the shot, receiver, and frequency dimensions, respectively.

In equations 7 and 8 the Green functions are computed by means of the one-way wave equation (Ehinger et al., 1996) and the extrapolation is performed using the adequate paraxial wave equations (flux conservation) (Bamberger et al., 1988).

The quadratic cost function is

$$\begin{aligned} S(\mathbf{m}) &= \frac{1}{2} \sum_{\omega} \sum_{\mathbf{x}_s} \sum_{\mathbf{x}_r} \|\mathbf{d} - \mathbf{d}_{obs}\|^2 \\ &= \frac{1}{2} \sum_{\omega} \sum_{\mathbf{x}_s} \sum_{\mathbf{x}_r} [\mathbf{d}(\mathbf{x}_s, \mathbf{x}_r; \omega) - \mathbf{d}_{obs}]' [\mathbf{d}(\mathbf{x}_s, \mathbf{x}_r; \omega) - \mathbf{d}_{obs}], \end{aligned} \quad (9)$$

while its first derivative, with respect to the model parameters $\mathbf{m}(\mathbf{x}, \mathbf{h})$, is

$$\begin{aligned} \frac{\partial S(\mathbf{m})}{\partial \mathbf{m}(\mathbf{x}, \mathbf{h})} = & \frac{1}{2} \sum_{\omega} \sum_{\mathbf{x}_s} \sum_{\mathbf{x}_r} \{ \mathbf{G}'(\mathbf{x} - \mathbf{h}, \mathbf{x}_r; \omega) \mathbf{G}'(\mathbf{x} + \mathbf{h}, \mathbf{x}_s; \omega) [\mathbf{d}(\mathbf{x}_s, \mathbf{x}_r; \omega) - \mathbf{d}_{obs}] \\ & + [\mathbf{d}(\mathbf{x}_s, \mathbf{x}_r; \omega) - \mathbf{d}_{obs}]' \mathbf{G}(\mathbf{x} - \mathbf{h}, \mathbf{x}_r; \omega) \mathbf{G}(\mathbf{x} + \mathbf{h}, \mathbf{x}_s; \omega) \}, \end{aligned} \quad (10)$$

and its second derivative with respect to the model parameters $\mathbf{m}(\mathbf{x}, \mathbf{h})$ and $\mathbf{m}(\mathbf{x}', \mathbf{h}')$ is the subsurface offset Hessian:

$$\begin{aligned} \mathbf{H}(\mathbf{x}, \mathbf{h}; \mathbf{x}', \mathbf{h}') &= \frac{\partial^2 S(\mathbf{m})}{\partial \mathbf{m}(\mathbf{x}, \mathbf{h}) \partial \mathbf{m}(\mathbf{x}', \mathbf{h}')} \quad (11) \\ \mathbf{H}(\mathbf{x}, \mathbf{h}; \mathbf{x}', \mathbf{h}') &= \sum_{\omega} \sum_{\mathbf{x}_s} \mathbf{G}'(\mathbf{x} + \mathbf{h}, \mathbf{x}_s; \omega) \mathbf{G}'(\mathbf{x}' + \mathbf{h}', \mathbf{x}_s; \omega) \sum_{\mathbf{x}_r} \mathbf{G}'(\mathbf{x} - \mathbf{h}, \mathbf{x}_r; \omega) \mathbf{G}'(\mathbf{x}' - \mathbf{h}', \mathbf{x}_r; \omega). \end{aligned}$$

The next subsection shows how to go from subsurface offset to reflection and azimuth angle dimensions following the Sava and Fomel (2003) approach.

Angle-domain Hessian

Sava and Fomel (2003) define an image space transformation from subsurface offset to reflection and azimuth angle as:

$$\mathbf{m}(\mathbf{x}, \Theta) = \mathbf{T}'(\Theta, \mathbf{h}) \mathbf{m}(\mathbf{x}, \mathbf{h}), \quad (12)$$

where $\Theta = (\theta, \alpha)$ are the reflection and the azimuth angles, and $\mathbf{T}'(\Theta, \mathbf{h})$ is the adjoint of the angle-to-offset transformation operator (slant stack).

Substituting the prestack migration image (subsurface offset domain) in equation 7 into equation 12 we obtain the expression for the prestack migration image in the angle-domain that follows:

$$\begin{aligned} \mathbf{m}(\mathbf{x}, \Theta) &= \mathbf{T}'(\Theta, \mathbf{h}) \mathbf{L}' \mathbf{d}(\mathbf{x}_s, \mathbf{x}_r; \omega) \quad (13) \\ &= \mathbf{T}'(\Theta, \mathbf{h}) \sum_{\omega} \sum_{\mathbf{x}_s} \sum_{\mathbf{x}_r} \mathbf{G}'(\mathbf{x} + \mathbf{h}, \mathbf{x}_s; \omega) \mathbf{G}'(\mathbf{x} - \mathbf{h}, \mathbf{x}_r; \omega) \sum_{\mathbf{h}}' \sum_{\mathbf{x}}' \mathbf{d}(\mathbf{x}_s, \mathbf{x}_r; \omega). \end{aligned}$$

The synthetic data can be modeled (as the adjoint of equation 14) by the chain of linear operator \mathbf{L} and the angle-to-offset transformation operator acting on the model space,

$$\begin{aligned} \mathbf{d}(\mathbf{x}_s, \mathbf{x}_r; \omega) &= \mathbf{L} \mathbf{T}(\Theta, \mathbf{h}) \mathbf{m}(\mathbf{x}, \Theta) \\ &= \sum_{\mathbf{x}} \sum_{\mathbf{h}} \mathbf{G}(\mathbf{x} - \mathbf{h}, \mathbf{x}_r; \omega) \mathbf{G}(\mathbf{x} + \mathbf{h}, \mathbf{x}_s; \omega) \sum_{\mathbf{x}_r}' \sum_{\mathbf{x}_s}' \sum_{\omega}' \mathbf{T}(\Theta, \mathbf{h}) \mathbf{m}(\mathbf{x}, \Theta), \end{aligned} \quad (14)$$

The quadratic cost function is

$$\begin{aligned} S(\mathbf{m}) &= \frac{1}{2} \sum_{\omega} \sum_{\mathbf{x}_s} \sum_{\mathbf{x}_r} \|\mathbf{d} - \mathbf{d}_{obs}\|^2 \\ &= \frac{1}{2} \sum_{\omega} \sum_{\mathbf{x}_s} \sum_{\mathbf{x}_r} [\mathbf{d}(\mathbf{x}_s, \mathbf{x}_r; \omega) - \mathbf{d}_{obs}]' [\mathbf{d}(\mathbf{x}_s, \mathbf{x}_r; \omega) - \mathbf{d}_{obs}], \end{aligned} \quad (15)$$

while its first derivative with respect to the model parameters $\mathbf{m}(\mathbf{x}, \Theta)$ is

$$\frac{\partial S(\mathbf{m})}{\partial \mathbf{m}(\mathbf{x}, \Theta)} = \frac{1}{2} \sum_{\omega} \sum_{\mathbf{x}_s} \sum_{\mathbf{x}_r} \{ \mathbf{T}'(\Theta, \mathbf{h}) \mathbf{G}'(\mathbf{x} - \mathbf{h}, \mathbf{x}_r; \omega) \mathbf{G}'(\mathbf{x} + \mathbf{h}, \mathbf{x}_s; \omega) [\mathbf{d}(\mathbf{x}_s, \mathbf{x}_r; \omega) - \mathbf{d}_{obs}] + [\mathbf{d}(\mathbf{x}_s, \mathbf{x}_r; \omega) - \mathbf{d}_{obs}]' \mathbf{G}(\mathbf{x} - \mathbf{h}, \mathbf{x}_r; \omega) \mathbf{G}(\mathbf{x} + \mathbf{h}, \mathbf{x}_s; \omega) \mathbf{T}(\Theta, \mathbf{h}) \} \quad (16)$$

and its second derivative with respect to the model parameters $\mathbf{m}(\mathbf{x}, \Theta)$ and $\mathbf{m}(\mathbf{x}', \Theta')$ is the angle-domain Hessian

$$\begin{aligned} \mathbf{H}(\mathbf{x}, \Theta; \mathbf{x}', \Theta') &= \frac{\partial^2 S(\mathbf{m})}{\partial \mathbf{m}(\mathbf{x}, \Theta) \partial \mathbf{m}(\mathbf{x}', \Theta')} \\ &= \sum_{\omega} \sum_{\mathbf{x}_s} \sum_{\mathbf{x}_r} \mathbf{T}'(\Theta, \mathbf{h}) \mathbf{G}'(\mathbf{x} + \mathbf{h}, \mathbf{x}_s; \omega) \mathbf{G}(\mathbf{x}' + \mathbf{h}', \mathbf{x}_s; \omega) \\ &\quad \times \mathbf{G}'(\mathbf{x} - \mathbf{h}, \mathbf{x}_r; \omega) \mathbf{G}(\mathbf{x}' - \mathbf{h}', \mathbf{x}_r; \omega) \mathbf{T}(\Theta', \mathbf{h}') \\ &= \mathbf{T}'(\Theta, \mathbf{h}) \sum_{\omega} \sum_{\mathbf{x}_s} \sum_{\mathbf{x}_r} \mathbf{G}'(\mathbf{x} + \mathbf{h}, \mathbf{x}_s; \omega) \mathbf{G}(\mathbf{x}' + \mathbf{h}', \mathbf{x}_s; \omega) \\ &\quad \times \mathbf{G}'(\mathbf{x} - \mathbf{h}, \mathbf{x}_r; \omega) \mathbf{G}(\mathbf{x}' - \mathbf{h}', \mathbf{x}_r; \omega) \mathbf{T}(\Theta', \mathbf{h}') \\ &= \mathbf{T}'(\Theta, \mathbf{h}) \mathbf{H}(\mathbf{x}, \mathbf{h}; \mathbf{x}', \mathbf{h}') \mathbf{T}(\Theta', \mathbf{h}'). \end{aligned} \quad (17)$$

Explicit vs. implicit Hessian matrix computation

Equation 17 expresses the angle-domain Hessian as a chain of the offset-to-angle operator and the subsurface offset Hessian matrix. This implies that to implement the angle-domain wave-equation inversion using a conjugate gradient algorithm there is no need to explicitly compute the angle Hessian matrix. But the possible drawback is that, for each iteration, the offset-to-angle transformation needs to be performed.

A different strategy might be to explicitly compute the angle-domain Hessian matrix. This can be done by a simple manipulation the terms in equation 17

$$\begin{aligned} \mathbf{H}(\mathbf{x}, \Theta; \mathbf{x}', \Theta') &= \mathbf{T}'(\Theta, \mathbf{h}) \mathbf{H}(\mathbf{x}, \mathbf{h}; \mathbf{x}', \mathbf{h}') \mathbf{T}(\Theta', \mathbf{h}') \\ &= \mathbf{T}'(\Theta, \mathbf{h}) (\mathbf{T}'(\Theta', \mathbf{h}') \mathbf{H}'(\mathbf{x}, \mathbf{h}; \mathbf{x}', \mathbf{h}'))'. \end{aligned} \quad (18)$$

Due to the symmetry of the Hessian matrix equation 18 turns into:

$$\mathbf{H}(\mathbf{x}, \Theta; \mathbf{x}', \Theta') = \mathbf{T}'(\Theta, \mathbf{h}) (\mathbf{T}'(\Theta', \mathbf{h}') \mathbf{H}(\mathbf{x}, \mathbf{h}; \mathbf{x}', \mathbf{h}'))'. \quad (19)$$

In practice, equation 19 takes the subsurface offset Hessian matrix and applies an offset-to-angle transformation, then transposes the resulting matrix and reapplies the same offset-to-angle transformation.

This explicit angle Hessian matrix computation could be an expensive operation, but it has the advantage of only needing to be performed once. In contrast to the application of a chain of the offset-to-angle operator and the subsurface offset Hessian matrix (implicit approach) which needs to be performed at each conjugate gradient iteration. Each approach has its advantages and disadvantages, thus the specific application will dictate which path to follow.

CONCLUSIONS

The wave-equation angle-domain Hessian can be computed from the subsurface offset wave-equation Hessian via an angle-to-offset transformation following the approach presented by Sava and Fomel (2003). This result allow us to implement an angle-domain regularization that stabilizes the the wave equation inversion problem.

In order to perform the wave-equation angle-domain inversion, the angle-domain Hessian matrix can be used explicitly or, implicitly as a chain of the offset-to-angle operator and the subsurface offset Hessian matrix. Since each approach has its advantages and disadvantages the specific application will dictate which path to follow.

ACKNOWLEDGMENTS

We would like to thank Gabriel Alvarez for many insightful discussions.

REFERENCES

- Bamberger, A., Engquist, B., Halpern, L., and Joly, P., 1988, Paraxial approximation in heterogeneous media: *SIAM J. Appl. Math.*, **48**, 98–128.
- Chavent, G., and Plessix, R. E., 1999, An optimal true-amplitude least-squares prestack depth-migration operator: *Geophysics*, **64**, no. 2, 508–515.
- Claerbout, J. F., 1992, *Earth soundings analysis, processing versus inversion*: Blackwell Scientific Publications.
- Duquet, B., and Marfurt, K. J., 1999, Filtering coherent noise during prestack depth migration: *Geophysics*, **64**, no. 4, 1054–1066.
- Ehinger, A., Lailly, P., and Marfurt, K. J., 1996, Green's function implementation of common-offset wave-equation migration: *Geophysics*, **61**, no. 06, 1813–1821.
- Kuehl, H., and Sacchi, M., 2001, Generalized least-squares DSR migration using a common angle imaging condtion: *Soc. of Expl. Geophys.*, 71st Ann. Internat. Mtg, 1025–1028.
- Nemeth, T., Wu, C., and Schuster, G. T., 1999, Least-squares migration of incomplete reflection data: *Geophysics*, **64**, no. 1, 208–221.
- Prucha, M. L., Clapp, R. G., and Biondi, B., 2000, Seismic image regularization in the reflection angle domain: *SEP-103*, 109–119.
- Ronen, S., and Liner, C. L., 2000, Least-squares DMO and migration: *Geophysics*, **65**, no. 5, 1364–1371.

Sava, P. C., and Fomel, S., 2003, Angle-domain common-image gathers by wavefield continuation methods: *Geophysics*, **68**, no. 3, 1065–1074.

Tarantola, A., 1987, *Inverse problem theory*: Elsevier.

Valenciano, A. A., and Biondi, B., 2004, Target-oriented computation of the wave-equation imaging Hessian: SEP-**117**, 63–76.

Valenciano, A. A., Biondi, B., and Guitton, A., 2005a, Target-oriented wave-equation inversion: Sigsbee model: SEP-**123**.

Valenciano, A. A., Biondi, B., and Guitton, A., 2005b, Target-oriented wave-equation inversion: SEP-**120**, 23–40.

Short Note

Target-oriented wave-equation inversion: Sigsbee model

Alejandro A. Valenciano, Biondo Biondi, and Antoine Guitton¹

INTRODUCTION

Sigsbee model is often used as a benchmark for migration/inversion algorithms due to its geological complexity. The data was modeled by simulating the geological setting found on the Sigsbee escarpment in the deep-water Gulf of Mexico. The model exhibits illumination problems due to the complex salt shape, with a rugose salt top.

When the subsurface is complex, migration operators produce images with reflectors correctly positioned but biased amplitudes (Prucha et al., 2000; Kuehl and Sacchi, 2001). That is why an inversion formalism (Tarantola, 1987) needs to be used to account for that problem.

In this paper, we apply the target-oriented wave-equation inversion idea presented in Valenciano et al. (2005) to the Sigsbee data. Due to the complex velocity structure and the limited acquisition cable length, the reflectors are not illuminated from all reflection angles. That highlights the need of a more sophisticated regularization in the angle domain (Prucha et al., 2000; Kuehl and Sacchi, 2001; Valenciano and Biondi, 2005) than the simple damping proposed by Valenciano et al. (2005).

INVERSION SETTING

Linear least-squares inversion

Tarantola (1987) formalizes the geophysical inverse problem by giving a theoretical approach to compensate for experiment deficiencies (e.g., acquisition geometry, obstacles), while being consistent with the acquired data. His approach can be summarized as follows: given a linear modeling operator \mathbf{L} compute synthetic data, \mathbf{d} , using,

$$\mathbf{d} = \mathbf{L}\mathbf{m}, \quad (1)$$

where \mathbf{m} is a reflectivity model, and given the recorded data \mathbf{d}_{obs} , a quadratic cost function,

$$S(\mathbf{m}) = \|\mathbf{d} - \mathbf{d}_{obs}\|^2 = \|\mathbf{L}\mathbf{m} - \mathbf{d}_{obs}\|^2, \quad (2)$$

¹email: valencia@sep.stanford.edu, biondo@sep.stanford.edu, antoine@sep.stanford.edu

is formed. The model of the earth $\hat{\mathbf{m}}$ that minimizes $S(\mathbf{m})$ is given by

$$\hat{\mathbf{m}} = (\mathbf{L}'\mathbf{L})^{-1}\mathbf{L}'\mathbf{d}_{obs} \quad (3)$$

$$\hat{\mathbf{m}} = \mathbf{H}^{-1}\mathbf{m}_{mig}, \quad (4)$$

where \mathbf{L}' (migration operator) is the adjoint of the linear modeling operator \mathbf{L} , \mathbf{m}_{mig} is the migration image, and $\mathbf{H} = \mathbf{L}'\mathbf{L}$ is the Hessian of $S(\mathbf{m})$.

The main difficulty with this approach is the explicit calculation of the Hessian inverse. In practice, it is more feasible to compute the least-squares inverse image as the solution of the linear system of equations

$$\mathbf{H}\hat{\mathbf{m}} = \mathbf{m}_{mig}, \quad (5)$$

by using an iterative conjugate gradient algorithm.

Another difficulty with this approach is that the explicit calculation of the Hessian for the entire model space is impractical. Valenciano and Biondi (2004) and Valenciano et al. (2005) discuss a way to make this problem more tractable.

Non-stationary least-squares filtering

The condition number of the target-oriented Hessian matrix can be high, making the solution of the non-stationary least-squares filtering problem in equation (5) unstable. One solution is adding a smoothing regularization operator to equation (5):

$$\begin{aligned} \mathbf{H}\hat{\mathbf{m}} - \mathbf{m}_{mig} &\approx 0, \\ \epsilon\mathbf{I}\hat{\mathbf{m}} &\approx 0, \end{aligned} \quad (6)$$

where the choice of the identity operator (\mathbf{I}) as regularization operator is customary. A more sophisticated regularization scheme could involve applying a smoothing operator in the reflection angle (or offset ray-parameter) dimension (Prucha et al., 2000; Kuehl and Sacchi, 2001) or, more generally, in the reflection and azimuth angles as proposed by Valenciano and Biondi (2005).

NUMERICAL RESULTS: SIGSBEE MODEL

The Sigsbee data set was modeled by simulating the geological setting found on the Sigsbee escarpment in the deep-water Gulf of Mexico. The model exhibits the illumination problems due to the complex salt shape, characterized by a rugose salt top (see Figure 1). We choose a target zone (indicated with the "target" box in Figure 1) to see the effects of illumination on imaging close to the salt.

Figure 2 shows the shot-profile migration image (using cross-correlation imaging condition) corresponding to the portion of Sigsbee model shown in figure 1. Notice how the

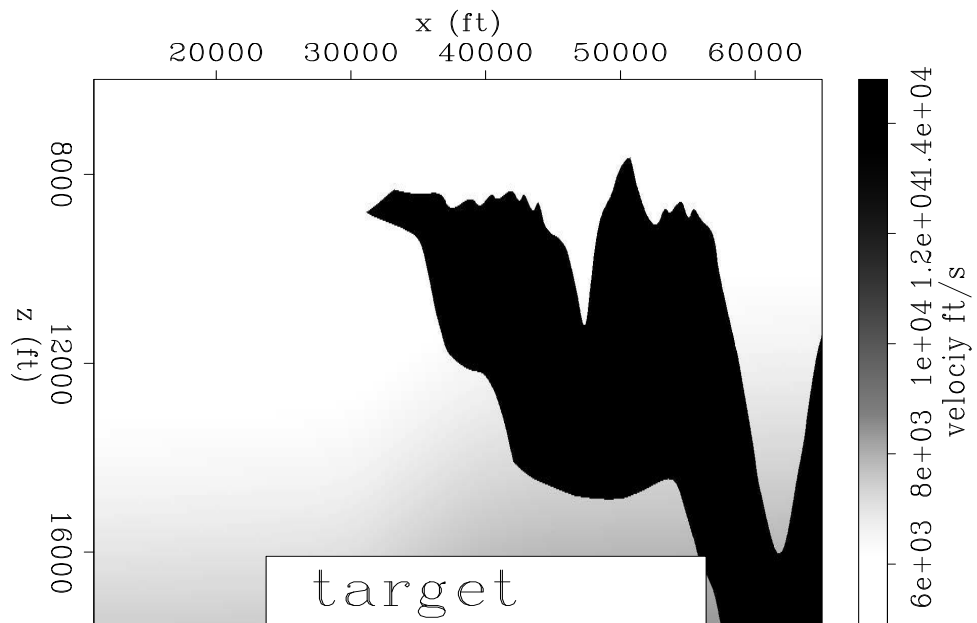


Figure 1: Sigsbee velocity model, target zone indicated with the "target" box.
[alejandros2-Sis_vel](#) [CR]

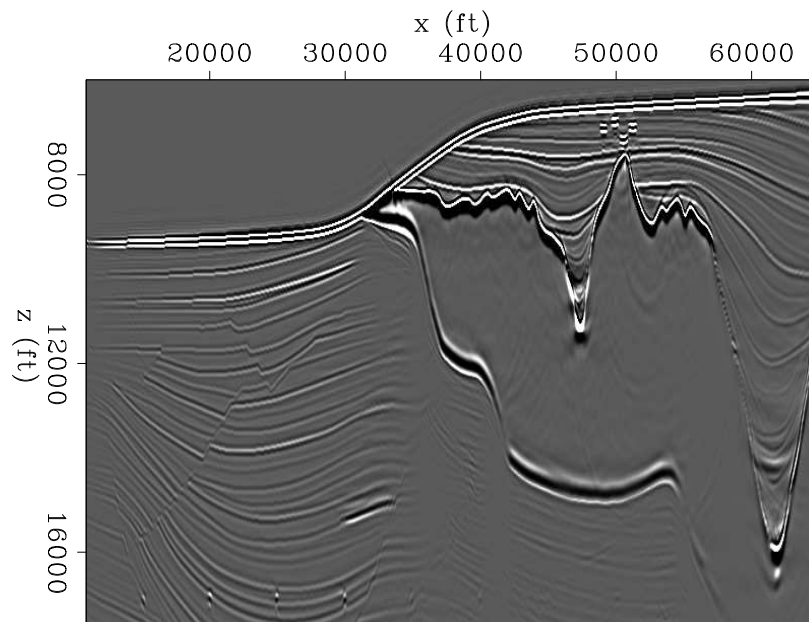


Figure 2: Sigsbee shot-profile migration image using cross-correlation imaging condition.
[alejandros2-mig_Sis](#) [CR]

diffractor amplitudes located at 17000 feet depth fade away as they get closer to the salt. The same happens to the reflectors as they get close to the salt.

Figure 3 shows a 21×7 coefficient filter (target-oriented Hessian) at constant depth as the x coordinate moves from the sediments to the salt boundary. Figure 3a shows point 1, with coordinates $\mathbf{x} = (17000, 30000) ft$ (far from the salt). Figure 3b shows point 2, with coordinates $\mathbf{x} = (17000, 34000) ft$. Figure 3c shows point 3, with coordinates $\mathbf{x} = (17000, 38000) ft$. Figure 3d shows point 4, with coordinates $\mathbf{x} = (17000, 42000) ft$.

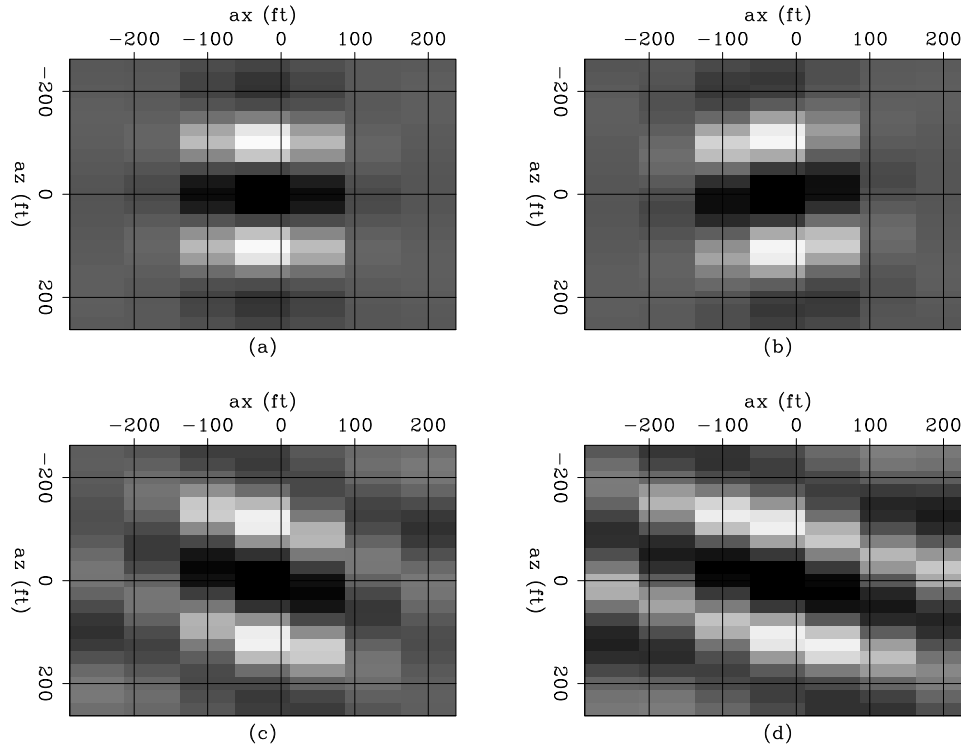


Figure 3: Hessian of the Sigsbee model, (a) point 1 $\mathbf{x} = (17000, 30000) ft$, (b) point 2 $\mathbf{x} = (17000, 34000) ft$, (c) point 3 $\mathbf{x} = (17000, 38000) ft$, and (d) point 4 $\mathbf{x} = (17000, 42000) ft$. [alejandro2-hessian_phase_Sis](#) [CR]

Unlike the constant velocity case (Valenciano et al., 2005), the shape of the filter is not dependent only on the acquisition geometry but the subsurface geometry (presence of the salt body). In the area unaffected by the salt the filter looks the same as is the constant velocity case, but as we get closer to the salt the illumination varies (in intensity and angle) and the filter behaves differently. This is due to a focusing and defocusing effect created by the salt. To correct this effect we computed the least-squares inverse image, by the method described in Valenciano et al. (2005).

Figure 4 shows a comparison between the migration and the inversion images in the target area. The stratigraphic model is shown in Figure 4a. Notice the seven equal-strength point diffractors and the position of the faults. Figure 4b shows the illumination, which is the diagonal of the Hessian matrix (dark is high illumination light is low illumination). Notice the decrease in the illumination as it gets closer to the salt with the exception of a narrow strip

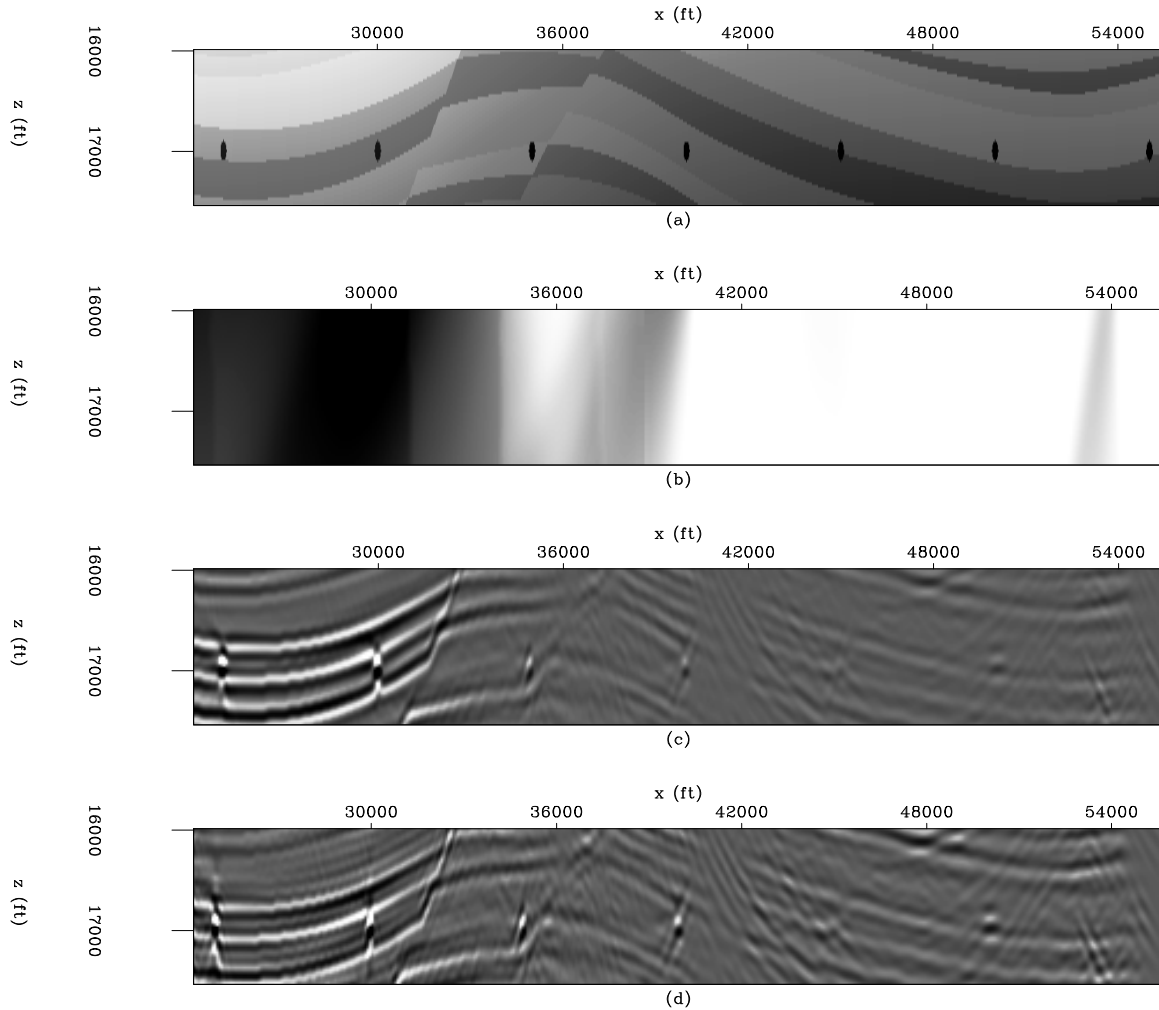


Figure 4: Target area comparison. (a) stratigraphic model, (b) illumination (dark is high and light is low), (c) migration, and (d) inversion. `alejandro2-comp_Sis_full` [CR]

where energy focuses close to the salt. The migration result is shown in Figure 4c. The reflectors dim out as they get closer to the salt. In contrast, Figure 4d shows the inversion result, the resolution increases (especially to the left of the image) and the section looks more balance. Also notice how the diffractors amplitude is better balanced.

At the right of the image the resolution did not increase as much as to the left. This is due to the fact that data values (migration) to the left are bigger than to the right (Figure 4c), and so are the data residuals. Thus, the solver expends most of the time decreasing the residuals in that area.

To test the previous hypothesis we did the inversion only in the low-illumination, reduced target area (Figure 5). Figure 5a shows the illumination (diagonal of the Hessian matrix) in the low-illumination area. Figure 5b shows the migration in the low-illumination area. Figure 5c shows the inversion performed in the full target area to match the dimensions of the inversion

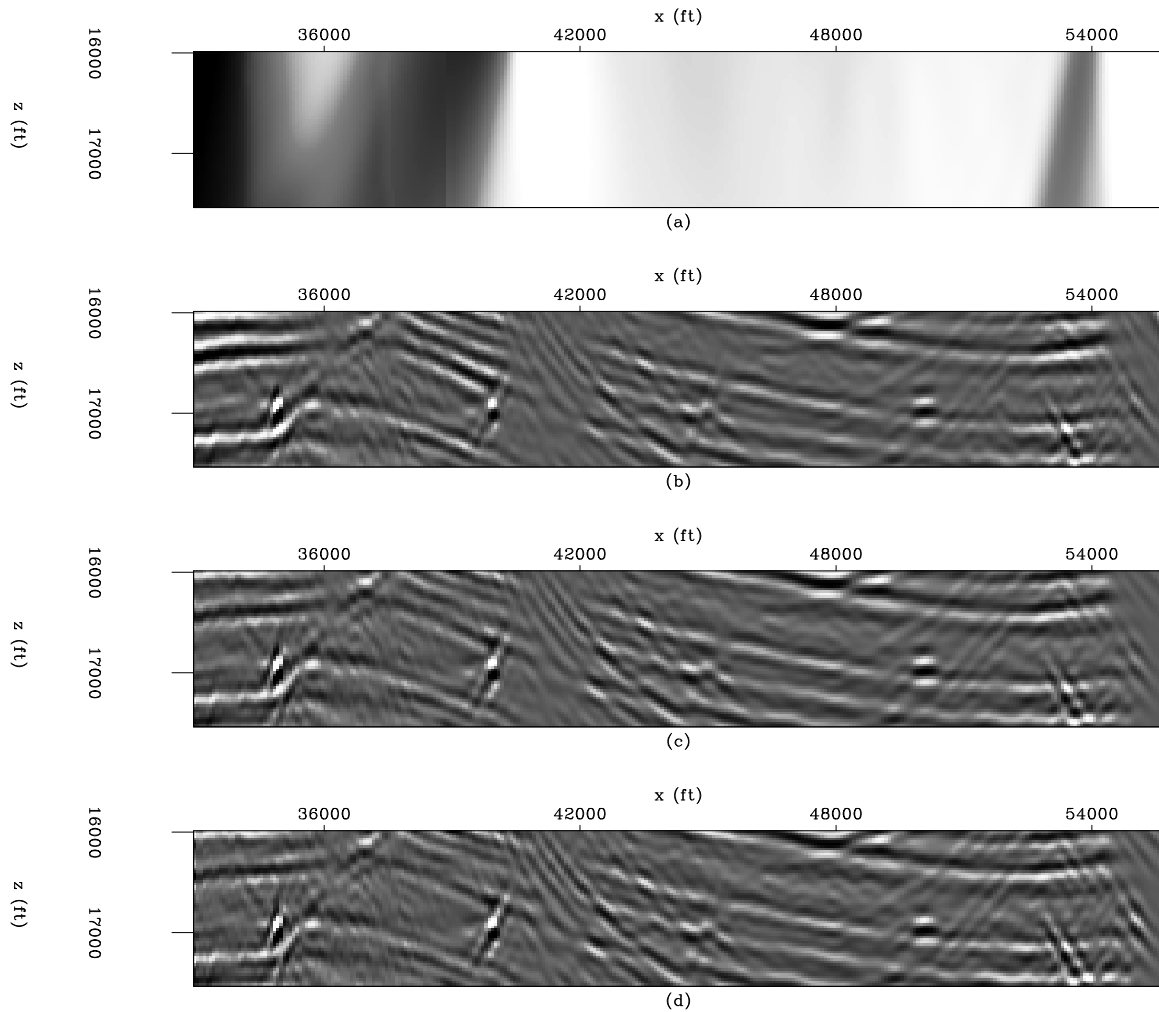


Figure 5: Reduced target area comparison. (a) illumination (dark is high and light is low), (b) migration, (c) inversion in the full target area, and (d) inversion in the reduced target area. `alejandro2-comp_Sis_wind` [CR]

on the low-illumination area which is shown in Figure 5d. There are substantial differences between the two inversion results: the result in the low-illumination area has better resolution than the one in the full target area, and the last diffractor (right corner) is more energetic in the result in the low-illumination than the one done in the full target area.

In general, even though inversion gives more balanced and better resolved images, it also produces more noisy results. Thus, a more sophisticated regularization might be necessary. Prucha et al. (2000) and Kuehl and Sacchi (2001) propose using a smoothing operator in the reflection angle (offset ray parameter) dimension. Valenciano and Biondi (2005) proposes a more general regularization in the reflection and azimuth angle dimensions.

CONCLUSIONS

Imaging the Sigsbee model highlights the need of a regularization in the angle domain of the target-oriented wave equation inversion problem (Prucha et al., 2000; Kuehl and Sacchi, 2001; Valenciano and Biondi, 2005). Even though the inversion gives a more balanced sections and higher resolution images, it also increases the noise.

REFERENCES

- Kuehl, H., and Sacchi, M., 2001, Generalized least-squares DSR migration using a common angle imaging condition: Soc. of Expl. Geophys., 71st Ann. Internat. Mtg, 1025–1028.
- Prucha, M. L., Clapp, R. G., and Biondi, B., 2000, Seismic image regularization in the reflection angle domain: SEP-**103**, 109–119.
- Tarantola, A., 1987, Inverse problem theory: Elsevier.
- Valenciano, A. A., and Biondi, B., 2004, Target-oriented computation of the wave-equation imaging Hessian: SEP-**117**, 63–76.
- Valenciano, A. A., and Biondi, B., 2005, Wave-equation angle-domain hessian: SEP-**123**.
- Valenciano, A. A., Biondi, B., and Guitton, A., 2005, Target-oriented wave-equation inversion: SEP-**120**, 23–40.

AMO inversion to a common azimuth dataset

Robert G. Clapp¹

ABSTRACT

I cast 3-D data regularization as a least-squares inversion problem. The model space is a four-dimensional $(t, \text{cmp}_x, \text{cmp}_y, h_x)$ hypercube. An interpolation operator maps to an irregular five dimensional space $(t, \text{cmp}_x, \text{cmp}_y, h_x, h_y)$ which is then mapped back into a four dimensional space by applying Azimuth Move-Out (AMO). A regularization term minimizes the difference between various $(t, \text{cmp}_x, \text{cmp}_y)$ cubes by applying a filter that acts along offset. AMO is used to transform the cubes to the same h_x before applying the filter. The methodology is made efficient by Fourier-domain implementation and pre-conditioning of the problem. I apply the methodology on a simple synthetic and to a real marine dataset.

INTRODUCTION

The irregularity of seismic data, particularly 3-D data, in both the model domain (in terms of subsurface position and reflection angle) and the data domain (in terms of midpoint, offset, and time) cause imaging problems. Migration methods desire a greater level of regularity than is often present in seismic surveys. There are two general approaches to deal with this problem. One approach is to treat the imaging problem as an inverse problem. The migration operator can be thought of as a linear transform from the recorded data to image space. Ronen and Liner (2000); Duquet and Marfurt (1999); Prucha et al. (2000) use the migration operator in a linear inverse problem to overcome irregular and limited data coverage. A regularized that encourages consistency over reflection angle is used to stabilize the inverse. These approaches have shown promise but are generally prohibitively expensive, and rely on an accurate subsurface velocity model.

Another approach is to try to regularize the data. AMO provides an effective regularization tool (Biondi et al., 1998) and is generally applied as an adjoint to create a more regularized volume. These regularized volumes still often contain in ‘acquisition footprint’ or more subtle amplitude effects. Chemingui (1999) used a log-stretch transform to make the AMO operator stationary in time. He then cast the regularization problem as a frequency-by-frequency inversion problem using a Kirchoff-style AMO operator. He showed that the acquisition footprint could be significantly reduced. The downside of this approach is the relatively high cost of Kirchoff implementation of AMO.

¹email: bob@sep.stanford.edu

Biondi and Vlad (2001) built on the work of Fomel (2001) and set up an inverse problem relating the irregular input data to a regular model space. They regularized the problem by enforcing consistency between the various $(t, \text{cmp}_x, \text{cmp}_y)$ cubes. The consistency took two forms. In the first, a simple difference between two adjacent in-line offset cubes was minimized. In the second, the difference was taken after transforming the cubes to the same offset AMO. Clapp (2005b) set up the data regularization with AMO as an inverse problem creating a full volume $(t, \text{cmp}_x, \text{cmp}_y, h_x, h_y)$.

In this paper, I modify the approach of Clapp (2005b) so that the model space is a common azimuth volume. I introduce an additional mapping operator that maps from the full $(t, \text{cmp}_x, \text{cmp}_y, h_x, h_y)$ to $h_y = 0$ using AMO. In addition, I show that the combination of limited h_y and consistent coverage as a function of h_x in marine surveys can still produce undesired amplitude variation as a function of cmp_y . To solve this problem, I introduce an additional regularization term that creates consistency as a function of cmp_y .

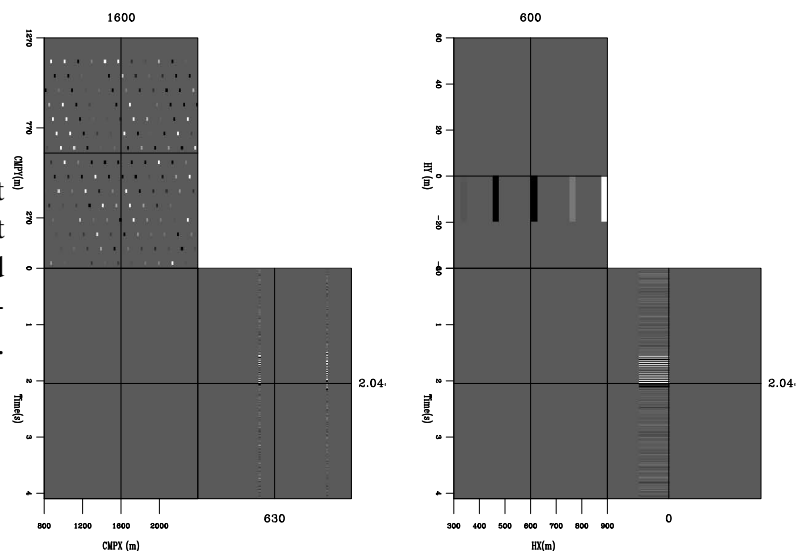
THEORY

Estimating a regularly sampled common-azimuth volume \mathbf{m} from our irregular input data \mathbf{d} can be set up as a least squares inversion problem. In this section, I will go over an approach to create a common azimuth volume by setting up an inverse problem. I will use a small synthetic to demonstrate the need for the various operators in the inversion process.

The data consists of irregular traces in a 5-D space $(t, \text{cmp}_x, \text{cmp}_y, h_x, h_y)$. The AMO operator acts on regularly sampled $(t, \text{cmp}_x, \text{cmp}_y)$ cubes, so we map from the irregular data space to the regular model space using a simple linear interpolation operator \mathbf{L} . Figure 1 shows two cube views from the five dimensional space the data is mapped into. Notice the sparseness of the data in these cubes. In standard marine acquisition, a single cross-line offset is acquired for each midpoint. The standard multi-streamer acquisition results in variation of the cross-line offset that is filled as we scan over cmp_y .

Figure 1: The location of the input traces for a simple synthetic. The left panel is a constant offset cube (fixed h_x and h_y). The right panel is a single midpoint (fixed cmp_x and cmp_y).

`bob1-interp` [CR,M]



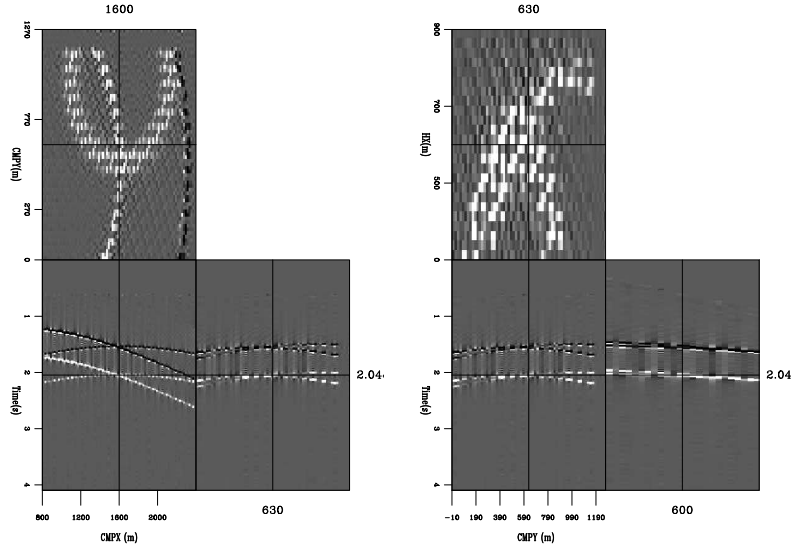


Figure 2: The result of applying \mathbf{Z} to the data shown in Figure 1. The left panel shows three slice from constant offset cube. The right panel shows three slice from a constant cmp_y cube.

`bob1-zero` [CR,M]

For common azimuth migration, we want all of our data to reside at $h_y = 0$. As a result, we need to use AMO to transform from the h_y that the data was recorded at to $h_y = 0$. The operator \mathbf{Z}' is a sum over the $(t, \text{cmp}_x, \text{cmp}_y)$ cubes that have been transformed to $h_y = 0$. Figure 2 shows two cube views of the result of applying \mathbf{Z}' to the small synthetic. In this case we still have significant holes along cmp_y . I will discuss why I created these holes later in the section.

Finally, we need to add in our regularization term. Generally, after NMO, our data should be smooth as a function of offset. We can think of adding a derivative operator along the offset axis. We can improve this estimate even further by applying a derivative on cubes that have been transformed to the same offset using $\text{AMO}^2 \mathbf{D}_h$. We can write our fitting goals as

$$\begin{aligned} \mathbf{d} &\approx \mathbf{LZm} \\ \mathbf{0} &\approx \epsilon \mathbf{D}_h \mathbf{m}, \end{aligned} \quad (1)$$

where ϵ controls the importance of consistency along the offset axis. We can speed up the convergence of this problem by preconditioning the model with the inverse of our regularization operator. In this case, we replace taking the derivative of AMO cubes with performing causal integration of AMO cubes \mathbf{C}_h . Our new fitting goals then become

$$\begin{aligned} \mathbf{d} &\approx \mathbf{LZC}_h \mathbf{p} \\ \mathbf{0} &\approx \epsilon \mathbf{p}, \end{aligned} \quad (2)$$

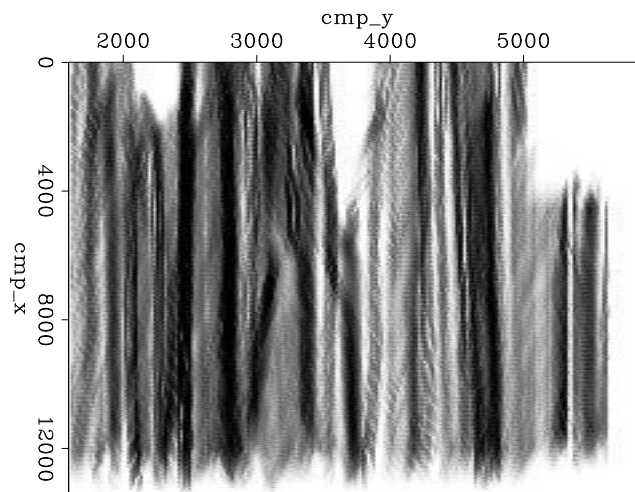
where $\mathbf{m} = \mathbf{C}_h \mathbf{p}$.

²In this case AMO simplifies to Dip Move-out because it is being applied simply along the h_x axis

Large holes

This set of fitting goals can run into problems when we deal with real marine geometry. To demonstrate the problem we will look at where data was recorded for a real 3-D marine survey. We can calculate where we have traces in the $h_x, \text{cmp}_x, \text{cmp}_y$ plane. If our acquisition lines are perfectly straight, we are able to acquire data throughout our survey. If our grid is perfectly oriented with acquisition geometry, we should have consistent fold in this cube. Figure 3 shows that this is far from the case. The figure shows the result of stacking over all offsets. Note that we have some areas where we don't have any data (white). If we use fitting goals (2) to estimate our model we run into a problem. The inversion result will show a dimming of amplitudes as we move away from our known data. Figure 5 shows the result of applying

Figure 3: Fold of a real marine dataset. Note how we have some regions with zero fold (white). `bob1-fold` [CR]



fitting goals (2) to our synthetic. Note how the amplitude declines markedly as we move away from locations where we have data. Even more problematic than dimming is when we see significant unrealistic, brightening of amplitudes for certain cmp_y . The brightening is caused by the fold pattern seen in Figure 4. The three panels represent the fold in the $(\text{cmp}_x, \text{cmp}_y)$ plane as we increase in offset from left to right. Note how we have fairly regular coverage at the near offsets and much more variable coverage as we move to larger offsets. This inconsistency is mainly caused by cable feathering. For some cmp_y we only have near offset traces. The near offset traces tend to be of higher amplitude and are more consistent as function of h (the tops of hyperbolas are insensitive to velocity errors). Our model covariance operator puts these unrealistically large amplitudes at all offsets, resulting in a striping of the amplitudes as a function of cmp_y .

Both of these problems are due to the lack of ‘mixing’ of information along the y direction. By mixing I mean that a column of the matrix implied by fitting goals (2) has very few non-zero elements at cmp_y 's different from the cmp_y associated with its corresponding model point. Our regularization is just DMO, which produces no mixing in the y direction. Our zeroing operator produces a limited amount of mixing, but the range is limited due to the small offset in the h_y direction inherent in marine surveys. As a result our inversion can have realistic kinematic but unrealistic amplitude behavior as a function of cmp_y . A simple solution to this problem is to introduce another operator to our model covariance description that tends to

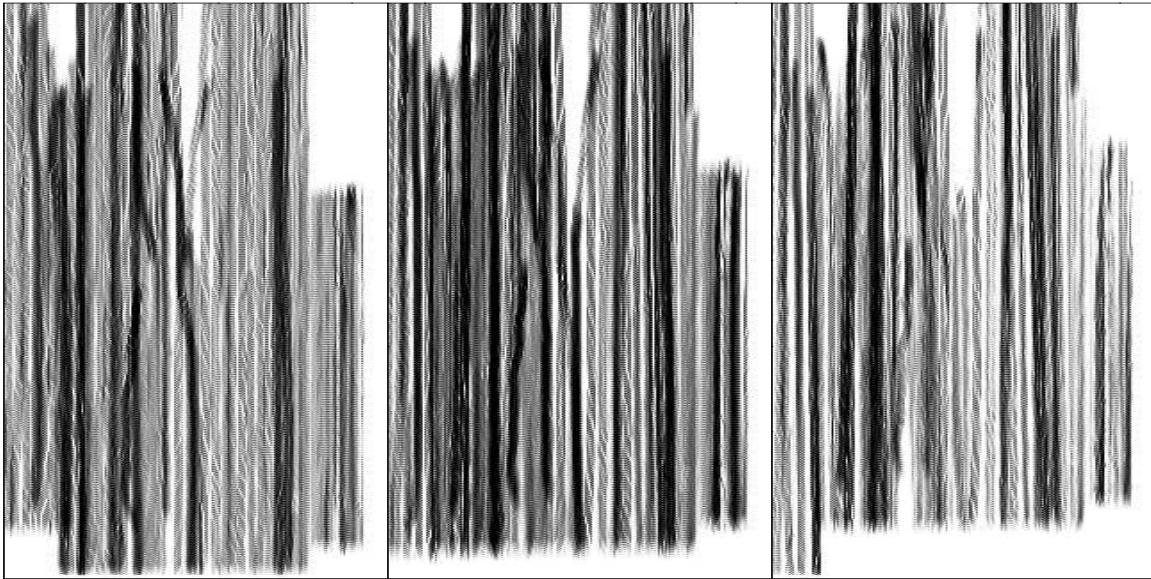


Figure 4: The three panels represent the fold in the (cmp_x, cmp_y) plane as we increase in offset from left to right. Note how we have fairly regular coverage at the near offsets and much more variable coverage as we move to larger offsets. For some cmp_y we only have near offset traces.

`bob1-fold-off` [CR]

produce consistency as a function of cmp_y . We must be careful to avoid introducing unrealistic smoothness in the cmp_y direction by our choice of preconditioners. I chose leaky integration along the cmp_y plane \mathbf{B}_y . The leaky integration will encourage the inversion to keep consistent amplitudes unless the data says otherwise. Using a relatively small leaky parameter and a very small ϵ should force it to have only an amplitude balancing effect rather than an effect on the kinematics of the solution.

Combining our two model preconditioners we get a new operator \mathbf{S} ,

$$\mathbf{S} = \mathbf{C}_h \mathbf{B}_y, \quad (3)$$

and a new set of fitting goals

$$\begin{aligned} \mathbf{d} &\approx \mathbf{LZSp} \\ \mathbf{0} &\approx \epsilon \mathbf{p}. \end{aligned} \quad (4)$$

Figure 6 shows the result of applying fitting goals (4) to the small synthetic. Note how the amplitude behavior is much more consistent than the result shown in Figure 5.

Fitting goals (4) should be avoided when possible. They introduce a smoothing along the cmp_y axis that is often unrealistic. Unfortunately when encountering large acquisition holes, some additional regularization is needed.

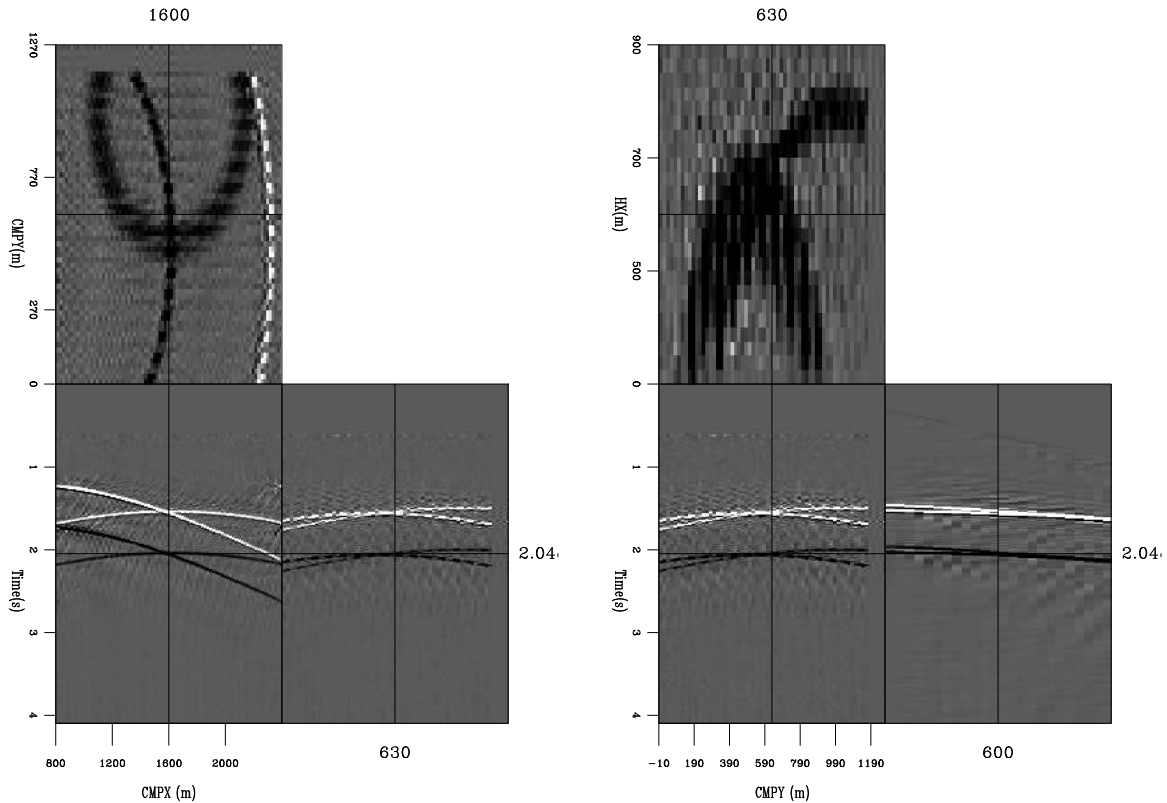


Figure 5: Two views of the result of applying fitting goals (2). The left panel is a three dimensional view at a fixed h_x . The right panel is a three dimensional view at a fixed cmp_x . Note the inconsistent, unrealistic amplitude behavior as a function of cmp_y . bob1-bad-syn [CR,M]

IMPLEMENTATION

A cost-effective implementation of fitting goals (2) or (4) is challenging. The obvious domain to parallelize the inversion is over frequency. In this case the model and data's time axis is log-stretched and transformed into the frequency domain. The resulting model and data space are approximately three times their time domain representation due to the oversampling necessitated by the log-stretch operation. In addition, both these volumes need to be transposed. To apply the log-stretch FFT operation, the natural ordering is for the time/frequency axis to be the inner axis while the inversion is more efficient with the time/frequency axis being the outer axis. An out-of-core transpose grows in cost with the square of the number of elements. For efficiency, I do a pre and post-step parallel transpose of the data in conjunction with the transformation to and from the log-stretched frequency domain. I split the data long the cmp_y axis. For the pre-step I log-stretch and FFT the input data, I then do an out-of-core transpose of this smaller volume. I then collect the transposed data. The post-step operation is simply the inverse, transpose and then FFT and unstretch.

A second major problem is the number of iterations necessary for convergence. The causal

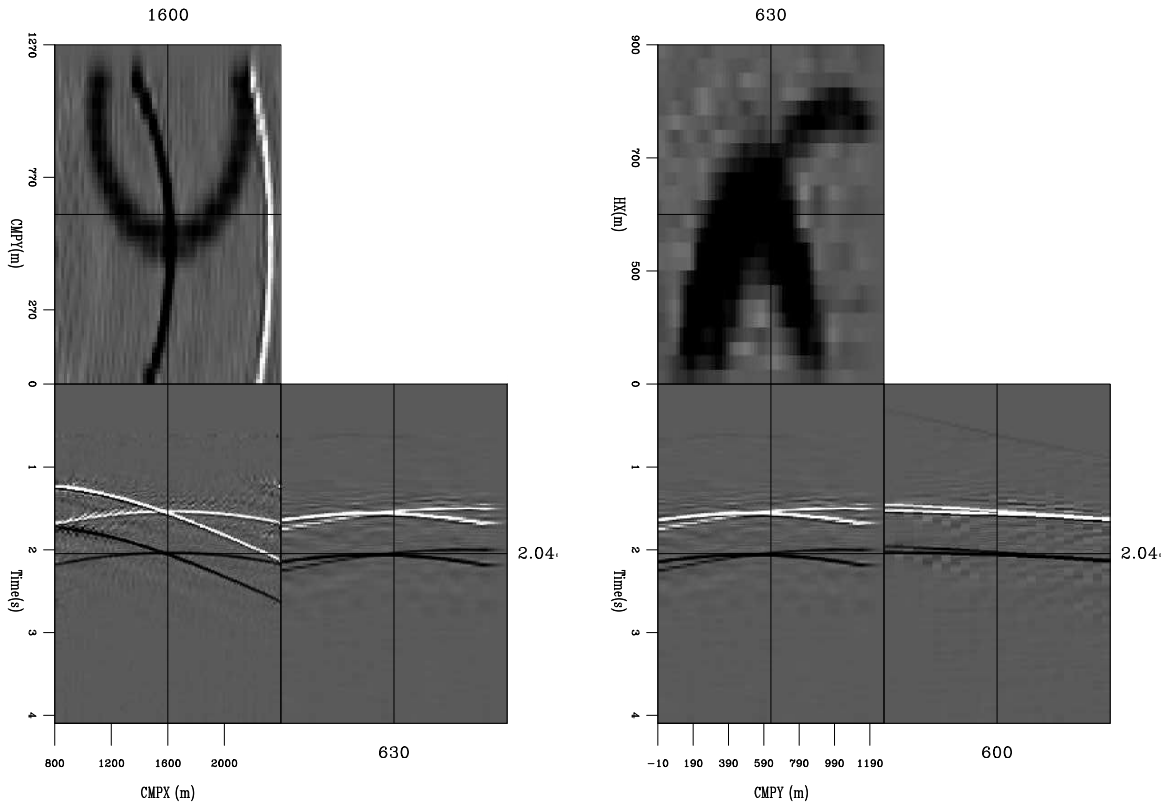


Figure 6: Two views of the result of applying fitting goals (4). The left panel is a three dimensional view at a fixed h_x . The right panel is a three dimensional view at a fixed cmp_x . Both views are identical the ones shown in Figure 5. Note how the unrealistic amplitude behavior seen in Figure 5 has been corrected. `bob1-inv-syn` [CR,M]

integration and leaky integration are good preconditioners (fast convergence) but the AMO portion tends to slow the inversion. As a result many (20-100 iterations) are desirable. The global inversion approach described in Clapp (2005b) is IO dominated. It also relies on hardware stability. Both of these factors make a frequency-by-frequency in-core inversion non-ideal but better choice. The major drawback to a frequency by frequency approach is that the frequencies might converge at significantly different rates resulting in an image that is unrealistically dominated by certain frequency ranges (most likely the low). To minimize this problem, I stopped the inversion after a set reduction in the data residual.

The final issue is the size of the problem. The domain of \mathbf{L} is four-dimensional and can be quite large even for a relatively small model space. In addition, for a conjugate gradient approach we still must keep three copies of our data space (data, data residual, previous step data residual) and five copies of our model space (gradient, model, previous step, previous step model residual, model residual). As a result, we need a machine with significant memory and/or break the problem into patches in the (cmp_x, cmp_y) plane.

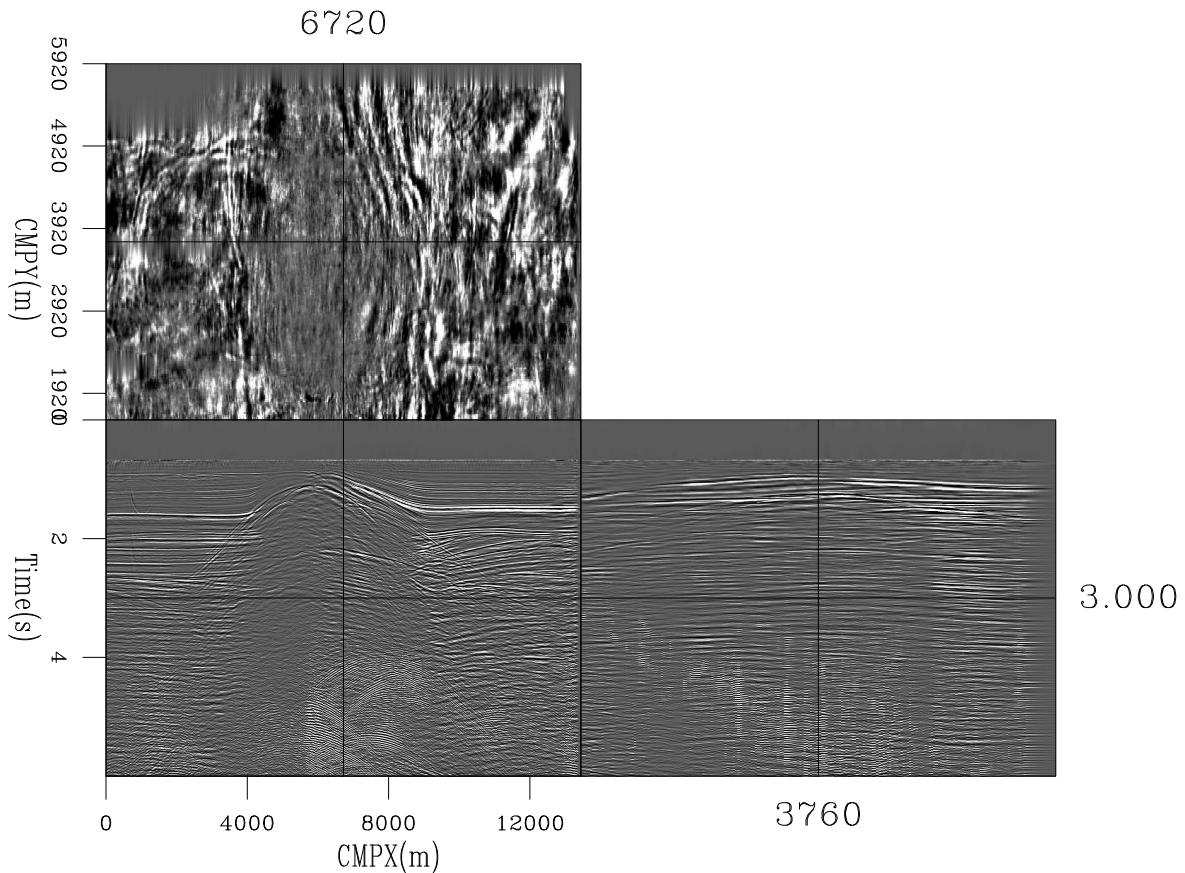


Figure 7: A constant offset section from a real 3-D marine dataset obtained by applying fitting goals (4). Note the absence of an acquisition footprint. `bob1-const-off` [CR]

REAL DATA EXAMPLE

I tested the methodology on a real 3-D marine dataset from the North Sea. Figures 3 and 4 are from this dataset. Previous uses of AMO and common azimuth migration have resulted in noticeable acquisition footprint in the first 1000 meters (Biondi, 1999; Vaillant and Sava, 1999). For the test I used a maximum of 40 iterations, with a maximum reduction in residual of 35%. A large reduction would be preferable but many frequencies did not reduce by even 20% after 40 iterations. Figure 7 shows a constant offset section after regularization with fitting goals (4). Note the absence of an acquisition footprint. Further, note how we have successfully filled even the large hole visible in the fold map of Figure 3.

I then applied common azimuth migration to the data. Figure 8 show three slices from the zero-offset migration cube. Pay particular attention to the depth slice. Note how the acquisition footprint has disappeared.

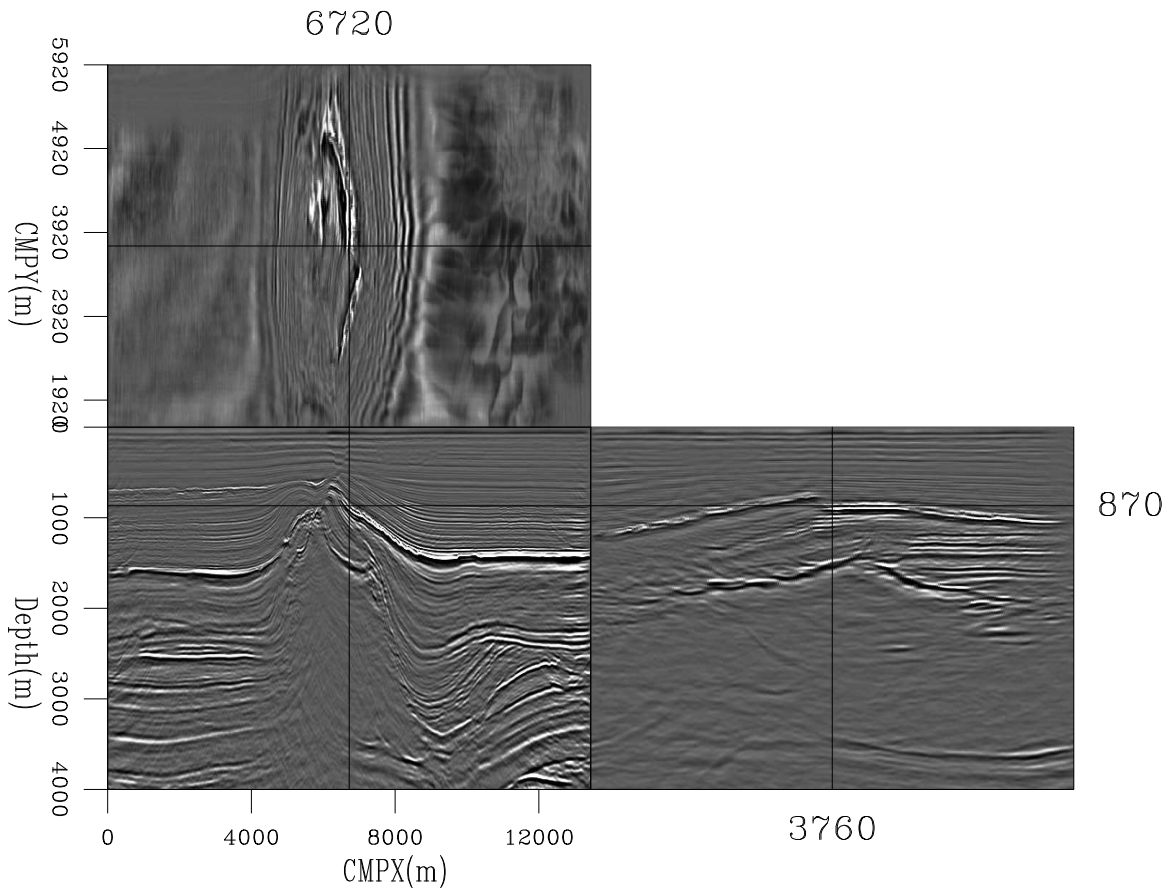


Figure 8: The result of migrating the data show in Figure 7. Note that virtually no acquisition footprint is visible in the data. `bob1-mig` [CR]

FUTURE WORK

The decay in the residual varies significantly as a function of frequency. At most frequencies the residual decreases only 40% between the first and 40th iteration. It appears that the large values in the residual are dominated by events at the cusp of the mute zone. Clapp (2005a) faced similar problems when inverting for an image using migration as her linear operator. Introducing a weight function in the frequency domain has the potential to speed up the inversion of both problems.

CONCLUSION

An inversion method to produce a dataset appropriate for common azimuth migration is introduced. The inversion problem uses AMO to both map the data to a constant $h_y = 0$ and as part of regularization operator to assure consistency between (cmp_x, cmp_y, hx) cubes.

ACKNOWLEDGMENTS

I would like to thank TotalFinaElf for providing the data used in this paper.

REFERENCES

- Biondi, B., and Vlad, I., 2001, Amplitude preserving prestack imaging of irregularly sampled 3-D data: *SEP-110*, 1–18.
- Biondi, B., Fomel, S., and Chemingui, N., 1998, Azimuth moveout for 3-D prestack imaging: *Geophysics*, **63**, no. 2, 574–588.
- Biondi, B. L., 1999, 3-D Seismic imaging: Stanford Exploration Project.
- Chemingui, N., 1999, Imaging irregularly sampled 3D prestacked data: *SEP-101*.
- Clapp, M. L., 2005a, Imaging under salt: illumination compensation by regularized inversion: Ph.D. thesis, Stanford University.
- Clapp, R. G., 2005b, Data regularization: Inversion with azimuth move-out: *SEP-120*, 187–196.
- Duquet, B., and Marfurt, K. J., 1999, Filtering coherent noise during prestack depth migration: *Geophysics*, **64**, no. 4, 1054–1066.
- Fomel, S., 2001, Three-dimensional seismic data regularization: Ph.D. thesis, Stanford University.
- Prucha, M. L., Clapp, R. G., and Biondi, B., 2000, Seismic image regularization in the reflection angle domain: *SEP-103*, 109–119.
- Ronen, S., and Liner, C. L., 2000, Least-squares DMO and migration: *Geophysics*, **65**, no. 5, 1364–1371.
- Vaillant, L., and Sava, P., 1999, Common-azimuth migration of a North Sea dataset: *SEP-102*, 1–14.

Iterative linearized migration and inversion

Huazhong Wang¹

ABSTRACT

The objective of seismic imaging is to obtain an image of the subsurface reflectors, which is very important for estimating whether a reservoir is beneficial for oil/gas exploration or not. It can also provide the relative changes or absolute values of three elastic parameters: compressional wave velocity V_p , shear wave velocity V_s , and density ρ . Two ways can achieve the objectives. In approach I, the angle reflectivity is given by prestack depth/time migration or linearized inversion, and the relative changes of the three elastic parameters are estimated from the angle reflectivity by AVO/AVA inversion. In, approach II, the relative changes (by linearized inversion) or absolute values (by nonlinear waveform inversion) are obtained directly. I compare non-iterative linearized migration/inversion imaging, iterative linearized migration/inversion imaging, and non-linear waveform inversion. All of these imaging methods can be considered as back-projection and back-scattering imaging. From backscattering imaging, we know that seismic wave illumination has a key influence on so-called true-amplitude imaging, and I give an analysis for the possibility of relative true-amplitude imaging. I also analyze the factors that affect the imaging quality. Finally, I point out that the Born approximation is not a good approximation for linearized migration/inversion imaging, and that the De Wolf approximation is a better choice.

INTRODUCTION

The main objective of migration imaging is to generate an image of the reflectors, that is, to position reflection points and scattering points at their true subsurface locations. The methodology is to downward continue the observed wavefield to the reflection points or scattering points using a known macro-velocity model with appropriate propagators, and to pick out the focused wavefield with an imaging condition. The focused wavefield displays the image of reflectors or scatterers. Therefore, I give the definition for migration imaging: **Based on some assumptions about the geological medium and with the help of mathematical models, the observed seismic wavefield is extrapolated to the subsurface reflectors using a macro-velocity model with a propagator, and the imaging amplitudes are extracted with an imaging condition.** Generally, the geological medium is assumed to be an acoustic medium, and the mathematical model is either the one-way wave equation or the Kirchhoff integral operator. However, migration imaging has not completely satisfied the needs of oil and gas exploration, since many reservoirs found recently are controlled not only by their

¹email: wang@sep.stanford.edu

geological structures but also by their lithology. Therefore, the lithological parameters are increasingly important to oil and gas exploration. Lithological parameter estimation is typically an inverse problem. In essence, migration imaging is an inverse problem, and it is also ill-posed. However, migration imaging is changed into an apparently well-posed problem by splitting it into two processes: wavefield extrapolation and macro-velocity analysis. The main objective of inversion imaging is to estimate lithological parameters or their disturbances, including reflectivity, P-wave velocity, S-wave velocity, and the density. There are linearized and non-linear inversions. The basis of linearized inversion is to linearize the formula characterizing the scattering wavefield with the Born approximation. The Born approximation is a "physical" approximation, with which only the primaries are modeled. The analytical (for constant background) or formal (for variable background) inversion formulas can be derived from the linearized forward-modeling formulas. This is a non-iterative linearized inversion. Based on least-squares theory, an iterative linearized inversion approach can be derived from linearized forward modeling. For the non-linear waveform inversion, only the wave propagator is linearized at a point in the model space. With the propagator, all of the wave phenomena are characterized. We call this linearization as a "mathematical" approximation, with which both primaries and multiples are simulated. This is the main difference between the two inversion approaches. Theoretically, the non-linear inversion (Tarantola, 1984; Mora, 1987) is superior to the linearized inversion (Bleistein et al., 1987; Bleistein, 1987). In practice, it is very difficult to recover all wavenumber components of the lithological parameters, since the seismic data is frequency-band-limited and aperture-limited and polluted with non-Gaussian noise. Therefore, the linearized migration/inversion is becoming more and more important, especially the iterative linearized migration/inversion approach. Stolt and Weglein (1985) discussed the relation between the migration and the linearized inversion. Gray (1997) gave a comparison of three different examples of true-amplitude imaging. So-called true-amplitude imaging tries to recover the reflectivity of the reflectors.

In this paper, I compare non-iterative linearized migration/inversion imaging, iterative linearized migration/inversion imaging, and nonlinear waveform inversion. All of these imaging methods can be considered as back-projection and backscattering imaging. From backscattering imaging, we know that seismic wave illumination has a key influence on so-called true-amplitude imaging, and I give an analysis for the possibility of relative true-amplitude imaging. I also analyze the factors which affect the image quality. Finally, I point out that the Born approximation is not a good approximation for linearized migration/inversion imaging, and that the De Wolf approximation is a better choice.

WAVE PROPAGATOR AND ITS LINEARIZATION

[1] Acoustic wave equation

Based on inverse theory, the characterization of seismic wave propagation is important for parameter estimation. Here I use the acoustic wave equation with two elastic parameters — bulk modulus and density — to model seismic wave propagation in a geological medium,

though we know that this is a simplification.

$$LP \equiv \left(\nabla \cdot \frac{1}{\rho(\vec{x})} \nabla + \frac{\omega^2}{\kappa(\vec{x})} \right) P(\vec{x}, \vec{x}_s, \omega) = \delta(\vec{x} - \vec{x}_s) S(\omega), \quad (1)$$

where κ is the bulk modulus and ρ is the density. Both parameters vary horizontally as well as vertically. $P(\vec{x}, \vec{x}_s, \omega)$ is the acoustic pressure wave field, and $S(\omega)$ is the monochromatic source function. We can carry out the full waveform inversion with equation (1). Tarantola (1984) gave a detailed theoretical framework. Pratt and Hicks (1998) discussed in detail how to implement seismic waveform inversion in the frequency domain. Now I introduce a background model which is so close to the true model that we can neglect the second and higher-order reflection and transmission effects caused by the interaction between the incident wave and the scattering potential. The background wavefield obeys the following equation:

$$L_0 P \equiv \left(\nabla \cdot \frac{1}{\rho_0} \nabla + \frac{\omega^2}{\kappa_0} \right) P(\vec{x}, \vec{x}_s, \omega) = \delta(\vec{x} - \vec{x}_s) S(\omega). \quad (2)$$

With the definition $V = L - L_0$, the identity $A = B + B(B^{-1} - A^{-1})A$ becomes

$$G = G_0 + G_0 V G, \quad (3)$$

if we associate G with A and G_0 with B . And equation (3) is further rearranged to

$$G = (I - G_0 V)^{-1} G_0. \quad (4)$$

Performing a Taylor expansion on the right term of equation (4) yields

$$G = \left[\sum_{j=0}^{\infty} (G_0 V)^j \right] G_0. \quad (5)$$

Equation (3) is called the Lippmann-Schwinger equation (Clayton and Stolt, 1981). Clearly, if $j \geq 2$, equation (5) depicts second and higher-order scattering terms of wave propagation, which are neglected. The linearized propagator characterizes only the first scattering of wave propagation. That is,

$$G = G_0 + G_0 V G_0. \quad (6)$$

This is the Born approximation, the physical meaning of which is clearly demonstrated by equations (5) and (6). From $L = -\left(\nabla \cdot \frac{1}{\rho} \nabla + \frac{\omega^2}{\kappa}\right)$ and $L_0 = -\left(\nabla \cdot \frac{1}{\rho_0} \nabla + \frac{\omega^2}{\kappa_0}\right)$, the scattering potential V is defined as follows:

$$\begin{aligned} V &= \left(\nabla \cdot \frac{1}{\rho} \nabla + \frac{\omega^2}{\kappa} \right) - \left(\nabla \cdot \frac{1}{\rho_0} \nabla + \frac{\omega^2}{\kappa_0} \right) \\ &= \nabla \cdot \left(\frac{1}{\rho} - \frac{1}{\rho_0} \right) \nabla + \omega^2 \left(\frac{1}{\kappa} - \frac{1}{\kappa_0} \right) \\ &= \nabla \cdot \frac{1}{\rho_0} \left(\frac{\rho_0}{\rho} - 1 \right) \nabla + \omega^2 \frac{1}{\kappa_0} \left(\frac{\kappa_0}{\kappa} - 1 \right) \\ &= \nabla \cdot \frac{a_1}{\rho_0} \nabla + \omega^2 \frac{a_2}{\kappa_0} \end{aligned} \quad (7)$$

where $a_1 = \frac{\rho_0}{\rho} - 1 = \frac{\Delta\rho}{\rho}$ and $\Delta\rho = \rho_0 - \rho$; $a_2 = \frac{\kappa_0}{\kappa} - 1 = \frac{\Delta\kappa_0}{\kappa}$ and $\Delta\kappa = \kappa_0 - \kappa$. Therefore the linearized synthetic wave field is composed of two parts: one is the background wave field described by the background Green's function; the other is the scattering wavefield caused by the scattering potential V . According to equation (3), the total wave field is written as

$$P(\vec{x}_r, \vec{x}_s, \omega) = G_0(\vec{x}_r, \vec{x}_s, \omega) + \omega^2 \int d^3x G_0(\vec{x}_r, \vec{x}, \omega) V(\vec{x}) P(\vec{x}, \vec{x}_s, \omega), \quad (8)$$

and the scattering wavefield after the Born approximation from equation (6) is

$$P_s(\vec{x}_r, \vec{x}_s, \omega) = \omega^2 \int d^3x G_0(\vec{x}_r, \vec{x}, \omega) V(\vec{x}) G_0(\vec{x}, \vec{x}_s, \omega). \quad (9)$$

[2] Scalar wave equation

In seismic wave imaging, the scalar wave equation is much more commonly used. Given the Fourier transform of the scalar wave equation for a point source,

$$LP(\vec{x}, \vec{x}_s, \omega) = \left(\nabla^2 + \frac{\omega^2}{v^2(\vec{x})} \right) P(\vec{x}, \vec{x}_s, \omega) = -\delta(\vec{x} - \vec{x}_s) S(\omega). \quad (10)$$

Equation (10) is a Helmholtz equation. Here $P(\vec{x}, \vec{x}_s, \omega)$ is a total pressure field, $v(\vec{x})$ is the variable acoustic velocity, the density is assumed to be constant, and $S(\omega)$ is a source function. Taking an initial estimation of the medium velocity, $v(\vec{x})$, as the background velocity $v_0(\vec{x})$, $v(\vec{x})$ can be split into the known and unknown parts by the following:

$$\frac{1}{v^2(\vec{x})} = \frac{1}{v_0^2(\vec{x})} (1 + a(\vec{x})), \quad (11)$$

where the background velocity $v_0(\vec{x})$ need not be constant. The variable $a(\vec{x})$ is the unknown velocity perturbation to be determined from the data, which is called the scattering potential of the medium, since it is a measure of the scattering strength at points where the actual medium differs from the background medium. Substituting equation (11) into equation (10) yields

$$LP(\vec{x}, \vec{x}_s, \omega) = \left(\nabla^2 + \frac{\omega^2}{v_0^2(\vec{x})} \right) P(\vec{x}, \vec{x}_s, \omega) = -\delta(\vec{x} - \vec{x}_s) S(\omega) - \omega^2 a(\vec{x}) P(\vec{x}, \vec{x}_s, \omega). \quad (12)$$

For the background medium, the background Green's function satisfies the following equation:

$$L_0 G_0(\vec{x}, \vec{x}_s, \omega) = \left(\nabla^2 + \frac{\omega^2}{v_0^2(\vec{x})} \right) G_0(\vec{x}, \vec{x}_s, \omega) = -\delta(\vec{x} - \vec{x}_s). \quad (13)$$

Therefore, with the help of the Lippman-Schwinger equation of equation (3), the total pressure wave is

$$P(\vec{x}_r, \vec{x}_s, \omega) = G_0(\vec{x}_r, \vec{x}_s, \omega) + \omega^2 \int d^3x G_0(\vec{x}_r, \vec{x}, \omega) a(\vec{x}) P(\vec{x}, \vec{x}_s, \omega), \quad (14)$$

and the scattering wave field caused by the scattering potential $a(\vec{x})$ is

$$P_s(\vec{x}_r, \vec{x}_s, \omega) = \omega^2 \int d^3x G_0(\vec{x}_r, \vec{x}, \omega) a(\vec{x}) G_0(\vec{x}, \vec{x}_s, \omega). \tag{15}$$

Equations (9) and (15) create a link between the scattered wavefield and the scattering potentials. They are Fredholm integral equations of the first kind and are the bases of the linearized inversion. Given the observed scattered wavefield, the scattering potentials can be solved.

[3] The scattering potential and the reflectivity

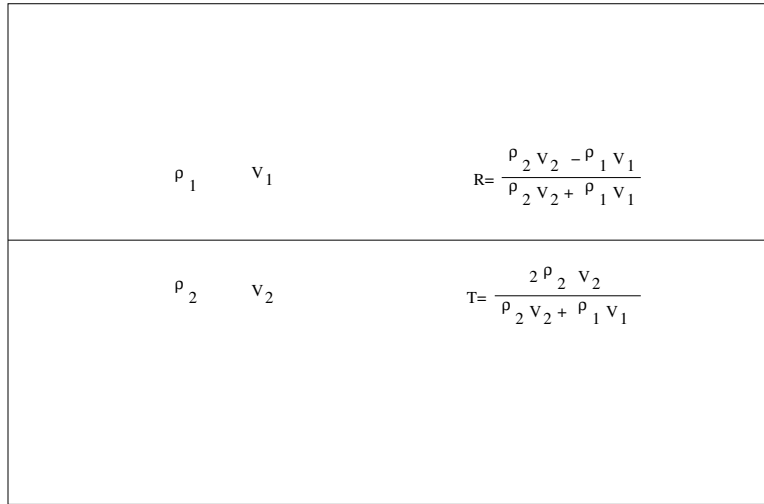


Figure 1: The acoustic wave reflectivity and the transmission of a planar reflector in the case of zero incident angle huazhong1-reflectivity [CR]

From Fig.1, and assuming that the density is constant, the normal reflectivity is defined as

$$RV_{\theta=0} = \frac{v_2 - v_1}{v_2 + v_1}, \tag{16}$$

and the transmission coefficient is

$$TV_{\theta=0} = \frac{2v_2}{v_2 + v_1}, \tag{17}$$

where θ is the incident angle. Therefore, defining the scattering potential as $1 + a(\vec{x}) = \left(\frac{v_0(\vec{x})}{v(\vec{x})}\right)^2$, equation (16) and (17) can be rewritten as

$$RV_{\theta=0} = \frac{1 - \sqrt{1 + a}}{1 + \sqrt{1 + a}}, \tag{18}$$

and

$$TV_{\theta=0} = \frac{2}{1 + \sqrt{1 + a}}, \tag{19}$$

respectively. If waves meet a reflector with a non-zero incident angle, the reflectivity and transmission coefficient are

$$R(\theta_1) = \frac{v_2 \cos \theta_1 - v_1 \cos \theta_2}{v_2 \cos \theta_1 + v_1 \cos \theta_2}, \quad (20)$$

and

$$T(\theta_1) = \frac{2v_2 \cos \theta_1}{v_2 \cos \theta_1 + v_1 \cos \theta_2}. \quad (21)$$

Similarly, they can be expressed with the scattering potential as

$$R(\theta_1) = \frac{\cos \theta_1 - \sqrt{1 + a \cos \theta_2}}{\cos \theta_1 + \sqrt{1 + a \cos \theta_2}}, \quad (22)$$

and

$$T(\theta_1) = \frac{2 \cos \theta_1}{\cos \theta_1 + \sqrt{1 + a \cos \theta_2}}, \quad (23)$$

respectively. The angle reflectivity has a close relation to the scattering potentials. Generally, the angle reflectivity is estimated by amplitude-preserved imaging, and lithological parameter disturbances are evaluated from them by AVO/AVA inversion.

ITERATIVE INVERSION IMAGING ALGORITHMS

[1] Operator linearization in non-linear inversion

A linear operator L depicts a physics process. It can be written as

$$L\mathbf{m} = \mathbf{d}, \quad (24)$$

where \mathbf{d} is the synthetic wavefield and \mathbf{m} is a medium model. The linear operator L can be seen as a function, which can be expanded into a Taylor series near a known model \mathbf{m}_0 as follows:

$$L\mathbf{m} = L\mathbf{m}_0 + \frac{\partial L}{\partial \mathbf{m}} \Delta \mathbf{m} + \frac{\partial^2 L}{\partial \mathbf{m}^2} (\Delta \mathbf{m})^2 + \dots + \frac{\partial^n L}{\partial \mathbf{m}^n} (\Delta \mathbf{m})^n + \dots \quad (25)$$

Omitting all the terms that are higher than second-order yields a linearized equation:

$$\frac{\partial L}{\partial \mathbf{m}} \Delta \mathbf{m} \approx L\mathbf{m} - L\mathbf{m}_0. \quad (26)$$

If $L\mathbf{m}$ stands for the observed data, and if $L\mathbf{m}_0$ synthesizes a wavefield with a known background model and a given operator, equation (26) can be rewritten as

$$\frac{\partial L}{\partial \mathbf{m}} \Delta \mathbf{m} \approx \mathbf{d}^{obs} - \mathbf{d}^{cal}. \quad (27)$$

Equation (27) can be regarded as a matrix equation, which may be ill-conditioned. The model disturbance can be solved by many linear algebraic algorithms. If the background model \mathbf{m}_0 is very close to the true model, the true model can be approached by some iterative algorithms. This idea is meaningful, but impractical. In fact, equation (27) can be simplified to

$$A\delta\mathbf{m} = \delta\mathbf{d}, \quad (28)$$

where $A = \partial L / \partial \mathbf{m}$ and $\delta\mathbf{d} = \mathbf{d}^{obs} - \mathbf{d}^{cal}$. Least-squares methods are then used to solve the inverse problem. Equations (9) and (15) can also be expressed in the form of equation (28). Comparing equation (28) with equations (9) and (15), it is clearly seen that the main difference between linearized inversion and non-linear waveform inversion consists in the forward modeling operator. The operator after Born approximation models only the primaries; however, the Fréchet derivative $A = \partial L / \partial \mathbf{m}$ models all the wave phenomena. The Born approximation should be replaced by the De Wolf approximation. The non-linear inversion incurs much higher calculation costs.

[2] L_2 norm or cost function definition

Based on least-squares theory, a minimizing problem can be defined, which aims to find $\delta\mathbf{m}^*$ in order to minimize the cost function. The L_2 norm or cost function definition is given by

$$f(\delta\mathbf{m}) = \|A\delta\mathbf{m} - \delta\mathbf{d}\|_2^2. \quad (29)$$

In order to constrain the inverse problem, or to use some prior information to bound the solution of the inverse problem, regularization is commonly used. In this case, the cost function needs to be modified.

[3] Iterative algorithms

Many algorithms can be chosen to solve the minimizing problem which is determined by the property of matrix A . The matrix A is hoped to be positive definite. Here only Newton's iterative algorithms are listed. **[A] Initial Newton's approach** Performing a Taylor expansion of $f(\delta\mathbf{m})$ near the point $\delta\mathbf{m}^{(k)}$ yields

$$\begin{aligned} f(\delta\mathbf{m}) &\approx \phi(\delta\mathbf{m}) \\ &= f(\delta\mathbf{m}^{(k)}) + \nabla f(\delta\mathbf{m}^{(k)}) (\delta\mathbf{m} - \delta\mathbf{m}^{(k)}) \\ &\quad + \frac{1}{2} (\delta\mathbf{m} - \delta\mathbf{m}^{(k)})^T \nabla^2 f(\delta\mathbf{m}^{(k)}) (\delta\mathbf{m} - \delta\mathbf{m}^{(k)}). \end{aligned} \quad (30)$$

Letting $\partial\phi(\delta\mathbf{m})/\partial\delta\mathbf{m} = 0$ yields $\nabla f(\delta\mathbf{m}^{(k)}) + \nabla^2 f(\delta\mathbf{m}^{(k)}) (\delta\mathbf{m} - \delta\mathbf{m}^{(k)}) = 0$. If the Hessian $\nabla^2 f(\delta\mathbf{m}^{(k)})$ is invertible, the Newton iterative algorithm is

$$\delta\mathbf{m}^{(k+1)} = \delta\mathbf{m}^{(k)} - [\nabla^2 f(\delta\mathbf{m}^{(k)})]^{-1} \nabla f(\delta\mathbf{m}^{(k)}). \quad (31)$$

Clearly, the simple Newton iterative algorithm lacks 1D searching. The Newton iterative algorithm with 1D searching is called the damping Newton algorithm. Algorithm procedure:

(a) Assign the initial model $\delta \mathbf{m}^{(1)}$ and the acceptable error $\varepsilon < 0$ and set the iterative number $k = 1$.

(b) Calculate $\nabla f(\delta \mathbf{m}^{(k)})$ and $[\nabla^2 f(\delta \mathbf{m}^{(k)})]^{-1}$.

(c) If $\|\nabla f(\delta \mathbf{m}^{(k)})\| \leq \varepsilon$, then stop iteration; otherwise, $\mathbf{d}^{(k)} = -[\nabla^2 f(\delta \mathbf{m}^{(k)})]^{-1} \nabla f(\delta \mathbf{m}^{(k)})$.

(d) Starting from $\delta \mathbf{m}^{(k)}$, carry out 1D searching along the searching direction $\mathbf{d}^{(k)}$ for $\lambda^{(k)}$ satisfying $f[(\delta \mathbf{m}^{(k)}) + \lambda \mathbf{d}^{(k)}] = \min \{f[(\delta \mathbf{m}^{(k)}) + \lambda \mathbf{d}^{(k)}]\}_{\lambda \geq 0}$.

(e) Letting $\delta \mathbf{m}^{(k+1)} = \delta \mathbf{m}^{(k)} + \lambda_k \mathbf{d}^{(k)}$ and $k := k + 1$, go to step (b). If the Hessian $\nabla^2 f(\delta \mathbf{m}^{(k)})$ is not positive definite, the Newton algorithm should be modified further. That means $\nabla^2 f(\delta \mathbf{m}^{(k)})$ is replaced with $\nabla^2 f(\delta \mathbf{m}^{(k)}) + \varepsilon_k I$. If the ε_k is chosen suitably, the matrix $\nabla^2 f(\delta \mathbf{m}^{(k)}) + \varepsilon_k I$ will be positive definite. **[B] Quasi-Newton algorithm:** The main feature of this algorithm is that the inverse of the Hessian matrix is not explicitly calculated. Further implementing the differential operation on both sides of equation (30) yields

$$\nabla f(\delta \mathbf{m}^{(k)}) \approx \nabla f(\delta \mathbf{m}^{(k+1)}) + \nabla^2 f(\delta \mathbf{m}^{(k+1)})(\delta \mathbf{m}^{(k)} - \delta \mathbf{m}^{(k+1)}), \quad (32)$$

and defining $\mathbf{p}^{(k)} = \delta \mathbf{m}^{(k)} - \delta \mathbf{m}^{(k+1)}$ and $\mathbf{q}^{(k)} = \nabla f(\delta \mathbf{m}^{(k+1)}) - \nabla f(\delta \mathbf{m}^{(k)})$ yields the Quasi-Newton condition,

$$\mathbf{p}^{(k)} = H_{k+1} \mathbf{q}^{(k)}, \quad (33)$$

where $H_{k+1} = [\nabla^2 f(\delta \mathbf{m}^{(k+1)})]^{-1}$. A series of formulas for calculating H_{k+1} is listed below: Formula 1: $H_{k+1} = H_k + \frac{(\mathbf{p}^{(k)} - H_k \mathbf{q}^{(k)})(\mathbf{p}^{(k)} - H_k \mathbf{q}^{(k)})^T}{(\mathbf{q}^{(k)})^T (\mathbf{p}^{(k)} - H_k \mathbf{q}^{(k)})}$. Formula 2: $H_{k+1}^{DFP} = H_k + \frac{\mathbf{p}^{(k)}(\mathbf{p}^{(k)})^T}{(\mathbf{p}^{(k)})^T \mathbf{q}^{(k)}} - \frac{(H_k \mathbf{q}^{(k)})(H_k \mathbf{q}^{(k)})^T}{(\mathbf{q}^{(k)})^T H_k \mathbf{q}^{(k)}}$, which is the DFP (Davidon-Fletcher-Powell) algorithm. Formula 3: $H_{k+1}^{BFGS} = H_k + \left(1 + \frac{(\mathbf{q}^{(k)})^T H_k \mathbf{q}^{(k)}}{(\mathbf{p}^{(k)})^T \mathbf{q}^{(k)}}\right) \frac{\mathbf{p}^{(k)}(\mathbf{p}^{(k)})^T}{(\mathbf{p}^{(k)})^T \mathbf{q}^{(k)}} - \frac{\mathbf{p}^{(k)}(\mathbf{q}^{(k)})^T H_k + H_k \mathbf{q}^{(k)}(\mathbf{p}^{(k)})^T}{(\mathbf{p}^{(k)})^T \mathbf{q}^{(k)}}$, which is the BFGS (Broyden-Fletcher-Goldfarb-Shanno) algorithm. Formula 4: $H_{k+1}^\phi = (1 - \phi) H_{k+1}^{DFP} + \phi H_{k+1}^{BFGS}$, where ϕ is an parameter. The algorithm procedure is as follows:

(a) Assign the initial model $\delta \mathbf{m}^{(1)}$ and the acceptable error $\varepsilon < 0$.

(b) Setting $H_1 = I_n$ and the iterative number $k = 1$, calculate $\mathbf{g}_1 = \nabla f(\delta \mathbf{m}^{(1)})$.

(c) Let $\mathbf{d}^{(k)} = -H_k \mathbf{g}_k$.

(d) Starting from $\delta \mathbf{m}^{(k)}$, carry out 1D searching along the searching direction $\mathbf{d}^{(k)}$ for $\lambda^{(k)}$ satisfying $f[(\delta \mathbf{m}^{(k)}) + \lambda \mathbf{d}^{(k)}] = \min \{f[(\delta \mathbf{m}^{(k)}) + \lambda \mathbf{d}^{(k)}]\}_{\lambda \geq 0}$.

(e) If $\|\nabla f(\delta \mathbf{m}^{(k)})\| \leq \varepsilon$, then stop iteration; otherwise, go to Step (f).

(f) If $k = n$, then let $\|\delta \mathbf{m}^{(1)} = \delta \mathbf{m}^{(k+1)}\|$, go to Step(b); Otherwise, go to Step (g).

(g) Letting $\mathbf{g}_{k+1} = \nabla f(\delta \mathbf{m}^{(k+1)})$, $\mathbf{p}^{(k)} = \delta \mathbf{m}^{(k)} - \delta \mathbf{m}^{(k+1)}$ and $\mathbf{q}^{(k)} = \nabla f(\delta \mathbf{m}^{(k+1)}) - \nabla f(\delta \mathbf{m}^{(k)})$, calculate H_{k+1} with any of Formula 1-4. Setting $k := k + 1$, go to Step (c).

COMPARISON AMONG MIGRATION/INVERSION METHODS

(A) Non-iterative linearized migration/inversion

(1) Wave equation prestack migration/inversion

Near the scattering point \vec{x} , we can define an error function or a norm as

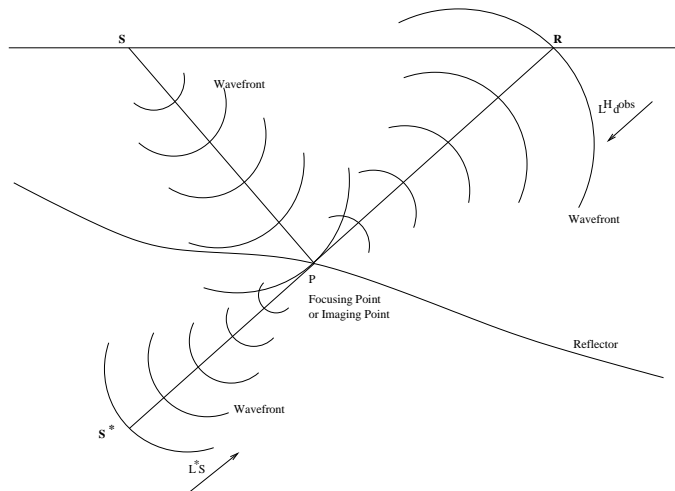
$$E(R(\vec{x})) = \sum_{\omega_{min}}^{\omega_{max}} (U_S(\vec{x}, \omega) - U_I(\vec{x}, \omega) R(\vec{x}))^2 d\omega, \quad (34)$$

where $R(\vec{x})$ is the reflectivity, $U_S(\vec{x}, \omega)$ is the upcoming wavefield, which is downward extrapolated to a reflector, and $U_I(\vec{x}, \omega)$ is the incident wavefield propagated to the reflector. At the scattering point \vec{x} , the scattering wavefield $U_S(\vec{x}, \omega)$ should be equal or close to the convolution between the incident wavefield $U_I(\vec{x}, \omega)$ and the reflectivity function. From equation (34), the imaging condition of the migration/inversion is as follows:

$$R(\vec{x}) = \frac{\sum_{\omega_{min}}^{\omega_{max}} U_S(\vec{x}, \omega) U_I^*(\vec{x}, \omega)}{\sum_{\omega_{min}}^{\omega_{max}} (U_I(\vec{x}, \omega) U_I^*(\vec{x}, \omega) + \varepsilon)}. \quad (35)$$

The term in the numerator is a correlation imaging for prestack migration. The term in the denominator expresses the illumination of the scattering points. Fig.2 geometrically explains the imaging condition, which says that the imaging occurs at the arrival time of the incident wave which equals the take-off time of the upcoming wave. In the frequency domain, the

Figure 2: The geometry explication of the cross-correlation imaging condition. S^* is a virtual source of the real source S . The propagator L^* is the conjugate of the downward propagator L . Therefore, both the propagator L^H and L^* collapse the wavefronts into a point—the imaging point P . huazhong1-Imaging_fig [CR]



extrapolated upcoming wavefield at the scattering point is

$$U_S(\vec{x}, \omega) = G^H(\vec{x}_r, \vec{x}, \omega) \mathbf{d}^{obs}(\vec{x}_r, \vec{x}_s, \omega), \quad (36)$$

and the incident wavefield at the same point is

$$U_I(\vec{x}, \omega) = G(\vec{x}, \vec{x}_s, \omega). \quad (37)$$

Substituting equations (36) and (37) into equation (35) and applying the WKBJ approximation to the Green's functions, we can rewrite equation (35) as follows:

$$\begin{aligned} R(\vec{x}) &= \frac{\sum_{\omega_{min}}^{\omega_{max}} G(\vec{x}, \vec{x}_s, \omega) G^H(\vec{x}_r, \vec{x}, \omega) \mathbf{d}^{obs}(\vec{x}_r, \vec{x}_s, \omega)}{\sum_{\omega_{min}}^{\omega_{max}} [G(\vec{x}, \vec{x}_s, \omega) (G(\vec{x}, \vec{x}_s, \omega))^* + \varepsilon]} \\ &= \frac{\sum_{\omega_{min}}^{\omega_{max}} A(\vec{x}, \vec{x}_s, \omega) e^{i\omega\tau(\vec{x}, \vec{x}_s, \omega)} A(\vec{x}_r, \vec{x}, \omega) e^{i\omega\tau(\vec{x}_r, \vec{x}, \omega)} \mathbf{d}^{obs}(\vec{x}_r, \vec{x}_s, \omega)}{\sum_{\omega_{min}}^{\omega_{max}} V A(\vec{x}, \vec{x}_s, \omega) V^2} \\ &= \frac{\sum_{\omega_{min}}^{\omega_{max}} A(\vec{x}_r, \vec{x}, \vec{x}_s, \omega) e^{i\omega\tau(\vec{x}_r, \vec{x}, \vec{x}_s, \omega)} \mathbf{d}^{obs}(\vec{x}_r, \vec{x}_s, \omega)}{\sum_{\omega_{min}}^{\omega_{max}} V A(\vec{x}, \vec{x}_s, \omega) V^2}, \end{aligned} \quad (38)$$

where $A(\vec{x}_r, \vec{x}, \vec{x}_s, \omega) = A(\vec{x}, \vec{x}_s, \omega) A(\vec{x}_r, \vec{x}, \omega)$ and $\tau(\vec{x}_r, \vec{x}, \vec{x}_s, \omega) = \tau(\vec{x}, \vec{x}_s, \omega) + \tau(\vec{x}_r, \vec{x}, \omega)$. From equation (38), it is clear that the seismic illumination plays a key role in migration/inversion imaging. The possibility of relative true-amplitude imaging will be discussed later.

(2) Wave theory tomography

(a) Fourier Diffraction Tomography for constant background Wu and Toksoz (1987) gave the plane-wave response in the direction \vec{r} from an incident wave \vec{i} :

$$P_S^{pl}(\vec{i}, \vec{r}) = -k^2 \tilde{O} \left[k(\vec{r} - \vec{i}) \right] \quad (39)$$

where $\tilde{O} \left[k(\vec{r} - \vec{i}) \right]$ is the 3D Fourier transform of the object function $O(\vec{r})$. $P_S^{pl}(\vec{i}, \vec{r})$ is some kind of projection. Comparing this to linear Radon transform, we know that the object function can be accurately restored if the angles of the plane waves continuously change around the object. Fig.3 shows the projection from the real plane wave source and from the virtual plane wave source.

(b) Inverse Generalized Radon Transform for variable background The scattered wavefield after Bron and WKBJ approximation is of the following form:

$$\begin{aligned} P_S(\vec{r}, \vec{s}, t) &= -\frac{\partial^2}{\partial t^2} \int_{\Omega} A(\vec{r}, \vec{x}, \vec{s}) \delta[t - \tau(\vec{r}, \vec{x}, \vec{s})] f(\vec{x}) d^3\vec{x} \\ &= -\int_{\Omega} A(\vec{r}, \vec{x}, \vec{s}) \delta''[t - \tau(\vec{r}, \vec{x}, \vec{s})] f(\vec{x}) d^3\vec{x}, \end{aligned} \quad (40)$$

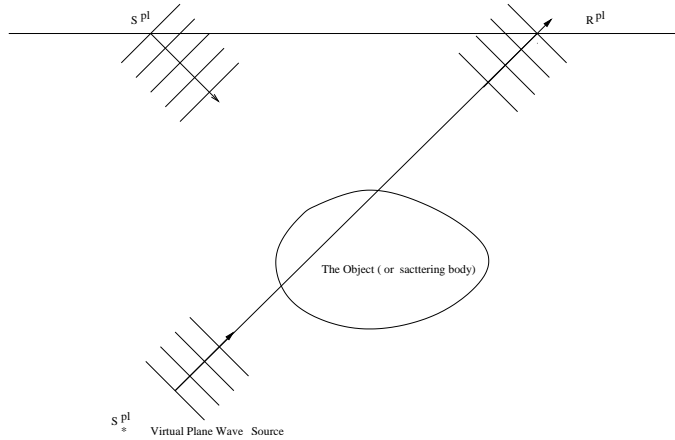


Figure 3: The geometry of plane wave propagation.
[huazhong1-planewave_tomography](#)
 [CR]

where $A(\vec{r}, \vec{x}, \vec{s}) = A(\vec{r}, \vec{x})A(\vec{x}, \vec{s})$ and $\tau(\vec{r}, \vec{x}, \vec{s}) = T(\vec{s}, \vec{x}) + T(\vec{r}, \vec{x})$. It is known that the diffraction-time surface $R_x = \{\mathbf{d} : t = T(\vec{s}, \vec{x}) + T(\vec{r}, \vec{x})\}$ in the data space is a counterpart of the isochron surface $I_d = \{\mathbf{x} : t = T(\vec{s}, \vec{x}) + T(\vec{r}, \vec{x})\}$ in the model space. These dual geometric associations naturally give rise to a corresponding pair of projection operators. Equation (40) can be written as

$$P_S(\mathbf{d}) = -\frac{\partial^2}{\partial t^2} \int_{I_d} A(\vec{r}, \vec{x}, \vec{s}) f(\mathbf{x}). \quad (41)$$

The diffraction curve in the data space is a projection of an isochron in the model space. This is a kind of Radon transform (Miller et al., 1987; Hubral et al., 1996). The standard Radon transform and inverse Radon transform in three dimensions are given by

$$f^\Delta(\vec{\xi}, p) = \int \delta(p - \vec{\xi} \cdot \vec{x}) f(\vec{x}) d^3 \vec{x} \quad (42)$$

and

$$f(\vec{x}_0) = -\frac{1}{8\pi^2} \int \left[\frac{\partial^2}{\partial p^2} f^\Delta(\vec{\xi}, p) V_{p=\vec{\xi} \cdot \vec{x}_0} \right] d^2 \xi \quad (43)$$

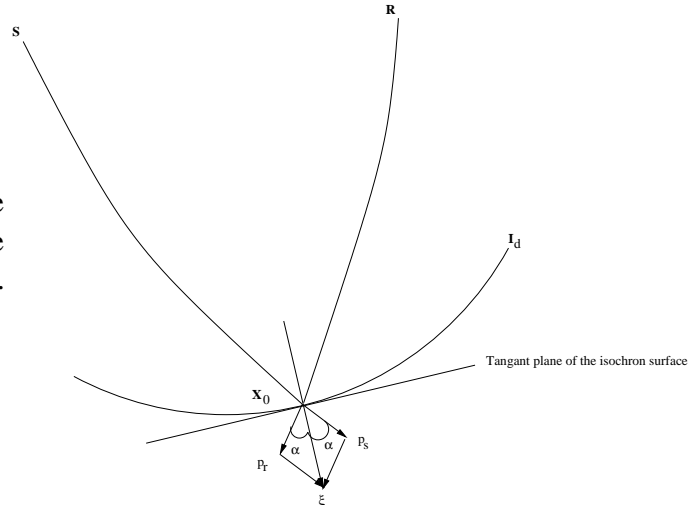
respectively, where p is the distance from the origin to a plane which cuts through the object body, ξ is the unity direction vector which is normal to the plane, and \vec{x} is a point on the plane. Comparing this with the classical Radon transform and its inverse, the final 3D inversion formula can be given as

$$f(\vec{x}_0) = \frac{1}{\pi^2} \int d^2 \xi(\vec{r}, \vec{x}_0, \vec{s}) \frac{V \cos^3 \alpha(\vec{r}, \vec{x}_0, \vec{s})}{v_0^3(\vec{x}_0) A(\vec{r}, \vec{x}_0, \vec{s})} P_S(\vec{r}, \vec{s}, t = \tau_0). \quad (44)$$

In equation (44), the angle variable $\xi(\vec{r}, \vec{x}_0, \vec{s})$ near the imaging point \vec{x}_0 is used, rather than the measurement configuration at the surface. Fig.4 illustrates this. The angle variable is related to the measurement configuration and reflects the seismic wave illumination aperture. Only if the aperture is large can a high resolution image be obtained. The relative true-amplitude imaging is severely affected by the angle variable. Bleistein and Stockwell (2001); Zhang (2004) gave some similar true-amplitude migration/inversion formulas.

Figure 4: The geometry between the incident and scattering rays near the scattering point, or imaging point \mathbf{x}_0 .

`huazhong1-GRT_fig` [CR]



(3) Least-squares migration/inversion

The conventional prestack migration can be characterized as

$$\delta \mathbf{m}_{mig} = A^H \delta \mathbf{d}, \quad (45)$$

where A^H is a conjugate transpose matrix, which is a back-propagator of the wavefield. The least-squares prestack migration/inversion imaging can be carried out by the following equation:

$$\delta \mathbf{m}_{inv} = (A^H A)^{-1} (A^H \delta \mathbf{d}) = H^{-1} (A^H \delta \mathbf{d}) = H^{-1} \delta \mathbf{m}_{mig}, \quad (46)$$

where $H = A^H A$ is a Hessian matrix. The meaning of the Hessian will be discussed in detail. Equation (46) says that the deconvolution of the conventional prestack migration by the inverse of the Hessian produces the migration/inversion results.

(B) Iterative linearized migration/inversion

We can define a minimizing problem that aims at finding δm^* by minimizing the following cost function:

$$f(\delta \mathbf{m}) = \|A \delta \mathbf{m} - \delta \mathbf{d}\|_2^2. \quad (47)$$

The Newton iterative algorithms can be used for solving the minimizing problem. The standard Newton iterative algorithm is

$$\delta \mathbf{m}^{(k+1)} = \delta \mathbf{m}^{(k)} - [\nabla^2 f(\delta \mathbf{m}^{(k)})]^{-1} \nabla f(\delta \mathbf{m}^{(k)}). \quad (48)$$

However, the inverse of the Hessian is difficult to calculate. The Quasi-Newton algorithms are used commonly. The inverse of the Hessian matrix can be calculated with the DFP formula:

$$H_{k+1}^{DFP} = H_k + \frac{\mathbf{p}^{(k)} (\mathbf{p}^{(k)})^T}{(\mathbf{p}^{(k)})^T \mathbf{q}^{(k)}} - \frac{(H_k \mathbf{q}^{(k)}) (H_k \mathbf{q}^{(k)})^T}{(\mathbf{q}^{(k)})^T H_k \mathbf{q}^{(k)}} \quad (49)$$

where $\mathbf{p}^{(k)} = \delta\mathbf{m}^k - \delta\mathbf{m}^{(k+1)}$, and $\mathbf{q}^{(k)} = \nabla f(\delta\mathbf{m}^{(k+1)}) - \nabla f(\delta\mathbf{m}^{(k)})$.

The Quasi-Newton iterative algorithm is

$$\delta\mathbf{m}^{(k+1)} = \delta\mathbf{m}^{(k)} - H_{k+1} \nabla f(\delta\mathbf{m}^{(k)}). \quad (50)$$

(C) Non-linear waveform inversion

The basic procedure for non-linear waveform inversion is similar to the linearized iterative migration/inversion. It is worth mentioning again that the Frechét derivative in the non-linear waveform inversion is quite different from the propagator after the Born approximation in the linearized migration/inversion.

ASPECTS OF LINEARIZED MIGRATION/INVERSION

[1] Numerical calculation of Green's function

The forward and backward propagations of the wavefield play a key role in the migration/inversion imaging. The Helmholtz equation is commonly used for depicting wave propagation in acoustic media. Based on it, I derive the formulas for traveltime and amplitude calculation corresponding to the main seismic wave energy. In spherical coordinates, the Helmholtz equation is of the following form:

$$\begin{aligned} \nabla^2 \tilde{U}(\theta, \varphi, r; \omega) &= \left\{ \frac{1}{r^2} \frac{\partial}{\partial r} \left(r^2 \frac{\partial}{\partial r} \right) + \frac{1}{r^2} \frac{\partial}{\partial \theta} \left(\sin \theta \frac{\partial}{\partial \theta} \right) + \frac{1}{r^2 \sin^2 \theta} \frac{\partial^2}{\partial \varphi^2} \right\} \tilde{U}(\theta, \varphi, r; \omega) \\ &= -\frac{\omega^2}{v^2} \tilde{U}(\theta, \varphi, r; \omega). \end{aligned} \quad (51)$$

Equation (51) can be rewritten as

$$\left(\frac{\partial}{\partial r} + \frac{1}{r} \right)^2 \tilde{U} + \left[\frac{1}{r^2 \sin^2 \theta} \sin \theta \frac{\partial}{\partial \theta} \left(\sin \theta \frac{\partial}{\partial \theta} \right) + \frac{1}{r^2 \sin^2 \theta} \frac{\partial^2}{\partial \varphi^2} \right] \tilde{U} = \left(-\frac{\omega^2}{v^2} + \frac{1}{r^2} \right) \tilde{U}(\theta, \varphi, r; \omega), \quad (52)$$

The outward one-way wave equation can be derived from equation (52) as follows:

$$\left(\frac{\partial}{\partial r} + \frac{1}{r} \right) \tilde{U}(\theta, \varphi, r; \omega) = i\sqrt{\alpha} \sqrt{1 + \frac{1}{r^2 \sin^2 \theta} \left[\sin \theta \frac{\partial}{\partial \theta} \left(\sin \theta \frac{\partial}{\partial \theta} \right) + \frac{1}{r^2 \sin^2 \theta} \frac{\partial^2}{\partial \varphi^2} \right]} \tilde{U}(\theta, \varphi, r; \omega), \quad (53)$$

where α is defined as $\alpha = -\frac{\omega^2}{v^2} + \frac{1}{r^2}$. Equation (53) can be expanded as

$$\left(\frac{\partial}{\partial r} + \frac{1}{r} \right) \tilde{U}(\theta, \varphi, r; \omega) = i\sqrt{\alpha} \tilde{U}(\theta, \varphi, r; \omega) + \frac{\frac{ia}{\sqrt{\alpha r^2 \sin^2 \theta}} \left[\sin \theta \frac{\partial}{\partial \theta} \left(\sin \theta \frac{\partial}{\partial \theta} \right) + \frac{\partial^2}{\partial \varphi^2} \right]}{1 + \frac{b}{\alpha r^2 \sin^2 \theta} \left[\sin \theta \frac{\partial}{\partial \theta} \left(\sin \theta \frac{\partial}{\partial \theta} \right) + \frac{\partial^2}{\partial \varphi^2} \right]} \tilde{U}(\theta, \varphi, r; \omega), \quad (54)$$

where a and b are the optimal coefficients. Then, equation (54) is split into two equations:

$$\frac{\partial}{\partial r} \tilde{U}(\theta, \varphi, r; \omega) = \left(-\frac{1}{r} + i\sqrt{\alpha} \right) \tilde{U}(\theta, \varphi, r; \omega), \quad (55)$$

$$\begin{aligned} & \left\{ 1 + \frac{b}{\alpha r^2 \sin^2 \theta} \left[\sin \theta \frac{\partial}{\partial \theta} \left(\sin \theta \frac{\partial}{\partial \theta} \right) + \frac{\partial^2}{\partial \varphi^2} \right] \right\} \frac{\partial}{\partial r} \tilde{U}(\theta, \varphi, r; \omega) \\ & = \frac{ia}{\sqrt{\alpha} r^2 \sin^2 \theta} \left[\sin \theta \frac{\partial}{\partial \theta} \left(\sin \theta \frac{\partial}{\partial \theta} \right) + \frac{\partial^2}{\partial \varphi^2} \right] \tilde{U}(\theta, \varphi, r; \omega). \end{aligned} \quad (56)$$

Obviously, equation (55) can be solved analytically, and equation (56) can be solved by finite-differences. The finite-difference scheme can be written in the following form:

$$[I - (\alpha_\theta - i\beta_\theta) T_\theta] [I - (\alpha_\varphi - i\beta_\varphi) T_\varphi] \tilde{U}_{i,j}^n = [I - (\alpha_\theta + i\beta_\theta) T_\theta] [I - (\alpha_\varphi + i\beta_\varphi) T_\varphi] \tilde{U}_{i,j}^n, \quad (57)$$

where $\tilde{U}_{i,j}^n = U(i\Delta\theta, j\Delta\varphi, n\Delta r)$, $\alpha_\theta = \frac{b}{r^2 \alpha \Delta\theta^2}$, $\alpha_\varphi = \frac{b}{r^2 \alpha \Delta\varphi^2}$, $\beta_\theta = \frac{a\Delta r}{2\sqrt{\alpha} r^2 \Delta\theta^2}$ and $\beta_\varphi = \frac{a\Delta r}{2\sqrt{\alpha} r^2 \Delta\varphi^2}$. The one-way wave extrapolation in the spherical coordinate system can be implemented by solving equation (55) and (57) in the frequency-space domain. The traveltimes and amplitudes corresponding to the maximum energy can be picked out in the frequency domain or time domain. With the picked traveltimes and amplitudes, we carried out a 3D integral prestack depth migration which gave a high-quality imaging result (Huazhong, 2003). This demonstrates that the method can be used for constructing the Green's functions in the migration/inversion imaging.

[2] The matrix expression of linearized migration/inversion

The linearized migration/inversion can be formulated from the integral expressed in equation (15). It can be regarded as an inverse generalized Radon transform. Equation (15) can be expressed as a matrix equation. The process for solving the equation set is just the migration/inversion imaging. Following Berkhout (1997), we first give a matrix expression of wave propagation from a source to a scatterer and then to a receiver:

$$W^U R(\theta) W^D = \begin{bmatrix} g_{11}^U & g_{12}^U & \cdots & g_{1P}^U \\ g_{21}^U & g_{22}^U & \cdots & g_{2P}^U \\ \cdots & \cdots & \cdots & \cdots \\ g_{M1}^U & g_{M2}^U & \cdots & g_{MP}^U \end{bmatrix} \begin{bmatrix} r_{11} & r_{12} & \cdots & r_{1Q} \\ r_{21} & r_{22} & \cdots & r_{2Q} \\ \cdots & \cdots & \cdots & \cdots \\ r_{P1} & r_{P2} & \cdots & r_{PQ} \end{bmatrix} \begin{bmatrix} g_{11}^D & g_{12}^D & \cdots & g_{1N}^D \\ g_{21}^D & g_{22}^D & \cdots & g_{2N}^D \\ \cdots & \cdots & \cdots & \cdots \\ g_{Q1}^D & g_{Q2}^D & \cdots & g_{QN}^D \end{bmatrix}, \quad (58)$$

where W^U is a discretized Green's function for upward wave propagation, W^D is a discretized Green's function for downward wave propagation, and $R(\theta)$ is a reflectivity matrix, which is related to the incident angle. If the variation of reflectivity with angle is neglected, $R(\theta)$ becomes a diagonal matrix. The reflectivity in this case is assumed to be the normal reflectivity. In practice, the reflectivity of a reflector varies with the incident angle. This is called

an AVO/AVA phenomenon in seismology. The prestack migration/inversion aims at estimating the angle reflectivity to evaluate lithological variations. On the other hand, the residual moveout of the angle reflectivity indicates whether the macro migration/inversion velocity is reasonable or not. The synthetic wave field can be written as follows:

$$P(\vec{x}_r, \vec{x}_s, \omega) = \sum_{i_z=Z_1}^{Z_N} W^U R(\theta) W^D V_{i_z} = \sum_{i_z=Z_1}^{Z_N} \left[\begin{array}{ccc} (g^U r g^D)_{11} & (g^U r g^D)_{12} & \cdots & (g^U r g^D)_{1N} \\ (g^U r g^D)_{21} & (g^U r g^D)_{22} & \cdots & (g^U r g^D)_{2N} \\ \cdots & \cdots & \cdots & \cdots \\ (g^U r g^D)_{M1} & (g^U r g^D)_{M2} & \cdots & (g^U r g^D)_{MN} \end{array} \right]_{i_z}. \quad (59)$$

In equation (59), each element of the matrix P is a recorded seismic trace in the time domain and a recorded amplitude value for a shot-receiver pair in the frequency domain. Each column is a shot gather, and each row is a common receiver gather. Therefore, equation (59) can be regarded as the matrix expression of equation (15). The classical prestack migration can be formulated as the following:

$$[W^U(z_0, z_1)]^H P(\vec{x}_r, \vec{x}_s, z_0, \omega) [W^D(z_1, z_0)]^H = R(z_1). \quad (60)$$

The detailed matrix expression of equation (60) is

$$\begin{aligned} & \left[\begin{array}{ccc} \tilde{g}_{11}^U & \tilde{g}_{21}^U & \cdots & \tilde{g}_{M1}^U \\ \tilde{g}_{12}^U & \tilde{g}_{22}^U & \cdots & \tilde{g}_{M2}^U \\ \cdots & \cdots & \cdots & \cdots \\ \tilde{g}_{1P}^U & \tilde{g}_{2P}^U & \cdots & \tilde{g}_{MP}^U \end{array} \right] \left[\begin{array}{ccc} P_{11}^{rs} & P_{12}^{rs} & \cdots & P_{1N}^{rs} \\ P_{21}^{rs} & P_{22}^{rs} & \cdots & P_{2N}^{rs} \\ \cdots & \cdots & \cdots & \cdots \\ P_{M1}^{rs} & P_{M2}^{rs} & \cdots & P_{MN}^{rs} \end{array} \right] \left[\begin{array}{ccc} \tilde{g}_{11}^D & \tilde{g}_{21}^D & \cdots & \tilde{g}_{Q1}^D \\ \tilde{g}_{12}^D & \tilde{g}_{22}^D & \cdots & \tilde{g}_{Q2}^D \\ \cdots & \cdots & \cdots & \cdots \\ \tilde{g}_{1N}^D & \tilde{g}_{2N}^D & \cdots & \tilde{g}_{QN}^D \end{array} \right] \\ & = \left[\begin{array}{ccc} r_{11} & r_{12} & \cdots & r_{1Q} \\ r_{21} & r_{22} & \cdots & r_{2Q} \\ \cdots & \cdots & \cdots & \cdots \\ r_{P1} & r_{P2} & \cdots & r_{PQ} \end{array} \right], \quad (61) \end{aligned}$$

where $R(z_1)$ is **the image of the first layer**. In $R(z_1)$, each row is an angle gather at an imaging point, and each column is a common angle gather. The multiplication of the p th row in the matrix $[W^U(z_0, z_1)]^H$ by any column in the matrix $P(\vec{x}_r, \vec{x}_s, \omega)$ corresponds to a detection focusing of a shot gather; the multiplication of the q th column in the matrix $[W^D(z_1, z_0)]^H$ by any row in the matrix $P(\vec{x}_r, \vec{x}_s, \omega)$ corresponds to an emission focusing. Then, **the image of the second layer** can be obtained with

$$[W^U(z_0, z_2)]^H P(\vec{x}_r, \vec{x}_s, z_0, \omega) [W^D(z_2, z_0)]^H = R(z_2). \quad (62)$$

Generally, **the image of the z_i th layer** is

$$[W^U(z_0, z_i)]^H P(\vec{x}_r, \vec{x}_s, z_0, \omega) [W^D(z_i, z_0)]^H = R(z_i). \quad (63)$$

Here, the matrices $[W^U]^H$ and $[W^D]^H$ are non-recursive. Otherwise, equation (62) and (63) will be of the following forms:

$$[W^U(z_1, z_2)]^H [W^U(z_0, z_1)]^H P(\vec{x}_r, \vec{x}_s, z_0, \omega) [W^D(z_1, z_0)]^H [W^D(z_2, z_1)]^H = R(z_2), \quad (64)$$

or

$$[W^U(z_1, z_2)]^H P(\vec{x}_r, \vec{x}_s, z_1, \omega) [W^D(z_2, z_1)]^H = R(z_2), \quad (65)$$

and

$$[W^U(z_{i-1}, z_i)]^H \cdots [W^U(z_0, z_1)]^H P(\vec{x}_r, \vec{x}_s, z_0, \omega) [W^D(z_1, z_0)]^H \cdots [W^D(z_i, z_{i-1})]^H = R(z_i), \quad (66)$$

or

$$[W^U(z_{i-1}, z_i)]^H P(\vec{x}_r, \vec{x}_s, z_{i-1}, \omega) [W^D(z_i, z_{i-1})]^H = R(z_i). \quad (67)$$

Defining the cost function as

$$E(R(\theta)) = \|W^U R(\theta) W^D - P(\vec{x}_r, \vec{x}_s, \omega)\|_2^2 \quad (68)$$

yields the formula of the linearized migration/inversion:

$$R(\theta) = \frac{[W^U]^H P(\vec{x}_r, \vec{x}_s, \omega) [W^D]^H}{[W^U]^H [W^U] [W^D] [W^D]^H}. \quad (69)$$

The matrix expression of the migration/inversion in equation (69) is

$$\begin{aligned} & \frac{\begin{bmatrix} \tilde{g}_{11}^U & \tilde{g}_{21}^U & \cdots & \tilde{g}_{M1}^U \\ \tilde{g}_{12}^U & \tilde{g}_{22}^U & \cdots & \tilde{g}_{M2}^U \\ \cdots & \cdots & \cdots & \cdots \\ \tilde{g}_{1P}^U & \tilde{g}_{2P}^U & \cdots & \tilde{g}_{MP}^U \end{bmatrix} \begin{bmatrix} P_{11}^{rs} & P_{12}^{rs} & \cdots & P_{1N}^{rs} \\ P_{21}^{rs} & P_{22}^{rs} & \cdots & P_{2N}^{rs} \\ \cdots & \cdots & \cdots & \cdots \\ P_{M1}^{rs} & P_{M2}^{rs} & \cdots & P_{MN}^{rs} \end{bmatrix} \begin{bmatrix} \tilde{g}_{11}^D & \tilde{g}_{21}^D & \cdots & \tilde{g}_{Q1}^D \\ \tilde{g}_{12}^D & \tilde{g}_{22}^D & \cdots & \tilde{g}_{Q2}^D \\ \cdots & \cdots & \cdots & \cdots \\ \tilde{g}_{1N}^D & \tilde{g}_{2N}^D & \cdots & \tilde{g}_{QN}^D \end{bmatrix}}{[M]} \\ & = \begin{bmatrix} r_{11} & r_{12} & \cdots & r_{1Q} \\ r_{21} & r_{22} & \cdots & r_{2Q} \\ \cdots & \cdots & \cdots & \cdots \\ r_{P1} & r_{P2} & \cdots & r_{PQ} \end{bmatrix}, \quad (70) \end{aligned}$$

where the denominator term $[M]$ is

$$\begin{aligned} [M] & = \begin{bmatrix} \tilde{g}_{11}^D & \tilde{g}_{21}^D & \cdots & \tilde{g}_{Q1}^D \\ \tilde{g}_{12}^D & \tilde{g}_{22}^D & \cdots & \tilde{g}_{Q2}^D \\ \cdots & \cdots & \cdots & \cdots \\ \tilde{g}_{1N}^D & \tilde{g}_{2N}^D & \cdots & \tilde{g}_{QN}^D \end{bmatrix} \begin{bmatrix} \tilde{g}_{11}^U & \tilde{g}_{21}^U & \cdots & \tilde{g}_{M1}^U \\ \tilde{g}_{12}^U & \tilde{g}_{22}^U & \cdots & \tilde{g}_{M2}^U \\ \cdots & \cdots & \cdots & \cdots \\ \tilde{g}_{1P}^U & \tilde{g}_{2P}^U & \cdots & \tilde{g}_{MP}^U \end{bmatrix} \\ & \quad \begin{bmatrix} g_{11}^U & g_{12}^U & \cdots & g_{1P}^U \\ g_{21}^U & g_{22}^U & \cdots & g_{2P}^U \\ \cdots & \cdots & \cdots & \cdots \\ g_{M1}^U & g_{M2}^U & \cdots & g_{MP}^U \end{bmatrix} \begin{bmatrix} g_{11}^D & g_{12}^D & \cdots & g_{1N}^D \\ g_{21}^D & g_{22}^D & \cdots & g_{2N}^D \\ \cdots & \cdots & \cdots & \cdots \\ g_{Q1}^D & g_{Q2}^D & \cdots & g_{QN}^D \end{bmatrix}. \quad (71) \end{aligned}$$

From equation (61) and (70), the migration/inversion can be locally implemented, because all elements in the matrices W^U , $[W^U]^H$, W^D and $[W^D]^H$ relate only to a given layer. If the matrix $[W^U]^H$ is the inverse of the matrix W^U , it can be expressed as

$$[W^U]^H W^U = E, \quad (72)$$

where the matrix E is an identity matrix. Similarly, if the matrix $[W^D]^H$ is the inverse of the matrix W^D , we have

$$W^D [W^D]^H = E. \quad (73)$$

In practice, $[W^U]^H$ and $[W^D]^H$ are the conjugates of W^U and W^D respectively. Therefore, the matrix $[M]$ is a band-width-limited diagonal matrix. The velocity structure and the acquisition geometry affect the inner structure of the matrix. In fact, M is a Hessian which will be discussed in detail later.

[3] The meaning and calculation of $\nabla f(\delta m)$ and $\nabla^2 f(\delta m)$

The iterative formula of the least-squares migration/inversion is:

$$\delta \mathbf{m}^{(k+1)} = \delta \mathbf{m}^{(k)} - H^{k+1} \nabla f(\delta \mathbf{m}^{(k)}), \quad (74)$$

where H^{k+1} is the inverse of the Hessian. The first-order derivative $\nabla f(\delta \mathbf{m}^{(k)})$ of the cost function with respect to the medium parameters is

$$\nabla f(\delta \mathbf{m}) = 2A^H (A\delta \mathbf{m} - \delta \mathbf{d}^{obs}). \quad (75)$$

If the residual wavefield is defined as

$$\mathbf{P}^{residual} = A\delta \mathbf{m} - \delta \mathbf{d}^{obs}, \quad (76)$$

and equation (75) is rewritten as

$$\nabla f(\delta \mathbf{m}) = 2A^H \mathbf{P}^{residual}, \quad (77)$$

then the first-order derivative means that the residual wavefield is back-propagated. It is further equivalent to the classical prestack migration if the parameter disturbance $\delta \mathbf{m}$ is set to zero at the first iteration. The residual wavefield $\mathbf{P}^{residual}$ belongs to the data space $D(\vec{x}_r, \vec{x}_s, t)$, and $\nabla f(\delta \mathbf{m})$ pertains to the image space $I(\vec{x})$. Calculating the first-order derivative requires one-time modeling $A\delta \mathbf{m}$, which can be implemented by a prestack demigration, and one-time classical prestack migration of $2A^H \mathbf{P}^{residual}$:

$$\nabla f(\delta \mathbf{m}) = 2 \begin{bmatrix} \tilde{g}_{11}^U & \tilde{g}_{21}^U & \cdots & \tilde{g}_{M1}^U \\ \tilde{g}_{12}^U & \tilde{g}_{22}^U & \cdots & \tilde{g}_{M2}^U \\ \cdots & \cdots & \cdots & \cdots \\ \tilde{g}_{1P}^U & \tilde{g}_{2P}^U & \cdots & \tilde{g}_{MP}^U \end{bmatrix} \begin{bmatrix} \mathbf{P}_{11}^{residual-rs} & \mathbf{P}_{12}^{residual-rs} & \cdots & \mathbf{P}_{1N}^{residual-rs} \\ \mathbf{P}_{21}^{residual-rs} & \mathbf{P}_{22}^{residual-rs} & \cdots & \mathbf{P}_{2N}^{residual-rs} \\ \cdots & \cdots & \cdots & \cdots \\ \mathbf{P}_{M1}^{residual-rs} & \mathbf{P}_{M2}^{residual-rs} & \cdots & \mathbf{P}_{MN}^{residual-rs} \end{bmatrix} \begin{bmatrix} \tilde{g}_{11}^D & \tilde{g}_{21}^D & \cdots & \tilde{g}_{Q1}^D \\ \tilde{g}_{12}^D & \tilde{g}_{22}^D & \cdots & \tilde{g}_{Q2}^D \\ \cdots & \cdots & \cdots & \cdots \\ \tilde{g}_{1N}^D & \tilde{g}_{2N}^D & \cdots & \tilde{g}_{QN}^D \end{bmatrix}. \quad (78)$$

In the first iterative step, $\delta \mathbf{m} = 0$, equation (78) is rewritten as

$$\begin{aligned} \nabla f(\delta \mathbf{m}) &= -2 \begin{bmatrix} \tilde{g}_{11}^U & \tilde{g}_{21}^U & \cdots & \tilde{g}_{M1}^U \\ \tilde{g}_{12}^U & \tilde{g}_{22}^U & \cdots & \tilde{g}_{M2}^U \\ \cdots & \cdots & \cdots & \cdots \\ \tilde{g}_{1P}^U & \tilde{g}_{2P}^U & \cdots & \tilde{g}_{MP}^U \end{bmatrix} \begin{bmatrix} \delta \mathbf{d}_{11}^{obs-rs} & \delta \mathbf{d}_{12}^{obs-rs} & \cdots & \delta \mathbf{d}_{1N}^{obs-rs} \\ \delta \mathbf{b}_{21}^{obs-rs} & \delta \mathbf{d}_{22}^{obs-rs} & \cdots & \delta \mathbf{d}_{2N}^{obs-rs} \\ \cdots & \cdots & \cdots & \cdots \\ \delta \mathbf{d}_{M1}^{obs-rs} & \delta \mathbf{d}_{M2}^{obs-rs} & \cdots & \delta \mathbf{d}_{MN}^{obs-rs} \end{bmatrix} \\ &= -2 \begin{bmatrix} \tilde{g}_{11}^D & \tilde{g}_{21}^D & \cdots & \tilde{g}_{Q1}^D \\ \tilde{g}_{12}^D & \tilde{g}_{22}^D & \cdots & \tilde{g}_{Q2}^D \\ \cdots & \cdots & \cdots & \cdots \\ \tilde{g}_{1N}^D & \tilde{g}_{2N}^D & \cdots & \tilde{g}_{QN}^D \end{bmatrix} \begin{bmatrix} r_{11} & r_{12} & \cdots & r_{1Q} \\ r_{21} & r_{22} & \cdots & r_{2Q} \\ \cdots & \cdots & \cdots & \cdots \\ r_{P1} & r_{P2} & \cdots & r_{PQ} \end{bmatrix}. \end{aligned} \quad (79)$$

The Hessian is the second-order derivative of the cost function with respect to the medium parameters. It is of the following form:

$$\nabla^2 f(\delta \mathbf{m}) = 2A^H A. \quad (80)$$

In the least-squares migration/inversion, the Hessian is a deconvolution operator. It is used for de-blurring the image of the classical prestack migration. Physically, the Hessian is an indicator of the illumination. The energy of the wave propagating through a certain medium is expressed as follows:

$$E(\delta \mathbf{m}) = \|\delta \mathbf{d}\|^2 = \delta \mathbf{d}^H \delta \mathbf{d} = \delta \mathbf{m}^H A^H A \delta \mathbf{m} = [W^D]^H [\delta \mathbf{m}]^H [W^U]^H [W^U] [\delta \mathbf{m}] [W^D]. \quad (81)$$

For a given layer and from the modeling equation (58), equation (81) can be rewritten as

$$E(\delta \mathbf{m}) = \begin{bmatrix} g_{11}^D & g_{12}^D & \cdots & g_{1N}^D \\ g_{21}^D & g_{22}^D & \cdots & g_{2N}^D \\ \cdots & \cdots & \cdots & \cdots \\ g_{Q1}^D & g_{Q2}^D & \cdots & g_{QN}^D \end{bmatrix}^H \begin{bmatrix} r_{11} & r_{12} & \cdots & r_{1Q} \\ r_{21} & r_{22} & \cdots & r_{2Q} \\ \cdots & \cdots & \cdots & \cdots \\ r_{P1} & r_{P2} & \cdots & r_{PQ} \end{bmatrix}^H \begin{bmatrix} g_{11}^U & g_{12}^U & \cdots & g_{1P}^U \\ g_{21}^U & g_{22}^U & \cdots & g_{2P}^U \\ \cdots & \cdots & \cdots & \cdots \\ g_{M1}^U & g_{M2}^U & \cdots & g_{MP}^U \end{bmatrix}^H \\ \begin{bmatrix} g_{11}^U & g_{12}^U & \cdots & g_{1P}^U \\ g_{21}^U & g_{22}^U & \cdots & g_{2P}^U \\ \cdots & \cdots & \cdots & \cdots \\ g_{M1}^U & g_{M2}^U & \cdots & g_{MP}^U \end{bmatrix} \begin{bmatrix} r_{11} & r_{12} & \cdots & r_{1Q} \\ r_{21} & r_{22} & \cdots & r_{2Q} \\ \cdots & \cdots & \cdots & \cdots \\ r_{P1} & r_{P2} & \cdots & r_{PQ} \end{bmatrix} \begin{bmatrix} g_{11}^D & g_{12}^D & \cdots & g_{1N}^D \\ g_{21}^D & g_{22}^D & \cdots & g_{2N}^D \\ \cdots & \cdots & \cdots & \cdots \\ g_{Q1}^D & g_{Q2}^D & \cdots & g_{QN}^D \end{bmatrix}. \quad (82)$$

Clearly, for a horizontal reflector with an even reflectivity and only the zero-offset reflectivity considered, $A^H A$ determines the energy of the wave which propagates to the layer. Equation

(82) can be rewritten as follows:

$$\begin{aligned}
A^H A &= [W^D]^H [W^U]^H [W^U] [W^D] \\
&= \begin{bmatrix} g_{11}^D & g_{12}^D & \cdots & g_{1N}^D \\ g_{21}^D & g_{22}^D & \cdots & g_{2N}^D \\ \cdots & \cdots & \cdots & \cdots \\ g_{Q1}^D & g_{Q2}^D & \cdots & g_{QN}^D \end{bmatrix}^H \begin{bmatrix} g_{11}^U & g_{12}^U & \cdots & g_{1P}^U \\ g_{21}^U & g_{22}^U & \cdots & g_{2P}^U \\ \cdots & \cdots & \cdots & \cdots \\ g_{M1}^U & g_{M2}^U & \cdots & g_{MP}^U \end{bmatrix}^H \\
&= \begin{bmatrix} g_{11}^U & g_{12}^U & \cdots & g_{1P}^U \\ g_{21}^U & g_{22}^U & \cdots & g_{2P}^U \\ \cdots & \cdots & \cdots & \cdots \\ g_{M1}^U & g_{M2}^U & \cdots & g_{MP}^U \end{bmatrix} \begin{bmatrix} g_{11}^D & g_{12}^D & \cdots & g_{1N}^D \\ g_{21}^D & g_{22}^D & \cdots & g_{2N}^D \\ \cdots & \cdots & \cdots & \cdots \\ g_{Q1}^D & g_{Q2}^D & \cdots & g_{QN}^D \end{bmatrix} \\
&= \begin{bmatrix} \tilde{g}_{11}^D & \tilde{g}_{21}^D & \cdots & \tilde{g}_{Q1}^D \\ \tilde{g}_{12}^D & \tilde{g}_{22}^D & \cdots & \tilde{g}_{Q2}^D \\ \cdots & \cdots & \cdots & \cdots \\ \tilde{g}_{1N}^D & \tilde{g}_{2N}^D & \cdots & \tilde{g}_{QN}^D \end{bmatrix} \begin{bmatrix} \tilde{g}_{11}^U & \tilde{g}_{21}^U & \cdots & \tilde{g}_{M1}^U \\ \tilde{g}_{12}^U & \tilde{g}_{22}^U & \cdots & \tilde{g}_{M2}^U \\ \cdots & \cdots & \cdots & \cdots \\ \tilde{g}_{1P}^U & \tilde{g}_{2P}^U & \cdots & \tilde{g}_{MP}^U \end{bmatrix} \\
&= \begin{bmatrix} g_{11}^U & g_{12}^U & \cdots & g_{1P}^U \\ g_{21}^U & g_{22}^U & \cdots & g_{2P}^U \\ \cdots & \cdots & \cdots & \cdots \\ g_{M1}^U & g_{M2}^U & \cdots & g_{MP}^U \end{bmatrix} \begin{bmatrix} g_{11}^D & g_{12}^D & \cdots & g_{1N}^D \\ g_{21}^D & g_{22}^D & \cdots & g_{2N}^D \\ \cdots & \cdots & \cdots & \cdots \\ g_{Q1}^D & g_{Q2}^D & \cdots & g_{QN}^D \end{bmatrix}. \tag{83}
\end{aligned}$$

The row in the matrix $[W^U]^H$ multiplied by the column of the matrix $[W^U]$ and the row in the matrix $[W^D]$ multiplied by the column of the matrix $[W^D]^H$ are the cross-correlation between the conjugate of the Green's function and the Green's function at different receiver or shot positions respectively. The auto-correlation has a peak value, and the cross-correlation decreases rapidly as the distance increases between the receiver and shot positions. The auto-correlation values are on the diagonal. Therefore, the Hessian is a band-width-limited diagonal matrix. Its inverse is also a kind of band-width-limited diagonal matrix. In the extreme case, where only the elements on the diagonal of the Hessian are left, with non-diagonal set to zero, the elements on the diagonal of the inverse of the Hessian are the reciprocals of the elements on the diagonal of the Hessian. Therefore, the inverse of the Hessian plays the role of decreasing strong illumination and enhancing poor illumination. The Hessian itself reflects the illumination of each imaging point. The matrix expression of migration/inversion can be

summarized as follows:

$$\begin{aligned}
 & \begin{bmatrix} r_{11} & r_{12} & \cdots & r_{1Q} \\ r_{21} & r_{22} & \cdots & r_{2Q} \\ \cdots & \cdots & \cdots & \cdots \\ r_{P1} & r_{P2} & \cdots & r_{PQ} \end{bmatrix}_{P \times Q}^{k+1} = \begin{bmatrix} r_{11} & r_{12} & \cdots & r_{1Q} \\ r_{21} & r_{22} & \cdots & r_{2Q} \\ \cdots & \cdots & \cdots & \cdots \\ r_{P1} & r_{P2} & \cdots & r_{PQ} \end{bmatrix}_{P \times Q}^k \\
 - 2 & \left\{ \begin{bmatrix} \tilde{g}_{11}^U & \tilde{g}_{21}^U & \cdots & \tilde{g}_{M1}^U \\ \tilde{g}_{12}^U & \tilde{g}_{22}^U & \cdots & \tilde{g}_{M2}^U \\ \cdots & \cdots & \cdots & \cdots \\ \tilde{g}_{1P}^U & \tilde{g}_{2P}^U & \cdots & \tilde{g}_{MP}^U \end{bmatrix} \begin{bmatrix} g_{11}^U & g_{12}^U & \cdots & g_{1P}^U \\ g_{21}^U & g_{22}^U & \cdots & g_{2P}^U \\ \cdots & \cdots & \cdots & \cdots \\ g_{M1}^U & g_{M2}^U & \cdots & g_{MP}^U \end{bmatrix} \right\}_{P \times P}^{-1} \\
 & \begin{bmatrix} \tilde{g}_{11}^U & \tilde{g}_{21}^U & \cdots & \tilde{g}_{M1}^U \\ \tilde{g}_{12}^U & \tilde{g}_{22}^U & \cdots & \tilde{g}_{M2}^U \\ \cdots & \cdots & \cdots & \cdots \\ \tilde{g}_{1P}^U & \tilde{g}_{2P}^U & \cdots & \tilde{g}_{MP}^U \end{bmatrix} \begin{bmatrix} P_{11}^{rs} & P_{12}^{rs} & \cdots & P_{1N}^{rs} \\ P_{21}^{rs} & P_{22}^{rs} & \cdots & P_{2N}^{rs} \\ \cdots & \cdots & \cdots & \cdots \\ P_{M1}^{rs} & P_{M2}^{rs} & \cdots & P_{MN}^{rs} \end{bmatrix} \begin{bmatrix} \tilde{g}_{11}^D & \tilde{g}_{21}^D & \cdots & \tilde{g}_{Q1}^D \\ \tilde{g}_{12}^D & \tilde{g}_{22}^D & \cdots & \tilde{g}_{Q2}^D \\ \cdots & \cdots & \cdots & \cdots \\ \tilde{g}_{1N}^D & \tilde{g}_{2N}^D & \cdots & \tilde{g}_{QN}^D \end{bmatrix}_{P \times Q} \\
 & \left\{ \begin{bmatrix} \tilde{g}_{11}^D & \tilde{g}_{21}^D & \cdots & \tilde{g}_{Q1}^D \\ \tilde{g}_{12}^D & \tilde{g}_{22}^D & \cdots & \tilde{g}_{Q2}^D \\ \cdots & \cdots & \cdots & \cdots \\ \tilde{g}_{1N}^D & \tilde{g}_{2N}^D & \cdots & \tilde{g}_{QN}^D \end{bmatrix} \begin{bmatrix} g_{11}^D & g_{12}^D & \cdots & g_{1N}^D \\ g_{21}^D & g_{22}^D & \cdots & g_{2N}^D \\ \cdots & \cdots & \cdots & \cdots \\ g_{Q1}^D & g_{Q2}^D & \cdots & g_{QN}^D \end{bmatrix} \right\}_{Q \times Q}^{-1} \cdot \quad (84)
 \end{aligned}$$

Substituting the residual imaging matrix into equation (84), it can be rewritten as follows:

$$\begin{aligned}
 & \begin{bmatrix} r_{11} & r_{12} & \cdots & r_{1Q} \\ r_{21} & r_{22} & \cdots & r_{2Q} \\ \cdots & \cdots & \cdots & \cdots \\ r_{P1} & r_{P2} & \cdots & r_{PQ} \end{bmatrix}_{P \times Q}^{k+1} = \begin{bmatrix} r_{11} & r_{12} & \cdots & r_{1Q} \\ r_{21} & r_{22} & \cdots & r_{2Q} \\ \cdots & \cdots & \cdots & \cdots \\ r_{P1} & r_{P2} & \cdots & r_{PQ} \end{bmatrix}_{P \times Q}^k \\
 - 2 & \left\{ \begin{bmatrix} \tilde{g}_{11}^U & \tilde{g}_{21}^U & \cdots & \tilde{g}_{M1}^U \\ \tilde{g}_{12}^U & \tilde{g}_{22}^U & \cdots & \tilde{g}_{M2}^U \\ \cdots & \cdots & \cdots & \cdots \\ \tilde{g}_{1P}^U & \tilde{g}_{2P}^U & \cdots & \tilde{g}_{MP}^U \end{bmatrix} \begin{bmatrix} g_{11}^U & g_{12}^U & \cdots & g_{1P}^U \\ g_{21}^U & g_{22}^U & \cdots & g_{2P}^U \\ \cdots & \cdots & \cdots & \cdots \\ g_{M1}^U & g_{M2}^U & \cdots & g_{MP}^U \end{bmatrix} \right\}_{P \times P}^{-1} \\
 & \begin{bmatrix} r_{11}^{residual} & r_{12}^{residual} & \cdots & r_{1Q}^{residual} \\ r_{21}^{residual} & r_{22}^{residual} & \cdots & r_{2Q}^{residual} \\ \cdots & \cdots & \cdots & \cdots \\ r_{P1}^{residual} & r_{P2}^{residual} & \cdots & r_{PQ}^{residual} \end{bmatrix}_{P \times Q} \\
 & \left\{ \begin{bmatrix} \tilde{g}_{11}^D & \tilde{g}_{21}^D & \cdots & \tilde{g}_{Q1}^D \\ \tilde{g}_{12}^D & \tilde{g}_{22}^D & \cdots & \tilde{g}_{Q2}^D \\ \cdots & \cdots & \cdots & \cdots \\ \tilde{g}_{1N}^D & \tilde{g}_{2N}^D & \cdots & \tilde{g}_{QN}^D \end{bmatrix} \begin{bmatrix} g_{11}^D & g_{12}^D & \cdots & g_{1N}^D \\ g_{21}^D & g_{22}^D & \cdots & g_{2N}^D \\ \cdots & \cdots & \cdots & \cdots \\ g_{Q1}^D & g_{Q2}^D & \cdots & g_{QN}^D \end{bmatrix} \right\}_{Q \times Q}^{-1} \cdot \quad (85)
 \end{aligned}$$

With the quasi-Newton condition $\mathbf{p}^{(k)} = H_{k+1} \mathbf{q}^{(k)}$, and $\mathbf{p}^{(k)} = \delta \mathbf{m}^k - \delta \mathbf{m}^{(k+1)}$, $\mathbf{q}^{(k)} = \nabla f(\delta \mathbf{m}^{(k+1)}) - \nabla f(\delta \mathbf{m}^{(k)})$, the DFP algorithm for calculating the inverse of the Hessian matrix is

$$H_{k+1}^{DFP} = H_k + \frac{\mathbf{p}^{(k)} (\mathbf{p}^{(k)})^T}{(\mathbf{p}^{(k)})^T \mathbf{q}^{(k)}} - \frac{(H_k \mathbf{q}^{(k)}) (H_k \mathbf{q}^{(k)})^T}{(\mathbf{q}^{(k)})^T H_k \mathbf{q}^{(k)}}, \quad (86)$$

where

$$\mathbf{p}^{(k)} = \begin{bmatrix} r_{11} & r_{12} & \cdots & r_{1Q} \\ r_{21} & r_{22} & \cdots & r_{2Q} \\ \cdots & \cdots & \cdots & \cdots \\ r_{P1} & r_{P2} & \cdots & r_{PQ} \end{bmatrix}^k - \begin{bmatrix} r_{11} & r_{12} & \cdots & r_{1Q} \\ r_{21} & r_{22} & \cdots & r_{2Q} \\ \cdots & \cdots & \cdots & \cdots \\ r_{P1} & r_{P2} & \cdots & r_{PQ} \end{bmatrix}^{k+1} \quad (87)$$

and

$$\begin{aligned} \mathbf{q}^{(k)} &= [2A^H \mathbf{P}^{residual}]^{k+1} - [2A^H \mathbf{P}^{residual}]^k \\ &= \begin{bmatrix} r_{11}^{residual} & r_{12}^{residual} & \cdots & r_{1Q}^{residual} \\ r_{21}^{residual} & r_{22}^{residual} & \cdots & r_{2Q}^{residual} \\ \cdots & \cdots & \cdots & \cdots \\ r_{P1}^{residual} & r_{P2}^{residual} & \cdots & r_{PQ}^{residual} \end{bmatrix}^{k+1} \\ &\quad - \begin{bmatrix} r_{11}^{residual} & r_{12}^{residual} & \cdots & r_{1Q}^{residual} \\ r_{21}^{residual} & r_{22}^{residual} & \cdots & r_{2Q}^{residual} \\ \cdots & \cdots & \cdots & \cdots \\ r_{P1}^{residual} & r_{P2}^{residual} & \cdots & r_{PQ}^{residual} \end{bmatrix}^k, \end{aligned} \quad (88)$$

where $r_{ij}^{residual}$ is the image with the residual wavefield.

[4] Analysis of some factors that influence imaging

It is worthwhile to analyze the factors which affect the imaging quality and how they do so. We list four main factors: (1) too coarse sampling, (2) uneven sampling intervals or missing data, (3) illumination deficiency, (4) migration operator. All these factors will slow the convergence of iterative migration/inversion algorithms. It is obvious that too coarse sampling produces aliasing. Fig.5 demonstrates that uneven sampling intervals or missing data will cause imaging noise. Because the reflections from the vicinity of a reflecting point can not cancel each other, imaging noise appears. The illumination greatly affects the imaging quality in the case of a complex medium. From the view of the Radon transform and its inverse, if the seismic data set is band-width-unlimited, and the acquisition geometry is continuously distributed around an object body, the object can be uniquely restored with the inverse of the Radon transform. This is theoretically true. According to ray theory tomography, if rays are missing which should pass through the region of interest, the image of the region will be blurred. In fact, this is an amplitude distortion of the image. Therefore, the true medium parameters can never be recovered from real seismic data. The possibility of relative true-amplitude imaging is analyzed later. Propagators describe wave propagation in the background medium. Given the seismic data and the background parameters, only the propagators affect the iterative algorithms. Propagators should characterize wave propagation as accurately as possible. However, commonly used propagators are not so accurate and many wave phenomena are neglected. This can cause amplitude and phase distortion, as well as errors in Hessian calculation. Further, these will slow down the convergence of migration/inversion.

[5] The imaging gather of migration/inversion

Equation (84) or (85) gives the imaging matrix:

$$\begin{bmatrix} r_{11} & r_{12} & \cdots & r_{1Q} \\ r_{21} & r_{22} & \cdots & r_{2Q} \\ \cdots & \cdots & \cdots & \cdots \\ r_{P1} & r_{P2} & \cdots & r_{PQ} \end{bmatrix}_{P \times Q}, \quad (89)$$

where P is the number of scatterers and Q is the number of incident angles for a scatterer. A row of the reflectivity matrix is an angle gather. However, the angle is not evenly sampled in a constant angle interval in complex medium. Physically, a reflection point or scatterer is not illuminated with a constant incident angle interval; mathematically, an angle gather evenly sampled with a constant angle interval for the point can be yielded with Fourier transform approaches. Weglein and Stolt (1999) and Sava and Fomel (2003) gave an approach for creating the angle gathers from the imaged data set. However, in our mind, we should know the difference. The uneven-incident-angle illumination will cause imaging noises. And this will also cause amplitude distortions in angle gathers. Fig.5 shows that a reflection point or scatterer is not illuminated with a constant incident angle interval.

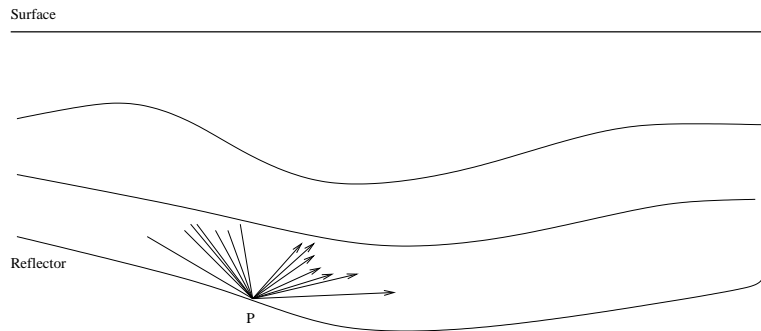


Figure 5: the illumination with the uneven incident angles huazhong1-even_incident_angle [CR]

[6] The resolution of migration/inversion

To understand which factors influence the resolution of the migration/inversion, we analyze the following matrices:

$$\left\{ [W^U]^H [W^U] \right\}^{-1} \left\{ [W^U]^H [W^U] \right\} [R(\theta)] \left\{ [W^D]^H [W^D] \right\} \left\{ [W^D]^H [W^D] \right\}^{-1}. \quad (90)$$

Ideally, all the matrices $\left\{ [W^U]^H [W^U] \right\}^{-1}$, $\left\{ [W^U]^H [W^U] \right\}$, $\left\{ [W^D]^H [W^D] \right\}$ and $\left\{ [W^D]^H [W^D] \right\}^{-1}$ are the identity matrix E , and at this time the image $[R(\theta)]$ is of the highest resolution. From ray theory tomography, resolution is closely related to acquisition aperture. The larger the aperture, the higher the resolution. If the matrices in equation (90) are required to be an

identity, besides the aperture, the spatial and temporal sampling and the propagator also have obvious effects. Theoretically, the Hessian blurs the true image of reflectivity, and the inverse of the Hessian deblurs the blurred image. In practice, the calculation of the Hessian is affected by many factors. As a result, the imaging quality is not improved distinctly.

[7] The regularization of the migration/inversion algorithms

In probability theory, the cost function is defined as (Tarantola, 1984)

$$2S(\mathbf{m}) = (g(\mathbf{m}) - \mathbf{d}_{obs})^T C_D^{-1} (g(\mathbf{m}) - \mathbf{d}_{obs}) + (\mathbf{m} - \mathbf{m}_{prior}) C_M^{-1} (\mathbf{m} - \mathbf{m}_{prior}) \quad (91)$$

where C_D and C_M are the covariance matrices for the data sets and models respectively. It is relatively easy to analyze the role of the covariance matrix C_M . The second term of equation (91) can be expressed in the following matrix form:

$$\begin{pmatrix} m_1 & m_2 & m_3 & \cdots & m_N \end{pmatrix} \left\{ \begin{array}{ccccc} c_{11} & c_{12} & c_{13} & \cdots & c_{1N} \\ c_{21} & c_{22} & c_{23} & \cdots & c_{2N} \\ \vdots & \vdots & \vdots & \ddots & \vdots \\ c_{N1} & c_{N2} & c_{N3} & \cdots & c_{NN} \end{array} \right\} \begin{pmatrix} m_1 \\ m_2 \\ m_3 \\ \vdots \\ m_N \end{pmatrix}. \quad (92)$$

The vector $\mathbf{m} - \mathbf{m}_{prior}$ represents a stochastic process. The covariance matrix C_M stands for the linear relation of the stochastic process at two different times. If the value of the covariance is very small, the stochastic process at the two different times changes a little. Therefore, the uncertainty of the stochastic process is also low. Small values are chosen for the elements in the matrix C_M if we have enough a priori information of the model. The similarity between two images produced by two successive iterative migration/inversion steps are used to generate the covariance matrix. The correlation coefficients of the two images can be used to fill the covariance matrix C_M . Of course, the reciprocal of the correlation coefficients of the two images can be used to fill the covariance matrix C_M^{-1} . The local singular values (from SVD) of an image reflect the local continuity of an event, which can be used for constraints.

[8] The convergence of the iterative migration/inversion

Again, the iterative formula for migration/inversion imaging is

$$\delta \mathbf{m}^{(k+1)} = \delta \mathbf{m}^{(k)} - H^{k+1} \nabla f(\delta \mathbf{m}^{(k)}). \quad (93)$$

The choice of background parameters and the method for linearizing the propagators determine whether the cost function is (or approaches) a quadratic function. Therefore, the Born approximation should be replaced by De Wolf approximation or other more accurate approximations. On the other hand, to produce the image at the first iterative step with the so-called true-amplitude imaging approaches will accelerate the convergence of the iterative migration/inversion.

THE POSSIBILITY OF RELATIVE TRUE-AMPLITUDE IMAGING

Beylkin (1985) gave a formula for estimating the (locations of) discontinuities of the unknown function describing the medium, rather than for estimating the function itself. The generalized back-projection operator R^* dual to the generalized Radon transform R is defined as

$$(R^*u)(y) = \int_{\partial X} u(t, \xi) V_{t=\phi(y, \xi, \eta)} b(y, \xi) d\xi, \quad (94)$$

where $b(y, \xi) \in C^\infty(X \times \partial X)$ is a weighting function which is a smooth, non-negative function on $X \times \partial X$. It is defined as

$$b(y, \xi) = \frac{h(y, \xi)}{a(y, \xi)} \chi(y, \xi), \quad (95)$$

where $h(y, \xi)$ is a Jacobian determinant, $\chi(y, \xi)$ is a cut-off function, $u(t, \xi)$ can be regarded as a generalized projection, which is the observed scattered wavefield on the surface. With the help of a Fourier integral operator (FIO), the following formula can be obtained:

$$\left(I_{\partial X_\eta^0 f}\right)(y) = \frac{1}{8\pi^3} \int_{\Omega_\eta(y)} e^{-ip \cdot y} f^\wedge(p) dp, \quad (96)$$

where $p = k\nabla_y \phi(y, \xi, \eta)$, which is the direction normal to the reflector at the imaging point. ∂X_η^0 is the limited aperture on the surface, and $\Omega_\eta(y)$ is the corresponding limited aperture near the imaging point. And $f^\wedge(p)$ is the Fourier transform of the object function. From **Theorem 1** in Beylkin (1985), the inverse transform of the Fourier transform of the object function, $\left(I_{\partial X_\eta^0 f}\right)(y)$, approximately equals the generalized back-projection defined by equation (94). Clearly, if the observation aperture ∂X_η^0 or $\Omega_\eta(y)$ is unlimited, the discontinuities of the object function can be accurately estimated with equation (94) under some assumptions. That is to say, true-amplitude imaging can be theoretically implemented under some conditions. Here, we point that the relative true-amplitude imaging can be obtained in practice even though the observation aperture is always limited. Equation (96) can be considered as a summation. If the distribution of the Fourier transform of the object function on $\Omega_\eta(y)$ is even, and the range of the distribution is the same at every imaging point (or scattering point), the summation will be same. Even though the summation is not the true estimation for the discontinuities of the object function, the relative relation among these discontinuities at each imaging point is correct. This is the essence of the relative true-amplitude imaging or true-amplitude imaging. What prevent relative true-amplitude imaging? Missing data and limited aperture are the two main factors, assuming that the the back-projection operator is suitable. Beylkin (1985); Bleistein and Stockwell (2001); Zhang (2004) discussed how to construct a suitable back-projection operator or true-amplitude imaging operator. From the above point, we can further understand the meaning of the illumination analysis. The objective of the illumination analysis is to make clear how to map the observations on ∂X_η^0 to $\Omega_\eta(y)$. If, on $\Omega_\eta(y)$, the distribution of the Fourier transform of the object function is even, and the range of the distribution is the same at every imaging point (or scattering point), then relative true-amplitude imaging can be achieved. It is worth to point out that the distribution should be symmetrical about the normal to the reflector at the imaging point.

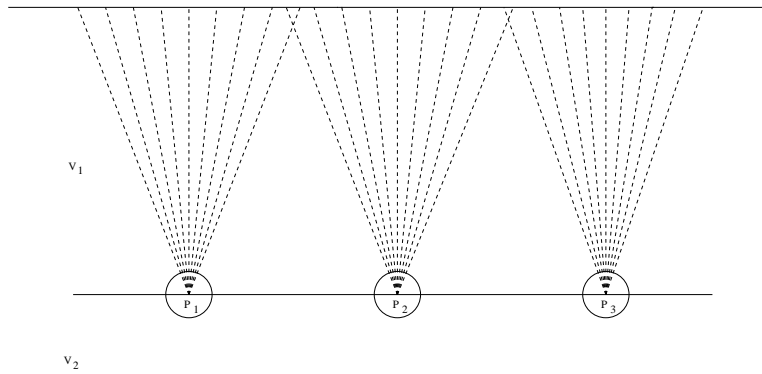


Figure 6: the possibility interpretation of the relative true-amplitude imaging in the case of simple medium structure. [huazhong1-true_amplitude_and_illumination](#) [CR]

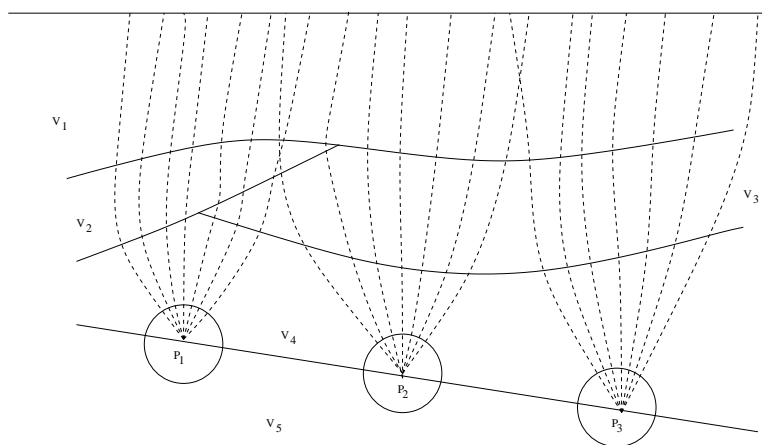


Figure 7: the possibility interpretation of the relative true-amplitude imaging in the case of complex medium structure. [huazhong1-true_amplitude_and_illum22](#) [CR]

CONCLUSION AND DISCUSSION

Comparing non-iterative linearized migration/inversion, iterative linearized migration/inversion, and nonlinear waveform inversion, linearized migration/inversion has been carefully reviewed. The following statements reflect my opinions about linearized migration/inversion.

(1) There exists a paradox: linearized migration/inversion requires that the background velocity is as close as possible to the true velocity distribution; however the Born approximation needs a very smooth background velocity, so that the incident wavefield only includes downward propagating waves. The Born approximation is not a good linearization method and it should be replaced by more accurate approximations, such as De Wolf approximation.

(2) In essence, non-iterative linearized migration/inversion, iterative linearized migration/inversion, and nonlinear waveform inversion, are all inverse scattering imaging methods.

(3) Relative true-amplitude imaging is possible, the condition is that the distribution of the Fourier transform of the object function on $\Omega_\eta(y)$ is even, and the range of the distribution is the same at every imaging point (or scattering point).

(4) The Hessian matrix is band-limited and its inverse is also band-limited, its inner structure has close relation with the complexity of the velocity and the acquisition geometry. It reflects the energy illuminating imaging points.

ACKNOWLEDGMENT

The first author thanks the SEP Group at Stanford University for providing an opportunity for him to serve as a visiting scholar.

REFERENCES

- Berkhout, A. J., 1997, Pushing the limits of seismic imaging, part I: Prestack migration in terms of double dynamic focusing: *Geophysics*, **62**, 937–953.
- Beylkin, G., 1985, Imaging of discontinuities in the inverse scattering problem by inversion of a causal generalized radon transform: *J. Math. Phys.* 26(1), 99–108.
- Bleistein, N. Cohen, J., and Stockwell, J., 2001, *Mathematics of multidimensional seismic imaging, migration, and inversion* Springer, 299.
- Bleistein, N., 1987, On the imaging of reflectors in the Earth: *Geophysics*, **52**, 931–942.
- Bleistein, N., Cohen, J. K., and Hagin, F. G., 1987, Two and one-half dimensional Born inversion with an arbitrary reference: *Geophysics*, **52**, 26–36.

- Clayton, R. W., and Stolt, R. H., 1981, A born-WKBJ inversion method for acoustic reflection data: *Geophysics*, **46**, 1559–1567.
- Gray, S. H., 1997, True-amplitude seismic migration: A comparison of three approaches: *Geophysics*, **62**, 929–936.
- Huazhong, W., 2003, Seismic imaging research report: Reflection Seismology Research Group, School of Ocean and Earth Science, Tongji University.
- Hubral, P., Schleicher, J., and Tygel, M., 1996, A unified approach to 3-D seismic reflection imaging, part I: Basic concepts: *Geophysics*, **61**, 742–758.
- Miller, D., Oristaglio, M., and Beylkin, G., 1987, A new slant on seismic imaging - Migration and integral geometry: *Geophysics*, **52**, 943–964.
- Mora, P. R., 1987, Nonlinear two-dimensional elastic inversion of multioffset seismic data: *Geophysics*, **52**, 1211–1228.
- Pratt, R. G., S. C., and Hicks, G. J., 1998, Gauss-newton and full newton methods in frequency-space seismic waveform inversion: *Geophys. J. Int.*, **133**, 341–362.
- Sava, P. C., and Fomel, S., 2003, Angle-domain common-image gathers by wavefield continuation methods: *Geophysics*, **68**, 1065–1074.
- Stolt, R. H., and Weglein, A. B., 1985, Migration and inversion of seismic data: *Geophysics*, **50**, 2458–2472.
- Tarantola, A., 1984, Inversion of seismic reflection data in the acoustic approximation: *Geophysics*, **49**, 1259–1266.
- Weglein, A., and Stolt, R., 1999, Migration-inversion revisited: *The Leading Edge*, August, 950–952, 975.
- Wu, R. S., and Toksoz, M. N., 1987, Diffraction tomography and multisource holography applied to seismic imaging: *Geophysics*, **52**, 11–25.
- Zhang, Y., 2004, True amplitude migration based on one-way wave equations: *Lecture Notes for UCSC WTOPi 2004 Workshop*, 1–24.

Mapping of water-bottom and diffracted 2D multiple reflections to image space

Gabriel Alvarez¹

ABSTRACT

Wave-equation migration with the velocity of the primaries maps non-diffracted water-bottom multiples to an hyperbola in subsurface-offset-domain-common-image-gathers. Furthermore, for positive surface offsets, the multiples are mapped to non-positive subsurface offsets if sediment velocity is faster than water. The larger the offset in the data space, the larger the subsurface offset and the shallower the image point. When migrated with the velocity of the water, the multiples are mapped to zero subsurface offset just as primaries migrated with the exact velocity. Diffracted multiples, on the other hand, map to positive or negative subsurface offsets depending on the relative position of the diffractor with respect to the common-midpoint. I present the equations of the image point coordinates in terms of the data space coordinates for diffracted and non-diffracted multiples from flat or dipping water-bottom in both subsurface-offset-domain common-image-gathers and angle-domain common-image-gathers. I illustrate the results with simple synthetic models.

INTRODUCTION

Attenuation of multiples in the image space is attractive because prestack wave-equation migration accurately handles the complex wave propagation of primaries. In subsurface-offset-domain common-image-gathers (SODCIG) the primaries are imaged at zero subsurface offset at the depth of the reflector if migrated with the correct velocity. Correspondingly, in angle-domain common-image-gathers (ADCIG) the primaries are imaged with flat moveout. Attenuation of multiples in image space depends on the difference in residual moveout between the primaries and the multiples, either in SODCIGs or ADCIGs (Sava and Guitton, 2003; Hargreaves et al., 2003; Alvarez et al., 2004). Understanding how wave-equation migration maps the multiples into SODCIGs and ADCIGs is therefore of paramount importance in order to design a proper strategy to attenuate the multiples in the image space.

Non-diffracted water-bottom multiples from a flat or dipping water-bottom are imaged as primaries. Thus, if the migration velocity is that of the water, they are mapped to zero

¹email: gabriel@sep.stanford.edu

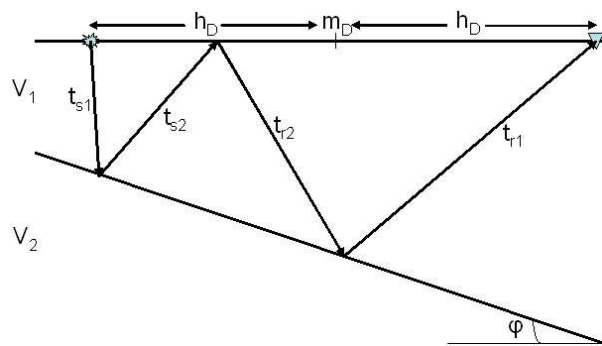
subsurface-offset in SODCIGs. Consequently, in ADCIGs, these multiples exhibit flat move-out just as primaries do (Alvarez, 2005). In the usual case of migration with velocities faster than water velocity, these multiples are mapped to subsurface offsets with the opposite sign with respect to the sign of the surface offsets. I will analytically show the moveout curve of these multiples in SODCIGs and ADCIGs.

Water-bottom diffracted multiples, on the other hand, even if from a flat water-bottom, do not migrate as primary reflections (Alvarez, 2005). That is, they do not focus to zero subsurface offset even if migrated with the water velocity. Obviously this happens because at the diffractor the reflection is not specular. I will show that these multiples migrate to both positive and negative subsurface offsets in SODCIGs depending on the relative position of the diffractor with respect to the receiver (for receiver-side diffracted multiples).

The next section presents a general formulation for computing the kinematics of diffracted and non-diffracted water-bottom multiples for both SODCIGs and ADCIGs. The following section then looks in detail at the special case of flat water-bottom where the equations simplify and some insight can be gained as to the analytical representation of the residual moveout of the multiples in both SODCIGs and ADCIGs. The next section presents a similar result for multiples from a dipping water-bottom. Although the equations are more involved and difficult to encapsulate in one single expression than those for the flat water-bottom, I show that we can still compute the image space coordinates of both the diffracted and non-diffracted multiples in terms of their data space coordinates. The last section discusses some of the implications of the results and the possibility that they can be used to attenuate the multiples in the image space. Detailed derivation of all the equations is included in the appendices.

KINEMATICS OF WATER-BOTTOM MULTIPLES IN IMAGE SPACE

Figure 1: Water-bottom multiple. The subscript s refers to the source and the subscript r to the receiver. `gabriel1-mul_sketch1` [NR]



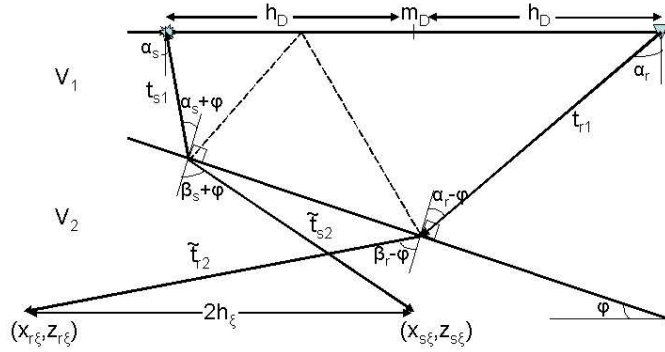
The propagation path of a water-bottom multiple, as shown in Figure 1, consists of four segments, such that the total travel-time for the multiple is given by

$$t_m = t_{s1} + t_{s2} + t_{r2} + t_{r1}, \quad (1)$$

where the subscript s refers to the source-side rays and the subscript r refers to the receiver-side rays. The data space coordinates are (m_D, h_D, t_m) where m_D is the horizontal position of the CMP gather and h_D is the half-offset between source and receiver. Wave-equation

migration maps the CMP gathers to SODCIGs with coordinates (m_ξ, h_ξ, z_ξ) where m_ξ is the horizontal position of the image gather, and h_ξ and z_ξ are the half subsurface-offset and the depth of the image, respectively. As illustrated in the sketch of Figure 2, at any given depth

Figure 2: Imaging of water-bottom multiple in SODCIG. The subscript ξ refers to the image point. gabriel1-mul_sktch2 [NR]



the image space coordinates of the migrated multiple are given by:

$$\begin{aligned} x_{s\xi} &= m_D - h_D + V_1(t_{s1} \sin \alpha_s + \rho \tilde{t}_{s2} \sin \beta_s), \\ x_{r\xi} &= m_D + h_D - V_1(t_{r1} \sin \alpha_r + \rho \tilde{t}_{r2} \sin \beta_r), \\ h_\xi &= \frac{x_{r\xi} - x_{s\xi}}{2} = h_D - \frac{V_1}{2} [t_{s1} \sin \alpha_s + t_{r1} \sin \alpha_r + \rho(\tilde{t}_{s2} \sin \beta_s + \tilde{t}_{r2} \sin \beta_r)], \end{aligned} \quad (2)$$

$$z_\xi = V_1(t_{s1} \cos \alpha_s + \rho \tilde{t}_{s2} \cos \beta_s) = V_1(t_{r1} \cos \alpha_r + \rho \tilde{t}_{r2} \cos \beta_r), \quad (3)$$

$$m_\xi = \frac{x_{r\xi} + x_{s\xi}}{2} = m_D + \frac{V_1}{2} (t_{s1} \sin \alpha_s - t_{r1} \sin \alpha_r + \rho(\tilde{t}_{s2} \sin \beta_s - \tilde{t}_{r2} \sin \beta_r)), \quad (4)$$

where V_1 is the water velocity, $\rho = V_2/V_1$ with V_2 the sediment velocity, and α_s, α_r are the acute takeoff angles of the source and receiver rays with respect to the vertical. The traveltime of the refracted ray segments \tilde{t}_{s2} and \tilde{t}_{r2} can be computed from two conditions: (1) at the image point the depth of both rays has to be the same (since we are computing horizontal subsurface offset gathers) and (2) $t_{s2} + t_{r2} = \tilde{t}_{s2} + \tilde{t}_{r2}$ which follows immediately from equation 1 since at the image point the extrapolated time equals the traveltime of the multiple. As shown in Appendix A, the traveltimes of the refracted rays are given by

$$\tilde{t}_{s2} = \frac{t_{r1} \cos \alpha_r - t_{s1} \cos \alpha_s + \rho(t_{s2} + t_{r2}) \cos \beta_r}{\rho(\cos \beta_s + \cos \beta_r)}, \quad (5)$$

$$\tilde{t}_{r2} = \frac{t_{s1} \cos \alpha_s - t_{r1} \cos \alpha_r + \rho(t_{s2} + t_{r2}) \cos \beta_s}{\rho(\cos \beta_s + \cos \beta_r)}. \quad (6)$$

The refracted angles are related to the takeoff angles by Snell's law: $\sin(\beta_s + \varphi) = \rho \sin(\alpha_s + \varphi)$ and $\sin(\beta_r - \varphi) = \rho \sin(\alpha_r - \varphi)$, from which we get

$$\sin \beta_s = \rho \sin(\alpha_s + \varphi) \cos \varphi - \sqrt{1 - \rho^2 \sin^2(\alpha_s + \varphi)} \sin \varphi, \quad (7)$$

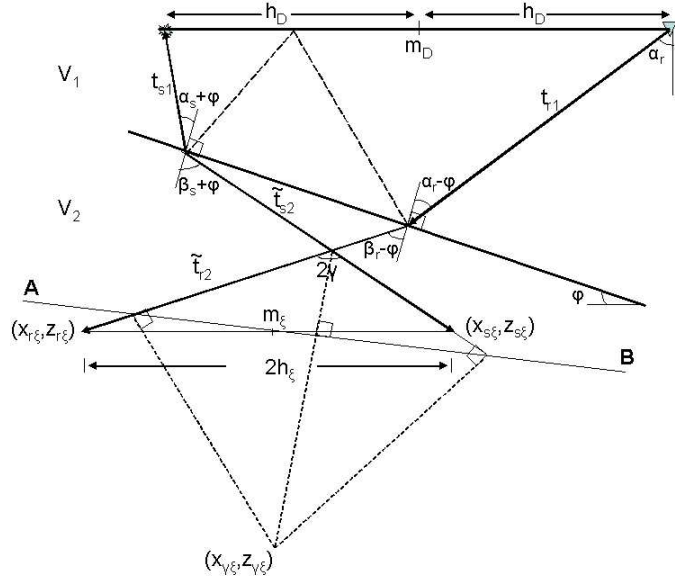
$$\sin \beta_r = \rho \sin(\alpha_r - \varphi) \cos \varphi + \sqrt{1 - \rho^2 \sin^2(\alpha_r - \varphi)} \sin \varphi, \quad (8)$$

$$\cos \beta_s = \sqrt{1 - \rho^2 \sin^2(\alpha_s + \varphi)} \cos \varphi + \rho \sin(\alpha_s + \varphi) \sin \varphi, \quad (9)$$

$$\cos \beta_r = \sqrt{1 - \rho^2 \sin^2(\alpha_r - \varphi)} \cos \varphi - \rho \sin(\alpha_r - \varphi) \sin \varphi. \quad (10)$$

Equations 2–10 are valid for any water-bottom multiple, whether from a flat or dipping water-bottom. They even describe the migration of source- or receiver-side diffraction multiples, since no assumption has been made relating α_r and α_s or the individual traveltime segments. In ADCIGs, the mapping of the multiples can be directly related to the previous equations by

Figure 3: Imaging of water-bottom multiple in ADCIG. The subscript ξ refers to the image point. The line AB represents the apparent reflector at the image point. gabriel1-mul_skch3
[NR]



the geometry shown in Figure 3. The half-aperture angle is given by

$$\gamma = \frac{\beta_r + \beta_s}{2}, \quad (11)$$

which is the same equation used for converted waves (Rosales and Biondi, 2005). The depth of the image point ($z_{\xi\gamma}$) is given by (Appendix B)

$$z_{\xi\gamma} = z_{\xi} - h_{\xi} \tan \gamma. \quad (12)$$

Equations 2–12 formally describe the image coordinates in terms of the data coordinates. They are, however, of little practical use unless we can relate the individual traveltime segments (t_{s1} , t_{s2} , \tilde{t}_{s2} , t_{r2} , \tilde{t}_{r2} , t_{r1}), and the angles α_s and α_r (which in turn determine β_s and β_r) to the known data space parameters (m_D , h_D , t_m , V_1 , ϕ and ρ). This may not be easy or even possible analytically for all situations, but it is for some simple but important models that I will now examine.

FLAT WATER-BOTTOM

Non-diffracted multiple

The traveltime of the water-bottom multiple is given by (Alvarez, 2005)

$$t_m = \frac{4}{V_1} \sqrt{\left(\frac{h_D}{2}\right)^2 + Z_{wb}^2} = \sqrt{t_m^2(0) + \left(\frac{2h_D}{V_1}\right)^2}, \quad (13)$$

which is simply the traveltime of a primary at twice the depth of the water-bottom $Z_{wb} = \frac{V_1 t_m(0)}{4}$. From Figure 4 it is clear that due to the symmetry of the problem, $t_{s1} = t_{s2} = t_{r1} =$

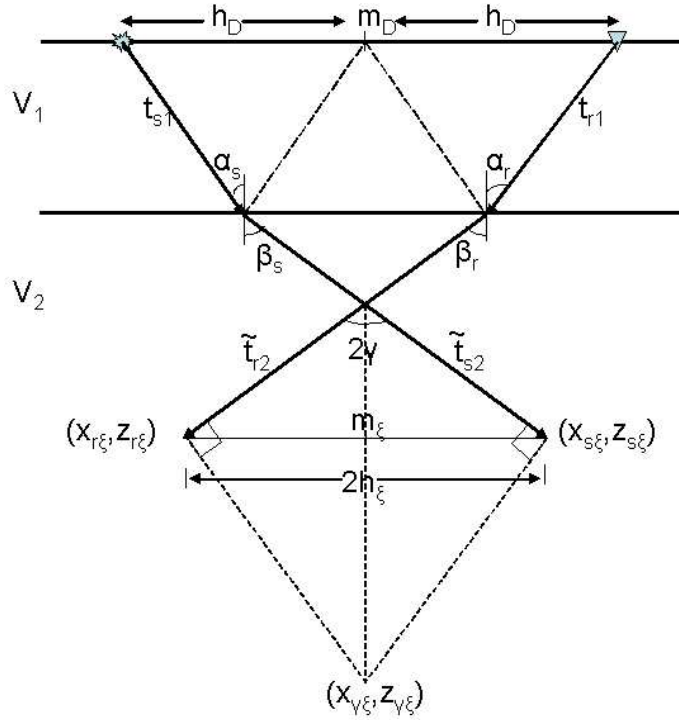


Figure 4: Imaging of water-bottom multiple for a flat water-bottom. Notice that $m_D = m_\xi$ and that the apparent reflector at the image point is flat. gabriel1-mul_sketch4 [NR]

$t_{r2} = t_m/4$ and $\alpha_s = \alpha_r$, which in turn means $\beta_s = \beta_r$. Furthermore, from Equations 5 and 6 it immediately follows that $\tilde{t}_{s2} = t_{s2}$ and $\tilde{t}_{r2} = t_{r2}$ which says that the traveltimes of the refracted rays are equal to the corresponding traveltimes of the multiple. Equation 2 thus simplifies to

$$h_\xi = \frac{h_D}{2}(1 - \rho^2), \quad (14)$$

which indicates that the subsurface offset at the image point of a trace with half surface offset h_D depends only on the velocity contrast between the water and the sediments. In particular, if the trace is migrated with the water velocity, *i.e.* $\rho = 1$, then $h_\xi = 0$ which proves the claim that the trace is imaged exactly as a primary since it is mapped to zero subsurface offset irrespective of its surface offset. It should also be noted that, since usually sediment velocity is faster than water velocity, then $\rho^2 > 1$ and therefore the multiples are mapped to subsurface offsets with the opposite sign with respect to the sign of the surface offset h_D when migrated with sediment velocity.

From Equation 3, the depth of the image point can be easily computed as

$$z_\xi = Z_{wb} + \frac{\rho}{2} \sqrt{h_D^2(1 - \rho^2) + 4Z_{wb}^2}, \quad (15)$$

which for migration with the water velocity reduces to $z_\xi = 2Z_{wb}$, which shows that the multiple is migrated as a primary at twice the water depth. Finally, from Equation 4, the horizontal position of the image point reduces to

$$m_\xi = m_D. \quad (16)$$

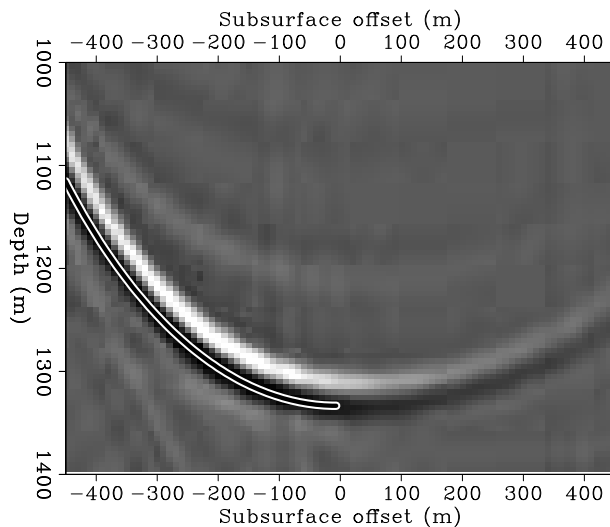
This result shows that the multiple is mapped in the image space to the same horizontal position as the corresponding CMP even if migrated with sediment velocity. This result is obviously a direct consequence of the symmetry of the raypaths of the multiple reflection in this case.

Equations 14–16 give the image space coordinates in terms of the data space coordinates. An important issue is the functional relationship between the subsurface offset and the image depth, since it determines the moveout of the multiples in the subsurface-offset-domain common-image-gathers (SODCIGs). Replacing $h_D = 2h_\xi/(1 - \rho^2)$ and $Z_{wb} = z_\xi(0)/(1 + \rho)$ in Equation 15 we get

$$z_\xi = \frac{z_\xi(0)}{1 + \rho} + \rho \sqrt{\left(\frac{z_\xi(0)}{1 + \rho}\right)^2 + \frac{h_\xi^2}{1 - \rho^2}} \quad (\rho \neq 1) \quad (17)$$

which shows that the moveout is an hyperbola (actually half of an hyperbola since we already established that $h_\xi \leq 0$ if $h_D \geq 0$). Figure 5 shows an SODCIG for a non-diffracted water-

Figure 5: Subsurface offset domain common image gather of a water-bottom multiple from a flat water-bottom. Water velocity is 1500 m/s, water depth 500 m, sediment velocity 2500 m/s and surface offsets from 0 to 2000 m. Overlaid is the residual moveout curve computed with Equation 17. `gabriel1-odcig1` [CR]



bottom multiple from a flat water-bottom 500 m deep. The data was migrated with a two-layer velocity model: the water layer of 1500 m/s and a sediment layer of velocity 2500 m/s. Larger subsurface offsets (which according to Equation 14 correspond to larger surface offsets) map to shallower depths (for the normal situation of $\rho > 1$), as we should expect since the rays are refracted to increasingly larger angles until the critical reflection angle is reached. Also notice that the hyperbola is shifted down by a factor $(1 + \rho)$ with respect to the image point when migrated with water velocity.

In angle-domain common-image-gathers (ADCIGs), the half-aperture angle reduces to $\gamma = \beta_s = \beta_r$, which in terms of the data space coordinates is given by

$$\gamma = \sin^{-1} \left[\frac{2\rho h_D}{V_1 t_m} \right]. \quad (18)$$

The depth of the image can be easily computed from Equation 12. In particular, if the data are migrated with the velocity of the water, $\rho = 1$, and therefore $z_{\xi\gamma} = 2Z_{wb}$ which means a

horizontal line in the $(z_{\xi\gamma}, \gamma)$ plane. Equivalently, we can say that the residual moveout in the $(z_{\xi\gamma}, \gamma)$ plane is zero, once again corroborating that the water-bottom multiple is migrated as a primary if $\rho = 1$. Equation 12 can be expressed in terms of the data space coordinates using Equations 14 and 15 and noting that

$$\tan \gamma = \tan \beta_s = \frac{\rho \sin \alpha_s}{\sqrt{1 - \rho^2 \sin^2 \alpha_s}} = \frac{2\rho h_D}{\sqrt{V_1^2 t_m^2 - 4\rho^2 h_D^2}} = \frac{\rho h_D}{\sqrt{4Z_{wb}^2 + h_D^2(1 - \rho^2)}} \quad (19)$$

If $\rho = 1$ this expression simplifies to $\tan \gamma = \frac{h_D}{2Z_{wb}}$, which is the aperture angle of a primary at twice the water-bottom depth. As we did with the SODCIG, it is important to find the

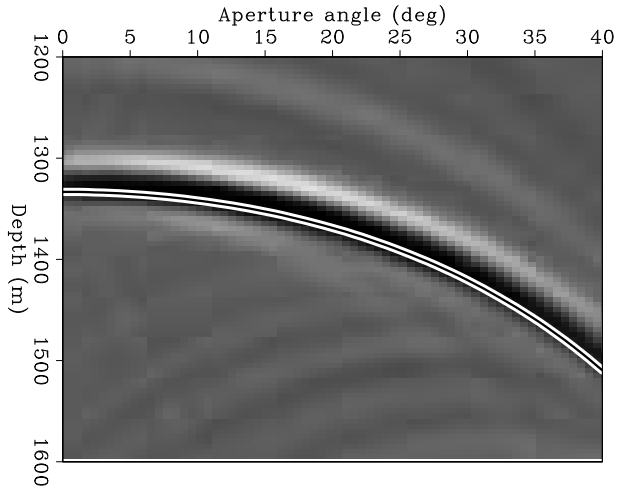


Figure 6: Angle domain common image gather corresponding to the SODCIG shown in Figure 5. Overlaid is the residual moveout curve computed with equation 20. `gabriel1-adcig1` [CR]

functional relationship between $z_{\xi\gamma}$ and γ since it dictates the residual moveout of the multiple in the ADCIG. Plugging Equations 14 and 15 into equation 12, using Equations 13, and 18 to eliminate h_D and simplifying we get

$$z_{\xi\gamma} = Z_{wb} \left[1 + \frac{\cos \gamma (\rho^2 - \tan^2 \gamma (1 - \rho^2))}{\sqrt{\rho^2 - \sin^2 \gamma}} \right] = \frac{z_{\xi\gamma}(0)}{1 + \rho} \left[1 + \frac{\cos \gamma (\rho^2 - \tan^2 \gamma (1 - \rho^2))}{\sqrt{\rho^2 - \sin^2 \gamma}} \right]. \quad (20)$$

Once again, when the multiple is migrated with the water velocity ($\rho = 1$) we get the expected result $z_{\xi\gamma} = z_{\xi\gamma}(0)$, that is, flat moveout (no angular dependence). Figure 6 shows the ADCIG corresponding to the SODCIG shown in Figure 5. Notice that the migrated depth at zero aperture angle is the same as that for zero sub-surface offset in Figure 5. For larger aperture angles, however, the migrated depth increases as indicated in equation 20 and as seen in the schematic of Figure 4.

Diffracted multiple

Consider now a diffractor sitting at the water-bottom as illustrated in the sketch in Figure 7. The source- and receiver-side multiples are described by equations 2–4 as did the water-bottom

whereas the traveltimes of the refracted rays can be computed from equation 5:

$$\tilde{t}_{s_2} = \frac{t_{s_2}(2\rho \cos \beta_r - \cos \alpha_s) + t_{r_1} \cos \alpha_r}{\rho(\cos \beta_r + \cos \beta_s)}, \quad \text{and} \quad \tilde{t}_{r_2} = \frac{t_{s_2}(2\rho \cos \beta_s + \cos \alpha_s) - t_{r_1} \cos \alpha_r}{\rho(\cos \beta_r + \cos \beta_s)}. \quad (27)$$

where, according to equations 9 and 10:

$$\cos \beta_s = \sqrt{1 - \rho^2 \sin^2 \alpha_s} \quad \text{and} \quad \cos \beta_r = \sqrt{1 - \rho^2 \sin^2 \alpha_r}. \quad (28)$$

In order to express h_ξ , z_ξ and m_ξ entirely in terms of the data space coordinates, all we need to do is compute the sines and cosines of α_s and α_r which can be easily done from the sketch of Figure 7:

$$\sin \alpha_s = \frac{X_{diff} - (m_D - h_D)}{3\sqrt{((X_{diff} - (m_D - h_D))/3)^2 + Z_{wb}^2}} \quad \cos \alpha_s = \frac{Z_{wb}}{\sqrt{((X_{diff} - (m_D - h_D))/3)^2 + Z_{wb}^2}}$$

$$\sin \alpha_r = \frac{(m_D + h_D) - X_{diff}}{\sqrt{((m_D + h_D) - X_{diff})^2 + Z_{wb}^2}} \quad \cos \alpha_r = \frac{Z_{wb}}{\sqrt{((m_D + h_D) - X_{diff})^2 + Z_{wb}^2}}$$

Notice that the diffraction multiple does not migrate as a primary even if migrated with water velocity. In other words, even if $\rho = 1$, $h_\xi \neq 0$. The only exception is when $X_{diff} = m_D + h_D/2$ since then the diffractor is in the right place to make a specular reflection and therefore is indistinguishable from a non-diffracted water-bottom multiple. In that case, $\alpha_r = \alpha_s$ (which in turn implies $\beta_r = \beta_s$) and from equations 5 and 6, $\tilde{t}_{r_2} = \tilde{t}_{s_2} = t_{s_2}$ and therefore equations 23–25 reduce to equations 14–16, respectively. Figure 8 shows two subsurface-offset sections

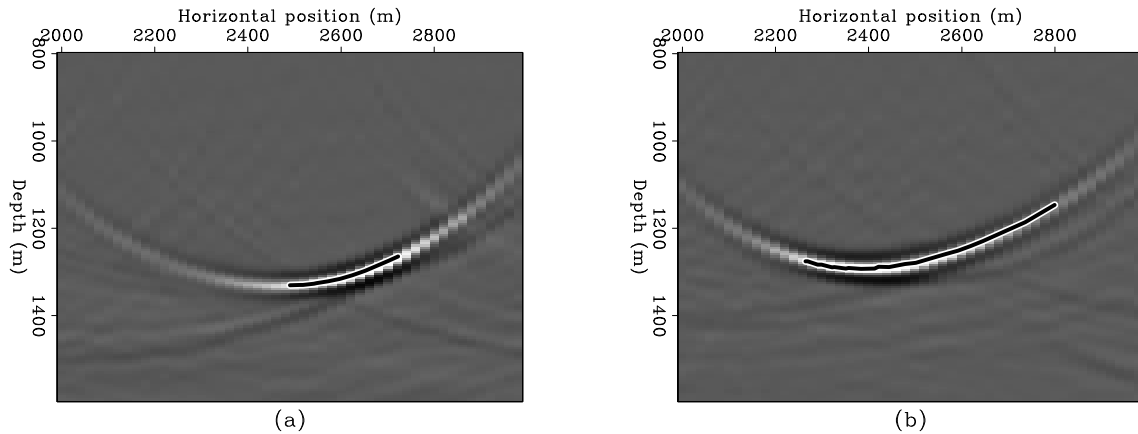


Figure 8: image sections at 0 and -400 m subsurface offset for a diffracted multiple from a flat water-bottom. The depth of the water-bottom is 500 m and the diffractor is located at 2500 m. The solid line represents image reflector computed with equations 24 and 25. [gabriel1-image2](#) [CR]

of a migrated diffracted multiple from a diffractor sitting on top of a flat reflector as in the

schematic of Figure 7. The diffractor position is $X_{diff} = 2,500$ m, the CMP range is from 2,000 m to 3,000 m, the offsets range from 0 to 2,000 m and the water depth is 500 m. The data were migrated with the same two-layer model described before. Panel (a) corresponds to zero subsurface offset ($h_\xi = 0$) whereas panel (b) corresponds to subsurface offset of -400 m. Overlaid are the residual moveout curves computed with equations 24 and 25. Obviously, the zero subsurface offset section is not a good image of the water-bottom or the diffractor.

Figure 9 shows three SODCIGs taken at locations 2,300 m, 2,500 m and 2,700 m. Unlike the non-diffracted multiple, this time energy maps to positive or negative subsurface offset depending on the relative position of the CMP with respect to the diffractor. In ADCIGs the aperture angle is given by equation 11 which, given the geometry of Figure 7, reduces to

$$\gamma = \frac{1}{2} \sin^{-1} [\beta_s + \beta_r] = \frac{1}{2} \sin^{-1} \left[\rho \sin \alpha_r \sqrt{1 - \rho^2 \sin^2 \alpha_s} + \rho \sin \alpha_s \sqrt{1 - \rho^2 \sin^2 \alpha_r} \right]. \quad (29)$$

The depth of the image is given by equation 12,

$$z_{\xi\gamma} = z_\xi - h_\xi \tan \left(\frac{1}{2} \sin^{-1} \left[\rho \sin \alpha_r \sqrt{1 - \rho^2 \sin^2 \alpha_s} + \rho \sin \alpha_s \sqrt{1 - \rho^2 \sin^2 \alpha_r} \right] \right). \quad (30)$$

Again, this equation shows that the diffracted multiple is not migrated as a primary even if

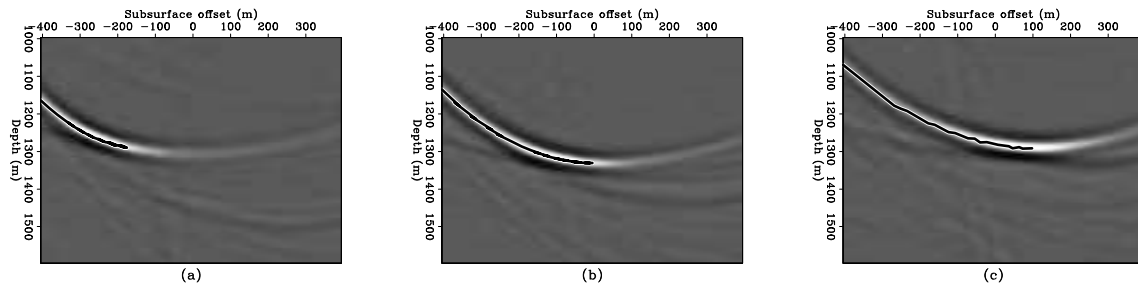


Figure 9: SODCIGs from a diffracted multiple from a flat water-bottom at locations 2,300 m, 2,500 m and 2,700 m. The diffractor is at 2,500 m. The overlaid residual moveout curves were computed with equations 23 and 24. [gabriel1-odcig2](#) [CR]

$\rho = 1$ (except in the trivial case $X_{diff} = m_D + h_D/2$ discussed before for which, since $\alpha_r = \alpha_s$, $\gamma = \beta_s = \beta_r$ in agreement with equation 19 and so equation 30 reduces to equation 20). Figure 10 shows the angle gathers corresponding to the SODCIGs of Figure 9. Notice the shift in the apex of the moveout curves.

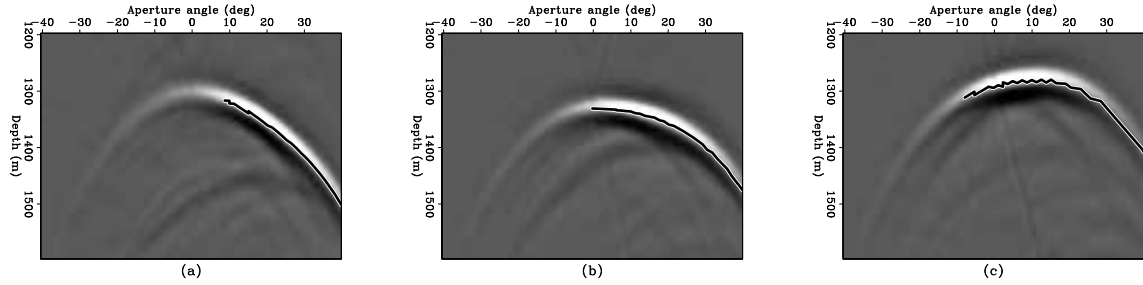


Figure 10: ADCIGs corresponding to the SODCIGs in Figure 9. The overlaid curves are the residual moveout curves computed with equations 24 and 30. `gabriel1-adcig2` [CR]

DIPPING WATER-BOTTOM

Water-bottom multiple

The water-bottom multiple from a dipping reflector has exactly the same kinematics as a primary from a reflector with twice the dip (Alvarez, 2005), that is,

$$t_m = \sqrt{\left(\frac{2\hat{Z}_D}{V_1}\right)^2 + \left(\frac{2h_D}{\hat{V}_{NMO}}\right)^2} = \sqrt{t_m^2(0) + \left(\frac{2h_D}{\hat{V}_{NMO}}\right)^2}, \quad (31)$$

where φ is the dip of the reflector, \hat{Z}_D is the perpendicular depth to the equivalent reflector with twice the dip (at the CMP location) and \hat{V}_{NMO} is the NMO velocity of the equivalent primary $\hat{V}_{NMO} = V_1/\cos(2\varphi)$.

Following the same procedure as for the flat water-bottom, we compute the coordinates of the image point using equations 2–4 and noting that in this case $\alpha_r = \alpha_s + 4\varphi$,

$$h_\xi = h_D - \frac{V_1}{2} [t_{s1} \sin \alpha_s + t_{r1} \sin(\alpha_s + 4\varphi) + \rho (\tilde{t}_{s2} \sin \beta_s + \tilde{t}_{r2} \sin \beta_r)], \quad (32)$$

$$z_\xi = V_1 \left(t_{r1} \cos \alpha_s + \rho \tilde{t}_{s2} \left[\sqrt{1 - \rho^2 \sin^2(\alpha_s + \varphi)} \cos \varphi + \rho \sin(\alpha_s + \varphi) \sin \varphi \right] \right), \quad (33)$$

$$m_\xi = m_D + \frac{V_1}{2} (t_{s1} \sin \alpha_s - t_{r1} \sin(\alpha_s + 4\varphi) + \rho (\tilde{t}_{s2} \sin \beta_s - \tilde{t}_{r2} \sin \beta_r)). \quad (34)$$

where, according to equations 7–10,

$$\sin \beta_s = \rho \sin(\alpha_s + \varphi) \cos \varphi - \sqrt{1 - \rho^2 \sin^2(\alpha_s + \varphi)} \sin \varphi, \quad (35)$$

$$\sin \beta_r = \rho \sin(\alpha_s + 3\varphi) \cos \varphi + \sqrt{1 - \rho^2 \sin^2(\alpha_s + 3\varphi)} \sin \varphi, \quad (36)$$

$$\cos \beta_s = \sqrt{1 - \rho^2 \sin^2(\alpha_s + \varphi)} \cos \varphi + \rho \sin(\alpha_s + \varphi) \sin \varphi, \quad (37)$$

$$\cos \beta_r = \sqrt{1 - \rho^2 \sin^2(\alpha_s + 3\varphi)} \cos \varphi - \rho \sin(\alpha_s + 3\varphi) \sin \varphi. \quad (38)$$

The traveltimes of the individual ray segments are computed by repeated application of the law of sines as shown in Appendix C:

$$t_{s1} = \frac{\tilde{Z}_s}{V_1 \cos(\alpha_s + \varphi)} = \frac{\tilde{Z}_D - h_D \sin \varphi}{V_1 \cos(\alpha_s + \varphi)}, \quad (39)$$

$$t_{s2} = \frac{t_{s1} \cos \alpha_s}{\cos(\alpha_s + 2\varphi)} = \frac{(\tilde{Z}_D - h_D \sin \varphi) \cos \alpha_s}{V_1 \cos(\alpha_s + \varphi) \cos(\alpha_s + 2\varphi)}, \quad (40)$$

$$t_{r2} = \frac{t_{s2} \cos(\alpha_s + \varphi)}{\cos(\alpha_s + 3\varphi)} = \frac{(\tilde{Z}_D - h_D \sin \varphi) \cos \alpha_s}{V_1 \cos(\alpha_s + 2\varphi) \cos(\alpha_s + 3\varphi)}, \quad (41)$$

$$t_{r1} = \frac{t_{r2} \cos(\alpha_s + 2\varphi)}{\cos(\alpha_s + 4\varphi)} = \frac{(\tilde{Z}_D - h_D \sin \varphi) \cos \alpha_s}{V_1 \cos(\alpha_s + 3\varphi) \cos(\alpha_s + 4\varphi)}, \quad (42)$$

where \tilde{Z}_D is the perpendicular depth to the reflector at the CMP location and is given by (Appendix C):

$$\tilde{Z}_D = \frac{V_1 t_m(0) \cos \varphi}{2[1 + \cos(2\varphi)]}. \quad (43)$$

Notice that this is not the same as \hat{Z}_D in equation 31, which corresponds to the perpendicular depth to the equivalent reflector whose primary has the same kinematics as the water-bottom multiple.

The traveltimes of the refracted ray segments are given by equations 5 and 6 with

$$\cos \alpha_r = \sqrt{1 - \sin^2(\alpha_s + 4\varphi)}, \quad \text{and} \quad \cos \alpha_s = \sqrt{1 - \sin^2 \alpha_s}. \quad (44)$$

In order for equation 32–34 to be useful in practice, we need to express them entirely in terms of the known data coordinates, which means that we need to find an expression for α_s in terms of (t_m, h_D, m_D, φ) . In Appendix C it is shown that

$$\alpha_s = \sin^{-1} \left[\frac{2h_D \cos(2\varphi)}{V_1 t_m} \right] - 2\varphi. \quad (45)$$

We now have all the pieces to compute the image space coordinates, since \tilde{t}_{s2} and \tilde{t}_{r2} can be computed from equations 5 and 6 using equations 35–45.

Appendix D shows that equations 32–34 reduce to the corresponding equations for the non-diffracted multiple from a flat water bottom when $\varphi = 0$, as they should.

Figure 11 shows the zero subsurface offset section from a migrated non-diffracted multiple from a dipping water-bottom. The overlaid curve was computed with equations 32–34. The dip of the water-bottom is 15 degrees and intercepts the surface at CMP location zero. The CMP range of the data is from 2000 to 3000 m and the surface offsets from 0 to 2000 m. The multiple was migrated with the same two-layer model described before. Notice how the multiple was migrated as a primary. Since the migration velocity is faster than water-velocity, the multiple is over-migrated and appears much steeper and shallower than it should (recall that it would be migrated as a reflector with twice the dip if the migration velocity were that

Figure 11: image section at zero subsurface offset for a non-diffracted multiple from a dipping water-bottom. The overlaid curve was computed with equation 34 and 33. `gabriel1-image3` [CR]

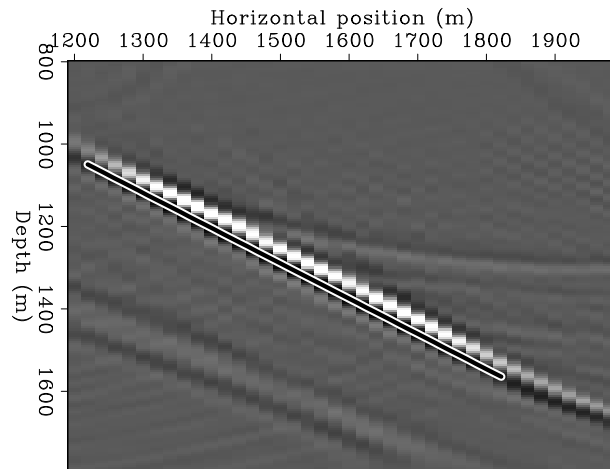
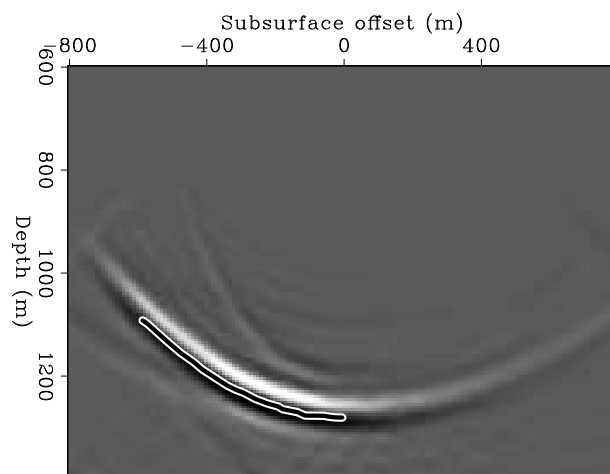


Figure 12: SODCIG from a non-diffracted multiple from a dipping water-bottom. The overlaid residual moveout curve was computed with equation 32 and 33. `gabriel1-odcig3` [CR]



of the water.) Figure 12 shows the SODCIG at CMP 1500 m in i Figure 11. Just as for the flat water-bottom, the multiple energy is mapped to negative subsurface offsets since $\rho > 1$. The overlaid curve is the moveout computed with equations 32–34. The aperture angle is given by equation 11 with

$$\beta_r = \sin^{-1}(\rho \sin(\alpha_s + 3\varphi)) - \varphi \quad \text{and} \quad \beta_s = \sin^{-1}(\rho \sin(\alpha_s + \varphi)) - \varphi \quad (46)$$

and α_s given by equation 45. The image depth in the ADCIG is given by equation 12 with β_s and β_r given by equation 46 and h_ξ and z_ξ given by equations 32 and 33. Figure 13 shows the ADCIG corresponding to the SODCIG in Figure 12. Notice that the apex is at zero aperture angle.

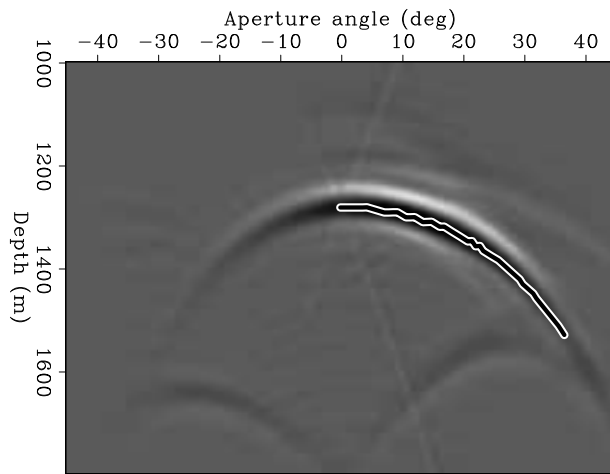


Figure 13: ADCIG corresponding to the SODCIG shown in Figure 12. The overlaid residual moveout curve was computed with equation 33, 11, 12, and 46. `gabriel1-adcig3` [CR]

Diffracted multiple

Figure 14 shows the raypath of a diffracted multiple from a dipping reflector. The image-space coordinates of the diffracted multiple are given by the same equations as the water-bottom multiple, *i.e.* equations 32–34. The main difference is that now $\alpha_r \neq \alpha_s + 4\varphi$. In fact, α_r depends exclusively on the position of the diffractor with respect to the receiver and is given by (Appendix E)

$$\alpha_r = \tan^{-1} \left[\frac{h_D + m_D - X_{diff}}{Z_{diff}} \right]. \quad (47)$$

The depth of the diffractor Z_{diff} can be computed as (Appendix E):

$$Z_{diff} = \tilde{Z}_D \cos \varphi + (X_{diff} - m_D) \tan \varphi, \quad (48)$$

where \tilde{Z}_D , as before, is the perpendicular distance between the CMP and the reflector. It can be computed from the traveltime of the diffracted multiple of the zero surface-offset trace as shown in Appendix E. The traveltime segments from the source to the diffractor are the same

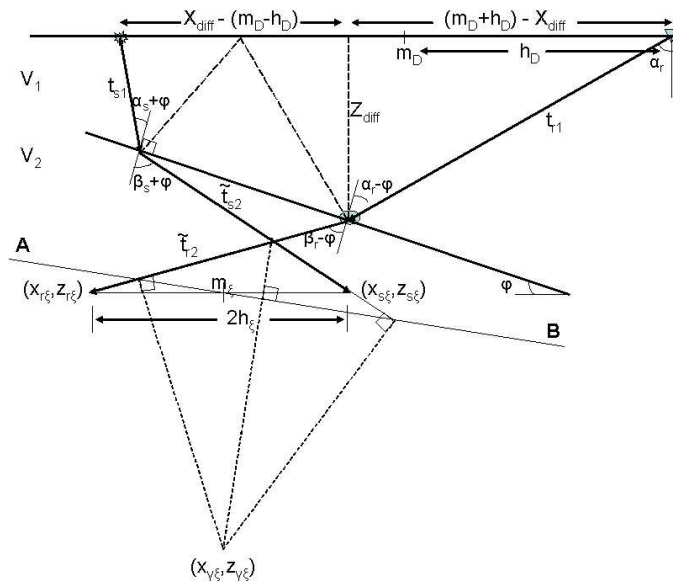


Figure 14: Diffracted multiple from a dipping water-bottom. Note that the receiver ray does not satisfy Snell's law at the diffractor. gabriel1-mul_sktch6 [NR]

as before and given by equations 39–41, while the traveltime from the diffractor to the receiver is simply

$$t_{r1} = \frac{1}{V_1} \sqrt{(h_D + (m_D - X_{diff}))^2 + Z_{diff}^2}. \tag{49}$$

In order to have the image coordinates entirely in terms of the data space coordinates all that is left is to compute α_s (Appendix E):

$$\alpha_s = \sin^{-1} \left[\frac{2\tilde{Z}_D \sin \phi + (h_D + X_{diff} - m_D)}{V_1 t_m - \sqrt{(h_D + m_D - X_{diff})^2 + Z_{diff}^2}} \right] - 2\phi. \tag{50}$$

Figure 15 shows three image sections at subsurface offsets of 0, -200 and 200 m. These

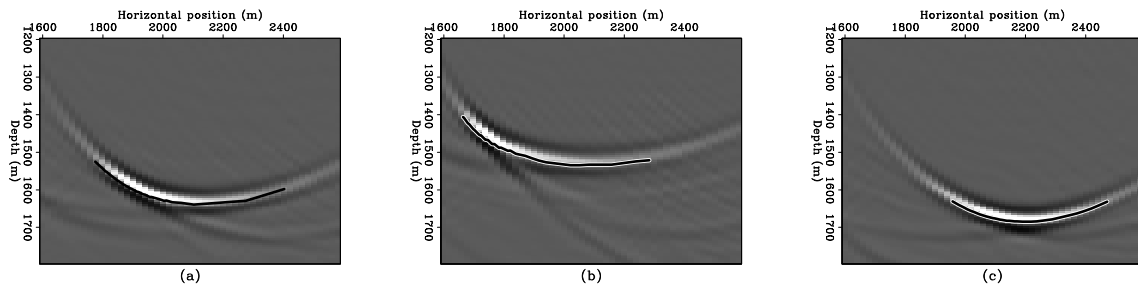


Figure 15: image sections at 0, -200 and 200 m subsurface offset for a diffracted multiple from a dipping water-bottom. gabriel1-image4 [CR]

sections are a poor representation of either the reflector or the diffractor since the diffracted multiple is not imaged as a primary. Figure 16 shows three SODCIGs at CMP locations 1800, 2200 and 2600 m. Again, we see that the SODCIGs are very different depending on their

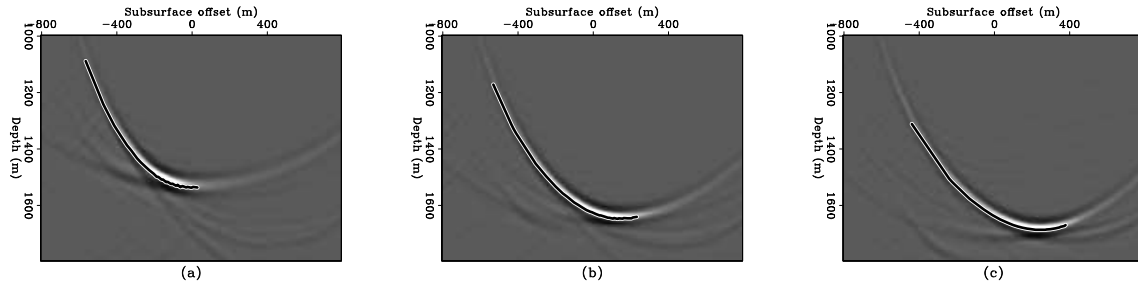


Figure 16: SODCIGs at three different CMP locations: 1,800, 2,000 and 2,200 m for a diffracted multiple from a dipping water-bottom. `gabriel1-odcig4` [CR]

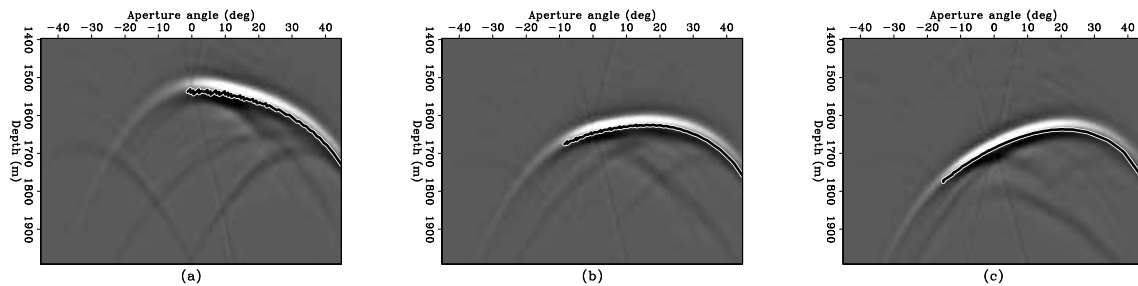


Figure 17: ADCIGs corresponding to the three SODCIGs of Figure 16. `gabriel1-adcig4` [CR]

relative position to the diffractor, unlike the situation with the non-diffracted multiple which maps to negative subsurface offsets (for $h_D \geq 0$) for all SODCIGs. The aperture angle and the image depth of the diffracted multiple in ADCIGs can also be computed with equations 11 and 12 with β_r and β_s given by equation 46. Figure 17 shows the ADCIG corresponding to the same ODCIG in Figure 16. Again, notice that the apex is shifted away from zero aperture angle.

DISCUSSION

The results of the previous sections illustrate that non-diffracted water-bottom multiples (whether from flat or dipping water-bottom) map to negative subsurface offsets (since $h_D \geq 0$ in this case), whereas primaries migrated with slower velocities would map to positive subsurface offsets. This suggests an easy strategy to attenuate these multiples. Migrate the data with a constant velocity that is faster than water velocity but slower than sediment velocity. Keep only the positive subsurface offsets and demigrate with the same velocity. In principle, the primaries would be restored (at least kinematically) whereas the multiples would be attenuated. Although not shown here, the same conclusion can be reached for higher-order non-diffracted water-bottom multiples. This strategy, however, would not work for diffracted multiples since they may map to positive subsurface offsets even when migrated with a velocity faster than water velocity as illustrated schematically in Figure 18. We can still separate these multiples from the primaries, but that requires the application of an appropriate Radon transform. An

apex-shifted tangent-squared Radon transform was applied by Alvarez et. al. (2004) to a real 2D section with good results, but the basic assumption there was that of no ray-bending at the water-bottom interface. It is expected that the more accurate equations derived here will allow the design of a better Radon transform and therefore a better degree of separation between primaries and diffracted multiples. This is the subject of continuing research. For

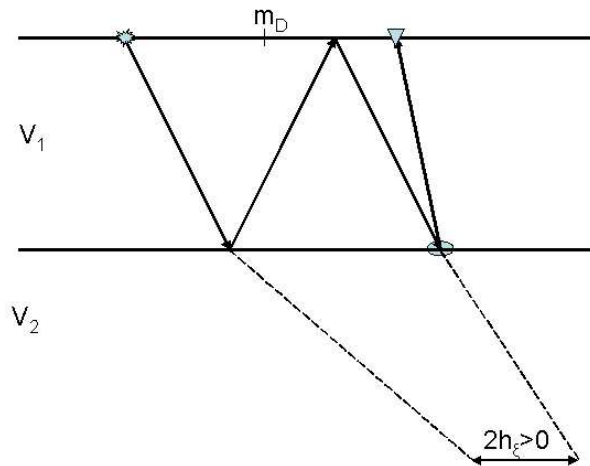


Figure 18: Sketch illustrating that diffracted multiples may map to positive subsurface offsets. [gabriel1-mul_sketch7](#) [NR]

the non-diffracted multiple from a flat water-bottom the mapping between the image-space coordinates and the data-space coordinates is essentially 2D since $m_D = m\xi$, which allowed the computation of closed-form expressions for the residual moveout of the multiples in both SODCIGs and ADCIGs. For diffracted multiples in particular, it is not easy to compute equivalent closed-form expressions, but we can compute numerically the residual moveout curves given the expression for (h_ξ, z_ξ, m_ξ) in terms of the data-space coordinates (t_m, h_D, m_D) , φ and X_{diff} . In principle, the dip of the water-bottom can be estimated from the data and the position of the diffractor corresponds to the lateral position of the apex of the multiple diffraction in a shot gather as illustrated in the sketch of Figure 19.

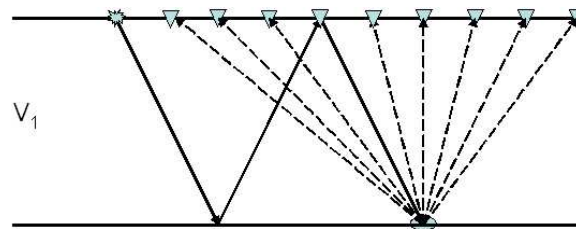


Figure 19: Sketch illustrating the raypaths of a diffracted multiple in a shot gather. The lateral position of the diffractor corresponds to the apex of the moveout curve. [gabriel1-mul_sketch8](#) [NR]

CONCLUSIONS

Non-diffracted water-bottom multiples, whether from a flat or dipping water-bottom, map to zero or negative subsurface offsets when migrated with the velocity of the sediments $\rho > 1$ for $h_D \geq 0$. On the other hand, primaries migrated with slower velocities map to positive subsurface offsets. It may be possible to exploit this fact to attenuate these multiples.

Diffracted water-bottom multiples, in contrast, map to both positive and negative subsurface offsets depending on the relative position of the CMP and the diffractor. To attenuate these multiples we need an accurate representation of their residual moveouts in either SODCIGs or ADCIGs as presented here to design a suitable Radon transform that focuses these multiples to predictable locations in the Radon domain. This is the subject of ongoing research.

REFERENCES

- Alvarez, G., Biondi, B., and Guitton, A., 2004, Attenuation of diffracted multiples in angle-domain common-image gathers:, *in* 74th Ann. Internat. Mtg. Soc. of Expl. Geophys., 1301–1304.
- Alvarez, G., 2005, Water-bottom and diffracted 2D multiple reflections in data space and image space: SEP-120, 363–374.
- Biondi, B., and Symes, W., 2004, Angle-domain common-image gathers for migration velocity analysis by wavefield-continuation imaging: Angle-domain common-image gathers for migration velocity analysis by wavefield-continuation imaging:, Soc. of Expl. Geophys., Geophysics, 1283–1298.
- Hargreaves, N., Wombell, R., and West, B. V., 2003, Multiple attenuation using an apex-shifted radon transform: 65th Conference and Exhibition, EAEG, Strategies towards multi-dimensional multiple attenuation.
- Rosales, D. A., and Biondi, B., 2005, Converted-mode angle-domain common-image gathers for migration velocity analysis: SEP-120, 283–296.
- Sava, P., and Guitton, A., 2003, Multiple attenuation in the image space: SEP-113, 31–44.

APPENDIX A

COMPUTATION OF TRAVELTIME FOR REFRACTED RAYS

In this Appendix I derive equations 5 and 6. From equation 3 we have:

$$t_{s_1} \cos \alpha_s + \rho \tilde{t}_{s_2} \cos \beta_s = t_{r_1} \cos \alpha_r + \rho \tilde{t}_{r_2} \cos \beta_r, \quad (\text{A-1})$$

and, from the condition that the sum of the traveltimes of the extrapolated rays at the image point has to be equal to the traveltimes of the multiple we have

$$t_{s_2} + t_{r_2} = \tilde{t}_{s_2} + \tilde{t}_{r_2}. \quad (\text{A-2})$$

Solving those two equations for \tilde{t}_{s_2} and \tilde{t}_{r_2} we get

$$\tilde{t}_{s_2} = \frac{t_{r_1} \cos \alpha_r - t_{s_1} \cos \alpha_s + \rho(t_{s_2} + t_{r_2}) \cos \beta_r}{\rho(\cos \beta_s + \cos \beta_r)}, \quad (\text{A-3})$$

$$\tilde{t}_{r_2} = \frac{t_{s_1} \cos \alpha_s - t_{r_1} \cos \alpha_r + \rho(t_{s_2} + t_{r_2}) \cos \beta_s}{\rho(\cos \beta_s + \cos \beta_r)}. \quad (\text{A-4})$$

It is interesting to check these equations in two particular cases. For a non-diffracted flat water-bottom multiple, we have $\alpha_s = \alpha_r$, $\beta_s = \beta_r$, $t_{s_1} = t_{s_2} = t_{r_2} = t_{r_1}$ and therefore we get $\tilde{t}_{s_2} = t_{s_2}$ and $\tilde{t}_{r_2} = t_{r_2}$ as the geometry of the problem requires. Notice that this is true for any ρ . The second case is for a non-diffracted water-bottom multiple migrated with water velocity. In that case, $\beta_s = \alpha_s$ and $\beta_r = \alpha_r$. Furthermore, since the multiple behaves as a primary, $(t_{s_1} + t_{s_2}) \cos \alpha_s = (t_{r_1} + t_{r_2}) \cos \alpha_r$ and we again get $\tilde{t}_{s_2} = t_{s_2}$ and $\tilde{t}_{r_2} = t_{r_2}$.

APPENDIX B

COMPUTATION OF IMAGE DEPTH IN ADCIGS

Figure B-1: Sketch to show the computation of the image depth in an ADCIG. [gabriel1-mul_sketch17](#) [NR]

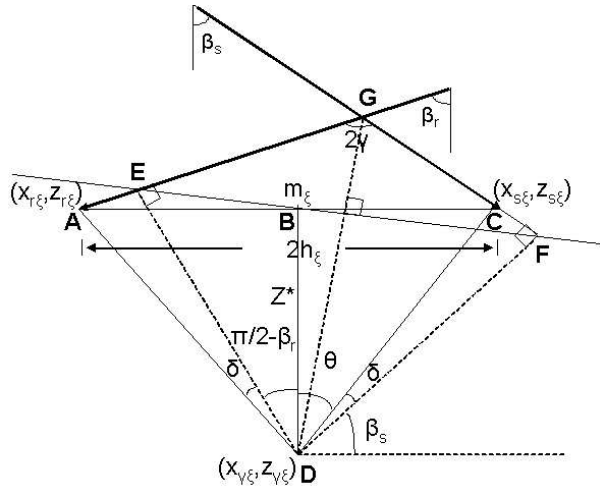


Figure B-1 shows the basic construction to compute the image depth in ADCIGs based on the image depth is SOCIGs. Triangles ABD and CBD are congruent since they have one side common and the other equal because $|AB|=|BC|=h_\xi$. Therefore, $\theta = \pi/2 - \beta_r + \delta$. Also, triangles AED and FCD are congruent because $|AD|=|CD|$ and also $|AE|=|CF|$ (Biondi and Symes, 2004). Therefore, the angle δ in triangle DCF is the same as in triangle AED. We can compute δ from the condition

$$\begin{aligned} \theta + \delta + \beta_s &= \frac{\pi}{2}, \\ \frac{\pi}{2} - \beta_r + \delta + \delta + \beta_s &= \frac{\pi}{2}, \\ \delta &= \frac{\beta_r - \beta_s}{2}. \end{aligned}$$

Figure C-2: Sketch to show the computation of t_{r_2} and t_{r_1} for a non-diffracted multiple from a dipping water-bottom. gabriel1-mul_skтч10 [NR]

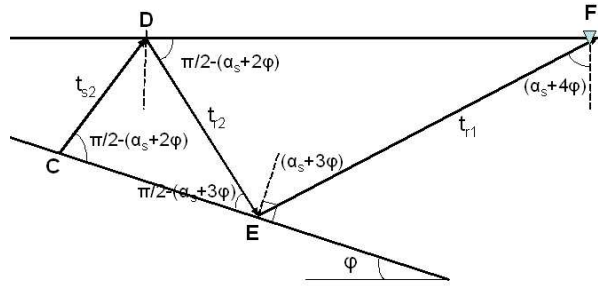
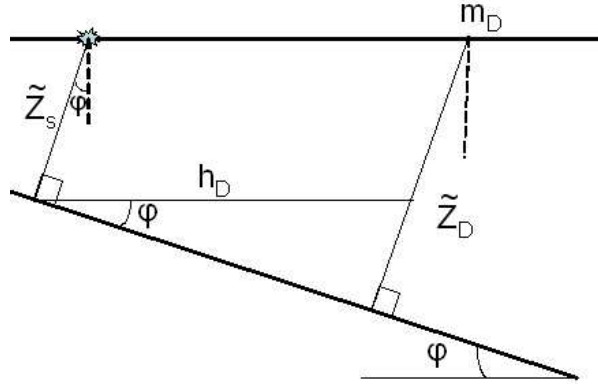


Figure C-3: Sketch to show the computation of \tilde{Z}_s in equation C-5. gabriel1-mul_skтч11 [NR]



These equations are in terms of \tilde{Z}_s , which is not known. However, from Figure C-3 we see that

$$\tilde{Z}_s = \tilde{Z}_D - h_D \sin \varphi, \quad (\text{C-5})$$

and \tilde{Z}_D can be computed from the traveltime of the zero surface-offset trace, since, according to Figure C-4

$$t_m(0) = \frac{2\tilde{Z}_D}{V_1 \cos \varphi} + \frac{2\tilde{Z}_D \cos(2\varphi)}{V_1 \cos \varphi} = \frac{2\tilde{Z}_D(1 + \cos(2\varphi))}{V_1 \cos \varphi}, \quad (\text{C-6})$$

from which it follows immediately that

$$\tilde{Z}_D = \frac{V_1 t_m(0) \cos \varphi}{2[1 + \cos(2\varphi)]}. \quad (\text{C-7})$$

Finally, we need to compute α_s . Applying the law of sines to triangle ABC in Figure C-5 we get

$$\sin(\alpha_s + 2\varphi) = \frac{2h_D \cos(2\varphi)}{V_1 t_m}, \quad (\text{C-8})$$

from which we get

$$\alpha_s = \sin^{-1} \left[\frac{2h_D \cos(2\varphi)}{V_1 t_m} \right] - 2\varphi. \quad (\text{C-9})$$

Figure C-4: Sketch to show the computation of \tilde{Z}_D in equation C-7.

`gabriel1-mul_skth12` [NR]

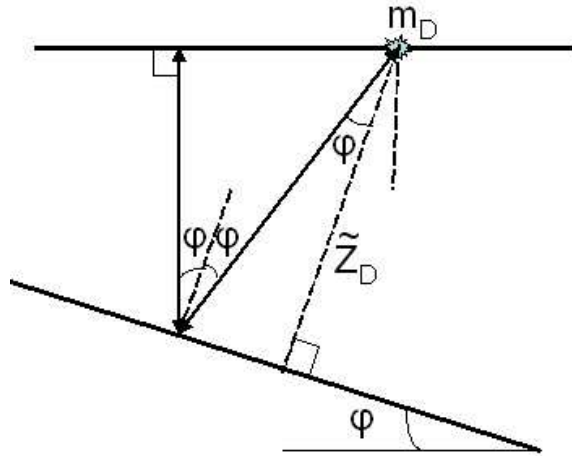
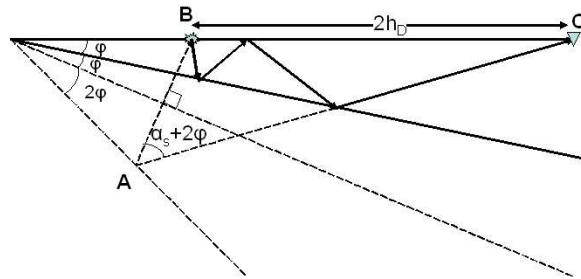


Figure C-5: Sketch to compute the takeoff angle of the source ray from a non-diffracted multiple from a dipping water-bottom.

`gabriel1-mul_skth16` [NR]



APPENDIX D

FROM DIP TO NO DIP FOR NON-DIFFRACTED MULTIPLE

In this Appendix, I show that the equations for the non-diffracted multiple from a dipping water-bottom reduce to the equations for a flat water-bottom when $\varphi = 0$ as they should. Setting $\varphi = 0$ in equations 39 through 42 we obtain

$$t_{s_2} = t_{r_2} = t_{r_1} = t_{s_1} = \frac{\tilde{Z}_s}{\cos \alpha_s} \quad (\text{D-1})$$

and from equations 5 and 6 we get (as discussed at the end of Appendix A) $\tilde{t}_{r_2} = t_{r_2}$ and $\tilde{t}_{s_2} = t_{s_2}$. Therefore,

$$h_\xi = 2h_D - V_1[t_{s_1} \sin \alpha_s + t_{r_1} \sin \alpha_r + \rho(\tilde{t}_{s_2} \sin \beta_s + \tilde{t}_{r_2} \sin \beta_r)] \quad (\text{D-2})$$

$$= 2h_D - V_1[2t_{s_1} \sin \alpha_s + \rho^2(t_{s_2} \sin \alpha_s + t_{s_2} \sin \alpha_s)] \quad (\text{D-3})$$

$$= 2(h_D - V_1 t_{s_1} \sin \alpha_s (1 + \rho^2)) \quad (\text{D-4})$$

$$= 2h_D - h_D(1 + \rho^2) = h_D(1 - \rho^2) \quad (\text{D-5})$$

Similarly,

$$z_{\xi} = V_1(t_{r_1} + \rho \tilde{t}_{s_2}) \sqrt{1 - \rho^2 \sin^2 \alpha_s} \quad (\text{D-6})$$

$$= V_1 t_{s_1} [\cos \alpha_s + \rho \sqrt{1 - \rho^2 \sin^2 \alpha_s}] \quad (\text{D-7})$$

$$= Z_{wb} + \frac{\rho V_1 t_m}{4} \sqrt{1 - \rho^2 \left(\frac{2h_D}{V_1 t_m} \right)^2} \quad (\text{D-8})$$

$$= Z_{wb} + \frac{\rho}{4} \sqrt{(V_1 t_m)^2 - \rho^2 (2h_D)^2} \quad (\text{D-9})$$

$$= Z_{wb} + \frac{\rho}{4} \sqrt{4Z_{wb}^2 + 4h_D^2(1 - \rho^2)} = Z_{wb} + \frac{\rho}{2} \sqrt{Z_{wb}^2 + h_D^2(1 - \rho^2)} \quad (\text{D-10})$$

Finally,

$$m_{\xi} = m_D + \frac{V_1}{2} (t_{s_1} \sin \alpha_s - t_{r_1} \sin \alpha_s) + \rho (\tilde{t}_{s_2} \sin \beta_s - \tilde{t}_{r_2} \sin \beta_r) \quad (\text{D-11})$$

$$= m_D + \frac{V_1}{2} (t_{s_1} \sin \alpha_s - t_{s_1} \sin \alpha_s) + \rho^2 (t_{s_2} \sin \alpha_s - t_{s_2} \sin \alpha_s) = m_D \quad (\text{D-12})$$

APPENDIX E

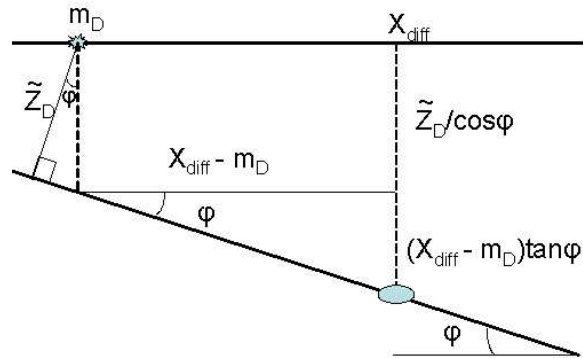
COMPUTATION OF TAKEOFF ANGLES FOR DIFFRACTED MULTIPLE

From Figure 14 we can immediately compute the takeoff angle of the diffracted receiver ray as

$$\alpha_r = \tan^{-1} \left[\frac{h_D + m_D - X_{diff}}{Z_{diff}} \right]. \quad (\text{E-1})$$

In this equation the depth of the diffractor is not known, but it can be calculated from the

Figure E-1: Sketch showing the geometry of the zero surface half-offset diffracted multiple from a dipping water-bottom. gabriell-mul_sktch13 [NR]



geometry of Figure E-1:

$$Z_{diff} = \frac{\tilde{Z}_D}{\cos \varphi} + (X_{diff} - m_D) \tan \varphi \quad (\text{E-2})$$

As we did for the diffracted multiple from the flat water-bottom, we can use the traveltime of the multiple at the zero surface-offset trace to compute \tilde{Z}_D , except that this time the computation is much more involved. Figure E-2 shows the basic geometry. From triangle ABC we have

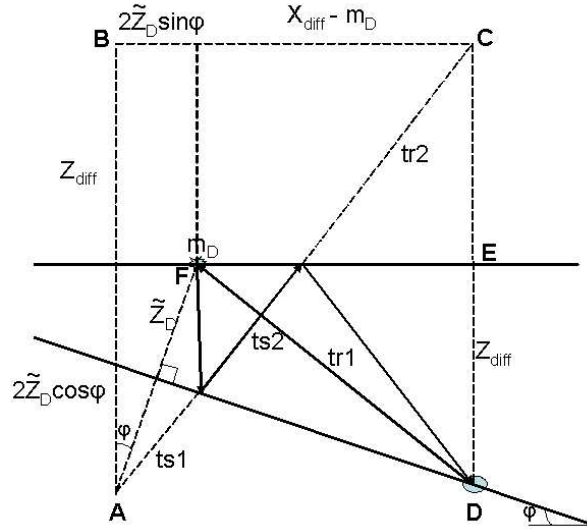
$$[V_1(t_m(0) - t_{r_1}(0))]^2 = (2\tilde{Z}_D \cos \varphi + Z_{diff})^2 + (2\tilde{Z}_D \sin \varphi + (X_{diff} - m_D))^2, \quad (E-3)$$

where t_{r_1} is the traveltime of the diffracted segment that, according to triangle DEF in Figure E-2 is given by

$$[V_1 t_{r_1}(0)]^2 = Z_{diff}^2 + (X_{diff} - m_D)^2. \quad (E-4)$$

Replacing equations E-2 and E-4 into equation E-3 gives a quartic equation for \tilde{Z}_D which can

Figure E-2: Sketch to compute \tilde{Z}_D in equations A-1, E-3 and E-4. gabriel1-mul_sktch14 [NR]



be solved numerically. Once \tilde{Z}_D is known, we can easily compute Z_{diff} with equation E-2 and therefore α_r with equation E-1 in terms of the known quantities h_D , m_D , X_{diff} and $t_m(0)$. In order to compute α_s , we apply the law of sines to triangle ABC in Figure E-3 to get

$$\sin(\alpha_s + 2\varphi) = \frac{2\tilde{Z}_s \sin \varphi + (X_{diff} - m_D + h_D)}{V_1(t_m - t_{r_1})}, \quad (E-5)$$

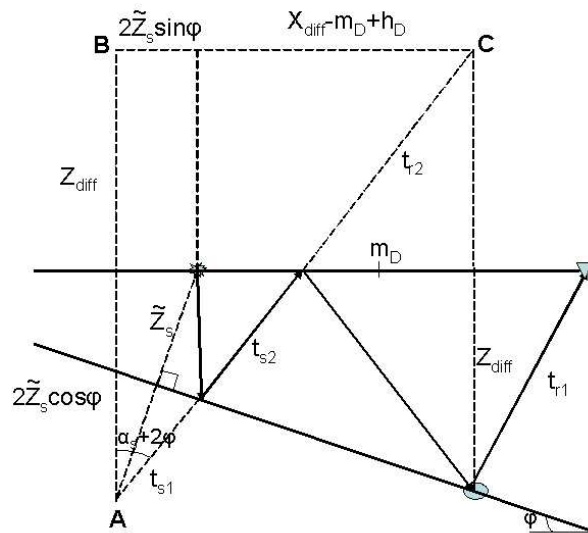
where $\tilde{Z}_s = \tilde{Z}_D - h_D \sin \varphi$ and $V_1 t_{r_1}$ is the length of the diffracted receiver ray and is given by

$$V_1 t_{r_1} = \sqrt{(h_D + m_D - X_{diff})^2 + Z_{diff}^2} \quad (E-6)$$

Therefore, plugging equation E-6 into equation E-5 we get equation 50:

$$\alpha_s = \sin^{-1} \left[\frac{2\tilde{Z}_D \sin \varphi + (h_D + X_{diff} - m_D)}{V_1 t_m - \sqrt{(h_D + m_D - X_{diff})^2 + Z_{diff}^2}} \right] - 2\varphi. \quad (E-7)$$

Figure E-3: Sketch to compute the takeoff angle of the source ray from a diffracted multiple.
 gabriell-mul_sktch15 [NR]



Imaging primaries and multiples simultaneously with depth-focusing

Huazhong Wang¹

ABSTRACT

Seismic imaging amplitudes are extracted with the imaging conditions $t = 0$ and $h = 0$, where $t = 0$ means that the take-off time of the upward-coming wave is zero, and $h = 0$, with h the half-offset between the source and receiver position, means that the downward-going and upward-coming waves meet together during the wavefield extrapolation. However, $h = 0$ makes no sense for multiples imaging. This imaging condition is suitable for imaging the primary, where the source position must be known. I introduce an imaging condition for imaging primaries and multiples simultaneously. The imaging condition, in essence, states that the take-off time of the upcoming wave equals zero, and that the radius of curvature of the wavefront of the upcoming scattered wavefield equals zero. It is known that the primary and multiple scattered waves will be focused during the wavefield depth extrapolation, but the primary and multiple scattered waves at the same depth focus at different times; this is because the traveltimes from the source to the scattering point are different for the primaries and multiples, even for the same scattering point. The focused scattered wave can be picked out, and the image is formed at the focusing point. The advantages of the method are several: the primary and multiples can be imaged simultaneously, only the up-coming wave must be downward extrapolated, all the scattered wavefields in the different shot gathers can be added together and simultaneously extrapolated, and the source position needs not be known. Its disadvantage is that the imaging condition is much more difficult to use.

INTRODUCTION

Usually, multiples in seismic data have been considered as noise for the imaging of the primaries (Berkhout and Verschuur, 1997). This is because it is difficult to put the multiples onto their scattering points, since the commonly used imaging conditions can not correctly and simultaneously pick up both the focused primaries and multiples. Schuster et al. (2003) proposed that if the source below the surface is unknown, the autocorrelation of each trace can be used to determine a pseudo source on the surface, since the autocorrelation of the direct wave is $t = 0$ time delay and the direct wave is thus eliminated in the autocorrelogram. The autocorrelogram can be thought to be acquired with the pseudo shot-receiver pair at the surface. Therefore, conventional prestack depth migration can focus and image ghost wave, or the

¹email: wang@sep.stanford.edu

first-order multiple. However, the disadvantages of the method are that the autocorrelogram does not satisfy the wave equation, and the traveltimes of the direct wave can not be correctly estimated and cancelled, which makes the travel time calculation in the integral migration not match the travel time in the autocorrelogram and the imaging noises occur. The crosstalk in the autocorrelogram also causes the imaging noise. On the other hand, the ghost wave is the first-order multiple and the imaging of higher-order multiples is ignored.

The imaging condition proposed by Claerbout (1971) should be modified if primaries and multiples are simultaneously imaged, whether the source position is known or unknown. The imaging condition I propose states that the radius of curvature of the wavefront equals zero. This is called the depth-focusing imaging condition. MacKay and Abma (1993) use depth focusing to carry out velocity analysis. If the migration velocity is larger than the medium velocity, then the focusing depth is less than the reflection depth, and the imaging depth is larger than the reflection depth; on the other hand, if the migration velocity is less than the medium velocity, then the focusing depth is greater than the reflection depth, and the imaging depth is less than the reflection depth. The real reflection depth lies at the mid-point between the focusing depth and the imaging depth. In that paper, the authors proposed a method for estimating the radius of the curvature of the wavefront. However the formula is suitable only for imaging the primaries. For a given scattering point, the primary and multiple scattering from it are simultaneously focused at the same depth in the model space and at different times in the data space with the downward wavefield continuation. The "focusing" means that the received scattered wavefield is collapsed into the scattering point, and the radius of curvature of the wavefront diminishes to zero. With the depth-focusing imaging condition, the focused imaging values of the primary and multiples can be simultaneously picked up from the depth-extrapolated wavefield, which is expressed in the time domain. The following are some advantages of depth-focusing imaging. The primaries and multiples (including the higher-order multiples) can be simultaneously imaged; the source position can be known (for the primaries) or unknown (for the multiples); all of the scattered wavefield can be added together, and computation efficiency can be improved. The disadvantage is that the depth-focusing imaging condition is difficult to use, especially for data with a lot of noise.

PRINCIPLES OF FOCUSING

Figure 1 geometrically shows the depth-focusing process of the primary scattered wavefield, and Figure 2 shows the same process for the multiple scattered wavefield. Comparing the two figures, it is clearly seen that the focusing process is the same for a scattering point, whether the scattered wavefield from it is primary or multiple scattering. The imaging condition of prestack migration is that the arrival time of the downgoing wave equals the take-off time of the upcoming wave (Claerbout, 1971). However, conventionally, the downgoing wave means the primary downgoing wave, not the multiple downgoing wave. It is difficult to determine the traveltimes of the multiple downgoing wave. Therefore, with this imaging condition, it is difficult to image the primaries and the multiples simultaneously. The conventional imaging condition implicitly tell us that the image of a reflector appears at the point, at which the received scattered wavefield is collapsed. At that point, the arrival time of the downgoing wave

Figure 1: The depth focusing of the primary scattering wavefield with the extrapolation. The radius of curvature of the wavefront diminishes to zero with the downward wavefield continuation.

`huazhong2-Scattering_primary`

[CR]

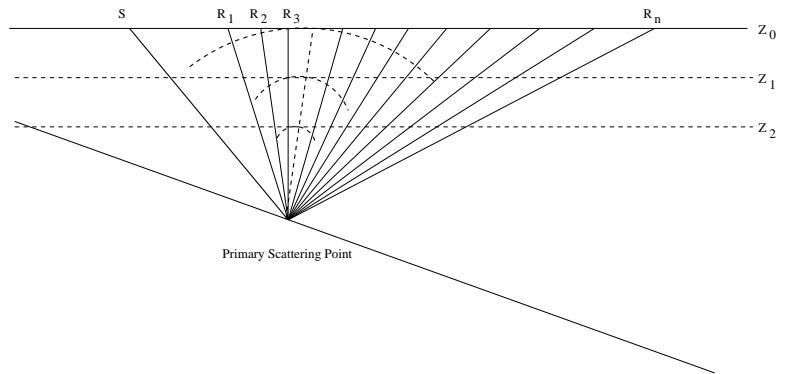
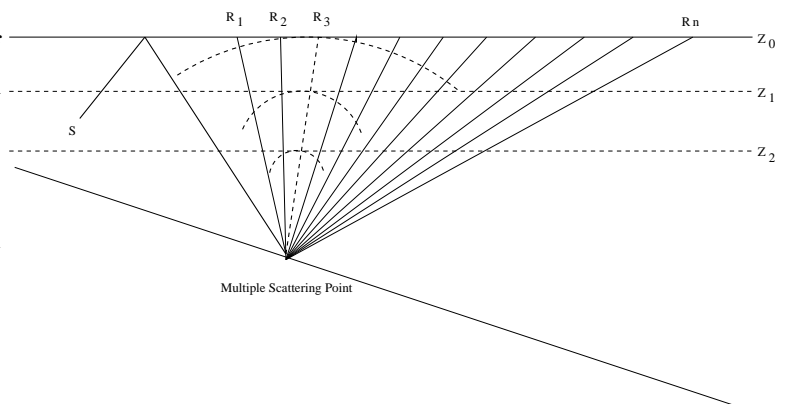


Figure 2: The depth focusing of the multiple scattering wavefield with the extrapolation. The source position can be unknown. The radius of curvature of the wavefront diminishes into zero with the downward wavefield continuation. The higher-order multiples can be focused also.

`huazhong2-Scattering_multiples`

[CR]



equals the take-off time of the upcoming wave, and the radius of curvature of the scattered wavefield diminishes to zero. The radius of curvature of the scattered wavefield diminishes to zero means that the scattered wavefield is focused to the scattering point. Unlike imaging for the primaries, for imaging of multiples, the concept of offset makes no sense. For multiples imaging, the offset should be calculated with the "pseudo" source and receiver position. However, it is not easy to determine the "pseudo" source position for the higher-order multiples. In fact, the statement that the arrival time of the downgoing wave equals the take-off time of the upcoming wave is equivalent to saying that the radius of curvature of the scattering wavefield diminishes to zero. However, the latter is much more prevalent than the former. The latter can be used to image the primaries and the multiples, whether the source position is known or unknown, because the only criterion is whether the scattering wavefield is focused or not. The latter can be called the depth-focusing imaging condition. The former is a model-driven process; the latter is a hybrid-driven process. Wavefield extrapolation is model-driven, and picking the focused amplitude is data-driven.

IMPLEMENTATION OF DEPTH-FOCUSING

Estimating whether the scattering wavefield is focused or not is difficult for simultaneously imaging primaries and multiples with depth-focusing. The wavefield extrapolation is carried out in the depth domain, and picking the image amplitude must be implemented in the time domain, since the traveltim from the source to the scattering point is not necessarily known.

Assuming that the macro velocity model is reliable, the horizontal positions of the focused scattering points are correct. The wavefield extrapolation depth determines the focused depth, which is also correct under the assumption. The obvious method is to use the amplitude of the focused scattering wavefield. When a scattered wavefield is focused, the amplitude at the focused point is maximized. During the process of wavefield extrapolation, the amplitude of the wavefield at every point fluctuates. Therefore, the amplitude itself can not be used as an indication. Other attributes should be used, such as the envelope of the amplitudes, the derivative of the envelope, and so on. Hence, several extrapolated wavefields should be saved, including the current extrapolated layer and its adjacent layers. This helps to avoid picking the wrong focused amplitude.

Another method is to estimate the radius of curvature of the wavefront of the scattering wave. MacKay and Abma (1993) present a method that, in the CMP geometry, uses the following formula:

$$R \approx \frac{(X^2 - \Delta t^2 V_r^2)}{2\Delta t V_r}, \quad (1)$$

where X is the offset, V_r is the medium velocity, and Δt is the time difference between the two-way vertical traveltimes and the observed traveltimes. However, this formula is not suitable here, because the time difference is unknown. For depth-focusing imaging, the source position is not a concern, and the traveltimes between the source and the scattering point is not explicitly used. I propose the following method to estimate the radius of curvature of the scattered wavefield. Assuming that the macro velocity is correct, and with the help of ray-tracing, the radius of curvature of the scattered wavefield can be estimated with the following formula:

$$R = V_r t_{scatter}, \quad (2)$$

where $t_{scatter}$ is the traveltimes from the scatterer to the receivers, V_r is the medium velocity, and $\Delta t = t - t_s = t_{scatter}$, where t is the observed two-way traveltimes and t_s is the traveltimes from the source to the scatter point. t_s may include the traveltimes of the multiples. According to equation 2, the radius of curvature of the scattered wavefield can be estimated with the extrapolated wavefield. Some ideas in Jager et al. (2001) suggest how to estimate the radius of curvature of the scattered wavefield.

DISCUSSION AND CONCLUSION

I propose a new imaging condition, with which the wavefield extrapolation is carried out in the depth domain, and the imaging amplitude is extracted from the focused scattered wavefield in the time domain, if the radius of curvature of the wavefront diminishes to zero. I call this imaging condition the depth-focusing imaging condition. I assert that the statement that the arrival time of the downgoing wave equals the take-off time of the upcoming wave is equivalent to saying that the radius of the curvature of the scattering wavefield diminishes to zero. With the imaging condition, the primaries and the multiples can be simultaneously imaged. The source position can be known or unknown; therefore the passive data can be imaged with

it. Some shot gathers can be added together according to the receiver positions, and then the new data set is imaged with the above method, thus improving the calculation efficiency. The depth-focusing imaging condition can be used for imaging multicomponent seismic data. However, since the focusing of the scattering wave is detected in the time domain, the data needs to have high S/N ratio. It will be best suited for processing marine data.

ACKNOWLEDGEMENT

The author thanks the SEP Group at Stanford University for providing an opportunity for him to serve as a visiting scholar.

REFERENCES

- Berkhout, A. J., and Verschuur, D. J., 1997, Estimation of multiple scattering by iterative inversion, part I: Theoretical considerations: *Geophysics*, **62**, 1586–1595.
- Claerbout, J. F., 1971, Toward a unified theory of reflector mapping: *Geophysics*, **36**, 467–481.
- Jager, R., Mann, J., Hocht, G., and Hubral, P., 2001, Common-reflection-surface stack: Image and attributes: *Geophysics*, **66**, 97–109.
- MacKay, S., and Abma, R., 1993, Depth-focusing analysis using a wavefront-curvature criterion: *Geophysics*, **58**, 1148–1156.
- Schuster, G. T., Followill, F., Katz, L. J., Yu, J., and Liu, Z., 2003, Autocorrelogram migration: Theory: *Geophysics*, **68**, 1685–1694.

Geomechanical analysis with rigorous error estimates for a double-porosity reservoir model

James G. Berryman¹

ABSTRACT

A model of random polycrystals of porous laminates is introduced to provide a means for studying geomechanical properties of double-porosity reservoirs having one class of possible microstructures. Calculations on the resulting earth reservoir model can proceed semi-analytically for studies of either the poroelastic or transport coefficients, but the poroelastic coefficients are emphasized here. Rigorous bounds of the Hashin-Shtrikman type provide estimates of overall bulk and shear moduli, and thereby also provide rigorous error estimates for geomechanical constants obtained from up-scaling based on a self-consistent effective medium method. The influence of hidden (or presumed unknown) microstructure on the final results can then be evaluated quantitatively. Detailed descriptions of the use of the model and some numerical examples showing typical results for the double-porosity poroelastic coefficients for the type of heterogeneous reservoir being considered are presented.

INTRODUCTION

Rapid progress in development of rigorous bounding methods for material coefficients in heterogeneous media (Milton, 2002; Torquato, 2002) has been made over the last fifty years. Effective medium theory, although very useful in many practical circumstances, nevertheless has not made such rapid progress. So a question that naturally arises is whether it might be possible to construct new effective medium formulas directly from the known bounds? Skeptics will immediately ask: Why do I need to do this at all if bounds are available? But the answer to this question is most apparent in poromechanics, where the bounds are frequently too far apart to be of much use in engineering and, especially, in field applications. Hill (1952) was actually the first to try constructing estimates from bounds. First he showed that the Voigt (1928) and Reuss (1929) averages/estimates in elasticity were in fact upper and lower bounds, respectively, on stiffness. Then he proceeded to suggest that estimates of reasonable accuracy were given by the arithmetic or geometric means obtained by averaging these two bounds together. Thus, the Voigt-Reuss-Hill estimates were born. Better bounds than the Voigt and Reuss bounds are now known and no doubt some attempts to update Hill's approach have been made. However, to make a direct connection to traditional approaches of effec-

¹email: berryman@sep.stanford.edu

tive medium theory, I apply a more technical procedure here in order to obtain estimates of up-scaled constants using the known analytical structure of the bounds, especially for Hashin-Shtrikman (1962) bounds. When this mathematical structure is not known — as might be the case if the bounds are expressed algorithmically rather than as analytical formulas — then I will see that it proves very worthwhile to expend the additional effort required to determine this structure. Whenever it is possible to carry the analysis further than has been done in the published literature, a self-consistent effective medium formula is fairly straightforward to obtain from the resulting expressions. The self-consistent predictions then lie within the bounds, as might be desired and expected. In the next section, one particular class of double-porosity models (Berryman, 2002; Berryman and Pride, 2002) is considered. [Other classes of models with different microstructures may also be of interest and some of these have also been discussed in previous work (Berryman, and Wang, 1995; Berryman and Pride, 2002), but other microstructures generally have less analytical structure that can be exploited, so unfortunately much less detailed information can be obtained about these models from analysis alone.] Results from double-porosity geomechanics analysis are presented. These results are general (for the model under consideration), and do not depend explicitly on generally unknown details of the spatial arrangement or microstructure of the porous constituents. Microstructure enters these formulas only through the overall drained bulk modulus K_d^* . Then, in the following section, a preferred model microstructure — that of a locally layered medium — is imposed. This microstructure has the advantage that it forms hexagonal (or transversely isotropic) “crystals” locally. Then, if I assume these crystals, or grains, are jumbled together randomly so as to form an overall isotropic medium, I have the “random polycrystal of porous laminates” reservoir model. Hashin-Shtrikman bounds are known for such polycrystals composed of grains having hexagonal symmetry. So bounds are easily found. From the form of the bounds, I also obtain estimates of both overall bulk modulus and shear modulus (Berryman, 2005), thus completing the semi-analytical poromechanics model. The final two sections show examples, and summarize my results. Although the language I use here tends to emphasize the analogy to polycrystals of laminates, the reader should keep in mind that the equations of elasticity — and for present purposes (I do not treat permeability here) also the equations of poroelasticity — are scale invariant. So the mathematics is the same whether the layering I am considering takes place at the scale of microns, meters, or kilometers. However, there is an obvious but implicit limitation that the scale considered cannot be so small that the continuum hypothesis fails to be valid.

DOUBLE-POROSITY GEOMECHANICS

The main results used here can be derived using uniform expansion, or self-similar, methods analogous to ideas used in thermoelasticity by Cribb (1968) and in single-porosity poroelasticity by Berryman and Milton (1991). Cribb’s method provided a simpler and more intuitive derivation of Levin’s earlier results on thermoelastic expansion coefficients (Levin, 1967). Our results also provide a simpler derivation of results obtained by Berryman and Pride (2002) for the double-porosity coefficients. Related methods in other applications to micromechanics are called “the theory of uniform fields” by some authors (Dvorak and Benveniste, 1997). First

assume two distinct phases at the macroscopic level: a porous matrix phase with the effective properties $K_d^{(1)}$, $G_d^{(1)}$, $K_m^{(1)}$, $\phi^{(1)}$ (which are drained bulk and shear moduli, grain or mineral bulk modulus, and porosity of phase 1 with analogous definitions for phase 2), occupying volume fraction $V^{(1)}/V = v^{(1)}$ of the total volume and a macroscopic crack or joint phase occupying the remaining fraction of the volume $V^{(2)}/V = v^{(2)} = 1 - v^{(1)}$. The key feature distinguishing the two phases — and therefore requiring this analysis — is the very high fluid permeability of the crack or joint phase and the relatively lower permeability (but higher fluid volume content) of the matrix phase. In the double-porosity model, there are three dis-

Figure 1: Schematic of the random polycrystals of laminates model. `jim1-laminated_poly_112` [NR]

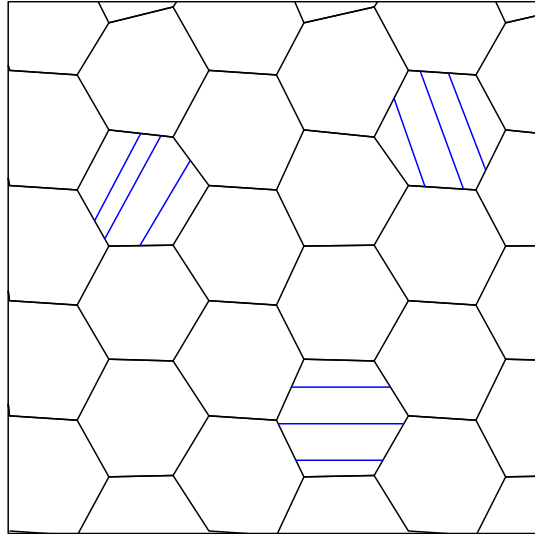
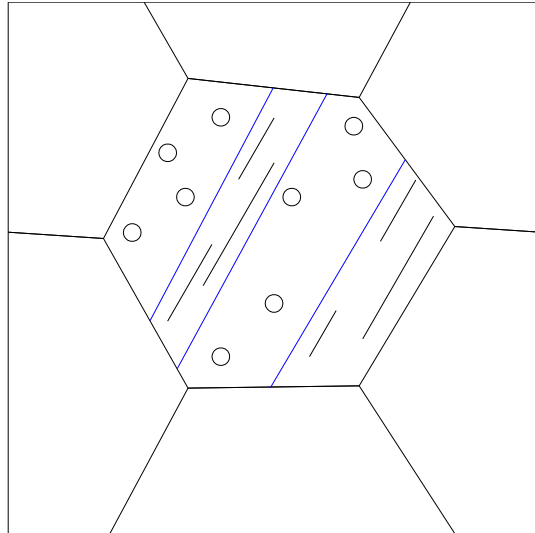


Figure 2: Blowup showing a detail that illustrates how each one of the grains is composed of two very different types of porous materials: one being a storage material (high porosity and low permeability) and one a transport material (low porosity and high permeability). `jim1-doublepor` [NR]



tinct pressures: confining pressure δp_c , pore-fluid pressure $\delta p_f^{(1)}$ [for the storage porosity], and joint-fluid pressure $\delta p_f^{(2)}$ [for the transport porosity]. (See Figures 1 and 2.) Treating δp_c , $\delta p_f^{(1)}$, and $\delta p_f^{(2)}$ as the independent variables in our double porosity theory, I define the dependent variables $\delta e \equiv \delta V/V$, $\delta \zeta^{(1)} = (\delta V_\phi^{(1)} - \delta V_f^{(1)})/V$, and $\delta \zeta^{(2)} = (\delta V_\phi^{(2)} - \delta V_f^{(2)})/V$, which are respectively the total volume dilatation, the increment of fluid content in the matrix phase,

and the increment of fluid content in the joints. The fluid in the matrix is the same as that in the cracks or joints, but the two fluid regions may be in different states of average stress and, therefore, need to be distinguished by their respective superscripts. Linear relations among strain, fluid content, and pressure take the symmetric form

$$\begin{pmatrix} \delta e \\ -\delta\zeta^{(1)} \\ -\delta\zeta^{(2)} \end{pmatrix} = \begin{pmatrix} a_{11} & a_{12} & a_{13} \\ a_{12} & a_{22} & a_{23} \\ a_{13} & a_{23} & a_{33} \end{pmatrix} \begin{pmatrix} -\delta p_c \\ -\delta p_f^{(1)} \\ -\delta p_f^{(2)} \end{pmatrix}, \quad (1)$$

following Berryman and Wang (1995) and Lewallen and Wang (1998). It is easy to check that $a_{11} = 1/K_d^*$, where K_d^* is the overall drained bulk modulus of the system. I now find analytical expressions for the remaining five constants for a binary composite system. The components of the system are themselves porous materials 1 and 2, but each is assumed to be what I call a ‘‘Gassmann material’’ satisfying

$$\begin{pmatrix} \delta e^{(1)} \\ -\delta\zeta^{(1)}/v^{(1)} \end{pmatrix} = \frac{1}{K_d^{(1)}} \begin{pmatrix} 1 & -\alpha^{(1)} \\ -\alpha^{(1)} & \alpha^{(1)}/B^{(1)} \end{pmatrix} \begin{pmatrix} -\delta p_c^{(1)} \\ -\delta p_f^{(1)} \end{pmatrix} \quad (2)$$

for material 1 and a similar expression for material 2. The new constants appearing on the right are the drained bulk modulus $K_d^{(1)}$ of material 1, the corresponding Biot-Willis (Biot and Willis, 1957) coefficient $\alpha^{(1)}$, and the Skempton (1954) coefficient $B^{(1)}$. The volume fraction $v^{(1)}$ appears here in order to correct for the difference between a global fluid content and the corresponding local variable for material 1. The main special characteristic of a Gassmann (1951) porous material is that it is composed of only one type of solid constituent, so it is ‘‘microhomogeneous’’ in its solid component, and in addition the porosity is randomly, but fairly uniformly, distributed so there is a well-defined constant porosity $\phi^{(1)}$ associated with material 1, etc. To proceed further, I ask this question: Is it possible to find combinations of $\delta p_c = \delta p_c^{(1)} = \delta p_c^{(2)}$, $\delta p_f^{(1)}$, and $\delta p_f^{(2)}$ so that the expansion or contraction of the system is spatially uniform or self-similar? Or equivalently, can I find uniform confining pressure δp_c , and pore-fluid pressures $\delta p_f^{(1)}$ and $\delta p_f^{(2)}$, so that all these scalar conditions can be met simultaneously? If so, then results for system constants can be obtained purely algebraically without ever having to solve equilibrium equations of the mechanics. I initially set $\delta p_c = \delta p_c^{(1)} = \delta p_c^{(2)}$, as this condition of uniform confining pressure is clearly a requirement for the self-similar thought experiment to be a valid solution of stress equilibrium equations. So, the first condition to be considered is the equality of the strains of the two constituents:

$$\delta e^{(1)} = -\frac{1}{K_d^{(1)}}(\delta p_c - \alpha^{(1)}\delta p_f^{(1)}) = \delta e^{(2)} = -\frac{1}{K_d^{(2)}}(\delta p_c - \alpha^{(2)}\delta p_f^{(2)}). \quad (3)$$

If this condition is satisfied, then the two constituents are expanding or contracting at the same rate and it is clear that self-similarity prevails, since

$$\delta e = v^{(1)}\delta e^{(1)} + v^{(2)}\delta e^{(2)} = \delta e^{(1)} = \delta e^{(2)}. \quad (4)$$

If I imagine that δp_c and $\delta p_f^{(1)}$ are fixed, then I need an appropriate value of $\delta p_f^{(2)}$, so that (3) is satisfied. This requires that

$$\delta p_f^{(2)} = \delta p_f^{(2)}(\delta p_c, \delta p_f^{(1)}) = \frac{1 - K_d^{(2)}/K_d^{(1)}}{\alpha^{(2)}}\delta p_c + \frac{\alpha^{(1)}K_d^{(2)}}{\alpha^{(2)}K_d^{(1)}}\delta p_f^{(1)}, \quad (5)$$

showing that, for undrained conditions, $\delta p_f^{(2)}$ can almost always be chosen so the uniform expansion takes place. Using (5), I now eliminate $\delta p_f^{(2)}$ from the remaining equality so

$$\delta e = - \left[a_{11} \delta p_c + a_{12} \delta p_f^{(1)} + a_{13} \delta p_f^{(2)} (\delta p_c, \delta p_f^{(1)}) \right] = \delta e^{(1)} = - \frac{1}{K_d^{(1)}} \left[\delta p_c - \alpha^{(1)} \delta p_f^{(1)} \right], \quad (6)$$

where $\delta p_f^{(2)} (\delta p_c, \delta p_f^{(1)})$ is given by (5). Making the substitution and then noting that δp_c and $\delta p_f^{(1)}$ were chosen independently and arbitrarily, I find the resulting coefficients must each vanish. The two equations I obtain are

$$a_{11} + a_{13} \left(1 - K_d^{(2)} / K_d^{(1)} \right) / \alpha^{(2)} = 1 / K_d^{(1)} \quad (7)$$

and

$$a_{12} + a_{13} \left(\alpha^{(1)} K_d^{(2)} / \alpha^{(2)} K_d^{(1)} \right) = -\alpha^{(1)} / K_d^{(1)}. \quad (8)$$

Since a_{11} is assumed to be known, (7) can be solved directly, giving

$$a_{13} = - \frac{\alpha^{(2)}}{K_d^{(2)}} \left(\frac{1 - K_d^{(1)} / K_d^*}{1 - K_d^{(1)} / K_d^{(2)}} \right). \quad (9)$$

Similarly, with a_{13} known, substituting into (8) gives

$$a_{12} = - \frac{\alpha^{(1)}}{K_d^{(1)}} \left(\frac{1 - K_d^{(2)} / K_d^*}{1 - K_d^{(2)} / K_d^{(1)}} \right). \quad (10)$$

So, formulas for three of the six coefficients are now known. [Also, note the similarity of the formulas (9) and (10), *i.e.*, interchanging indices 1 and 2 on the right hand sides takes us from one expression to the other.] To evaluate the remaining coefficients, I consider what happens to fluid increments during the self-similar expansion. I treat only material 1, but the equations for material 2 are completely analogous. From the preceding equations,

$$\delta \zeta^{(1)} = a_{12} \delta p_c + a_{22} \delta p_f^{(1)} + a_{23} \delta p_f^{(2)} (\delta p_c, \delta p_f^{(1)}) = \frac{v^{(1)}}{K_d^{(1)}} \left[-\alpha^{(1)} \delta p_c + (\alpha^{(1)} / B^{(1)}) \delta p_f^{(1)} \right]. \quad (11)$$

Again substituting for $\delta p_f^{(2)} (\delta p_c, \delta p_f^{(1)})$ from (5) and noting that the resulting equation contains arbitrary values of δp_c and $\delta p_f^{(1)}$, the coefficients of these terms must vanish separately. Resulting equations are

$$a_{12} + a_{23} (1 - K_d^{(2)} / K_d^{(1)}) / \alpha^{(2)} = -\alpha^{(1)} v^{(1)} / K_d^{(1)}, \quad (12)$$

and

$$a_{22} + a_{23} \left(\alpha^{(1)} K_d^{(2)} / \alpha^{(2)} K_d^{(1)} \right) = \alpha^{(1)} v^{(1)} / B^{(1)} K_d^{(1)}. \quad (13)$$

Solving these equations, I obtain

$$a_{23} = \frac{K_d^{(1)} K_d^{(2)} \alpha^{(1)} \alpha^{(2)}}{\left[K_d^{(2)} - K_d^{(1)} \right]^2} \left[\frac{v^{(1)}}{K_d^{(1)}} + \frac{v^{(2)}}{K_d^{(2)}} - \frac{1}{K_d^*} \right], \quad (14)$$

and

$$a_{22} = \frac{v^{(1)} \alpha^{(1)}}{B^{(1)} K_d^{(1)}} - \left(\frac{\alpha^{(1)}}{1 - K_d^{(1)} / K_d^{(2)}} \right)^2 \left[\frac{v^{(1)}}{K_d^{(1)}} + \frac{v^{(2)}}{K_d^{(2)}} - \frac{1}{K_d^*} \right]. \quad (15)$$

Performing the corresponding calculation for $\delta \zeta^{(2)}$ produces formulas for a_{32} and a_{33} . Since (14) is already symmetric in component indices, the formula for a_{32} provides nothing new. The formula for a_{33} is easily seen to be identical in form to a_{22} , but indices 1 and 2 are interchanged. Formulas for all five of the nontrivial coefficients of double porosity have now been determined. These results also show how the constituent properties K_d , α , B up-scale at the macrolevel for a two-constituent composite (Berryman and Wang, 1995; Berryman and Pride, 2002). I find

$$\alpha = -\frac{a_{12} + a_{13}}{a_{11}} = \frac{\alpha^{(1)}(K_d^* - K_d^{(2)}) + \alpha^{(2)}(K_d^{(1)} - K_d^*)}{K_d^{(1)} - K_d^{(2)}}, \quad (16)$$

and

$$\frac{1}{B} = -\frac{a_{22} + 2a_{23} + a_{33}}{a_{12} + a_{13}}. \quad (17)$$

Note that all the important formulas [(8),(9),(11)-(14)] depend on the overall drained bulk modulus K_d^* of the system. So far this quantity is unknown and therefore must still be determined independently either by experiment or by another analytical method. It should also be clear that some parts (but not all) of the preceding analysis generalize to the multi-porosity problem (*i.e.*, more than two porosity types). A discussion of the issues surrounding solvability of the multiporosity problem has been presented elsewhere (Berryman, 2002).

UP-SCALING MODEL FOR GEOMECHANICS OF RESERVOIRS

Elasticity of layered materials Next, to determine the overall drained (or undrained) bulk and shear moduli of the reservoir, assume a typical building block of the random system is a small (relative to the size of the reservoir) “grain” of laminate material whose elastic response for a transversely isotropic (hexagonal) system can be described locally by:

$$\begin{pmatrix} \sigma_{11} \\ \sigma_{22} \\ \sigma_{33} \\ \sigma_{23} \\ \sigma_{31} \\ \sigma_{12} \end{pmatrix} = \begin{pmatrix} c_{11} & c_{12} & c_{13} & & & \\ c_{12} & c_{11} & c_{13} & & & \\ c_{13} & c_{13} & c_{33} & & & \\ & & & 2c_{44} & & \\ & & & & 2c_{44} & \\ & & & & & 2c_{66} \end{pmatrix} \begin{pmatrix} e_{11} \\ e_{22} \\ e_{33} \\ e_{23} \\ e_{31} \\ e_{12} \end{pmatrix}, \quad (18)$$

where σ_{ij} are the usual stress components for $i, j = 1 - 3$ in Cartesian coordinates, with 3 (or z) being the axis of symmetry (the lamination direction for such a layered material). Displacement u_i is then related to strain component e_{ij} by $e_{ij} = (\partial u_i / \partial x_j + \partial u_j / \partial x_i) / 2$. This definition introduces some convenient factors of two into the 44, 55, 66 components of the matrix of stiffness coefficients shown in (18). For definiteness I also assume that the matrix of stiffness coefficients in (18) arises from the lamination of N isotropic constituents having bulk and shear moduli K_n, μ_n , in the $N > 1$ layers present in each building block. It is important that the thicknesses d_n always be in the same proportion in each of these laminated blocks, so that $f_n = d_n / \sum_n' d_n'$. But the order in which layers were added to the blocks is not important, as Backus's formulas (Backus, 1962) for the constants show. For the overall quasistatic (long wavelength) behavior of the system I am studying, Backus's results [also see Postma (1955), Berryman (1998; 2004b), Milton (2002)] state that

$$\begin{aligned} c_{33} &= \left\langle \frac{1}{K+4\mu/3} \right\rangle^{-1}, & c_{13} &= c_{33} \left\langle \frac{K-2\mu/3}{K+4\mu/3} \right\rangle, \\ c_{44} &= \left\langle \frac{1}{\mu} \right\rangle^{-1}, & c_{66} &= \langle \mu \rangle, \\ c_{11} &= \frac{c_{13}^2}{c_{33}} + 4c_{66} - 4 \left\langle \frac{\mu^2}{K+4\mu/3} \right\rangle, & c_{12} &= c_{11} - 2c_{66}. \end{aligned} \quad (19)$$

This bracket notation can be correctly viewed as a line integral along the symmetry axis x_3 . The bulk modulus K_n and shear modulus μ_n displayed in these averages can be either the drained or the undrained moduli for the individual layers. For the undrained case, the results are inherently assumed either to apply at very high frequencies, such as ultrasonic frequencies in laboratory experiments, or to situations wherein each layer is physically isolated so that fluid increments cannot move from one porous layer to the next. The bulk modulus for each laminated grain is that given by the compressional Reuss average K_R of the corresponding compliance matrix s_{ij} [the inverse of the usual stiffness matrix c_{ij} , whose nonzero components are shown in (18)]. The result is $e = e_{11} + e_{22} + e_{33} = \sigma / K_{\text{eff}}$, where $1/K_{\text{eff}} = 1/K_R = 2s_{11} + 2s_{12} + 4s_{13} + s_{33}$. Even though $K_{\text{eff}} = K_R$ is the same for every grain, since the grains themselves are not isotropic, the overall bulk modulus K^* of the random polycrystal does not necessarily have the same value as K_R for the individual grains (Hill, 1952). Hashin-Shtrikman bounds on K^* for random polycrystals whose grains have hexagonal symmetry (Peselnick and Meister, 1965; Watt and Peselnick, 1980) show in fact that the K_R value lies outside the bounds in many situations (Berryman, 2004). *Bounds for random polycrystals*

Voigt and Reuss bounds: hexagonal symmetry: For hexagonal symmetry, the nonzero stiffness constants are: $c_{11}, c_{12}, c_{13} = c_{23}, c_{33}, c_{44} = c_{55}$, and $c_{66} = (c_{11} - c_{12})/2$. The Voigt (1928) average for bulk modulus of hexagonal systems is well-known to be

$$K_V = [2(c_{11} + c_{12}) + 4c_{13} + c_{33}] / 9. \quad (20)$$

Similarly, for the overall shear modulus G^* , I have

$$G_V = \frac{1}{5} (G_{\text{eff}}^v + 2c_{44} + 2c_{66}), \quad (21)$$

where the new term appearing here is essentially defined by (21) and given explicitly by

$$G_{\text{eff}}^v = (c_{11} + c_{33} - 2c_{13} - c_{66}) / 3. \quad (22)$$

The quantity G_{eff}^v is the energy per unit volume in a grain when a “pure uniaxial shear” *strain* of unit magnitude [*i.e.*, $(e_{11}, e_{22}, e_{33}) = (1, 1, -2)/\sqrt{6}$], whose main compressive strain is applied to the grain along its axis of symmetry (Berryman, 2004a; 2004b). Note that the concept of “pure uniaxial shear” strain (or stress) is based on the observation that if a uniaxial principal strain (or stress) of magnitude 3 is applied along the symmetry axis, it can be decomposed according to $(0, 0, 3)^T = (1, 1, 1)^T - (1, 1, -2)^T$ into a pure compression and a pure shear contribution, which is then called for the sake of brevity the “pure uniaxial shear.” The Reuss (1929) average K_R for bulk modulus can also be written in terms of stiffness coefficients as

$$\frac{1}{K_R - c_{13}} = \frac{1}{c_{11} - c_{66} - c_{13}} + \frac{1}{c_{33} - c_{13}}. \quad (23)$$

The Reuss average for shear is

$$G_R = \left[\frac{1}{5} \left(\frac{1}{G_{\text{eff}}^r} + \frac{2}{c_{44}} + \frac{2}{c_{66}} \right) \right]^{-1}, \quad (24)$$

that defines G_{eff}^r – *i.e.*, the energy per unit volume in a grain when a pure uniaxial shear *stress* of unit magnitude [*i.e.*, $(\sigma_{11}, \sigma_{22}, \sigma_{33}) = (1, 1, -2)/\sqrt{6}$], whose main compressive pressure is applied to a grain along its axis of symmetry. For each grain having hexagonal symmetry, two product formulas found by Berryman (2004a) hold: $3K_R G_{\text{eff}}^v = 3K_V G_{\text{eff}}^r = \omega_+ \omega_- / 2 = c_{33}(c_{11} - c_{66}) - c_{13}^2$. The symbols ω_{\pm} stand for the quasi-compressional and quasi-uniaxial-shear eigenvalues for the crystalline grains. Thus, it follows that

$$G_{\text{eff}}^r = K_R G_{\text{eff}}^v / K_V \quad (25)$$

is a general formula, true for hexagonal symmetry. *Hashin-Shtrikman bounds*: It has been shown elsewhere (Berryman, 2004a; 2004b) that the Peselnick-Meister-Watt (Peselnick and Meister, 1965; Watt and Peselnick, 1980) bounds for bulk modulus of a random polycrystal composed of hexagonal (or transversely isotropic) grains are given by

$$K_{PM}^{\pm} = \frac{K_V(G_{\text{eff}}^r + \zeta_{\pm})}{(G_{\text{eff}}^v + \zeta_{\pm})} = \frac{K_R G_{\text{eff}}^v + K_V \zeta_{\pm}}{G_{\text{eff}}^v + \zeta_{\pm}}, \quad (26)$$

where G_{eff}^v (G_{eff}^v) is the uniaxial shear energy per unit volume for a unit applied shear strain (stress). The second equality follows directly from the product formula (25). Parameters ζ_{\pm} are defined by

$$\zeta_{\pm} = \frac{G_{\pm}}{6} \left(\frac{9K_{\pm} + 8G_{\pm}}{K_{\pm} + 2G_{\pm}} \right). \quad (27)$$

In (27), values of G_{\pm} (shear moduli of isotropic comparison materials) are given by inequalities

$$0 \leq G_- \leq \min(c_{44}, G_{\text{eff}}^r, c_{66}), \quad (28)$$

and

$$\max(c_{44}, G_{\text{eff}}^v, c_{66}) \leq G_+ \leq \infty. \quad (29)$$

The values of K_{\pm} (bulk moduli of isotropic comparison materials) are then given by algorithmic equalities

$$K_{\pm} = \frac{K_V(G_{\text{eff}}^r - G_{\pm})}{(G_{\text{eff}}^v - G_{\pm})}, \quad (30)$$

derived by Peselnick and Meister (1965) and Watt and Peselnick (1980). Also see Berryman (2004a). Bounds G_{hex}^{\pm} (+ is upper bound, - is the lower bound) on the shear moduli for random polycrystals of hexagonal crystals are then given by

$$\frac{1}{G_{\text{hex}}^{\pm} + \zeta_{\pm}} = \frac{1}{5} \left[\frac{1 + \gamma_{\pm}(K_V - K_{\pm})}{G_{\text{eff}}^v + \zeta_{\pm} + \delta_{\pm}(K_V - K_{\pm})} + \frac{2}{c_{44} + \zeta_{\pm}} + \frac{2}{c_{66} + \zeta_{\pm}} \right], \quad (31)$$

where γ_{\pm} and δ_{\pm} are given by

$$\gamma_{\pm} = \frac{1}{K_{\pm} + 4G_{\pm}/3}, \quad \text{and} \quad \delta_{\pm} = \frac{5G_{\pm}/2}{K_{\pm} + 2G_{\pm}}. \quad (32)$$

K_V is the Voigt average of the bulk modulus as defined previously.

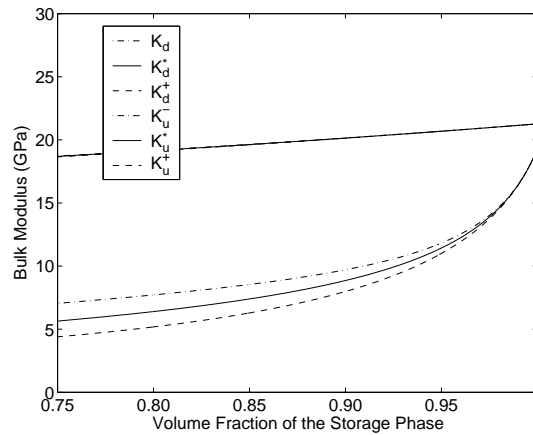
TABLE 1. Input Parameters for Weber Sandstone Model of Double-Porosity System.

K_s	$K_s^{(1)}$	$K_d^{(1)}$	$G_d^{(1)}$	$\phi^{(1)}$	$K_s^{(2)}$	$K_d^{(2)}$	$G_d^{(2)}$	$\phi^{(2)}$
(GPa)	(GPa)	(GPa)	(GPa)		(GPa)	(GPa)	(GPa)	
27.9	28.0	19.3	20.2	0.095	27.0	0.24	0.60	0.095

Note: Porosity ϕ is dimensionless.

EXAMPLE: WEBER SANDSTONE

Figure 3: Bulk modulus bounds and self-consistent estimates for the random polycrystal of porous laminates model of a Weber sandstone reservoir. `jim1-weberK` [NR]



Weber sandstone is one possible host rock for which the required elastic constants have been measured by Coyner (1984). TABLE 1 displays the values needed in the double-porosity theory presented here. These values follow from an analysis of Coyner's data if I assume the

Figure 4: Shear modulus bounds and self-consistent estimates for the random polycrystal of porous laminates model of a Weber sandstone reservoir. [jim1-weberG] [NR]

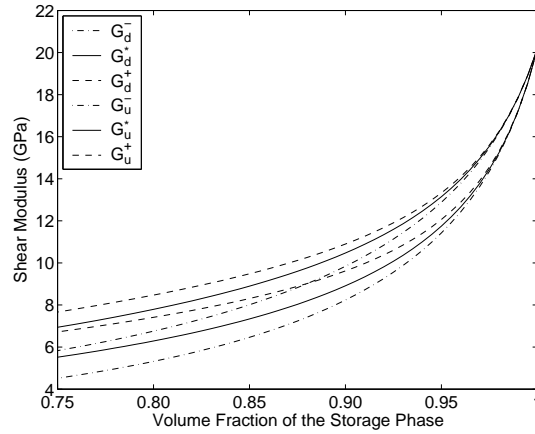
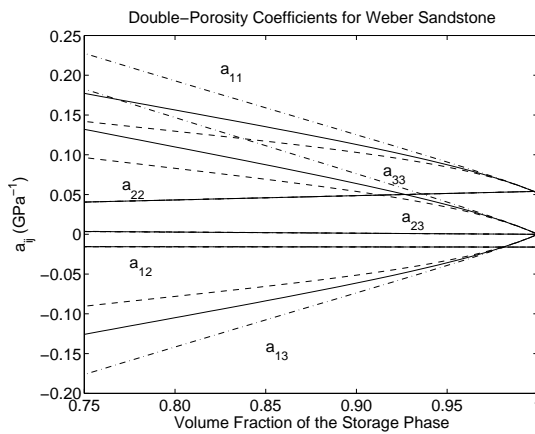


Figure 5: Values of double-porosity coefficients a_{ij} for a system similar to Weber sandstone. Values used for the input parameters are listed in TABLE 1. For each coefficient, three curves are shown, depending on which estimate of the overall bulk modulus is used: lower bound (dot-dash line), self-consistent (solid line), or upper bound (dashed line). [jim1-weberaij] [NR]



stiffer phase occupies about 92% of the volume and the more compliant phase the remaining 8% of total volume. The drained bulk moduli of the storage and fracture phases are used in the effective medium theory of the previous section to determine the overall drained and undrained bulk moduli of the random polycrystal of laminates system. Results for the self-consistent estimates (Berryman, 2004b), and the upper and lower bounds for the bulk moduli are all displayed in Figure 3. I see the undrained moduli are nearly indistinguishable, but the drained constants show some dispersion. Similarly, I show bounds and self-consistent estimates for the overall shear modulus of this model reservoir in Figure 4. Both undrained and drained shear moduli show some dispersion. Note that a correction must be applied to (31) before computing the self-consistent effective constants. The self-consistent estimates for bulk modulus are found correctly from the bounds (26) by taking $K_{\pm} \rightarrow K^*$, $G_{\pm} \rightarrow G^*$, and therefore $\zeta_{\pm} \rightarrow \zeta^*$. The resulting formula is

$$K^* = K_V \frac{(G_{\text{eff}}^r + \zeta^*)}{(G_{\text{eff}}^v + \zeta^*)}. \quad (33)$$

The self-consistent formula for shear modulus requires more effort. The difficulty is that the formula given in (31) has already made use of a constraint that is only true along the bounding curves defining the upper and lower bounds on shear modulus. Since the self-consistent estimate always falls at points away from this curve, a more general result must be employed. When the inappropriate constraint is replaced by the general formula and then (33) is substituted, I find instead that the self-consistent formula for shear modulus is given by

$$\frac{1}{G^* + \zeta^*} = \frac{1}{5} \left(\frac{1 + \gamma^*(K_V - K^*)}{G_{\text{eff}}^v + \zeta^*} + \frac{2}{c_{44} + \zeta^*} + \frac{2}{c_{66} + \zeta^*} \right), \quad (34)$$

where $\gamma^* = 1/(K^* + 4G^*/3)$. The main difference is that the denominator of the first term on the right hand side is simpler than it is in the formulas for the shear modulus bounds. Observed dispersion is small over the range of volume fractions considered. Then these drained values K_d^* , K_d^{\pm} are used in the formulas of the second section to determine both estimates and bounds on the double-porosity coefficients. These results are then displayed in Figure 5, which is also the main result of this paper. Note that the curves for a_{11} essentially repeat results shown in Figure 3, but for the compliance $1/K_d^*$, instead of the stiffness K_d^* . The coefficients a_{12} , a_{22} , and a_{23} show little dispersion. This is natural for a_{12} and a_{22} because the storage material contains no fractures, and therefore is not sensitive to fracture compliance, whereas those mechanical effects on the overall reservoir response can be very large. The behavior of a_{23} also shows little dispersion as this value is always very close to zero (Berryman and Wang, 1995; Berryman and Pride, 2002). The two remaining coefficients show a significant level of dispersion are a_{13} and a_{33} , where the third stress is the pore pressure $p_f^{(2)}$ of the fracture or joint phase. I generally expect that the joint phase is most tightly coupled to, and therefore most sensitive to, the fluctuations in overall drained bulk modulus K_d^* . So all these results are qualitatively consistent with our intuition. Since I have analytical formulas for all the a_{ij} 's, it is straightforward to check that the observed dispersion in a_{13} and a_{33} is directly proportional to the dispersion in $1/K_d^*$ (or, equivalently, a_{11}).

CONCLUSIONS

The methods presented have been successfully applied to determine geomechanical parameters for one reservoir model assuming Weber sandstone is the host rock. Although the details differ, the general ideas used above for elastic and poroelastic constants can also be used to obtain bounds and estimates of electrical formation factor and fluid permeability for the same random polycrystal of porous laminates model. Analysis of permeability and fluid flow for this model (and especially memory effects) requires some extra care, and so I defer this part of the work to another contribution. The present work has concentrated on an examination of the very low frequency (quasi-static, drained behavior) and very high frequency (undrained behavior) results for the double-porosity model using composites theory as the main analysis tool. This approach is justified in part because it is well-known (using one pertinent example) in the analysis of viscoelastic media (Hashin, 1966; 1983; Vinogradov and Milton, 2005) that the low and high frequency viscoelastic limits can both be treated using the methods of quasi-static composites analysis, since the complex moduli become real in these limits. The corresponding result is certainly pertinent for the full double-porosity reservoir analysis as well. Further work is needed of course to determine the behavior for all the intermediate frequencies, but this harder part of the work will necessarily be both partly analytical [for example: Pride *et al.* (2004)] and partly computational [for example: Lewallen and Wang (1998)] in nature, and will therefore be presented in future publications.

REFERENCES

- Backus, G. E., 1962, Long-wave elastic anisotropy produced by horizontal layering: *J. Geophys. Res.*, **67**, 4427–4440.
- Berryman, J. G., 1998, Transversely isotropic poroelasticity arising from thin isotropic layers: *Mathematics of Multiscale Materials*, edited by K. M. Golden, G. R. Grimmett, R. D. James, G. W. Milton, and P. N. Sen, Springer-Verlag, NY, 1998, pp. 37–50.
- Berryman, J. G., 2002, Extension of poroelastic analysis to double-porosity materials: New technique in microgeomechanics: *ASCE J. Engng. Mech.*, **128**, 840–847.
- Berryman, J. G., 2004a, Poroelastic shear modulus dependence on pore-fluid properties arising in a model of thin isotropic layers: *Geophys. J. Int.*, **127**, 415–425.
- Berryman, J. G., 2004b, Bounds on elastic constants for random polycrystals of laminates: *J. Appl. Phys.*, **96**, 4281–4287.
- Berryman, J. G., 2005, Bounds and self-consistent estimates for elastic constants of random polycrystals with hexagonal, trigonal, and tetragonal symmetries: *J. Mech. Phys. Solids*, **53**, 2141–2173.
- Berryman, J. G., and G. W. Milton, 1991, Exact results for generalized Gassmann's equations in composite porous media with two constituents: *Geophysics*, **56**, 1950–1960.

- Berryman, J. G., and S. R. Pride, 2002, Models for computing geomechanical constants of double-porosity materials from the constituents' properties: *J. Geophys. Res.*, **107**, 10.1029/2000JB000108.
- Berryman, J. G., and H. F. Wang, 1995, The elastic coefficients of double-porosity models for fluid transport in jointed rock: *J. Geophys. Res.*, **100**, 24611–24627.
- Biot, M. A., and D. G. Willis, 1957, The elastic coefficients of the theory of consolidation: *J. Appl. Mech.*, **24**, 594–601.
- Coyner, K. B., 1984, *Effects of Stress, Pore Pressure, and Pore Fluids on Bulk Strain, Velocity, and Permeability in Rocks*, Ph.D. Thesis, Massachusetts Institute of Technology, Cambridge, Massachusetts.
- Cribb, J. L., 1968, Shrinkage and thermal expansion of a two phase material: *Nature*, **220**, 576–577.
- Dvorak, G. J., and Y. Benveniste, 1997, On micromechanics of inelastic and piezoelectric composites: *Theoretical and Applied Mechanics 1996*, edited by T. Tatsumi, E. Watanabe, and T. Kambe, Elsevier Science, Amsterdam, 1997, pp. 65–81.
- Gassmann, F., 1951, Über die Elastizität poröser Medien: *Vierteljahrsschrift der Naturforschenden Gesellschaft in Zürich*, **96**, 1–23.
- Hashin, Z., 1966, Viscoelastic fiber reinforced materials: *Am. Inst. Aeronautics Astronautics J.*, **4**, 1411–1417.
- Hashin, Z., 1983, Analysis of composite materials – A survey: *Appl. Mech. Rev.*, **50**: 481–505.
- Hashin, Z., and S. Shtrikman, 1962, A variational approach to the theory of the elastic behaviour of polycrystals: *J. Mech. Phys. Solids*, **10**, 343–352.
- Hill, R., 1952, Elastic properties of reinforced solids: Some theoretical principles: *Proc. Phys. Soc. London A*, **65**, 349–354.
- Levin, V. M., 1967, Thermal expansion coefficients of heterogeneous materials: *Mech. Solids*, **2**, 58–61.
- Lewallen, K.T., and H. F. Wang, 1998, Consolidation of a double-porosity medium: *Int. J. Solids Structures*, **35**, 4845–4867.
- Milton, G. W., 2002, *The Theory of Composites*, Cambridge University Press, Cambridge, UK, pp. 77-78, 163, 457–498.
- Peselnick, L., and R. Meister, 1965, Variational method of determining effective moduli of polycrystals: (A) Hexagonal symmetry, (B) trigonal symmetry: *J. Appl. Phys.*, **36**, 2879–2884.
- Postma, G. W., 1955, Wave propagation in a stratified medium: *Geophysics*, **20**, 780–806.

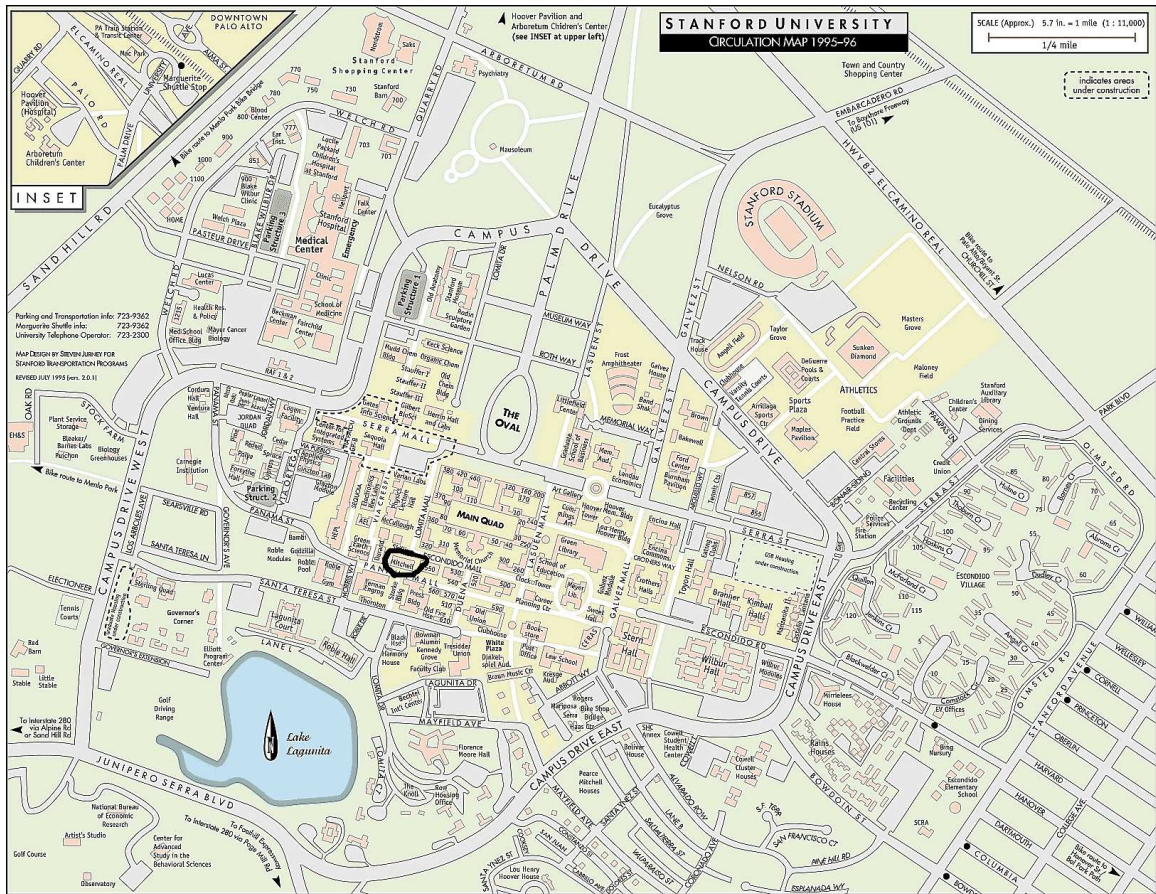
- Pride, S. R., J. G. Berryman, and J. M. Harris, 2004, Seismic attenuation due to wave induced flow: *J. Geophys. Res.*, **109**, B01201.
- Reuss, A., 1929, Berechnung der Fliesgrenze von Mischkristallen auf Grund der Plastizitätsbedingung für Einkristalle: *Z. Angew. Math. Mech.*, **9**, 49–58.
- Skempton, A. W., 1954, The pore-pressure coefficients *A* and *B*: *Geotechnique*, **4**, 143–147.
- Torquato, S., 2002, *Random Heterogeneous Materials: Microstructure and Macroscopic Properties*, Springer, NY.
- Vinogradov, V., and G. W. Milton, 2005, The total creep of viscoelastic composites under hydrostatic or antiplane loading: *J. Mech. Phys. Solids*, **53**, 1248–1279.
- Voigt, W., 1928, *Lehrbuch der Kristallphysik*, Teubner, Leipzig.
- Watt, J. P., and L. Peselnick, 1980, Clarification of the Hashin-Shtrikman bounds on the effective elastic moduli of polycrystals with hexagonal, trigonal, and tetragonal symmetries: *J. Appl. Phys.*, **51**, 1525–1531.

SEP ARTICLES PUBLISHED OR IN PRESS

- Alkhalifah, T., and Biondi, B., 2004, Numerical analysis of the azimuth moveout operator for vertically inhomogeneous media: *Geophysics*, **69**, 554–561.
- Alvarez, G., and Larner, K., 2004, Relative performance of moveout-based multiple-suppression methods for amplitude variation with offset (AVO) analysis and common mid-point (CMP) stacking: *Geophysics*, **69**, no. 1, 275–285.
- Alvarez, G., Biondi, B., and Guitton, A., 2004a, Attenuation of diffracted multiples in angle domain common image gathers: 74th Ann. Internat. Mtg., Soc. of Expl. Geophys., Expanded Abstracts, 1301–1304.
- Alvarez, G., Pereyra, V., and Carcione, L., 2004b, Model-based 3-D seismic survey design as an optimization problem: 74th Ann. Internat. Mtg., Soc. of Expl. Geophys., Expanded Abstracts, 63–66.
- Biondi, B., and Bevc, D., 2004, Seismic imaging of complex structures by reflection seismic data *in* Levander, A., and Nolet, G., Eds., *Data Analysis and Imaging with Global and Local Arrays*: American Geophysical Union, in press.
- Biondi, B., and Symes, W., 2004, Angle-domain common-image gathers for migration velocity analysis by wavefield-continuation imaging: *Geophysics*, **69**, 1283–1298.
- Biondi, B., and Tisserant, T., 2004, 3-D angle-domain common-image gathers for migration velocity analysis: *Geophysical Prospecting*, **52**, 575–591.
- Brown, M., and Guitton, A., 2004a, Efficient prestack modeling and imaging of pegleg multiples: 74th Ann. Internat. Mtg., Soc. of Expl. Geophys., Expanded Abstracts, 2148–2151.
- Brown, M., and Guitton, A., 2004b, Least-squares joint imaging of multiples and primaries: 74th Ann. Internat. Mtg., Soc. of Expl. Geophys., Expanded Abstracts, 1277–1280.
- Clapp, R. G., Biondi, B., and Claerbout, J. F., 2004, Geologically constrained migration velocity analysis: *Geophysics*, **69**, 533–546.
- Clapp, R. G., 2004, Reference velocity selection by a generalized Lloyd method: 74th Ann. Internat. Mtg., Soc. of Expl. Geophys., Expanded Abstracts, 981–984.
- Draganov, D., Wapenaar, K., Artman, B., and Biondi, B., 2004, Migration methods for passive seismic data: 74th Ann. Internat. Mtg., Soc. of Expl. Geophys., Expanded Abstracts, 1123–1126.
- Guitton, A., and Claerbout, J., 2004, Interpolation of bathymetry data from the Sea of Galilee: a noise attenuation problem: *Geophysics*, **69**, 608–616.
- Guitton, A., and Verschuur, D. J., 2004, Adaptive subtraction of multiples with the ℓ^1 norm: *Geophysical Prospecting*, **52**, 27–38.

- Guitton, A., Claerbout, J., and Lomask, J., 2004, First order lateral interval velocity estimates without picking: 74th Ann. Internat. Mtg., Soc. of Expl. Geophys., Expanded Abstracts, 2339–2342.
- Guitton, A., 2004, Amplitude and kinematic corrections of migrated images for non-unitary imaging operators: *Geophysics*, **69**, 1017–1024.
- Guitton, A., 2005a, Multiple attenuation in complex geology with a pattern-based approach: *Geophysics*, **70**, V97–V107.
- Guitton, A., 2005b, A pattern-based approach for multiple removal applied to a 3D Gulf of Mexico dataset: accepted for publication in *Geophysical Prospecting*.
- Haines, S., Pride, S., Klemperer, S., and Biondi, B., 2004, Development of electroseismic experimental methods: Symposium on the Application of Geophysics to Engineering and Environmental Problems, Environmental and Engineering Geophysical Society, Proceedings, 1490–1503.
- Liner, C. L., and Clapp, R. G., 2004a, Nonlinear pairwise alignment of seismic traces: 74th Ann. Internat. Mtg., Soc. of Expl. Geophys., Expanded Abstracts, 2072–2075.
- Liner, C. L., and Clapp, R. G., 2004b, Nonlinear pairwise alignment of seismic traces: *Geophysics*, in press.
- Liner, C., and Vlad, I., 2005, Analytical traveltimes for arbitrary multiples in constant velocity: 75th Ann. Internat. Mtg., Soc. of Expl. Geophys., Expanded Abstracts, accepted.
- Lomask, J., Biondi, B., and Shragge, J., 2004, Image segmentation for tracking salt boundaries: 74th Ann. Internat. Mtg., Soc. of Expl. Geophys., Expanded Abstracts, 2443–2446.
- Rosales, D., and Biondi, B., 2004a, Multicomponent azimuth moveout: submitted for publication in *Geophysics*.
- Rosales, D. A., and Biondi, B., 2004b, Acquisition geometry regularization for multicomponent data: 74th Ann. Internat. Mtg., Soc. of Expl. Geophys., Expanded Abstracts, 2052–2055.
- Rosales, D., and Biondi, B., 2005a, Converted waves common azimuth migration: 67th Mtg., Eur. Assoc. Geosc. Eng., Abstracts.
- Rosales, D. A., and Biondi, B., 2005b, Converted-waves angle-domain common-image gathers: 75th Ann. Internat. Mtg., Soc. of Expl. Geophys., Expanded Abstracts, accepted.
- Sava, P., and Biondi, B., 2004a, Wave-equation migration velocity analysis - I: Theory: *Geophysical Prospecting*, **52**, 593–606.
- Sava, P., and Biondi, B., 2004b, Wave-equation migration velocity analysis - II: Subsalt imaging examples: *Geophysical Prospecting*, **52**, 607–623.

- Sava, P., and Guitton, A., 2005, Multiple attenuation in the image space: *Geophysics*, **70**, V10–V20.
- Sava, P., Biondi, B., and Etgen, J., 2004a, Diffraction-focusing migration velocity analysis: 74th Ann. Internat. Mtg., Soc. of Expl. Geophys., Expanded Abstracts, 2395–2398.
- Sava, P., Biondi, B., and Etgen, J., 2004b, Diffraction-focusing migration velocity analysis with application to seismic and GPR data: *Geophysics*, in press.
- Shan, G., and Biondi, B., 2004, Imaging overturned waves by plane-wave migration in tilted coordinates: 74th Ann. Internat. Mtg., Soc. of Expl. Geophys., Expanded Abstracts, 969–972.
- Shan, G., and Biondi, B., 2005a, 3d wavefield extrapolation in laterally-varying tilted media: 75th Ann. Internat. Mtg., Soc. of Expl. Geophys., Expanded Abstracts, accepted.
- Shan, G., and Biondi, B., 2005b, Imaging steeply dipping reflectors in media by wavefield extrapolation: 75th Ann. Internat. Mtg., Soc. of Expl. Geophys., Expanded Abstracts, accepted.
- Shan, G., and Guitton, A., 2004, Migration of surface-related multiples: tests on the Sigsbee2B dataset: 74th Ann. Internat. Mtg., Soc. of Expl. Geophys., Expanded Abstracts, 1285–1288.
- Shragge, J., and Sava, P., 2004, Adaptive phase-rays wavefield extrapolation: 74th Ann. Internat. Mtg., Soc. of Expl. Geophys., Expanded Abstracts, 2044–2047.
- Tisserant, T., and Biondi, B., 2004, Residual move-out analysis with 3-D angle-domain common-image gathers: 74th Ann. Internat. Mtg., Soc. of Expl. Geophys., Expanded Abstracts, 2391–2394.
- Valenciano, A. A., Brown, M., Guitton, A., and Sacchi, M. D., 2004, Interval velocity estimation using edge-preserving regularization: 74th Ann. Internat. Mtg., Soc. of Expl. Geophys., Expanded Abstracts, 2431–2434.
- Valenciano, A. A., Biondi, B., and Guitton, A., 2005, Target-oriented wave-equation inversion: 75th Ann. Internat. Mtg., Soc. of Expl. Geophys., Expanded Abstracts.
- Wolf, K., Rosales, D., Guitton, A., and Claerbout, J., 2004, Robust moveout without velocity picking: 74th Ann. Internat. Mtg., Soc. of Expl. Geophys., Expanded Abstracts, 2423–2426.



SEP PHONE DIRECTORY

Name	Phone Login Name
Alvarez, Gabriel	723-1250 gabriel
Artman, Brad	723-9282 brad
Berryman, James	725-1334 berryman
Biondi, Biondo	723-1319 biondo
Claerbout, Jon	723-3717 jon
Clapp, Robert	725-1334 bob
Curry, Bill	723-0463 bill
Guitton, Antoine	725-1334 antoine
Jousselin, Pierre	723-3187 pierre
Lau, Diane	723-1703 diane
Lomask, Jesse	723-1250 lomask
Rosales, Daniel	723-1250 daniel
Sen, Satyakee	723-6006 ssen
Shan, Guojian	723-0463 shan
Shragge, Jeff	723-0463 jeff
Tang, Yaxun	723-3187 tang
Valenciano, Alejandro	723-9282 valencia
Vyas, Madhav	723-3187 madhav
Witten, Ben	723-3187 ben

SEP fax number: (650) 723-0683

E-MAIL

Our Internet address is “sep.stanford.edu”; i.e., send Jon electronic mail with the address “jon@sep.stanford.edu”.

WORLD-WIDE WEB SERVER INFORMATION

Sponsors who have provided us with their domain names are not prompted for a password when they access from work. If you are a sponsor, and would like to access our restricted area away from work, visit our website and attempt to download the material. You will then fill out a form, and we will send the username/password to your e-mail address at a sponsor company.

STEERING COMMITTEE MEMBERS, 2004-2005

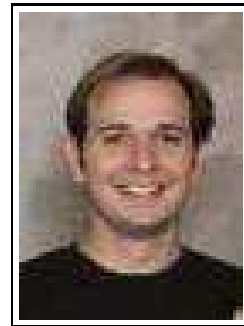
Name	Company	Telephone	E-Mail
Raymond Abma	BP	(281) 366-4604	abmar1@bp.com
Francois Audebert	CGG	(281) 646-2524	faudebert@cgg.com
Dimitri Bevc	3DGeo	(650) 969-3886	dimitri@3dgeo.com
Biondo Biondi	SEP	(650) 723-1319	biondo@sep.stanford.edu
Henri Calandra (Co-chair, 1st year)	TOTAL	(713) 647-3940	henri.calandra@total.com
Luis Canales	WesternGeco	(713) 806-5271	lcanales@houston.westerngeco.slb.com
Jon Claerbout	SEP	(650) 723-3717	jon@sep.stanford.edu
Richard Cook	Shell	(713) 245-7195	richard.cook@shell.com
Helmut Jakobowicz (Co-chair, 2nd year)	Veritas DGC	+44 1293 443219	helmut_jakubowicz@veritasdgc.com
Stewart Levin	Landmark Graphics	(303) 779-8080	salevin@lgc.com
Simon Spitz	CGG	(281) 646-2502	sspitz@cgg.com

Research Personnel

Gabriel Alvarez received a B.S. degree in Physics from the National University of Colombia in 1985 and an M.Sc. in Geophysics from the Colorado School of Mines in 1995, where he was a member of the Center for Wave Phenomena. From 1989 to 2000, he worked at the Instituto Colombiano del Petroleo (ICP), the Research and Development Division of Ecopetrol, the National Oil Company of Colombia. Joined SEP in 2000, and is currently working towards a Ph.D. in geophysics at Stanford University.



Brad Artman received his B.Sc. in Geophysical Engineering from the Colorado School of Mines in December 1996. He worked at Shell Deepwater Development Company in New Orleans in petrophysical and geophysical capacities until joining SEP in the fall of 2000 to work toward a Ph.D. Brad is a member of SEG and SPWLA.



James G. Berryman received a B.S. degree in physics from Kansas University (Lawrence) in 1969 and a Ph.D. degree in physics from the University of Wisconsin (Madison) in 1975. He subsequently worked on seismic prospecting at Conoco. His later research concentrated on seismic waves in rocks and sediments – at AT&T Bell Laboratories (1978-81) and at Lawrence Livermore National Laboratory (1981-), where he is currently a physicist in the Energy and Environment Directorate. He received the Maurice Anthony Biot Medal of the ASCE in May, 2005, for his work in the mechanics and acoustics of porous media containing fluids. Continuing research interests include acoustic, seismic, and electrical methods of geophysical imaging and studies of waves in porous media. He is a member of APS, AGU, ASA, and SEG.



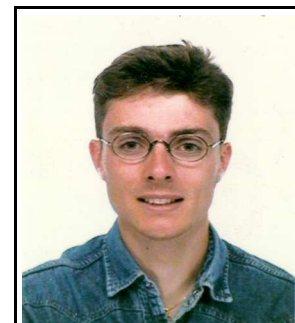
Biondo L. Biondi graduated from Politecnico di Milano in 1984 and received an M.S. (1988) and a Ph.D. (1990) in geophysics from Stanford. SEG Outstanding Paper award 1994. During 1987, he worked as a Research Geophysicist for TOTAL, Compagnie Francaise des Petroles in Paris. After his Ph.D. at Stanford, Biondo worked for three years with Thinking Machines Co. on the applications of massively parallel computers to seismic processing. After leaving Thinking Machines, Biondo started 3DGeo Development, a software and service company devoted to high-end seismic imaging. Biondo is now Associate Professor (Research) of Geophysics and leads SEP efforts in 3-D imaging. He is a member of SEG and EAGE.



Robert Clapp received his B.Sc. (Hons.) in Geophysical Engineering from Colorado School of Mines in May 1993. He joined SEP in September 1993, received his Masters in June 1995, and his Ph.D. in December 2000. He is a member of the SEG and AGU.



Antoine Guitton received a M.Sc. in geophysics from Université de Strasbourg, France in 1996 and from Stanford University in 2000. He received his Ph.D. from Stanford University in 2005. He was awarded Best Student Paper from the SEG in 1999 and received the EAGE Van Weelden award in 2004. He was research assistant at the Institut Francais du Petrole (Paris-1996/97) working on well seismic imaging and research geophysicist at CGG Houston (1997-98) working on multiples attenuation. He is now Senior Geophysicist for 3DGeo Inc. in Santa Clara, CA. He is a member of the SEG and EAGE.



Jeff Shragge graduated in 1998 with a BScH in Honours Physics from Queen's University in Kingston, Canada. After completing a MSc degree in 2001 in teleseismic imaging at the UBC in Vancouver, Canada, he spent 2001 and 2002 working for a small geophysical consulting company based out of Woburn, MA. He joined SEP in 2002, and is working towards a Ph.D. in Geophysics. His main research interest is migration and wavefield inversion. He is a member of SEG and AGU.



Alejandro A. Valenciano received a B.Sc. degree in Physics from Havana University (Cuba) in 1994, and a M.Sc. in Physics from Simon Bolivar University (Venezuela) in 1998. He worked in the Earth Science Department of PDVSA-INTEVEP from 1995 to 2001. He joined SEP to work towards a Ph.D in geophysics in the Fall of 2001.



Huazhong Wang graduated in April 1991 with M.S in Geophysics and in June 1997 with a Ph.D in Geophysics from School of Ocean and Earth Sciences, Tongji University, Shanghai, China. We worked with BGP for three years as a research engineer and he became a faculty member in Tongji University after receiving his Ph.D. He is a visitng scholar now at SEP. He is a member of SEG.



SPONSORS OF THE STANFORD EXPLORATION PROJECT, 2004-2005

Amerada Hess Corporation
 One Allen Center
 500 Dallas St.
 Houston, TX 77002-4800
 USA
 tel: (713) 609-5829
 fax: (713) 609-5666
 contact: Scott A. Morton
 email: morton@hess.com

ChevronTexaco E&P Technology Co.
 6001 Bollinger Canyon Rd.
 Bldg. D1084
 San Ramon, CA 94583-2324
 USA
 tel: (925) 842-0257
 fax: (925) 842-2061
 contact: Yue Wang
 email: yue.wang@chevrontexaco.com

Aramco Services Company
 Saudi Aramco
 P.O. Box 750
 EXPEC Bldg., X-1370
 Dhahran 31311
 Saudi Arabia
 tel: 966 (3) 874 7262
 fax: 966 (3) 873 1020
 contact: Mohammed N. Alfaraj
 email: mohammed.faraj@aramco.com

ConocoPhillips
 P.O. Box 2197
 600 N. Dairy Ashford St.
 Lobo 3000
 Houston, TX 77252-1100
 USA
 tel: (281) 293-5696
 fax: (281)
 contact: Robert M. Habiger
 email: rob.m.habiger@conocophillips.co

BP
 200 Westlake Park Blvd., #1018
 Houston, TX 77079-2604
 USA
 tel: (281) 366-3611
 fax: (281) 366-5856
 contact: John T. Etgen
 email: john.etgen@bp.com

ENI/AGIP
 dept. RIGE
 via Emilia 1
 I-20097 S. Donato Milanese
 Italy
 tel: 39 (02) 520 62153
 fax: 39 (02) 520 62173
 contact: Vittorio De Tomasi
 email: vittorio.detomasi@agip.it

CGG Americas, Inc.
 16430 Park Ten Place
 Houston, TX 77084
 USA
 tel: (281) 646-2525
 fax: (281) 646-2620
 contact: Francois S. Audebert
 email: faudebert@cgg.com

ExxonMobil Upstream Research Co.
 URC-GW3-953A
 P.O. Box 2189 (77252-2189)
 3319 Mercer St.
 Houston, TX 77027-6019
 USA
 tel: (713) 431-6011
 fax: (713) 431-6161
 contact: Thomas A. Dickens
 email: tom.a.dickens@exxonmobil.com

SPONSORS OF THE STANFORD EXPLORATION PROJECT, 2004-2005

Fairfield Industries Inc.
14100 Southwest Fwy.
Suite 100
Sugar Land, TX 77478
USA
tel: (281) 275-7597
fax: (281) 275-7660
contact: Bill Schneider, Jr.
email: bschneiderjr@fairfield.com

Paradigm Geophysical Corporation
Two Memorial City Plaza
820 Gessner, Suite 400
Houston, TX 77024-4262
USA
tel: (713) 393-4979
fax: (713) 393-4801
contact: Orhan Yilmaz
email: yilmaz@paradigmgeo.com

GX Technology Corporation
2101 Citywest Blvd.
Building III, Suite 900
Houston, TX 77042
USA
tel: (713) 789-7250
fax: (713) 789-7201
contact: Nick Bernitsas
email: nxb@gxt.com

Paulsson Geophysical Services, Inc.
1215 W. Lambert Rd.
Brea, CA 92821-2819
USA
tel: (562) 697-9711
fax: (562) 697-9773
contact: Martin Karrenbach
email: martin.karrenbach@paulsson.com

Landmark Graphics Corporation
1805 Shea Center Dr.
Suite 400
Highlands Ranch, CO 80129-2258
USA
tel: (303) 779-8080
fax: (303) 796-0807
contact: Stewart A. Levin
email: salevin@lgc.com

Petrobras - UN-EXP/ST/TG
Av. Rep. Chile 65
sala 1402-B3, Centro
Rio de Janeiro, RJ 20035-900
Brazil
tel: 55 (21) 2534-2706
fax: 55 (21) 2534-1076
contact: Carlos A. Cunha Filho
email: ccunha@petrobras.com.br

Norsk Hydro Produksjon a.s
PB 7190
Sandsliveien 90
Bergen, N-5020
Norway
tel: (47) 5599 6861
fax: (47) 5599 6970
contact: Arnfinn Sagehaug
email: sagehaug@hydro.com

PGS Technology Division
15150 Memorial Dr.
Houston, TX 77079
USA
tel: (713) 735-6322
fax: (713) 532-6774
contact: Ruben D. Martinez
email: ruben.martinez@pgs.com

SPONSORS OF THE STANFORD EXPLORATION PROJECT, 2004-2005

Shell International E&P Inc.
 P.O. Box 481 (77001-0481)
 3737 Bellaire Blvd., BTC-1036
 Houston, TX 77025-1206
 USA
 tel: (713) 245-7195
 fax: (713) 245-7339
 contact: Richard W. Cook
 email: richard.cook@shell.com

TOTAL E&P USA, Inc.
 One Memorial City
 800 Gessner Rd., Ste. 700
 Houston, TX 77024-4284
 USA
 tel: (713) 647-3940
 fax: (713) 647-3875
 contact: Henri Calandra
 email: henri.calandra@total.com

Statoil ASA
 Statoil Research Centre
 Arkitekt Ebbellsvei 10, Rotvoll
 Trondheim, N-7005
 Norway
 tel: (47) 73584917
 fax: (47) 73584665
 contact: Constantin Gerea
 email: geco@statoil.com

Deepwater USA, UNOCAL
 14141 Southwest Frwy.
 Sugar Land, TX 77478
 USA
 tel: (281) 287-7481
 fax: (281) 287-5360
 contact: Philip S. Schultz
 email: phil.schultz@unocal.com

TGS-NOPEC Geophysical Company
 4434 Bluebonnet Dr.
 Stafford, TX 77477-2904
 USA
 tel: (713) 860-2273
 fax: (713) 334-3308
 contact: Young Kim
 email: yckim@tgsnopec.com

Veritas DGC Ltd.
 Crompton Way
 Manor Royal Estate
 Crawley, W. Sussex RH10 2QR
 England, U.K.
 tel: 44 (1293) 443220
 fax: 44 (1293) 443010
 contact: Helmut Jakubowicz
 email: helmut_jakubowicz@veritasdgc.com

3DGeo Development Inc.
 4633 Old Ironsides Dr.
 Suite 401
 Santa Clara, CA 95054
 USA
 tel: (408) 450 7840, x102
 fax: (408) 450 7809
 contact: Dimitri Bevc
 email: dimitri@3dgeo.com

Weinman GeoScience
 17103 Preston Rd.
 Suite 200 N.
 Dallas, TX 75248-1332
 USA
 tel: (972) 818-2550
 fax: (972) 818-2553
 contact: Barry L. Weinman
 email: barryw@weinmangeoscience.com

SPONSORS OF THE STANFORD EXPLORATION PROJECT, 2004-2005

WesternGeco
Houston Technology Center
10001 Richmond Ave.
Houston, TX 77042-4205
USA
tel: (713) 806-5271
fax: (713) 689-5757
contact: Luis L. Canales
email: lcanales@houston.westerngeco.slb.com